
JSCSEN 89(7-8)939-1121(2024)

ISSN 1820-7421(Online)

Journal of the Serbian Chemical Society

VOLUME 89

NO 7-8

BELGRADE 2024

Available on line at



www.shd.org.rs/JSCS/

The full search of JSCS

is available through

DOAJ DIRECTORY OF

OPEN ACCESS

JOURNALS

www.doaj.org

The **Journal of the Serbian Chemical Society** (formerly Glasnik Hemijskog društva Beograd), one volume (12 issues) per year, publishes articles from the fields of chemistry. The **Journal** is financially supported by the **Ministry of Education, Science and Technological Development of the Republic of Serbia**.

Articles published in the **Journal** are indexed in Clarivate Analytics products: **Science Citation Index-Expanded™** – accessed via **Web of Science®** and **Journal Citation Reports®**.

Impact Factor announced on 28 June, 2023: **1.000; 5-year Impact Factor: 1.100.**

Articles appearing in the **Journal** are also abstracted by: **Scopus**, **Chemical Abstracts Plus (CAplusSM)**, **Directory of Open Access Journals**, **Referativni Zhurnal (VINITI)**, **RSC Analytical Abstracts**, **EuroPub**, **Pro Quest** and **Asian Digital Library**.

Publisher:

Serbian Chemical Society, Karnegijeva 4/III, P. O. Box 36, 1120 Belgrade 35, Serbia
tel./fax: +381-11-3370-467, E-mails: **Society** – shd@shd.org.rs; **Journal** – jscs@shd.org.rs
Home Pages: **Society** – <http://www.shd.org.rs/>; **Journal** – <http://www.shd.org.rs/JSCS/>
Contents, Abstracts and full papers (from Vol 64, No. 1, 1999) are available in the electronic form at the Web Site of the **Journal** (<http://www.shd.org.rs/JSCS/>).

Internet Service:

Former Editors:

Nikola A. Pušin (1930–1947), **Aleksandar M. Leko** (1948–1954),
Panta S. Tutundžić (1955–1961), **Miloš K. Mladenović** (1962–1964),
Dorđe M. Dimitrijević (1965–1969), **Aleksandar R. Despić** (1969–1975),
Slobodan V. Ribnikar (1975–1985), **Dragutin M. Dražić** (1986–2006).

Editor-in-Chief:

BRANISLAV Ž. NIKOLIĆ, Serbian Chemical Society (E-mail: jscs-ed@shd.org.rs)

Deputy Editor:

DUŠAN SLADIĆ, Faculty of Chemistry, University of Belgrade

Sub editors:

Organic Chemistry

DEJAN OPSENICA, Institute of Chemistry, Technology and Metallurgy, University of Belgrade

Biochemistry and Biotechnology

JÁNOS CSANÁDI, Faculty of Science, University of Novi Sad
OLGICA NEDIĆ, INEP – Institute for the Application of Nuclear Energy, University of Belgrade

Inorganic Chemistry

BILJANA GLIŠIĆ, Faculty of Science, University of Kragujevac

Theoretical Chemistry

IVAN JURANIĆ, Serbian Chemical Society

Physical Chemistry

LJILJANA DAMJANOVIĆ-VASILIĆ, Faculty of Physical Chemistry, University of Belgrade

Electrochemistry

SNEŽANA GOJKOVIĆ, Faculty of Technology and Metallurgy, University of Belgrade

Analytical Chemistry

RADA BAOŠIĆ, Faculty of Chemistry, University of Belgrade

Polymers

BRANKO DUNJIĆ, Faculty of Technology and Metallurgy, University of Belgrade

Thermodynamics

MIRJANA KIJEVČANIN, Faculty of Technology and Metallurgy, University of Belgrade

Chemical Engineering

TATJANA KALUDEROVIĆ RADOIĆIĆ, Faculty of Technology and Metallurgy, University of Belgrade

Materials

RADA PETROVIĆ, Faculty of Technology and Metallurgy, University of Belgrade

Metallic Materials and Metallurgy

ANA KOSTOV, Mining and Metallurgy Institute Bor, University of Belgrade

Environmental and Geochemistry

VESNA ANTIĆ, Faculty of Agriculture, University of Belgrade

History of and Education in Chemistry

DRAGICA TRIVIĆ, Faculty of Chemistry, University of Belgrade

English Language Editors:

LYNNE KATSIKAS, Serbian Chemical Society

Office:

VLATKA VAJS, Serbian Chemical Society

JASMINA NIKOLIĆ, Faculty of Technology and Metallurgy, University of Belgrade

Technical Editors:

VLADIMIR PANIĆ, Institute of Chemistry, Technology and Metallurgy, University of Belgrade

Journal Manager & Web Master:

MARIO ZLATOVIĆ, Faculty of Chemistry, University of Belgrade

Office:

VERA ĆUŠIĆ, Serbian Chemical Society

Editorial Board

From abroad: **R. Adžić**, Brookhaven National Laboratory (USA); **A. Casini**, University of Groningen (The Netherlands); **G. Cobb**, Baylor University (USA); **D. Douglas**, University of British Columbia (Canada); **G. Inzelt**, Etvos Lorand University (Hungary); **J. Kenny**, University of Perugia (Italy); **Ya. I. Korenman**, Voronezh Academy of Technology (Russian Federation); **M. D. Lechner**, University of Osnabrueck (Germany); **S. Macura**, Mayo Clinic (USA); **M. Spitteler**, INFU, Technical University Dortmund (Germany); **M. Stratakis**, University of Crete (Greece); **M. Swart**, University of Girona (Cataluna, Spain); **G. Vunjak-Novaković**, Columbia University (USA); **P. Worsfold**, University of Plymouth (UK); **J. Zagal**, Universidad de Santiago de Chile (Chile).

From Serbia: **B. Abramović**, **V. Antić**, **R. Baošić**, **V. Beškoski**, **J. Csanadi**, **Lj. Damjanović-Vasilić**, **A. Dekanski**, **V. Donđur**, **B. Dunjić**, **M. Duran**, **B. Glišić**, **S. Gojković**, **I. Gutman**, **B. Jovančićević**, **I. Juranić**, **T. Kaluderović**, **Radiović**, **L. Katsikas**, **M. Kijevečanin**, **A. Kostov**, **V. Leovac**, **S. Milonjić**, **V.B. Mišković-Stanković**, **O. Nedlić**, **B. Nikolić**, **J. Nikolić**, **D. Opsenica**, **V. Panić**, **M. Petkovska**, **R. Petrović**, **I. Popović**, **B. Radak**, **S. Ražić**, **D. Sladić**, **S. Sovilj**, **S. Šerbanović**, **B. Šolaja**, **Ž. Tešić**, **D. Trivić**, **V. Vajs**, **M. Zlatović**.

Subscription: The annual subscription rate is **150.00 €** including postage (surface mail) and handling. For Society members from abroad rate is **50.00 €**. For the proforma invoice with the instruction for bank payment contact the Society Office (E-mail: shd@shd.org.rs) or see JSCS Web Site: <http://www.shd.org.rs/JSCS/>, option Subscription.

Godišnja pretplata: Za članove SHD: **2.500,00 RSD**, za penzionere i studente: **1.000,00 RSD**, a za ostale: **3.500,00 RSD**: za organizacije i ustanove: **16.000,00 RSD**. Uplate se vrše na tekući račun Društva: **205-13815-62**, poziv na broj **320**, sa naznakom "pretplata za JSCS".

Nota: Radovi čiji su svi autori članovi SHD prioritetno se publikuju.
Odlukom Odbora za hemiju Republičkog fonda za nauku Srbije, br. 66788/1 od 22.11.1990. godine, koja je kasnije potvrđena odlukom Savete Fonda, časopis je uvršten u kategoriju međunarodnih časopisa (**M-23**). Takođe, aktom Ministarstva za nauku i tehnologiju Republike Srbije, 413-00-247/2000-01 od 15.06.2000. godine, ovaj časopis je proglašen za publikaciju od posebnog interesa za nauku. **Impact Factor** časopisa objavljen 28. juna 2023. godine je **1,000**, a petogodišnji **Impact Factor 1,100**.



Journal of the Serbian Chemical Society

JSCS-info@shd.org.rs • www.shd.org.rs/JSCS

J. Serb. Chem. Soc. Vol. 89, No. 7–8 (2024)

CONTENTS*

<i>E. J. Mollova, E. D. Ivanova, S. Ch. Turmanova and A. N. Dimitrov: Microplastics – Ecosystem pollutants (Review).....</i>	939
Organic Chemistry	
<i>P. Mishra, S. Nandi, A. Chatterjee, T. Nayek, S. Basak, A. Kumar Halder and A. Mukherjee: Development of 2D and 3D QSAR models of pyrazole derivatives as acetylcholine esterase inhibitors.....</i>	981
Biochemistry and Bioengineering	
<i>V. B. Jovanović, M. R. Nikolić and S. D. Stojanović: In silico studies of phycobilins as potential candidates for inhibitors of viral proteins associated with COVID-19.....</i>	997
Inorganic Chemistry	
<i>S. K. Belošević, S. B. Novaković, M. V. Rodić, V. M. Leovac, L.J. S. Vojinović-Ješić, G. A. Bogdanović and M. M. Radanović: Introducing a novel crystal form of pyruvic acid thiosemicarbazone and its sodium salt.....</i>	1011
Theoretical Chemistry	
<i>Y. Sivrikaya, H. C. Sakarya, G. Kılıç, S. F. Ekti and M. Yandımoğlu: New pyrene and fluorene-based π-conjugated Schiff bases: Theoretical and experimental investigation of optical properties</i>	1025
<i>A. S. Salihu, W. M. N. H. Wan Salleh and T. H. Ogunwa: Computational exploration of flavonoids from the genus <i>Knema</i> with anti-inflammatory potential.....</i>	1039
Analytical Chemistry	
<i>I. Jovančićević, M. Antić, G. Gajica and J. Schwarzbauer: Co-pyrolysis of various plastic waste components as an environmentally sustainable source of alternative fuels</i>	1053
Thermodynamics	
<i>M. B. Vraneš and J. J. Panić: The influence of conversion creatine and guanidinoacetic acid from zwitterionic to cationic form on their solubility in water – A thermodynamic study</i>	1067
Chemical Engineering	
<i>S. O. Meena, M. Vashishtha and Meenu: Neem (<i>Azadirachtaindica</i>) oil coated urea as a novel controlled release fertilizer: Physical and chemical analysis of structure and its nutrient release behaviour.....</i>	1077
Metallurgy and Metallic Materials	
<i>S. Rengarajan, R. Muhammed, D. Vijayan and M. Abrar: Enhancing longevity and performance: The effects of ZrO₂ and TaC coatings on pistons in internal combustion engines</i>	1093
Environmental	
<i>R. Ghibate, M. B. Baaziz, A. Amechrouq, R. Taouil and O. Senhaji: The performance of an eco-friendly adsorbent for methylene blue removal from aqueous solution: Kinetic, isotherm and thermodynamic approaches</i>	1107

Published by the Serbian Chemical Society
Karnegijeva 4/III, P.O. Box 36, 11120 Belgrade, Serbia
Printed by the Faculty of Technology and Metallurgy
Karnegijeva 4, P.O. Box 35-03, 11120 Belgrade, Serbia

* For colored figures in this issue please see electronic version at the Journal Home Page:
<http://www.shd.org.rs/JSCS/>



REVIEW

Microplastics – Ecosystem pollutants

ELENA J. MOLLOVA¹, EMILIA D. IVANOVA^{1,2}, SEVDALINA CH. TURMANOVA²
and ALEKSANDAR N. DIMITROV^{1*}

¹Faculty of Natural Sciences, Assen Zlatarov University, 8010 Burgas, Bulgaria and

²Faculty of Technical Sciences, Assen Zlatarov University, 8010 Burgas, Bulgaria

(Received 16 May, revised 10 July, accepted 6 October 2023)

Abstract: The presence of microplastics in different ecosystems has been intensively studied since the beginning of the 21st century. They have since been found in all components of the environment as well as in a number of organisms. Microplastics (MPs) is a term for particles whose size is 1 μm–5 mm that are formed during the breakdown of larger plastic products or are produced in microsizes for various industrial and cosmetic products. The distribution of these particles is due to their rapid transportation over large distances which is facilitated mainly by their small size and low density. There are still no uniform methods and standardised procedures for sampling and analysis. Therefore, the facts about the occurrence, distribution and threats to ecosystems and human health from MPs are not yet fully understood. This literature review is a broad presentation of the state of knowledge on the distribution of MPs in the atmosphere, water, soil and organisms. In addition, this document describes the most widely used methods for separation, identification and characterisation of MPs.

Keywords: microplastics; environmental protection; toxicological effects; health impacts.

CONTENTS

1. INTRODUCTION
2. IN THE AIR
3. IN THE WATER
4. IN THE SOIL
5. FROM THE TRAFFIC
6. IN HUMANS
 - 6.1. *To the digestive system*
 - 6.2. *To respiratory system*
 - 6.3. *To the nervous system*
 - 6.4. *To the placental barrier*

*Corresponding author. E-mail: adimitrov@uniburgas.bg
<https://doi.org/10.2298/JSC230516073M>

7. SEPARATION, IDENTIFICATION AND CHARACTERIZATION OF MICROPLASTICS
8. CONCLUSION

1. INTRODUCTION

Polymeric materials pose a serious threat to the environment and human health when they enter ecosystems. Once inside, they slowly degrade to microplastics, pollute soil, water, air and cause biodiversity loss. In 2021, more than 390 million tons of plastic were produced worldwide. “Plastics – The Facts” announced in 2022 that 90 % of plastic produced were polypropylene (PP), high- and low-density polyethylene (HDPE and LDPE), polyvinyl chloride (PVC), polyurethane (PUR), polyethylene terephthalate (PET) and polystyrene (PS), which are the most commonly used materials in packaging, construction, automotive, electronic and agricultural use.^{1–3}

Factors such as hydrolysis, ultraviolet light irradiation, wave and wind effects, oxidative decomposition, biodegradation and biological uptake gradually break down plastic waste into smaller particles. Physical, chemical and biological processes reduce the size and change their shape, color, concentration depending on the exposure time, which plays a crucial role in assessing their impact on the environment.^{3–7}

The size of plastics is the most commonly used criterion for determining their class and ecological importance. Depending on their size, plastics can be classified as nano-, micro- or macroplastics. The size of plastics affects the way they interact with biota and the environment. Some plastic particles can pass through the digestive tract of living organisms without harming them, while others (1–4 µm PE, 1–10 µm PS) can penetrate into cells and cause various cytotoxic effects.⁸ According to their size, plastic particles are divided into mega (>1 m), macro (25 mm–1 m), meso (5–25 mm), micro (1 µm–5 mm) and nano (<1 µm), Fig. 1.⁹

Microplastic (MP) are observed in most living environment and their concentrations are expected to increase in the coming decades, given the ongoing and in places increased production of synthetic polymer products.¹ Authors review the status of the occurrence and transfer of MP in and between three of the Earth’s subsystems – atmosphere, lithosphere and hydrosphere. Microplastics are observed in all possible environments from air, sediments, soils, freshwater, seawater and organisms, including humans. Their occurrence and distribution are influenced by their characteristics and interaction with the environment, particle mobility and transport processes.¹⁰ In the lithosphere, significant amounts of MP (PP, PE, PS, PET, PES) accumulate (25 particles/L in landfill sludge)¹¹.

The atmosphere plays an important role in the transfer of MP, with higher concentrations (175–300 particles/m³) occurring in the more densely populated

areas. In the hydrosphere, freshwater ecosystems alternate transfer of MP (rivers) and deposition (lakes), with flow velocity identified as a key factor determining the movement and fate of MP. Conversely, marine ecosystems act as a major sink for MP pollution (*e.g.*, MP comprise 94 %, approximately 1.7 trillion pieces, of plastic pieces in the Great Pacific Garbage Patch), driven by direct deposition or by transport *via* the atmosphere or fresh water conveyance systems (*e.g.*, streams, rivers or ice sheets). Once ingested by organisms, and confirmed trophic transfers and bioaccumulation, plastic particles can accumulate in or affect fauna, flora, microbes and humans (Fig. 2).¹¹

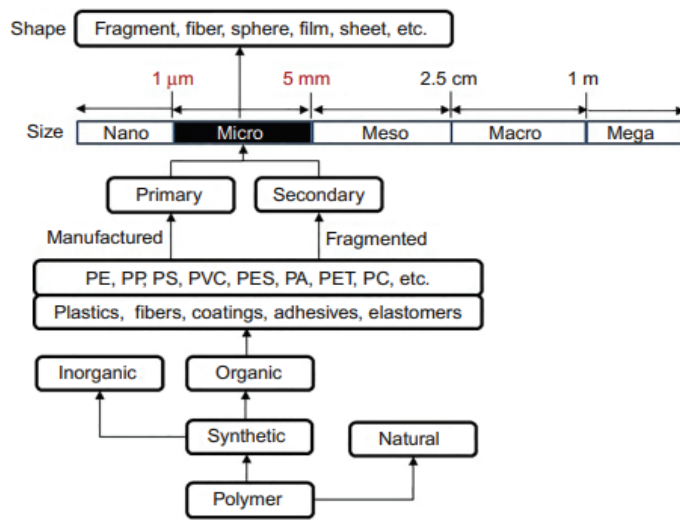


Fig. 1. Size and types of microplastics.⁹

High degradation resistance, lack of proper recycling and inadequate management lead to release and/or disposal of plastics into the environment and their significant accumulation as a heterogeneous group of particles in ecosystems (Fig. 1), where natural degradation plastic waste can persist for decades (Fig. 3).¹²

2. IN THE AIR

Air is the medium in which suspended atmospheric microplastics (SAMPs) are spread, which are small particles of plastic materials up to 5 mm in size. These particles can have different origins, shapes, colors and chemical compositions, depending on their source and the physical and chemical processes they are subjected to in the atmosphere. SAMPs can be carried over long distances by wind, dispersed by turbulence or deposited on the surface by precipitation, sedimentation or retrieval. The speed and direction of the transfer depend on many factors, such as the size, shape, density and electric charge of the MPs, as well as on the characteristics of the atmosphere, such as temperature, humidity, pressure, *etc.*¹³

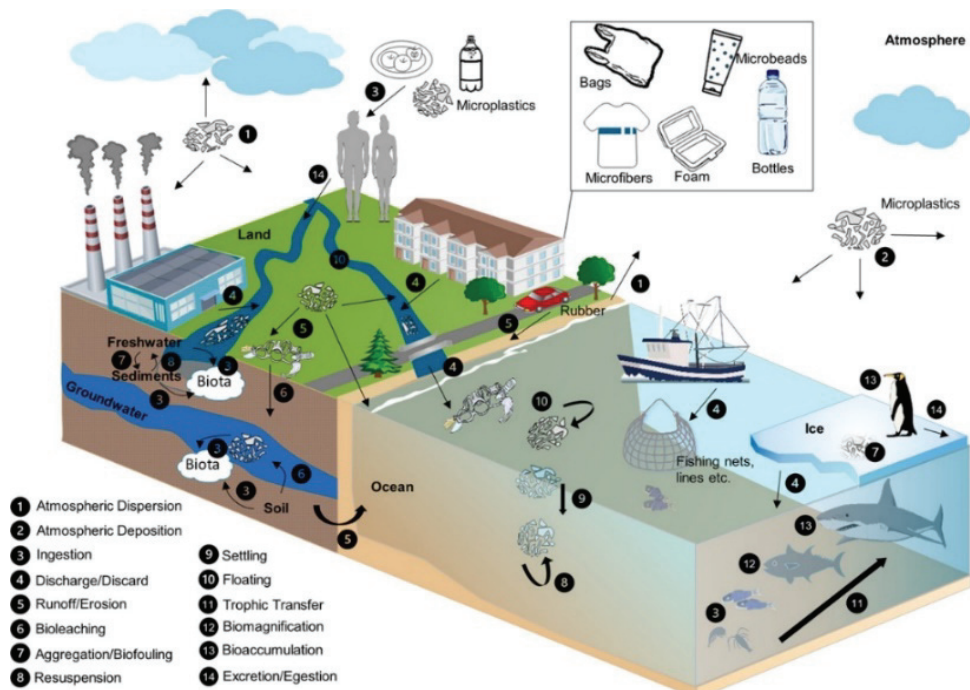


Fig. 2. Emergence and transport of microplastics.

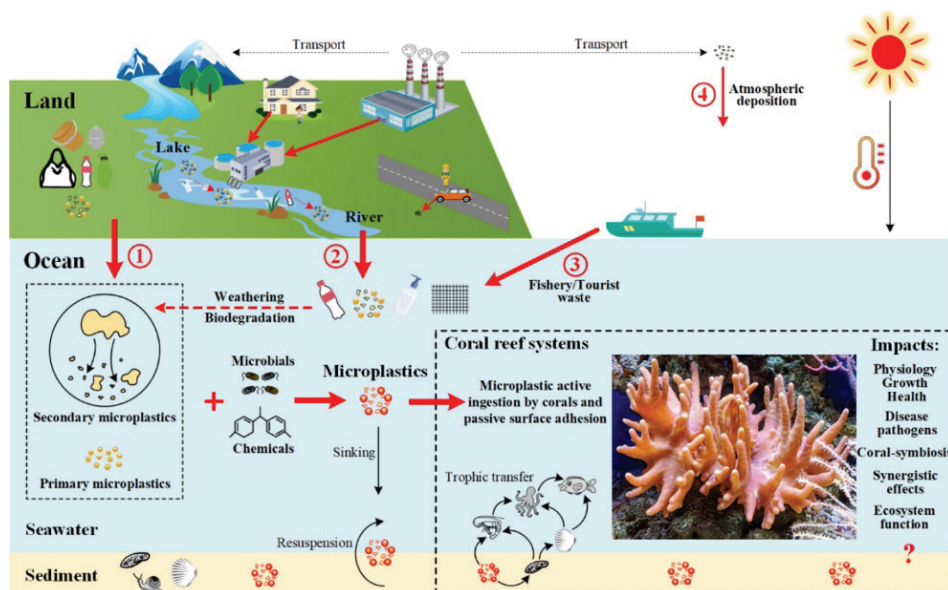


Fig. 3. Propagation of plastics.

SAMPs can be emitted from the atmosphere in various ways: by rain, snow or other types of precipitation, by sedimentation on surfaces such as soil, plants or buildings or by extraction from other agents namely gravity, magnetic field or chemical reactions. This process is called deposition and is important for the distribution of MPs in the environment.¹⁴

Some studies have shown that the atmosphere is a significant source of MPs for other environments, such as oceans, seas, rivers, lakes or soil. For example, in large cities such as Paris, Dongguan or London, high concentrations of microplastics in atmospheric deposition have been measured.^{15–17} These deposits can be influenced by urban rivers, which serve as secondary sources of MPs for the atmosphere.¹⁶

Also, it is shown that SAMPs can be transported from the oceans to the continents by aerosolization (by waves and bubble bursting) at the sea surface.¹³ The transport and deposition patterns of SAMPs play an important role in determining the sources and potential effects of these particles in different environments.¹⁸

SAMPs transport and deposition models are key to understanding pathways and the fate of plastic pollutants in the environment. These models can provide information on the sources, distribution and accumulation of MPs in different ecosystems, as well as on interactions between the marine and terrestrial environments.^{19,20} With the help of models, we can assess the risk of plastic pollution for human health and biodiversity.^{13,21,22}

For the modelling of SAMPs transport and deposition, different approaches are used, such as Lagrangian atmospheric models, Euler atmospheric models and global climate models (FLEXPART, HYSPLIT and LAGRANTO).^{13,23,24} Lagrangian atmospheric models trace the trajectories of individual particles in the atmosphere and can determine potential regions of origin and acceptance of SAMPs. These models can also give detailed information about the characteristics of the SAMPs, such as height, speed, distance and residence time in the atmosphere.^{13,25}

Factors that affect the transport and deposition of SAMPs include the size, shape, density and morphology of the particles.

According to Dris *et al.* the small particles, have a greater tendency to linger in the atmosphere and have the prospect of being transported to distant regions.¹⁴ The shape and density determine the transfer rate and the ability to mix with other atmospheric particles.¹⁹ The morphology can also determine the zone of influence for MPs deposition after they are carried away from the point sources. As an example, one can mention the morphology of the microfilm as thin and flat particles, with a wide surface area, facilitating their transfer compared to fragments of comparable sizes.¹³

It is noted that additional factors such as site topography, climate and meteorological conditions (*e.g.*, precipitation) also have a perceptible influence on the transport, dissipation and deposition of air MPs.¹³ Wind, snowfall, temperature,

precipitation and atmospheric pressure in the lower atmosphere have been proven to determine the deposition concentration profile of the MPs. Given the temperature, the vertical gradient supports the upward movement of MP, although they may be retained in the lower atmospheric layers, especially when there is temperature inversion, and subsequently cause episodic pollution.

There is a relationship between wind speed, turbulence, wind direction (vertical or horizontal), increase in dispersion and the amount of MPs in atmospheric precipitation. Research has found that small plastic materials can be carried to greater heights than the wind and subsequently subjected to dry or wet deposition.²⁶

The transfer of microplastics from the atmosphere to different environments is a serious environmental problem that requires deeper investigation. According to scientific sources, MPs were found inland, in marine and remote areas, polar regions and glaciers.^{27–30} This means that MPs can get into the water resources, soil and food chain. One of the main factors for the spread of MPs is atmospheric deposition, which depends on the concentration of particulate matter in the air. In urban areas where dust pollution is higher, street dust can accumulate in street dust and be washed away by rain or snow, therefore street dust is a potentially important source of microplastic pollution in the urban environment.³¹

Analysing the characteristics of atmospheric deposition in the urban area, the contribution of atmospheric deposition to microplastic pollution in urban waters was determined.³² The MPs deposition flux showed moderate to strong correlation with particulate matter (PM) concentrations in the atmosphere, especially PM_{2.5} concentration (R^2 0.76–0.93), suggesting that PM_{2.5} concentration could serve as an indicator to estimate the deposition flux of microplastics.

Because of their size, MPs can accumulate in dust and soil, and can eventually be carried into the food chain and hence to humans.^{33,34} In addition, they can be easily suspended in the atmosphere and retained due to their low density and, through external factors, can reach the respiratory tract of living organisms.³⁵

3. IN THE WATER

In the aquatic environment, microplastics are subject to various factors that affect their behaviour and fate. One of these factors is the degradation of larger plastic waste under the action of chemical, physical and biological processes. These processes lead to the formation of a heterogeneous group of particles that have different characteristics such as size, density, shape, chemical composition, colour and origin. The shape of MPs determines their origin and source. The density of microplastics determines their distribution in different layers of water. The chemical composition of MPs determines their stability and reactivity. These particles can be classified according to their residence time in the aquatic environment and their potential impact environment and human health.

MPs can be transported over long distances by atmospheric movement and wind directions, meteorological factors including wave currents, cyclones, tides, river hydrodynamics, water runoff and wastewater treatment plants. They can reach various aquatic ecosystems, such as rivers, estuaries, lakes, seas and oceans.³⁶ Some of the main routes for penetration of MPs into the aquatic environment are direct discharge, wastewater from treatment plants and surface runoff. According to recent studies, urban drainage systems can be an essential source of microplastics to aquatic ecosystems.^{37–39}

The presence and distribution of MPs in the marine environment depend on many factors, such as the salinity of seawater, polymer density, particle size and shape. Studies have shown that the marine environment that is closer to urban areas has higher levels of MPs and aquatic animals from these areas show a high accumulation of microplastics in their tissues. This can lead to disruption of their food chain, physiology and behaviour.⁴⁰ Size and shape are important physical properties for characterizing the source and origin (primary or secondary) as well as their potential to produce physical and/or physiological effects on biota. For example, the dominance of fibres found in samples collected in the Black Sea is associated with wastewater, runoff, ports, vessels and fishing activities.⁴¹

Although marine plastic litter is recognized as a global problem, there is insufficient data on the extent of pollution in the Black Sea.

The brief overview of scientific studies that look at the pollution of the Black Sea with marine plastic pollutants shows that the problem is serious and further studies are needed to clarify their extent and distribution.

A study conducted in 2020 found large amounts of floating marine litter (60.3–93.8 pieces/km² bottles, packaging, fragments and bags) and MPs with concentrations (1.14×10^4 – 1.91×10^5 pieces/km², 0.33–490.52 g/km²). However, MPs concentrations along the Southwest coast of the Black Sea are on average lower than those in other parts of the Black Sea, the Baltic Sea and the Mediterranean Sea.⁴²

Another study conducted during the period from 2009 to 2020 focused on the presence of MPs in seawater on the southeastern coast of the Black Sea. The study shows that MPs sizes range from 118 to 4998 µm and that the most common plastics are polyethylene (44.9 %) and polyethylene terephthalate (25.3 %). No significant spatio-temporal changes in the presence of MPs in seawater are noticeable (Fig. 4).⁴³

The comprehensive assessment of waste pollution along the Bulgarian Black Sea coast presents data collected during the period from 2016 to 2019 on the basis of studies conducted on 10 beaches and around the channel between the sea and Varna Lake during the summer and autumn seasons.⁴⁴ The summarized data show that over 150,000 elements have been registered, removed and classified into 8 main groups of material types on an aggregated basis. The largest amount

of pollutants, approximately 80,000 pieces were reported in 2017, followed by 50,000 units in 2019 and 40,000 in 2018. The majority of pollutants are in the category “artificial polymeric materials”, and their percentage varies slightly within the period from 2017 to 2018, decreasing to 60 % in 2018. The average annual density of pollutants within the entire coastline of the country ranges from 0.6 pieces/m² in 2017 to 0.2 pieces/m² in 2019 (Figs. 5 and 6). These data provide useful information on the pollution of the Black Sea coastal region of Bulgaria and can be used to formulate strategies to reduce pollution in the future.⁴⁴

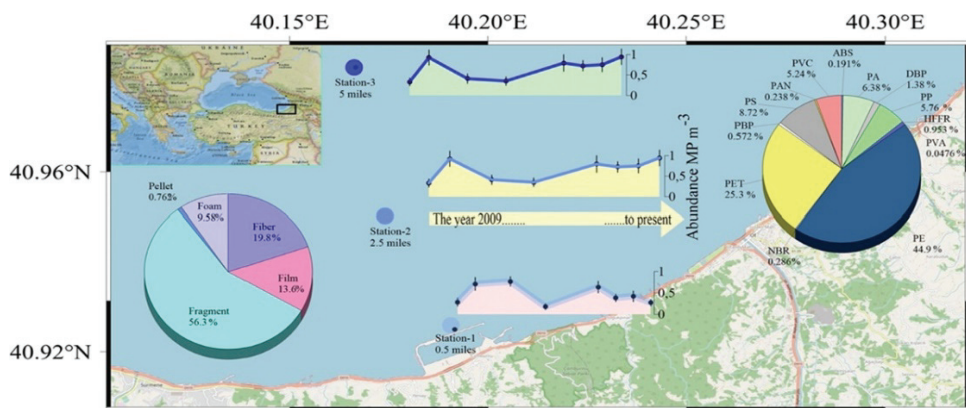


Fig. 4. Presence of microplastics in the Southeast coast of the Black Sea.



Fig. 5. Map with the surveyed beaches along the Bulgarian Black Sea coast.

One of the beaches is classified as “very dirty” due to intense pollution from land-based sources, such as coastal tourism, recreational fishing, people, *etc.* Scientists have analysed the most common plastic items on the beach and found that those associated with smoking are the most. Among them are cigarette butts and filters, as well as cups, caps and bottles. Over the past two years, there has been a decline in the amount of plastic on the beach, but action still needs to be

taken to reduce pollution and raise public awareness of the harm of plastic in the marine environment.^{44–46}

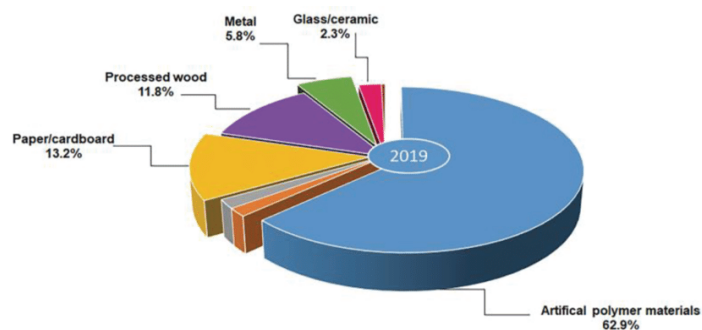


Fig. 6. Total litter items per category type in percentage, 2019.

In the scientific article from 2022, Terzi *et al.* have studied the distribution and properties of microplastics in the aquatic environment along the southern Black Sea coast in Turkey. They have found that 70 % of the MPs are very small (below 2.5 mm) and have a fibre or fragment shape. The average concentration of MPs in the sediment samples was 64.06 ± 8.95 particles/kg and in the seawater samples it was 18.68 ± 3.01 particles/m³. Analysis of the chemical composition of MPs has shown that styrene acrylonitrile copolymer (40.53 %), polyethylene terephthalate (38.75 %) and polyethylene (6.91 %), and in sea water – polyethylene terephthalate (57.26 %), polyethylene (13.52 %) and polypropylene (11.24 %). The authors found no correlation between the amount of MPs in sediments and in seawater, as well as between the demographic characteristics of adjacent settlements and pollution by MPs.⁴⁷

Scientists are investigating how microplastics are distributed in the sediments of the Black and Caspian Seas and what factors affect their distribution. They used a combination of methods to extract MPs from sediment samples, including density separation, elutriation and hydrophobic adhesion. They analyze the concentration and morphology of MPs depending on the distance to rivers, coasts, cities, sediment grain size and water depth. The results show that the average concentration of MPs in the sediments of the Black Sea is 2 times higher than that in the Caspian Sea. Furthermore, the concentration of MP fragments decreases as depth increases, which may be due to the movement of MPs in the aquatic environment. At the same time, the fiber concentration of microplastics does not depend on depth, which can be related to the ability of the fibers to persist in the sediment (Fig. 7). Furthermore, the study shows that the concentration of microplastics in sediments is interrelated with distance to rivers, coasts and cities. This may be related to the increase in water pollution near settlements and

industrial areas. Finally, the size of sediment grains may have an influence on the concentration of microplastics in sediments.⁴⁸

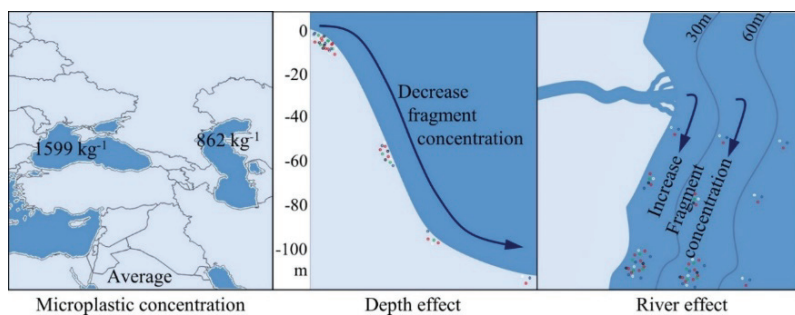


Fig. 7. Dependence of concentration of microplastics on rivers, coasts, cities, etc., in (semi-)closed water bodies.

In some sources, the presence, shape and determination of microplastics in Black Sea sediments taken from different depths (22–2131 m) are described (Fig. 8). The method is used, which includes filtration, followed by FT-IR 2D images to recognize natural and synthetic polymers – polyethylene, polypropylene, acrylonitrile, polyamides and fibres have been identified. MPs were found in 83 % of the sediment samples analysed. The average amount is about 100 pieces/kg. Contamination was found to be the highest in the northwestern shelf (10 times more) than in sediments from greater depths. The authors have also found textile fibres

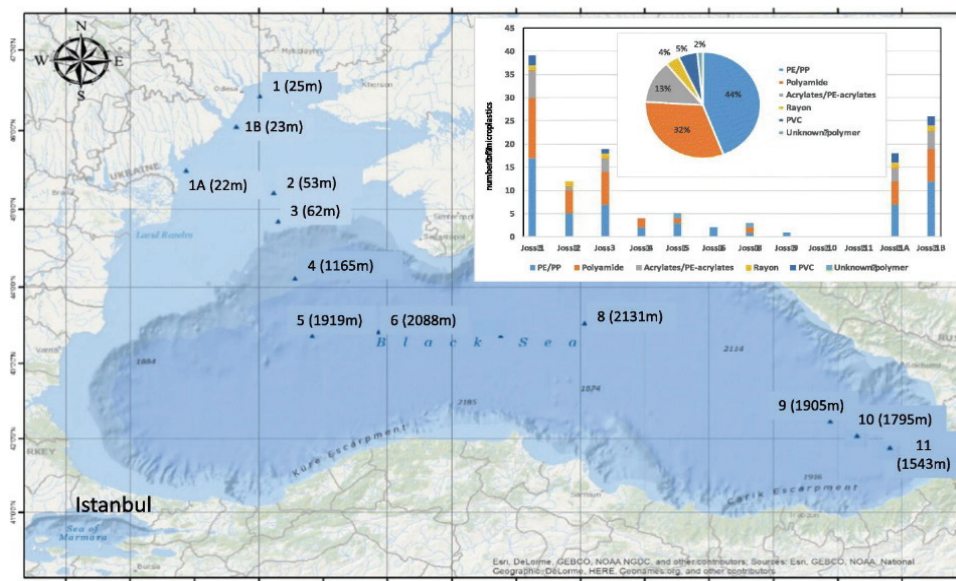


Fig. 8. Identification, morphology and identification of MPs in Black Sea sediments.

on a polyamide and cellulose basis. The most common colours of MPs are black, blue and transparent.⁴⁹

The analytical data from measurements are incomplete and cannot give a clear idea of the current state of the ecosystem and in the Black Sea region. Conducting systematic planning exploratory monitoring will allow tracking the trend of indicators, their interconnectedness, the impact of external pressure, the possibilities for self-purification and sustainable ecological response of the ecosystem.⁵⁰

The transport, distribution and accessibility to biota of MPs in the marine environment depend on their physical characteristics, such as size, shape, density and colour. The size of the MPs is an important factor in how they move in the water column and how it interacts with different types of marine organisms. The shape of the MPs also has significance for their hydrodynamics and potential for adsorption of pollutants. The density of the MPs determines whether they swim on surface, sink or remain in suspension in the water.⁵¹

The density of the MPs can vary greatly, depending on the type of polymer and the method of production. For example, the density of polystyrene foam is about 0,05 g/cm³, while the density of polytetrafluoroethylene (Teflon®) is about 2.1–2.3 g/cm³. Plastic particles have a lower specific density than sedimentary particles (about 2.65 g/cm³). This means that some types of MPs will be more accessible to filtering or planktonic-eating organisms that live in the upper part of the water column, while other types of MPs will be more accessible to detritophagous or benthic organisms that live in the lower part of the water column or in sediments.²

The rate of elevation or sinking of MPs in the marine environment is determined by the difference between polymer density and seawater density, and by the size and shape of microplastics. Studies have shown that MPs can be distributed throughout the water column by turbulent processes, with their concentration decreasing exponentially as the depth increases. The rate of breakdown of MPs decreases in stronger winds, and smaller fragments have a lower rise velocity and are more susceptible to vertical transport.⁵¹

The colours of marine microplastics are the result of the various additives that are used in the production of polymers. These additives aim to change colour, increase attractiveness, improve mechanical resistance or prevent materials from burning.^{52,53} On Fig. 9 are shown some examples of the diversity of MPs colours. Colour can also serve as an indicator of the time of exposure to the sea surface or the weathering process. Yellowing or darkening of plastics is associated with an increase in the carbonyl index, which reflects the degree of photo-oxidation or aging.^{2,54} Colours matter, because they can be misleading to some organisms that take them for food.

In the marine environment, MPs occur in two main forms based on origin – primary and secondary (Fig. 10).^{55–57} Primary MPs produced for industrial and

domestic use enter freshwater bodies by discharging domestic wastewater and eventually make their way into the marine environment.⁵⁸ They usually contain waste from cosmetic, pharmaceutical and personal care products, industrial raw materials and microfibers.^{14,59–61}



Fig. 9. Examples of the colour diversity of polymer mixtures.



Fig. 10. Primary and secondary MPs.⁶⁵

Secondary MPs are the result of physical, chemical and biological processes that can further degrade to nanoplastics.^{62,63} Their degradation in the marine environment into smaller fragments of secondary factors increases the risk of their intake by smaller aquatic organisms.⁶⁴

Various environmental factors influence the distribution of microplastics in ecosystems. These include atmospheric movement and wind directions, meteorological factors such as wave currents, cyclones and tides, river hydrodynamics and water flow and wastewater treatment plants (WWTPs). The WWTPs are a significant source of MPs, but can also contribute to their partial removal. There-

fore, it is necessary to study the transport and behaviour of MPs in waste water installations. Authors trace the types and sources of MPs in domestic wastewater, as well as the effectiveness of different treatment processes for their removal and migration. Also considered are biological activities that accelerate the transformation of MPs, and the interrelationships and ecological risks between surface water, soil and atmospheric environment. Finally, possibilities for future research on the influence of wastewater treatment plants on MP pollution are proposed.⁶⁶

Research by Liu *et al.* in 2022 focuses on methods of sampling, extraction (such as flotation, centrifugation, filtration and digesting) and wastewater analysis in treatment plants. The results of the research show that it is essential to remove interfering organic and inorganic constituents in wastewater and sludge samples in order to achieve visualization and identification of MPs using FTIR and Raman analytical methods. This is also important for the integration of FTIR and Raman analysis, spectra mapping and image processing (Fig. 11).⁶⁷

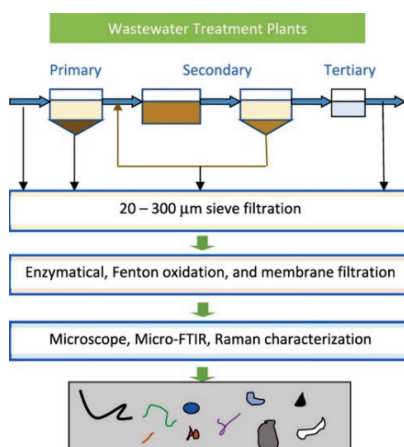


Fig. 11. Methods used to process and identify MPs in WWTPs.

Documenting the distribution of MPs in marine-coastal ecosystems is an important task for assessing ecological status and protecting biodiversity. MPs may contain toxic chemicals that can penetrate the food chain and affect the health of living organisms (Fig. 12). MPs are considered a new type of pollutant that requires special attention and monitoring.⁶⁸

Research has shown that microplastics are present in 93 % of sediment samples in estuaries and are likely to result from deposition processes in these areas. Estuaries are transition zones between freshwater and marine ecosystems that provide habitats for a variety of species, including mussels, fish and birds. MP in estuarine sediments are of different plastics, such as HDPE, nylon (polyhexamethylene adipamide) and PETE. Further research is needed to assess the risk of exposure to microplastics and the potential for bioaccumulation of these contaminants by wildlife species that feed on the surface of tidal flats in

estuaries. This is important, as microplastics can have a negative effect on ecosystems and the health of animals and people who consume products produced in these areas.^{69–71}

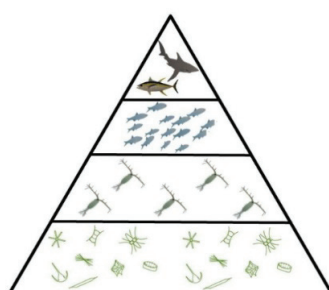


Fig. 12. Example of food chain.

One of the regions where MPs are abundant is the mouth of the Danube. It is the longest river in Europe and passes through ten countries before flowing into the Black Sea. The mouth of the Danube has been declared a reserve of the biosphere by UNESCO and is a unique wetland with rich flora and fauna. Different types of MPs have been found in this zone, such as fragments, fibres, granules and pellets. They originate from various sources, such as textile industry, fishing, shipping and household waste. MPs are found both in surface water and in lower layers and sediments. The composition of MPs is diverse and includes polymers such as PP, PVC, polystyrene (PS) and polycarbonate (PC). Some of these polymers have high persistence and toxicity and may pose a serious risk to animals and plants in the estuary.⁷²

In recent years, microplastics have become a serious environmental and potential human health problem.⁷³ These tiny particles of plastic pollute marine ecosystems and harm marine creatures. In addition, they are a suitable environment for the development of pathogenic microorganisms that form biofilms on their surface. MPs are found in beach sand, seabed, marine flora and fauna. Factors such as fishing, aquaculture and tourism increase the amount of MPs in the sea. They are also generated by the illegal and improper disposal of plastic rubbish. Therefore, it is essential to identify the areas with the highest level of pollution from MPs (Fig. 13). Studies should follow standardised methods of measurement and analysis of microplastics in order to make an adequate assessment of the degree of contamination.⁷⁴

Xue *et al.* (2020) investigated how fishing activities affect the horizontal distribution of MPs in the sediment (Fig. 14).⁷⁵ They have found that the main contaminants (polypropylene and polyethylene fibres) were associated with fishing gear wear and formed 61.6 % of the total amount of MPs in surface sediments. MPs can penetrate deep layers of sediment up to 60 cm. The estimate for the stock of microplastics in the deep layers (185 t) is 5 times that in the surface layers.

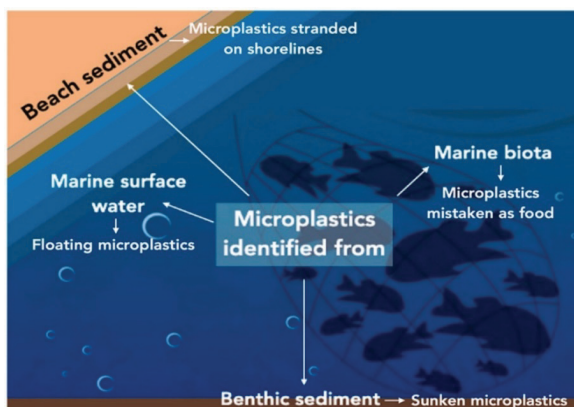


Fig. 13. Distribution of microplastics in marine and coastal ecosystems.

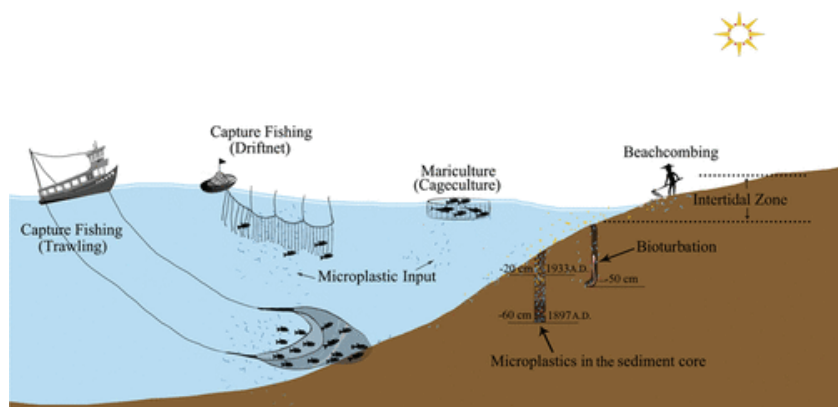


Fig. 14. The horizontal distribution of microplastics in the sediment.

The 2016 paper by Zalasiewicz *et al.* examines the important role of polymers, in particular plastics, in the environment and their geological footprint. The authors argue that plastics are a key indicator of the beginning of the Anthropocene, an era in which human activity is changing the planet. They discuss how plastics become widespread in sedimentary deposits both on land, as well as in the maritime sphere. The possibility of retaining and preserving plastics in Earth's geological layers has been considered as a potential factor that makes them significant to future geologists and archaeologists, as part of the planet's geological history over long periods of time.⁷²

The monitoring of plastic microparticles under UV irradiation can lead to the generation of organic matter that is released into the environment. This organic matter can affect the carbon balance and disrupt the global biogeochemical cycle of carbon. The biogeochemical cycle of carbon is a complex process that ensures the transport of carbon between the atmosphere, the hydrosphere, biosphere and

geosphere. This cycle includes important processes such as photosynthesis, respiration, degradation of organic matter and geological processes. Disruptions in the global biogeochemical cycle of carbon caused by microplastics can have an impact on the climate in the long term. Changes in the carbon balance can contribute to an increase in the concentration of greenhouse gases in the atmosphere, which can worsen the effect of the greenhouse effect and climate change.⁷⁶

The study of Seely *et al.* (2020) analyse the influence of microplastics on sedimentary microbial communities and biogeochemical carbon and nitrogen cycles. They performed experiments using different types of microplastics (polyethylene, polyvinyl chloride, polyurethane foam and polylactic acid) added to salt marsh sediment. The results show that the presence of microplastics alters the composition of the sedimentary microbial community and influences nitrogen cycle processes. Different types of MPs have different effects on nitrification and denitrification, with polyurethane foam and polylactic acid promoting these processes, while polyvinyl chloride inhibits them. This underlines the importance of investigating the influence of microplastics on global ecosystems and biogeochemical cycling, especially with increasing plastic pollution.⁷⁷

In addition, MPs can alter the chemical balance of the marine environment by transmitting certain chemicals and binding to toxins that can be accumulated in the body of the organisms that consume them. Uptake of MPs has been observed in many species of different size and diet.⁷⁸ Soft tissue adherence of organisms is another way of absorption of MPs by bivalve molluscs, crustaceans and algae *Fucus vesiculosus*.^{8,79}

In the study published in the journal *Marine Pollution Bulletin*, experts from the Institute of Oceanology at the Bulgarian Academy of Sciences studied the impact of MPs on small crustaceans in the Black Sea. This is the first such study for the region to analyse how MPs are ingested by zooplankton organisms and how this affects the marine ecosystem.

For this purpose, samples were taken from the water column at three places – the mouth of the Kamchia River, the coastal waters of Varna and the open waters of the Southeastern Black Sea. With the help of special methods of processing and analysis of samples, the composition, concentration and size of the MPs, as well as the species and number of crustaceans ingesting them, have been determined.

The results showed that the concentration of MPs in the water column averaged 2.04 counts/m³, with the highest values recorded at the mouth of the river (5.76 counts/m³). The most common types of MPs were fibres (66 %) and fragments (28 %), and the most commonly used materials were polyester (40 %) and polypropylene (28 %). The average size of MPs was 0.62 mm, with the smallest particles (0.062–0.100 mm) being most frequently ingested by crustaceans.

The study found that 16 % of crustaceans have MPs in their stomachs, with the species *Acartia clausi* (25 %) and *Oithona similis* (23 %) being the most affected. These species are part of the main food chain in the Black Sea and are food for larger organisms, such as fish and seabirds. The authors concluded that ingestion of MPs may have adverse effects on the health and functioning of zooplankton, also contribute to the transfer of MPs and related toxic chemicals to higher trophic levels, including humans.⁸⁰

MPs are retained in the different layers of the water column, which is the vertical distribution of water from the surface to the bottom. With a supplementary, MPs particles in the water column favour the regular intake of plastic particles by zooplankton (Fig. 15),⁸¹ which is a group of microscopic animals that float or drift in the water. Zooplankton are a major food source for many other aquatic organisms, such as fish and seabirds. In this way, MPs can be carried along the food chain and enter the bodies of larger animals.

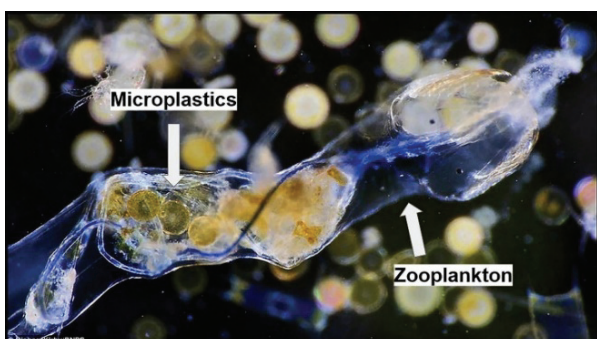


Fig. 15. This planktonic arrow worm, *Sagitta setosa*, has eaten a blue plastic fibre about 3 mm long. Photograph: Dr Richard Kirby.

Among the most vulnerable species to MPs contamination are bivalve molluscs due to their diet.⁸² MPs have been found in farmed blue mussels *Mytilus edulis* and Pacific oysters *Crassostrea gigas*, as well as in wild Manila mussels, *Venerupis philippinarum*.⁸³

The accumulation and effects of MPs after ingestion in predatory sea crabs (*Charybdis japonica*) were studied. Bioaccumulation (accumulation by consumption of microplastically contaminated mussels) was not observed, likely due to discarding of the plastic particles. Observations show that marine organisms have an innate ability to resist the acute effects of microplastics, but there is a limit beyond which defence mechanisms decrease and physiological functions are impaired.⁵⁷

Aquatic plants can accumulate microplastics in their tissues, thus transferring them to higher trophic levels through the food chain. It is possible that MPs take up several contaminants on their surface due to the high adsorption capacity. There is not much information on developed techniques for efficient removal of

MPs from wastewater. Some authors consider and discuss effective technologies such as flotation, filtration and membrane separation of MPs from aqueous media, given their advantages and disadvantages.⁸⁴

Coral reefs are unique and valuable ecosystems that provide numerous services to humanity, such as food, tourism and protection from the storms. But they are exposed to serious threats from human activities, including microplastic pollution. MP particles can penetrate coral tissues and cause stress, inflammation and death. Some studies, *e.g.*, Reichert *et al.* (2018), have shown that corals have different strategies for dealing with microplastics, such as ejection, ingestion or wrapping with mucus (Fig. 16).⁸⁵ But these mechanisms are not enough to protect against the negative effects of microplastics, such as bleaching and necrosis. Therefore, it is necessary to better understand how microplastics affect coral reefs and how to reduce their pollution in the marine environment.⁸⁶

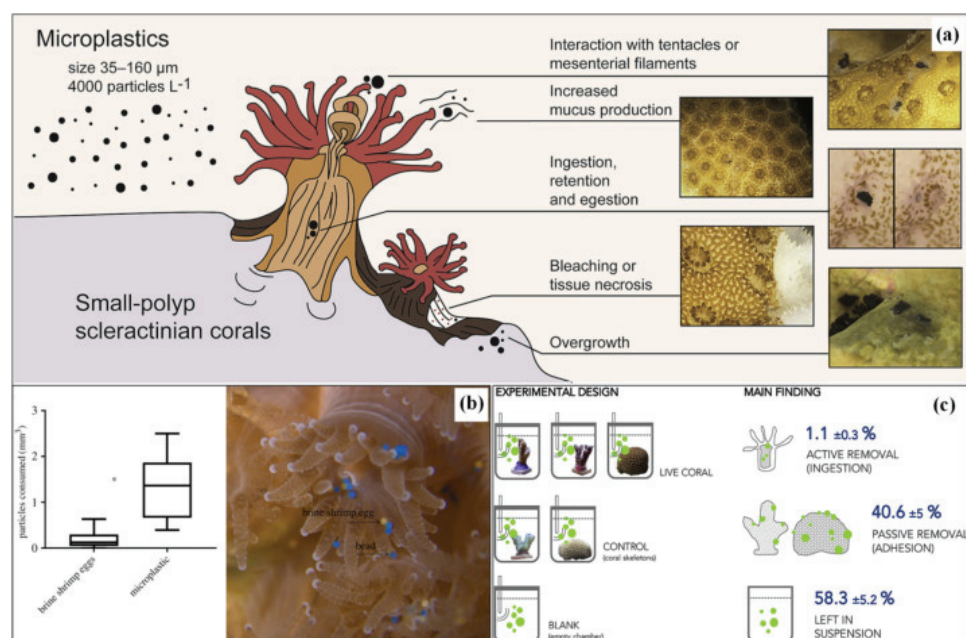


Fig. 16. Influence of microplastics on coral reefs.⁸⁵

MPs have been found in almost all freshwater environments, including remote lakes and rivers.^{87,88} MPs, similar in size to those of planktonic organisms, have been found in water columns and sediments of lakes and rivers worldwide. Their number and mass along the river can exceed those of living organisms such as zooplankton and fish larvae. In freshwater sediments, concentrations of MPs reach the same values as in the world's most polluted marine sediments. These

particles result from a unique biogeochemical cycle that ultimately impacts on ecosystem productivity, biodiversity and functioning (Fig. 17).⁸⁹

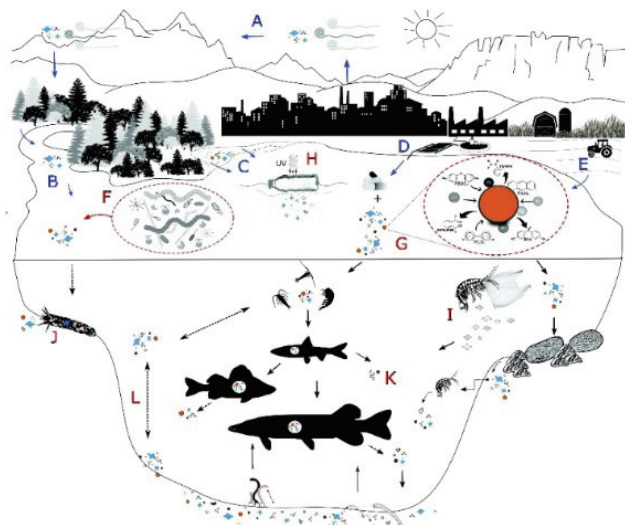


Fig. 17. Biogeochemical cycling of microplastics in inland waters.

Microplastics also act as carriers of toxic substances for invertebrates, fish and waterfowl.⁸⁸ The authors argue that MP is an environmentally significant parameter of inland water bodies due to its ubiquity, environmental sustainability, and interactions with key ecological processes. It is necessary to compare spatiotemporal variations in microplastic concentration within and between catchments. These data will allow more accurate modelling of the pollutant cycling and allow to identify sources, distribution and circulation pathways, and retention times.⁸⁸ MP can penetrate the food chain and cause hormonal disruptions, cancers or other diseases. According to research, people consume about 70,000 MP of particles per year.⁹⁰

4. IN THE SOIL

Soils are an important element of the natural environment and are of great importance for agriculture, biodiversity and climate. Soils are formed by various factors, such as material, climate, vegetation, animal organisms and human activity. Soils are characterized by a variety of properties, such as mechanical composition, chemical composition, organic matter, moisture, temperature and fertility.

MP particles can contaminate the soil and have an adverse impact on the environment and human and animal health. MP particles can enter the soil *via* different routes, such as from biosolid waste, irrigation, atmospheric deposition or degradation of polymer films for mulching (mulching is a process in which the

soil around plants is covered with various materials regulating water and air regimes in the surface layer of the soil (Fig. 18). MP particles can be absorbed by plants through their roots and penetrate their above-ground parts through the conductive system. This can affect plant growth, development and productivity, as well as crop quality. The effects of MP particles depend on polymer type, particle size and shape, plant species and experimental conditions.⁹¹



Fig. 18. Mulching in agriculture (<http://bg.gardenflowerspot.com/>).

In agriculture, a large amount of plastic is used for various purposes, such as covering the soil, irrigation, protection from pests and diseases. These products contribute to increase the harvest, but also lead to soil contamination by MPs (50–250 kg/ha). MPs can harm soil life, alter the physicochemical properties of the soil and pose a risk to human health and the environment. Therefore, it is necessary to better understand about the sources, distribution and consequences of MPs in soils and to take measures to reduce their formation and accumulation. Some of the main aspects of the MPs problem in agriculture are how they are distributed and migrated into it, what methods there are for their measurement and analysis, what ecological effects they have on soil life and how they can penetrate the human food chain (Fig. 19).⁹²

Some of the most common and used microplastics in the environment are PP, PE, PVC and PET. These MPs can have toxic effects on plants that are important for the food chain and the economy. To investigate their impact, experiments have been carried out with some of the world's most cultivated and consumed crops, such as wheat, rice, maize and soybeans. Plants were exposed to different concentrations of MPs in the soil and various parameters related to growth, photosynthesis and nutritive value were then measured. The results show that all MPs have a negative effect on plants, affecting the root system and leaf surface the most. Also, specific effects were found for each polymer, such as PVC reducing the chlorophyll content and photosynthetic activity the most, and PE being the least toxic. These data suggest that MPs pose a serious threat to plant health and productivity and may affect food safety and quality (Fig. 20).⁹³

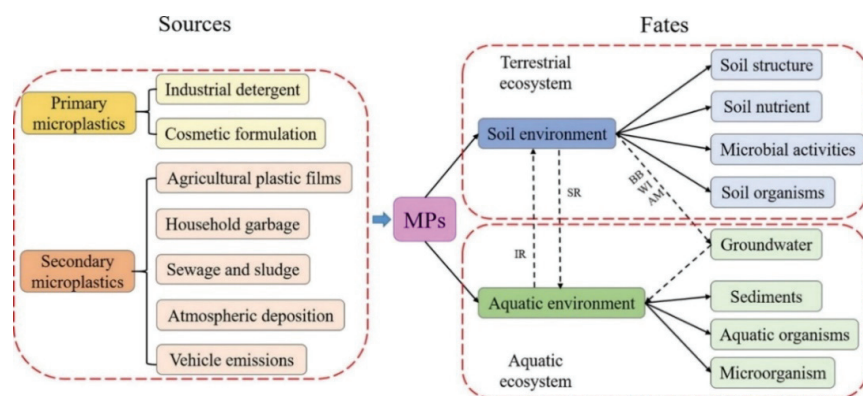


Fig. 19. Distribution and migration of microplastics in soils.

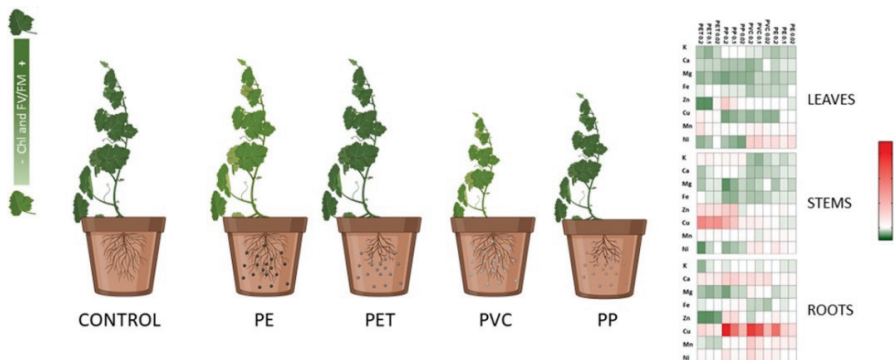


Fig. 20. The toxic effects of some microplastics.

5. FROM THE TRAFFIC

The literature examines the air pollution by MPs caused by motor vehicle traffic (Fig. 21).⁹⁴

The sources of primary microplastics in the urban environment are diverse and complex. One of them is the wear of tires made of synthetic rubber, which are used for cars and other vehicles. These tires contain various additives, such as black carbon, mineral oils and other chemical substances that can have adverse effects on the environment and human health.⁹⁵

When vehicles drive on the roads, they produce tire and road surface wear particles that disperse into the atmosphere or deposit on the surface. The size and quantity of these particles depend on many factors, such as the type and condition of tyres and roads, speed and driving patterns, climatic conditions, *etc.*⁹⁶ Tire and road wear particles can be transported by various roads to the environment. Some of them can be inhaled or ingested by humans and animals, which can cause respiratory or digestive problems. Others can be washed away by rain or snow

and reach rivers, lakes or oceans, where they can contaminate aquatic ecosystems and enter the food chain.⁹⁷

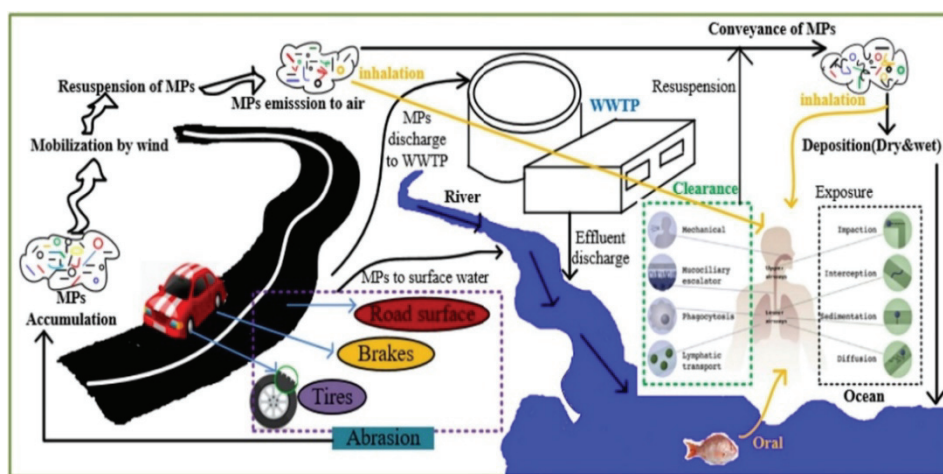


Fig. 21. Air–water exchange of abrasive traffic MPs and human.

The authors indicate that tire and road wear particles contribute substantially to primary MP pollution in urban areas. Kole *et al.* (2017) estimates that these particles make up approximately 0.1–10 % of PM₁₀ (fine particulate matter) and 3–7 % of PM_{2.5} in the atmosphere.^{96,98} The studies by Panko *et al.* (2013) and Kole *et al.* (2017) reveal that approximately 28–30 % of particulate matter found in the oceans and rivers worldwide originates from tire wear and tearing. These particles, ranging from 15–50 nm in size, consist mainly of mineral oils and black carbon fragments, as documented by Dahl *et al.* (2006).^{96,97,99}

After formation, tire wear particles spread to the environment by wind and watercourses. It is estimated that terrestrial sources contribute to about 70–80 % of ocean MPs, mainly transported by rivers.¹⁰⁰

In Europe, transport sources discharge 42 % of all road pollution vehicles, while textile MPs contribute only 29 %.¹⁰¹ Larger particles (> 10 µm) are uniquely susceptible to transport in the marine environment due to the gravitational force causing their deposition on the road surface, while small MPs from traffic are subject to direct emissions to the atmosphere and are carried through the air.¹⁰² It has been shown that up to 10 % of the particles generated by tyre wear are carried through the air.

The emitted particles can be transported to a greater distance and subsequently deposited in the ocean.¹⁰³ However, the distance to which they can be carried depends on the local conditions and characteristics of the particles. Research has shown that particles measuring 1 to 10 µm can be trapped in the atmosphere for minutes to hours and carried up to 50 km from their source.⁹⁶

6. IN HUMANS

MPs pose a serious threat to life on Earth. They are contained in seafood, salt and mineral water and can get into the human body in various ways – by ingesting contaminated with MP products and inhaling air polluted with MPs. MPs can enter the food chain and cause allergies, asthma or cancer.¹⁰⁴ Inhalation of MPs is especially dangerous because they have a high oxidation potential and can damage the respiratory system and other organs. The effects of MPs on human health depend on their size, shape, chemical composition and concentration. There are not enough regulations to limit emissions of MPs and to monitor their presence in the environment. Research in this area is still insufficient and more data are needed to assess the risk of MPs for human health.¹⁰⁵

Scientific evidence highlights the role of air as an important source of human exposure to MPs. They have been found in atmospheric samples both indoors (in house dust) and outdoors, and it has been shown that the indoor environment contains a large proportion of these particles.¹⁰⁶ The wide distribution of these particles is due to their rapid transport over large distances, which is facilitated mainly by their small size (from 1 to 5 mm) and their low density.¹⁰⁷

Studies have shown that airborne MPs consist in particular of fibres between 200 and 600 µm in size.^{14,95} These fibres can penetrate human lungs, where fibres up to 250 µm in size have been found that can cause respiratory diseases, especially in vulnerable individuals (Pauly *et al.*, 1998). According to estimates by the European Environment Agency (EEA), a person can be exposed to 26–130 MP pieces in the air per day. This is a serious health risk because MPs have pro-oxidative and pro-inflammatory effects, as well as they contain harmful additives, such as plasticizers, which act as endocrine disruptors. In addition, MPs can adsorb hazardous pollutants from the environment, such as persistent organic pollutants (POPs), and carry them into the body when inhaled. Therefore, it is necessary to take measures to reduce emissions of POPs and exposure to MPs in the air.^{12,108}

After inhalation, microplastics reach the respiratory tract and are deposited depending on the properties of the particles, the characteristics of the individual and the anatomy of the lungs. Smaller particles of lower density (*e.g.*, polyethylene) are more likely to reach the deep airways. Particles of 5–30 µm are deposited in the upper respiratory tract by impaction in the rhino-pharyngeal walls, while particles of 1–5 µm reach the small airways by sedimentation and diffusion.¹⁰⁹ Particle deposition <1 µm occurs by Brownian motion.^{109,110}

Although both MPs and nanoplastics (NPs) can reach the alveolar surface, the latter can pass into the bloodstream, overcoming the pulmonary epithelial barrier (Fig. 22). Despite the low reactivity, the number of atoms per surface per unit mass is large in MPs and NPs, which significantly increases the surface area for chemical reactions with body fluids and tissues in direct contact. This has

been demonstrated in workers, working with PVC and a group of people who are prone to persistent inflammatory stimulation leading to pulmonary fibrosis or even carcinogenesis.¹¹¹

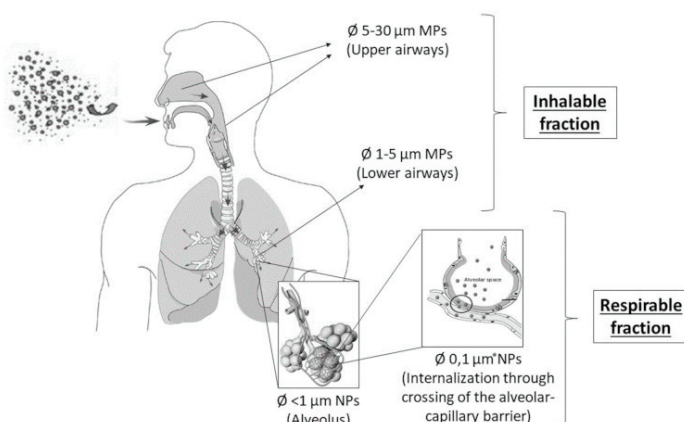


Fig. 22. Size-selective inhalation of airborne microplastics involves specific regions of the respiratory tract: inhalable fraction (upper and lower airways) and respirable fraction (deep airway).

MPs particle exposure by inhalation can trigger an inflammation-related bronchial reaction (similar to asthma), which can lead to toxic effects. The particles are positioned in the bronchi and stimulate immune cells to release substances such as reactive oxygen species, proteases and cytokines to deal with the foreign object. This inflammatory response can cause prolonged inflammation, which can lead to DNA damage and an increased risk of cancer. Inhalation of MPs is considered a more common form of exposure than ingestion and is considered more dangerous.¹¹²

Intense UV irradiation changes the morphology of airborne MPs, resulting in fragmentation and an increase in their surface area. Air MPs, due to their changed morphology and increased surface area, have a greater capacity to adsorb gaseous polluting chemicals on their surface. This means that MPs can retain a greater concentration of such chemicals relative to their size. This process can increase the potential of MPs to act as pollutant carriers and increase the risk of spreading and affecting these chemicals in the environment and on living organisms.¹¹³

The chemical toxicity of MPs is related to their hydrophobic behaviour and their ability to attract toxic chemicals. Size, shape, surface charge and ability to adsorb molecules and pathogens, as well as their bioresistance, are factors which may contribute to their toxicity.^{114,115} These substances attach to the surface of the particles due to electrostatic forces, biofilm growth and chemical additives in polymeric materials.¹¹⁶ MPs can adsorb persistent organic pollutants (POPs) like polycyclic arene hydrocarbons (PAHs), pyrene and phenanthrene, as highlighted

by Delgado-Saborit *et al.* (2013) and Allen *et al.* (1998).^{117,118} Additionally, MPs can also adsorb heavy metals, which are inorganic pollutants, as discussed by Wang and Wang (2018) and Zhang *et al.* (2018).^{119,120} Other types of pollutants, such as phthalates and phosphorus organic esters, have been found to be adsorbed on PS foam and PP microplastics from the marine environment.¹²¹

Comparisons with well-studied nonpolymeric microparticles in air (asbestos, silica, soot, wood, cotton, hay) allow the identification of putative mechanisms and are the basis for understanding the toxicity of MPs.¹²² With the accelerated atmospheric microplastics (SAMP) can be inhaled and deposited in human lungs, where the chemicals and pathogens associated with them can induce infections and other adverse effects. Also, SAMPs can be carriers of heavy metals, which can also be toxic to human health. Research works on phthalates and phenols, show that both they and other components of MPs can cause health problems, such as a shortened gestational period, a decrease in birth weight, a change in gene expression and endocrine disruption.^{123,124} According to the research conducted by Wang and Wang (2018), microplastics have the capability to adsorb pyrene and phenanthrene.¹¹⁹

A study by Law *et al.* (1990) confirmed that plastic fibres are more durable than vitreous fibres in synthetic extracellular lung fluid over a period of 180 days.¹²⁵ MPs can group and stay longer in human lungs. This process can contribute to chronic oxidative damage induced by reactive oxygen forms, which is associated with various diseases and injuries in the body.¹²⁵

Scientists are actively exploring technologies for the separation and identification of microplastics in food products and ecosystems. These technologies include flotation, chemical processing, enzyme processing and other methods that have their advantages and disadvantages. New techniques such as enzymatic degradation in combination with hyperspectral imaging are being investigated to achieve greater separation and characterization efficiency of microplastics with minimal impact on food sample. The choice of standard technology for analysing microplastics in food matrices is challenging, taking into account particle composition, size and shape, data visualization methods and costs (Fig. 23).¹²⁶

Research shows that microplastics spread widely in the fresh and marine aquatic environment and pose a threat to aquatic organisms. Trophic transfer processes (bioaccumulation is the process by which toxins gradually accumulate in certain organs of humans or other organisms) and biomagnification (the process by which toxins steadily increase their concentration as they move up the food chain) are pathways by which microplastics can penetrate the human body. Research focuses on adverse effects of microplastics on aquatic organisms, such as neurotoxicity, behavioural changes, histopathological damage, ignition, oxidative stress, biochemical and haematological changes and embryotoxicity. Also discussed are the main food sources contaminated with microplastics that can enter

the human food chain – sea salt, drinking water and seafood (fish, shells, crustaceans).¹²⁷ After administration, they can enter the gastrointestinal tract by endocytosis from M-cells, pass into tissues by paracellular transport, and then determine systemic exposure.¹²⁸ There is evidence that synthetic particles with a size of less than 150 µm can pass through the gastrointestinal epithelium of mammals. However, it is assumed that only 0.3 % of these particles are absorbed and only 0.1 % of particles that are larger than 10 µm should be able to reach organs and cell membranes.¹²⁹ Although no study has reported toxic effects of MPs in the human body, in several studies it has been suggested that large concentrations of these pollutants can produce toxic effects in various *in vitro* systems.

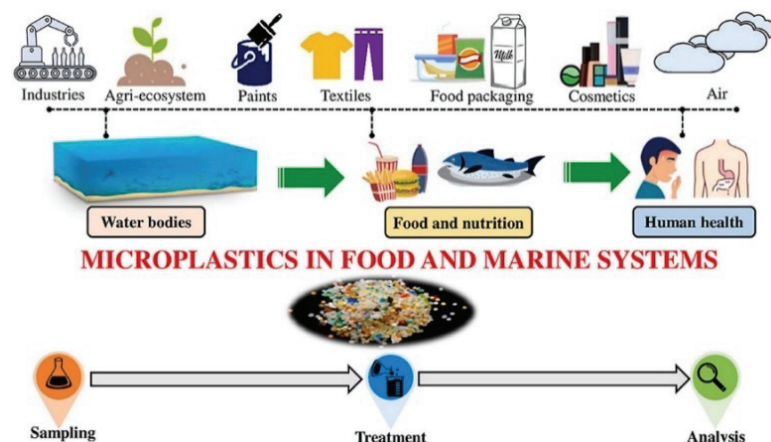


Fig. 23. Microplastics in food and marine systems.

6.1. To the digestive system

In their study on gastric adenocarcinoma cells, Forte *et al.* (2016) have found that unmodified polystyrene nanoparticles of sizes 44 and 100 nm were internalized by clathrin-mediated endocytosis.¹³⁰ This internalization process could potentially trigger inflammatory responses and induce morphological changes in the cells. Studies have demonstrated that high concentrations of polystyrene (PS; known as PS-MPs), with a diameter of 1 µm, increase cytotoxicity in three different *in vitro* systems.¹³¹

Other authors provide a probabilistic lifetime exposure model for children and adults, which accounts for intake via eight food types and inhalation, intestinal absorption, biliary excretion and plastic-associated chemical exposure *via* a physiologically based pharmacokinetic submodel.¹³²

6.2. To respiratory system

According to Paget *et al.* (2015), only positively charged polystyrene nanoparticles (PS-NPs) exhibited cytotoxicity in a dose-dependent manner. For cer-

tain cells, the LC_{50} (lethal concentration 50) was found to be 31 µg/mL, while for specific macrophages, it was 75 µg/mL.¹³³ The cytotoxic effects observed could be attributed to the ability of PS-NPs to induce DNA double-strand breaks and cause significant depletion of glutathione (GSH) in both cells and macrophages. Additionally, researchers suggest that PS-NPs could potentially contribute to impairment and functional disorders in the respiratory system of humans and mammals.¹³⁴

6.3. To the nervous system

In order to better understand the cytotoxicity of MPs at the cellular level with respect to oxidative stress and cell viability, brain human cells (T98G) were exposed to several concentrations (50 µg/mL to 10 mg/L) of PE-MPs and PS-MPs.¹³⁵ According to their results, none of the MPs resulted in a significant decrease in cell viability, suggesting that cytolysis was not induced. However, reactive oxygen species were significantly increased in T98G cells after exposure to both types of MPs. These results suggest that oxidative stress may be an important mechanism by which MPs exert their toxicity at the cellular level.

6.4. To the placental barrier

In a study conducted by Grafmueller *et al.* (2015), it was demonstrated that microplastics have the ability to cross the human placental barrier. The researchers utilized an *ex vivo* model of human placental perfusion to analyze the transport mechanisms involved in the placental transfer of PS-NPs ranging from 50 to 300 nm in size.¹³⁶ Their results showed that PS-NPs accumulate in the syncytiotrophoblast of placental tissue. Thus, syncytiotrophoblast has been suggested to be a key player in regulating the transfer of PS-NPs through the human placenta. Moreover, the underlying mechanism underlying this relocation can be based on an energy-dependent transport pathway. These results highlight the need for further research to help in the overall understanding of the mechanism of NPs transport across the placental barrier, as NPs can induce embryotoxicity. Lithner *et al.* (2011) conducted a study where they developed a comprehensive ranking of hazards associated with plastics. They based their ranking on internationally agreed criteria used to identify risks related to physical, environmental, and health factors.¹³⁷

Apart from the chemical nature, there are other factors inherent in polymers which may also affect toxicity. Free radicals are generated in the polymerisation process and subsequent processing of plastics which act as a common factor in promoting the production of reactive oxygen species (ROS).¹¹² Moreover, these free radicals easily increase their concentration in the particles due to the dissociation of C–H bonds induced by light exposure or interaction with transition metals during the weathering process.¹³⁸ It is therefore worth noting that photo-

degradation and biodegradation in the environment induces surface changes affecting their functional groups (*e.g.*, $-COOH$, $-NH_2$) which alter toxicological profiles.¹³⁹ Other properties of the particles, such as shape or surface charge, have also been identified as potential toxicity factors for MPs.¹⁴⁰

7. SEPARATION, IDENTIFICATION AND CHARACTERIZATION OF MICROPLASTICS

Despite the advanced stage in the areas of MP pollution, there are still no widely accepted and uniform standards for sample collection, laboratory analyses, quality control (QA/QC) and reporting of MPs in ecosystem samples. Based on a comprehensive assessment of MPs in water, sediments, fish, bivalve molluscs, rainwater and wastewater, some authors have developed and recommend best practices for collecting, analysing and reporting MP in the environment. They also recommend the factors to be considered in the design of the study for MPs, especially with regard to site selection and sampling methods. First emphasize the need for standard QA/QC practices, such as collection of field and laboratory samples, then use of methods outside microscopy for partial composition identification and standardized reporting practices, lastly proposal for a glossary for particle classification (Fig. 24).¹⁴¹

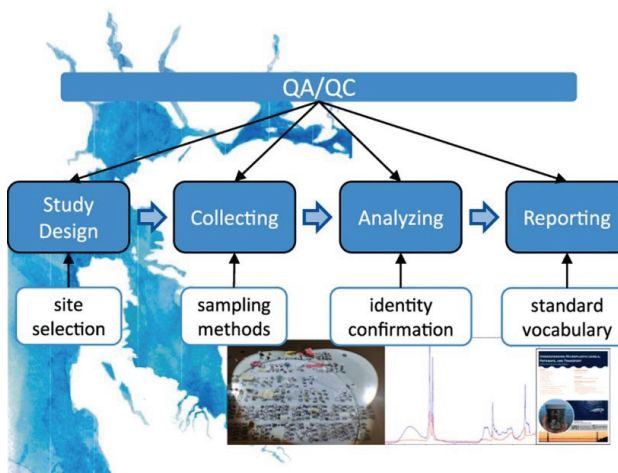


Fig. 24. Quality assurance/control (QA/QC).

Microplastics <5 mm in size are very difficult to remove from water bodies, sediments and air with available techniques. NPs are less than $1\text{ }\mu\text{m}$. Methods suitable for collecting MPs include sieving, filtration, visual sorting, grinding, density separation. Their isolation can be carried out by various physical, chemical and biological methods. In practice, the techniques for identification and characterization of MPs in the environment are SEM-EDS, FTIR, NIR, Raman,

NMR spectroscopy, *etc.* NMR spectroscopy can also be used to find concentrations. There is still a need for the development of similar more economical and portable techniques (Fig. 25).¹⁴²

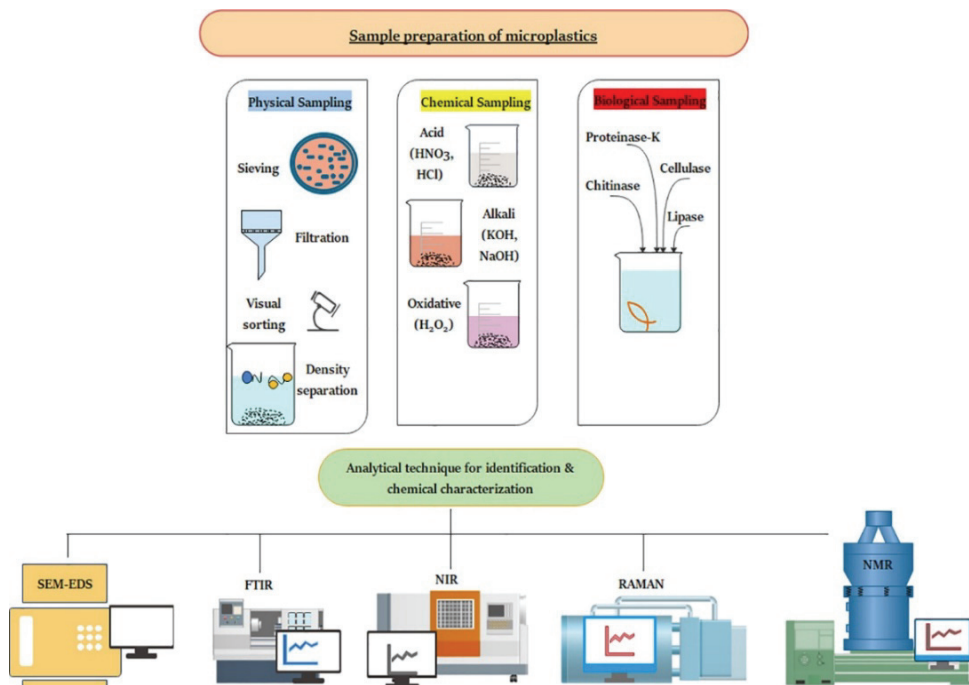


Fig. 25. Methods and techniques for the identification of microplastics in samples.

One way to quantify and classify microplastics of diverse chemical composition and shape is by scanning electron microscopy. It offers greater depth and finer detail, over a wider magnification range, than visible light microscopy or the digital camera, and allows further analysis of chemical composition. For the quantification of MPs, the authors propose two deep learning models with neural networks (U-Net and MultiResUNet) for semantic segmentation. To classify the shapes, they use a finely tuned VGG 16 network, which classifies microplastics based on their shapes with a high accuracy of 98.33%. With the trained models, only seconds are needed to segment and classify with high accuracy, which is remarkably cheaper and faster than manual labour.¹⁴³

In other studies, stable carbon isotope ratio mass spectrometry (IRMS), attenuated total reflectance-Fourier transform infrared spectroscopy (ATR-FTIR) and micro-Raman spectroscopy (μ -Raman) were investigated as complementary techniques for characterizing common MPs.

The polymer articles selected by the authors for comparative analysis include food packaging, containers, straws and polymer pellets. The ability of the

IRMS to discriminate between weathered samples was also investigated using simulated weathering conditions with ultraviolet (UV) light and heat. IRMS results show a difference between $\delta^{13}\text{C}$ values for polymers of plant origin and petroleum-based polymers. Differences were also found between plastic products composed of the same polymer but from different countries, and between some recycled and non-recycled plastics. In addition, there was an increase in $\delta^{13}\text{C}$ values after exposure to ultraviolet light. The authors discuss the results, advantages and disadvantages of the three techniques (Fig. 26).¹⁴⁴



Fig. 26. Spectroscopic techniques for the characterization of microplastics.

Other authors consider and analyse the strengths and weaknesses of the different instrumental methods for separation, morphological, physical classification, chemical characterization and quantification of MPs. This is due to the complex transformation, cross-contamination and heterogeneous properties of MPs in size and chemical composition (Fig. 27).

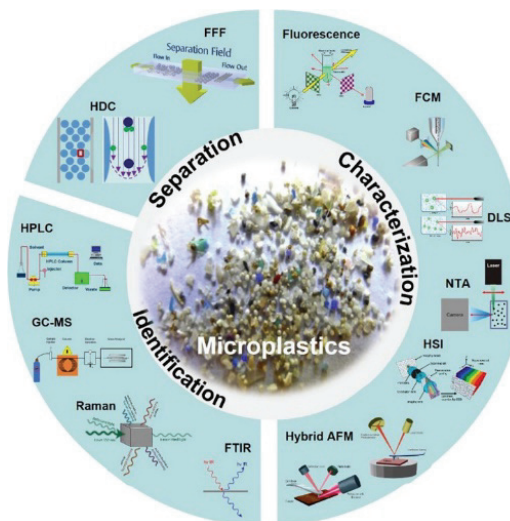


Fig. 27. Separation, characterisation and identification of MPs and NPs in the environment.

It is pointed out that future research efforts should be focused on the development and implementation of new analytical tools and combinations of technologies to complement detection constraints and provide reliable information for the characterization of MPs.¹⁴⁵

Different analytical techniques can be used to measure the levels of MPs and NPs in different matrices. The application of thermal analysis is also promising. The authors consider the importance and advantages of thermal analyses for assessing exposure to such plastics in ecotoxicological and toxicological studies.¹⁴⁶

Microplastics contained in food salts (marine, stone) may pose a potential hazard to human health. A visual assessment is performed for the identification of the shape, size, number and colour of the particles using light and fluorescence microscopy. The composition of the sample is analysed by Raman spectroscopy. A relatively large number of MPs are found in sea salts. The most common are PE, PP, PET) nylon and PS, effectively removed from seawater by microfiltration membranes. The membrane backwash technique is used to improve membrane efficiency.¹⁴⁷

Research teams are working on the use of near-infrared hyperspectral imaging (HSI-NIR) to automatically identify microplastics (Fig. 28).

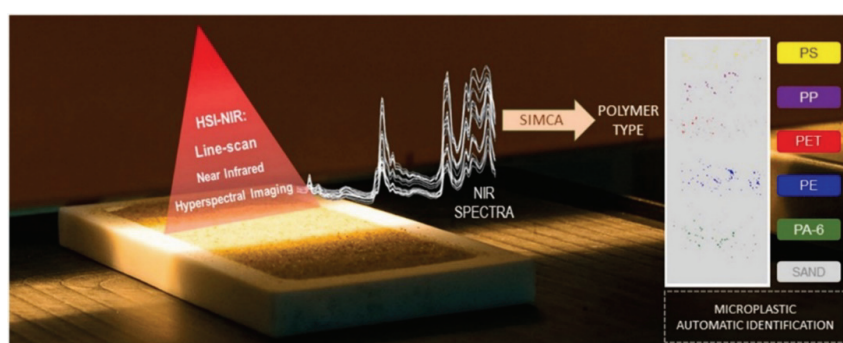


Fig. 28. A comprehensive and fast microplastics identification based on near-infrared hyperspectral imaging (NIR-HSI).

A high-throughput screening method utilizing near-infrared hyperspectral imaging (NIR-HSI) has been developed for the automatic identification of MPs in beach sand with minimal sample preparation. The method can analyse the whole sample or a fraction (150 µm to 5 mm) after sieving. It can detect small, colourless MPs (<600 µm) that may be difficult to identify through visual inspection or manual collection. Unlike conventional infrared spectrometers, no spectroscopic subsampling is required due to the high-speed analysis capability of the linear scan toolkit, allowing simultaneous evaluation of multiple MPs.

The NIR-HSI method investigates a scan region of 75 cm² in less than 1 min, with a pixel size of 156 µm×156 µm. A proprietary comprehensive spectral

data set, which includes weathered microplastics, is used to construct multidimensional supervised classification models using class analogy modelling (SIMCA). These chemometric models have been validated for hundreds of microplastics collected from the environment, taking into account particle size, colour and weathering. The models exhibit high sensitivity and specificity (over 99 %) for identifying specific types of MPs such as PE, PP, polyamide-6 (PA), PET and PS.

The method has been successfully applied to a sand sample, identifying 803 particles without prior visual sorting. This indicates the stability and reliability of automatic identification, even when analysing weathered microplastics alongside other matrix constituents. The NIR-HSI-SIMCA method is also applicable to MPs extracted from other matrices after sample preparation.

Comparisons have been made between the principles of NIR-HSI and other commonly used techniques for the chemical characterization of MPs. The results highlight the potential of using NIR-HSI in combination with classification models as a comprehensive screening approach for characterizing different types of MPs.

In the context of the marine environment being a major sink for MPs, there is an urgent need for monitoring methods that can detect synthetic particles in various marine components and sample matrices. Previously, the direct characterization of MPs in real marine matrices using near-infrared hyperspectral imaging (NIR-HSI) has not been explored. However, a study by Piarulli *et al.* (2022) introduced a fast NIR-HSI method coupled with a customized data processing strategy using normalized image differences (NDI). This method was utilized to detect MPs up to 50 µm in environmental matrices.¹⁴⁸

The proposed method is highly automated, eliminating the need for extensive data processing. It enables the successful identification of different polymer types in surface water, mussel soft tissue samples, and real field samples containing MPs in the environment. NIR-HSI is directly applied to filters, eliminating the requirement for pre-sorting of particles or repeated sample purification. This approach saves time, prevents air pollution, and avoids particle degradation and loss.

With its temporal and financial efficiency, the large-scale application of this method could facilitate comprehensive monitoring the presence of MPs in natural environments, allowing for the assessment of ecological risks associated with this form of pollution (Fig. 29).

One of the developing, environmentally friendly and clean technology for the reduction of MPs and NPs is microbial degradation. It is influenced by several biotic and abiotic factors, such as enzymatic mechanisms, concentration of substrates and co-substrates, temperature, pH, oxidative stress, *etc.*

Therefore, it is crucial to recognize the key pathways adopted by microbes to use polymer fragments as the sole source of carbon for the growth and development. Some authors critically discuss the role of different microbes and their

enzymatic mechanisms involved in the biodegradation of MPs and NPs in the wastewater stream, municipal sludge, municipal solid waste and composting, starting with biological and toxicological impacts of MPs/NPs.¹⁴⁹ The implementation of various MPs/NPs recovery technologies, such as enzymatic, advanced molecular and biomembrane technologies to promote their bioremediation from the environment, along with their pros, cons and perspectives, is also considered.

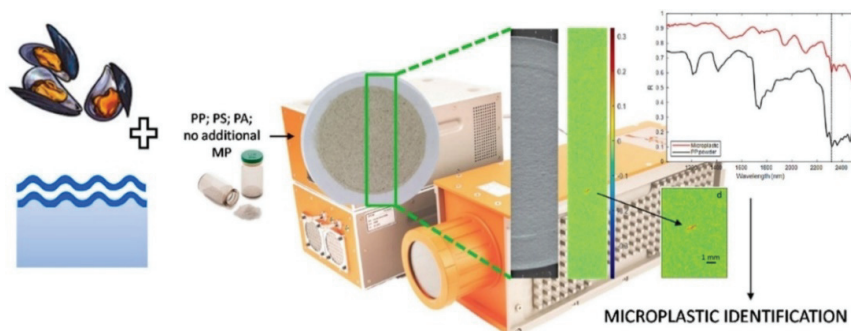


Fig. 29. A comprehensive and fast microplastics identification based on near-infrared hyperspectral imaging (HSI-NIR).

Therefore, it is crucial to recognize the key pathways adopted by microbes to use polymer fragments as the sole source of carbon for the growth and development. Some authors critically discuss the role of different microbes and their enzymatic mechanisms involved in the biodegradation of micro- and nanoplastics in the wastewater stream, municipal sludge, municipal solid waste and composting, starting with biological and toxicological impacts of MPs/NPs.¹⁴⁹ The implementation of various MPs/NPs recovery technologies, such as enzymatic, advanced molecular and biomembrane technologies to promote their bioremediation from the environment, along with their pros, cons and perspectives, is also considered.

8. CONCLUSION

We looked at where plastic waste comes from, where it goes and what its effect is on seas, living organisms and on us, humans. We have also shown available techniques for identifying plastic waste and how to prevent or reduce it. Knowledge of the consequences of plastic waste is constantly improving.

All types of organisms suffer consequences from the ingestion of plastic particles. Drifting waste can interfere with both the surface and the bottom of the ocean when it settles. Plastic particles concentrate on their surface both toxic substances disrupting a number of human systems and other persistent synthetic compounds, which are then collected in the natural way of life at different trophic levels.

Our study and other research of this type, especially those of a regional and local nature, can be part of training campaigns and efforts planned to reduce plastic waste around the world. Although ocean cleanup is probably one of the most outstanding ventures at present, the countless smaller and private shoreline cleanup activities around the world are contributing fundamentally to much needed change.

The circular economy is seen as the most promising path towards a more sustainable use of polymers. It aims to reduce resource consumption by keeping materials in the value chain for longer periods than traditional linear material flow.

MPs are a serious environmental and potential health problem. Therefore, it is necessary to take measures to reduce the production and disposal of plastics waste, as well as to better manage and process this waste. Raising general awareness and achieving a positive effect through cleaning and prevention activities can continue to develop. Institutional research strategies would ensure similarity of results in order to be able to form an increasingly stable picture of plastics pollution around the world. We will most likely tackle this problem if the contribution of new plastic junk is stopped in the long term or reduced radically earlier. Like this we should be able to protect biological systems and not cross any major natural boundaries.

Life on Earth depends on us!

ИЗВОД
МИКРОПЛАСТИКА – ЗАГАЂИВАЧИ ЕКОСИСТЕМА

ELENA J. MOLLOVA¹, EMILJA D. IVANOVA^{1,2}, SEVDALINA CH. TURMANOVA² и ALEKSANDAR N. DIMITROV¹

¹Faculty of Natural Sciences, Assen Zlatarov University, 8010 Burgas, Bulgaria и ²Faculty of Technical Sciences, Assen Zlatarov University, 8010 Burgas, Bulgaria

Присуство микропластике у различитим екосистемима интензивно се проучава од почетка 21. века, и од тада се налазе у свим деловима животне средине, као и у бројним организмима. Микропластика (МР) је термин за честице чија је величина 1 μm–5 mm која се формира током деградације већих пластичних производа или се производе у микро-величинама за различите индустријске и козметичке производе. Дистрибуција ових честица последица је њиховог брзог транспорта на великим раздаљинама, а углавном је олакшана њиховом малом величином и ниском густином. Још увек не постоје уједначене методе и стандардизоване процедуре за узорковање и анализу. Стога чињенице о појављивању, дистрибуцији и претњама екосистемима и људском здрављу од МР још увек нису у потпуности схваћене. Овај преглед литературе је широка презентација стања знања о расподели МР у атмосфери, води, земљишту и организмима. Поред тога, овај документ описује најраспрострањеније методе за раздавање, идентификацију и карактеризацију микропластике.

(Примљено 16. маја, ревидирано 10. јула, прихваћено 6. октобра 2023)

REFERENCES

1. *Plastics – the Facts*, October, 2022 (https://plasticseurope.org/wp-content/uploads/2022/10/PE-PLASTICS-THE-FACTS_V7-Tue_19-10-1.pdf)

2. A. Rodriguez-Seijo, R. Pereira, *Compr. Anal. Chem.* **75** (2017) 49 (<https://doi.org/10.1016/bs.coac.2016.10.007>)
3. M. Cole, T. S. Galloway, *Environ. Sci. Technol.* **49** (2015) 14625 (<https://doi.org/10.1021/acs.est.5b04099>)
4. N. B. Hartmann, T. Hüffer, R. C. Thompson, M. Hassellöv, A. Verschoor, A. E. Daugaard, S. Rist, T. Karlsson, N. Brennholt, M. Cole, M. P. Herrling, M. C. Hess, N. P. Ivleva, A. L. Lusher, M. Wagner, *Environ. Sci. Technol.* **53** (2019) 1039 (<https://doi.org/10.1021/acs.est.8b05297>)
5. C. Schmid, L. Cozzarini, E. Zambello, *Mar. Pollut. Bull.* **162** (2021) 111820 (<https://doi.org/10.1016/J.MARPOLBUL.2020.111820>)
6. R. C. Thompson, Y. Olson, R. P. Mitchell, A. Davis, S. J. Rowland, A. W. G. John, D. McGonigle, A. E. Russell, *Science* **304** (2004) 838 (<https://doi.org/10.1126/science.1094559>)
7. A. E. Christian, I. Köper, *Sci. Total Environ.* **864** (2023) 161083 (<https://doi.org/10.1016/J.SCITOTENV.2022.161083>)
8. N. A. Welden, A. Lusher, *Microplastics*, Elsevier Inc., Amsterdam, 2020 (<https://doi.org/10.1016/b978-0-12-817880-5.00009-8>)
9. W. J. Shim, Y. K. Song, S. H. Hong, M. Jang, *Mar. Pollut. Bull.* **113** (2016) 469 (<https://doi.org/10.1016/J.MARPOLBUL.2016.10.049>)
10. L. M. Rios Mendoza, D. Leon Vargas, M. Balcer, *Curr. Opin. Green Sustain. Chem.* **32** (2021) 100523 (<https://doi.org/10.1016/J.COGSC.2021.100523>)
11. F. Petersen, J. A. Hubbart, *Sci. Total Environ.* **758** (2021) 143936 (<https://doi.org/10.1016/J.SCITOTENV.2020.143936>)
12. W. Huang, B. Song, J. Liang, Q. Niu, G. Zeng, M. Shen, J. Deng, Y. Luo, X. Wen, Y. Zhang, *J. Hazard. Mater.* **405** (2021) 124187 (<https://doi.org/10.1016/J.JHAZMAT.2020.124187>)
13. S. Allen, D. Allen, V. R. Phoenix, G. Le Roux, P. Durández Jiménez, A. Simonneau, S. Binet, D. Galop, *Nat. Geosci.* **12** (2019) 339 (<https://doi.org/10.1038/s41561-019-0335-5>)
14. R. Dris, J. Gasperi, M. Saad, C. Mirande, B. Tassin, *Mar. Pollut. Bull.* **104** (2016) 290 (<https://doi.org/10.1016/J.MARPOLBUL.2016.01.006>)
15. R. Dris, First assessment of sources and fate of macro-and micro-plastics in urban hydrosystems: Case of Paris megacity (<https://theses.hal.science/tel-01541090/file/TH2016PESC1108.pdf>)
16. Y. Huang, T. He, M. Yan, L. Yang, H. Gong, W. Wang, X. Qing, J. Wang, *J. Hazard. Mater.* **416** (2021) 126168 (<https://doi.org/10.1016/J.JHAZMAT.2021.126168>)
17. S. L. Wright, J. Ulke, A. Font, K. L. A. Chan, F. J. Kelly, *Environ. Int.* **136** (2020) 105411 (<https://doi.org/10.1016/J.ENVINT.2019.105411>)
18. S. Kernchen, M. G. J. Löder, F. Fischer, D. Fischer, S. R. Moses, C. Georgi, A. C. Nölscher, A. Held, C. Laforsch, *Sci. Total Environ.* **818** (2022) 151812 (<https://doi.org/10.1016/J.SCITOTENV.2021.151812>)
19. A. A. Horton, S. J. Dixon, *Wiley Interdiscip. Rev. Water* **5** (2018) (<https://doi.org/10.1002/WAT2.1268>)
20. K. Liu, T. Wu, X. Wang, Z. Song, C. Zong, N. Wei, D. Li, *Environ. Sci. Technol.* **53** (2019) 10612 (<https://doi.org/10.1021/acs.est.9b03427>)
21. M. Bergmann, S. Mütszel, S. Primpke, M. B. Tekman, J. Trachsel, G. Gerdts, *White and wonderful? Microplastics prevail in snow from the Alps to the Arctic*, 2019
22. W. Zhang, J. Shen, J. Wang, *Environ. Pollut.* **285** (2021) 117501 (<https://doi.org/10.1016/j.envpol.2021.117501>)

23. R. Akhbarizadeh, S. Dobaradaran, M. Amouei Torkmahalleh, R. Saeedi, R. Aibaghi, F. Faraji Ghasemi, *Environ. Res.* **192** (2021) 110339 (<https://doi.org/10.1016/J.ENVRES.2020.110339>)
24. C. Liu, J. Li, Y. Zhang, L. Wang, J. Deng, Y. Gao, L. Yu, J. Zhang, H. Sun, *Environ. Int.* **128** (2019) 116 (<https://doi.org/10.1016/J.ENVINT.2019.04.024>)
25. Y. Zhang, S. Kang, S. Allen, D. Allen, T. Gao, M. Sillanpää, *Earth-Science Rev.* **203** (2020) 103118 (<https://doi.org/10.1016/J.EARSCIREV.2020.103118>)
26. K. Zhang, J. Su, X. Xiong, X. Wu, C. Wu, J. Liu, *Environ. Pollut.* **219** (2016) 450 (<https://doi.org/10.1016/J.ENVPOL.2016.05.048>)
27. M. Klein, E. K. Fischer, *Sci. Total Environ.* **685** (2019) 96 (<https://doi.org/10.1016/J.SCITOTENV.2019.05.405>)
28. Z. Zhang, Zulpiya·Mamat, Y. Chen, *Ecotoxicol. Environ. Saf.* **202** (2020) (<https://doi.org/10.1016/j.ecoenv.2020.110976>)
29. R. W. Obbard, S. Sadri, Y. Q. Wong, A. A. Khutun, I. Baker R. C. Thompson, *Earth's Futur.* **2** (2014) 315 (<https://doi.org/10.1002/2014ef000240>)
30. R. Ambrosini, R. S. Azzoni, F. Pittino, G. Diolaiuti, A. Franzetti, M. Parolini, *Environ. Pollut.* **253** (2019) 297 (<https://doi.org/10.1016/J.ENVPOL.2019.07.005>)
31. S. Dehghani, F. Moore, R. Akhbarizadeh, *Environ. Sci. Pollut. Res.* **24** (2017) 20360 (<https://doi.org/10.1007/s11356-017-9674-1>)
32. Y. Sun, L. Cao, Y. Wang, W. Chen, Y. Li, X. Zhao, *Environ. Pollut.* **311** (2022) 119910 (<https://doi.org/10.1016/J.ENVPOL.2022.119910>)
33. C. M. Rochman, A. Tahir, S. L. Williams, D. V. Baxa, R. Lam, J. T. Miller, F. C. Teh, S. Werorilangi, S. J. Teh, *Sci. Rep.* **5** (2015) (<https://doi.org/10.1038/srep14340>)
34. O. Setälä, V. Fleming-Lehtinen, M. Lehtiniemi, *Environ. Pollut.* **185** (2014) 77 (<https://doi.org/10.1016/J.ENVPOL.2013.10.013>)
35. J. C. Prata, *Environ. Pollut.* **234** (2018) 115 (<https://doi.org/10.1016/J.ENVPOL.2017.11.043>)
36. V. S. Koutnik, J. Leonard, S. Alkidim, F. J. DePrima, S. Ravi, E. M. V. Hoek, S. K. Mohanty, *Environ. Pollut.* **274** (2021) 116552 (<https://doi.org/10.1016/J.ENVPOL.2021.116552>)
37. J. Grbić, P. Helm, S. Athey, C. M. Rochman, *Water Res.* **174** (2020) 115623 (<https://doi.org/10.1016/J.WATRES.2020.115623>)
38. N. Ramírez-Álvarez, L. M. Rios Mendoza, J. V. Macías-Zamora, L. Oregel-Vázquez, A. Alvarez-Aguilar, F. A. Hernández-Guzmán, J. L. Sánchez-Osorio, C. J. Moore, H. Silva-Jiménez, L. F. Navarro-Olache, *Sci. Total Environ.* **703** (2020) 134838 (<https://doi.org/10.1016/J.SCITOTENV.2019.134838>)
39. X. Zhao, Y. Zhou, C. Liang, J. Song, S. Yu, G. Liao, P. Zou, K. H. D. Tang, C. Wu, *Sci. Total Environ.* **858** (2023) 159943 (<https://doi.org/10.1016/J.SCITOTENV.2022.159943>)
40. D. Gola, P. Kumar Tyagi, A. Arya, N. Chauhan, M. Agarwal, S. K. Singh, S. Gola, *Environ. Nanotechnol. Monit. Manage.* **16** (2021) (<https://doi.org/10.1016/j.enmm.2021.100552>)
41. A. Zayen, S. Sayadi, C. Chevalier, M. Boukthir, S. Ben Ismail, M. Tedetti, *Estuar. Coast. Shelf Sci.* **242** (2020) 106832 (<https://doi.org/10.1016/J.ECSS.2020.106832>)
42. D. Berov, S. Klajn, *Mar. Pollut. Bull.* **156** (2020) 111225 (<https://doi.org/10.1016/J.MARPOLBUL.2020.111225>)
43. A. R. Eryaşar, K. Gedik, A. Şahin, R. Ç. Öztürk, F. Yılmaz, *Mar. Pollut. Bull.* **173** (2021) 112993 (<https://doi.org/10.1016/J.MARPOLBUL.2021.112993>)

44. A. Simeonova, R. Chuturkova, *Reg. Stud. Mar. Sci.* **37** (2020) (<https://doi.org/10.1016/j.rsma.2020.101329>)
45. D. Toneva, T. Stankova, D. Dimova, *Contemporary Social Issues View project RG Achievement View project*, 2019 (https://www.researchgate.net/publication/326066341_Development_of_Wind_Energy_Projects_in_Bulgaria-Challenges_and_Opportunities)
46. V. Yaneva, A. Simeonova, D. Toneva, J. Vladimirova, Серия “Технически науки” Известия на съюза на учените – Варна 1 (2016) 50 ISSN 1310-5833 (https://www.researchgate.net/publication/317042467_Aneva_V_A_Simeonova_D_Toneva_Z_Vladimirova_R_Hristova_Proucvane_na_morskite_otpadci_po_bregovata_ivica_na_Nov_kanal_Varnensko_ezero_-_Cerno_More)
47. Y. Terzi, K. Gedik, A. R. Eryaşar, R. Ç. Öztürk, A. Şahin, F. Yilmaz, *Mar. Pollut. Bull.* **174** (2022) 113228 (<https://doi.org/10.1016/J.MARPOLBUL.2021.113228>)
48. A. D'Hont, A. Gittenberger, R. S. E. W. Leuven, A. J. Hendriks, *Mar. Pollut. Bull.* **173** (2021) 112982 (<https://doi.org/10.1016/J.MARPOLBUL.2021.112982>)
49. A. Cincinelli, C. Scopetani, D. Chelazzi, T. Martellini, M. Pogojeva, J. Slobodnik, *Sci. Total Environ.* **760** (2021) 143898 (<https://doi.org/10.1016/J.SCITOTENV.2020.143898>)
50. S. Turmanova, S. Nedkova, P. Atanasova, E. Ivanova, A. Veli, A. Dimitrov, N. Todorov, V. Georgieva, B. Midyurova, S. Naydenova, E. Mollova, *Cross-Border Regions Collaborate for Blue Growth. Part I. Exploratory monitoring of aquatic ecosystems*, 2021 (<https://conf.uni-ruse.bg/bg/?cmd=dPage&pid=bp-2021>)
51. J. Reisser, B. Slat, K. Noble, K. Du Plessis, M. Epp, M. Proietti, J. De Sonneville, T. Becker, C. Pattiarchi, *Biogeosci.* **12** (2015) 1249 (<https://doi.org/10.5194/bg-12-1249-2015>)
52. N. Billingham, *Plast. Addit. (third Ed.)* (1991) (<https://doi.org/10.1002/pi.4990250419>)
53. H. K. Imhof, C. Laforsch, A. C. Wiesheu, J. Schmid, P. M. Anger, R. Niessner, N. P. Ivleva, *Water Res.* **98** (2016) 64 (<https://doi.org/10.1016/J.WATRES.2016.03.015>)
54. A. Stolte, S. Forster, G. Gerdts, H. Schubert, *Mar. Pollut. Bull.* **99** (2015) 216 (<https://doi.org/10.1016/J.MARPOLBUL.2015.07.022>)
55. H. S. Auta, C. U. Emenike, S. H. Fauziah, *Environ. Int.* **102** (2017) 165 (<https://doi.org/10.1016/j.envint.2017.02.013>)
56. M. Lehtiniemi, S. Hartikainen, P. Näkki, J. Engström-Öst, A. Koistinen, O. Setälä, *Food Webs* **17** (2018) (<https://doi.org/10.1016/j.fooweb.2018.e00097>)
57. T. Wang, M. Hu, G. Xu, H. Shi, J. Y. S. Leung, Y. Wang, *Sci. Total Environ.* **754** (2021) 142099 (<https://doi.org/10.1016/J.SCITOTENV.2020.142099>)
58. S. A. Carr, J. Liu, A. G. Tesoro, *Water Res.* **91** (2016) 174 (<https://doi.org/10.1016/J.WATRES.2016.01.002>)
59. A. L. Andrade, *Mar. Pollut. Bull.* **119** (2017) 12 (<https://doi.org/10.1016/J.MARPOLBUL.2017.01.082>)
60. M. Cole, P. Lindeque, C. Halsband, T. S. Galloway, *Mar. Pollut. Bull.* **62** (2011) 2588 (<https://doi.org/10.1016/j.marpolbul.2011.09.025>)
61. D. Eerkes-Medrano, R. C. Thompson, D. C. Aldridge, *Water Res.* **75** (2015) 63 (<https://doi.org/10.1016/J.WATRES.2015.02.012>)
62. M. A. Browne, A. Dissanayake, T. S. Galloway, D. M. Lowe, R. C. Thompson, *Environ. Sci. Technol.* **42** (2008) 5026 (<https://doi.org/10.1021/es800249a>)
63. P. G. Ryan, C. J. Moore, J. A. Van Franeker, C. L. Moloney, *Philos. Trans. R. Soc., B* **364** (2009) 1999 (<https://doi.org/10.1098/rstb.2008.0207>)

64. C. M. Boerger, G. L. Lattin, S. L. Moore, C. J. Moore, *Mar. Pollut. Bull.* **60** (2010) 2275 (<https://doi.org/10.1016/J.MARPOLBUL.2010.08.007>)
65. A. Buzzell, C. Schroeder, J. Strauss, T. Alexander, *Interact. Qualif. Proj. (All Years)* (2018)
66. Y. Zhang, Y. Li, F. Su, L. Peng, D. Liu, *Sci. Total Environ.* **802** (2022) 149658 (<https://doi.org/10.1016/J.SCITOTENV.2021.149658>)
67. Y. Liu, B. Wang, V. Pileggi, S. Chang, *Case Study Chem. Environ. Eng.* **5** (2022) (<https://doi.org/10.1016/j.cscee.2022.100183>)
68. L. M. Rios Mendoza, M. Balcer, *Association of hazardous compounds with microplastics in freshwater ecosystems.* in *Microplastics in Water and Wastewater*, 2020 (https://doi.org/10.2166/9781789061697_0015)
69. K. I. Jayasanta, R. L. Laju, J. Patterson, M. Jayanthi, D. S. Bilgi, N. Sathish, J. K. P. Edward, *Sci. Total Environ.* **861** (2023) 160572 (<https://doi.org/10.1016/J.SCITOTENV.2022.160572>)
70. A. R. A. Lima, M. Barletta, M. F. Costa, *Estuar. Coast. Shelf Sci.* **165** (2015) 213 (<https://doi.org/10.1016/J.ECSS.2015.05.018>)
71. C. D. M. Lima, M. Melo Júnior, S. H. L. Schwamborn, F. Kessler, L. A. Oliveira, B. P. Ferreira, G. Mugrabe, J. Frias, S. Neumann-Leitão, *Environ. Pollut.* **322** (2023) 121072 (<https://doi.org/10.1016/J.ENVPOL.2023.121072>)
72. J. Zalasiewicz, C. N. Waters, J. A. Ivar do Sul, P. L. Corcoran, A. D. Barnosky, A. Cearreta, M. Edgeworth, A. Gałuszka, C. Jeandel, R. Leinfelder, J. R. McNeill, W. Steffen, C. Summerhayes, M. Wagreich, M. Williams, A. P. Wolfe, Y. Yonan, *Anthropocene* **13** (2016) 4 (<https://doi.org/10.1016/J.ANCENE.2016.01.002>)
73. I. Schrank, B. Trotter, J. Dummert, B. M. Scholz-Böttcher, M. G. J. Löder, C. Laforsch, *Environ. Pollut.* **255** (2019) 113233 (<https://doi.org/10.1016/J.ENVPOL.2019.113233>)
74. E. Curren, V. S. Kuwahara, T. Yoshida, S. C. Y. Leong, *Environ. Pollut.* **288** (2021) 117776 (<https://doi.org/10.1016/J.ENVPOL.2021.117776>)
75. B. Xue, L. Zhang, R. Li, Y. Wang, J. Guo, K. Yu, S. Wang, *Environ. Sci. Technol.* **54** (2020) 2210 (<https://doi.org/10.1021/acs.est.9b04850>)
76. C. Sabine, G. Bala, L. Bopp, V. Brovkin, J. Canadell, A. Chhabra, R. DeFries, J. Galloway, M. Heimann, C. Jones, C. Le Quéré, R. Myneni, S. Piao, P. Thornton, D. Qin, G. Plattner, M. Tignor, S. Allen, J. Boschung, A. Nauels, Y. Xia, V. Bex, P. Midgley, P. Ciais, C. Sabine, G. Bala, L. Bopp, V. Brovkin Germany, in *Climate Change 2013: The Physical Science Basis. Contribution of Working Group I to the Fifth Assessment Report of the Intergovernmental Panel on Climate Change Coordinating Lead Authors: Lead Authors: Contributing Authors*, Peter, 2013 (https://www.ipcc.ch/site/assets/uploads/2017/09/WG1AR5_Frontmatter_FINAL.pdf)
77. M. E. Seeley, B. Song, R. Passie, R. C. Hale, *Nat. Commun.* **11** (2020) (<https://doi.org/10.1038/s41467-020-16235-3>)
78. O. Setälä, J. Norkko, M. Lehtiniemi, *Mar. Pollut. Bull.* **102** (2016) 95 (<https://doi.org/10.1016/J.MARPOLBUL.2015.11.053>)
79. P. Kolandhasamy, L. Su, J. Li, X. Qu, K. Jabeen, H. Shi, *Sci. Total Environ.* **610–611** (2018) 635 (<https://doi.org/10.1016/J.SCITOTENV.2017.08.053>)
80. U. Aytan, F. B. Esenoy, Y. Senturk, *Sci. Total Environ.* **806** (2022) 150921 (<https://doi.org/10.1016/J.SCITOTENV.2021.150921>)
81. M. Cole, P. Lindeque, E. Fileman, C. Halsband, R. Goodhead, J. Moger, T. S. Galloway, *Environ. Sci. Technol.* **47** (2013) 6646 (<https://doi.org/10.1021/es400663f>)

82. P. Farrell, K. Nelson, *Environ. Pollut.* **177** (2013) 1 (<https://doi.org/10.1016/j.envpol.2013.01.046>)
83. A. Naji, M. Nuri, A. D. Vethaak, *Environ. Pollut.* **235** (2018) 113 (<https://doi.org/10.1016/J.ENVPOL.2017.12.046>)
84. A. M. Elgarahy, A. Akhdhar, K. Z. Elwakeel, *J. Environ. Chem. Eng.* **9** (2021) 106224 (<https://doi.org/10.1016/J.JECE.2021.106224>)
85. J. Reichert, J. Schellenberg, P. Schubert, T. Wilke, *Environ. Pollut.* **237** (2018) 955 (<https://doi.org/10.1016/J.ENVPOL.2017.11.006>)
86. W. Huang, M. Chen, B. Song, J. Deng, M. Shen, Q. Chen, G. Zeng, J. Liang, *Sci. Total Environ.* **762** (2021) 143112 (<https://doi.org/10.1016/J.SCITOTENV.2020.143112>)
87. R. Ding, L. Tong, W. Zhang, *Water. Air. Soil Pollut.* **232** (2021) (<https://doi.org/10.1007/s11270-021-05081-8>)
88. S. Sarajan, S. Azman, M. I. M. Said, M. H. Jamal, *Environ. Sci. Pollut. Res.* **28** (2021) 1341 (<https://doi.org/10.1007/s11356-020-11171-7>)
89. G. D'avignon, I. Gregory-Eaves, A. Ricciardi, *Environ. Rev.* **30** (2022) 228 (<https://doi.org/10.1139/er-2021-0048>)
90. D. Schymanski, C. Goldbeck, H. U. Humpf, P. Fürst, *Water Res.* **129** (2018) 154 (<https://doi.org/10.1016/J.WATRES.2017.11.011>)
91. W. Wang, W. Yuan, E. G. Xu, L. Li, H. Zhang, Y. Yang, *Environ. Res.* **203** (2022) 111867 (<https://doi.org/10.1016/J.ENVRES.2021.111867>)
92. R. Qi, D. L. Jones, Z. Li, Q. Liu, C. Yan, *Sci. Total Environ.* **703** (2020) 134722 (<https://doi.org/10.1016/J.SCITOTENV.2019.134722>)
93. I. Colzi, L. Renna, E. Bianchi, M. B. Castellani, A. Coppi, S. Pignattelli, S. Loppi, C. Gonnelli, *J. Hazard. Mater.* **423** (2022) 127238 (<https://doi.org/10.1016/J.JHAZMAT.2021.127238>)
94. J. Munyaneza, Q. Jia, F. A. Qaraah, M. F. Hossain, C. Wu, H. Zhen, G. Xiu, *Sci. Total Environ.* **822** (2022) 153339 (<https://doi.org/10.1016/J.SCITOTENV.2022.153339>)
95. R. Dris, H. Imhof, W. Sanchez, J. Gasperi, F. Galgani, B. Tassin, C. Laforsch, *Environ. Chem.* **12** (2015) 539 (<https://doi.org/10.1071/EN14172>)
96. P. Jan Kole, A. J. Löhr, F. G. A. J. Van Belleghem, A. M. J. Ragas, *Int. J. Environ. Res. Public Health* **14** (2017) (<https://doi.org/10.3390/ijerph14101265>)
97. J. M. Panko, J. Chu, M. L. Kreider, K. M. Unice, *Atmos. Environ.* **72** (2013) 192 (<https://doi.org/10.1016/J.ATMOSENV.2013.01.040>)
98. T. Grigoratos, G. Martini, *Non-exhaust traffic related emissions – Brake and tyre wear PM literature review*, European Commission. Joint Research Centre. Institute for Energy and Transport (<https://worldcat.org/fr/title/1044281650>)
99. A. Dahl, A. Gharibi, E. Swietlicki, A. Gudmundsson, M. Bohgard, A. Ljungman, G. Blomqvist, M. Gustafsson, *Atmos. Environ.* **40** (2006) 1314 (<https://doi.org/10.1016/J.ATMOSENV.2005.10.029>)
100. A. A. Horton, C. Svendsen, R. J. Williams, D. J. Spurgeon, E. Lahive, *Mar. Pollut. Bull.* **114** (2017) 218 (<https://doi.org/10.1016/J.MARPOLBUL.2016.09.004>)
101. M. Siegfried, A. A. Koelmans, E. Besseling, C. Kroese, *Water Res.* **127** (2017) 249 (<https://doi.org/10.1016/j.watres.2017.10.011>)
102. M. L. Kreider, J. M. Panko, B. L. McAtee, L. I. Sweet, B. L. Finley, *Sci. Total Environ.* **408** (2010) 652 (<https://doi.org/10.1016/J.SCITOTENV.2009.10.016>)
103. P. Q. Fu, K. Kawamura, J. Chen, B. Charrière, R. Sempéré, *Biogeosci.* **10** (2013) 653 (<https://doi.org/10.5194/bg-10-653-2013>)

104. K. M. Unice, M. P. Weeber, M. M. Abramson, R. C. D. Reid, J. A. G. van Gils, A. A. Markus, A. D. Vethaak, J. M. Panko, *Sci. Total Environ.* **646** (2019) 1639 (<https://doi.org/10.1016/j.scitotenv.2018.07.368>)
105. P. Ebrahimi, S. Abbasi, R. Pashaei, A. Bogusz, P. Oleszczuk, *Chemosphere* **289** (2022) 133146 (<https://doi.org/10.1016/J.CHEMOSPHERE.2021.133146>)
106. L. C. Jenner, J. M. Rotchell, R. T. Bennett, M. Cowen, V. Tentzeris, L. R. Sadofsky, *Sci. Total Environ.* **831** (2022) 154907 (<https://doi.org/10.1016/J.SCITOTENV.2022.154907>)
107. N. S. Soltani, M. P. Taylor, S. P. Wilson, *Environ. Pollut.* **283** (2021) 117064 (<https://doi.org/10.1016/J.ENVPOL.2021.117064>)
108. K. Vorkamp, F. F. Rigét, *Chemosphere* **111** (2014) 379 (<https://doi.org/10.1016/J.CHEMOSPHERE.2014.04.019>)
109. R. O. Williams, T. C. Carvalho, J. I. Peters, *Int. J. Pharm.* **406** (2011) 1 (<https://doi.org/10.1016/J.IJPHARM.2010.12.040>)
110. S. Bakand, A. Hayes, F. Dechsakulthorn, *Inhal. Toxicol.* **24** (2012) 125 (<https://doi.org/10.3109/08958378.2010.642021>)
111. A. Facciolià, G. Visalli, M. P. Ciarello, A. Di Pietro, *Int. J. Environ. Res. Public Health* **18** (2021) 1–17 (<https://doi.org/10.3390/ijerph18062997>)
112. S. L. Wright, F. J. Kelly, *Environ. Sci. Technol.* **51** (2017) 6634 (<https://doi.org/10.1021/acs.est.7b00423>)
113. C. Romera-Castillo, M. Pinto, T. M. Langer, X. A. Álvarez-Salgado, G. J. Herndl, *Nat. Commun.* **9** (2018) (<https://doi.org/10.1038/s41467-018-03798-5>)
114. E. L. Teuten, J. M. Saquing, D. R. U. Knappe, M. A. Barlaz, S. Jonsson, A. Björn, S. J. Rowland, R. C. Thompson, T. S. Galloway, R. Yamashita, D. Ochi, Y. Watanuki, C. Moore, P. H. Viet, T. S. Tana, M. Prudente, R. Boonyatumanond, M. P. Zakaria, K. Akkhavong, Y. Ogata, H. Hirai, S. Iwasa, K. Mizukawa, Y. Hagino, A. Imamura, M. Saha, H. Takada, *Philos. Trans. R. Soc., B* **364** (2009) 2027 (<https://doi.org/10.1098/rstb.2008.0284>)
115. A. W. Verla, C. E. Enyoh, E. N. Verla, K. O. Nwarnorh, *SN Appl. Sci.* **1** (2019) (<https://doi.org/10.1007/s42452-019-1352-0>)
116. L. Van Vaeck, K. Van Cauwenberche, J. Janssens, *The gas-particle distribution of organic aerosol constituents: measurement of the volatilisation artefact in hi-vol cascade impactor sampling*, 1984 (<https://ui.adsabs.harvard.edu/abs/1984AtmEn..18..417V/abstract>)
117. J. M. Delgado-Saborit, M. S. Alam, K. J. Godri Pollitt, C. Stark, R. M. Harrison, *Atmos. Environ.* **77** (2013) 974 (<https://doi.org/10.1016/J.ATMOSENV.2013.05.080>)
118. J. O. Allen, J. Durant, N. M. Dookeran, K. Taghizadeh, E. F. Plummer, A. L. Lafleur, A. F. Sarofim, K. A. A. Smith, *Environ. Sci. Technol.* **32** (1998) 1928 (<https://doi.org/10.1021/es970919r>)
119. W. Wang, J. Wang, *TrAC – Trends Anal. Chem.* **108** (2018) 195 (<https://doi.org/10.1016/j.trac.2018.08.026>)
120. J. Zhang, D. Yuan, Q. Zhao, S. Yan, S. Y. Tang, S. H. Tan, J. Guo, H. Xia, N. T. Nguyen, W. Li, *Sensors Actuators, B* **267** (2018) 14 (<https://doi.org/10.1016/J.SNB.2018.04.020>)
121. A. Bhattacharya, S. K. Khare, *J. Environ. Sci. Heal., C* **38** (2020) 1 (<https://doi.org/10.1080/10590501.2019.1699379>)
122. S. Wieland, A. Balmes, J. Bender, J. Kitzinger, F. Meyer, A. F. Ramsperger, F. Roeder, C. Tengelmann, B. H. Wimmer, C. Laforsch, H. Kress, *J. Hazard. Mater.* **428** (2022) 128151 (<https://doi.org/10.1016/J.JHAZMAT.2021.128151>)
123. T. C. Nardelli, H. C. Erythropel, B. Robaire, *PLoS One* **10** (2015) (<https://doi.org/10.1371/journal.pone.0138421>)

124. J. Peretz, L. Vrooman, W. A. Ricke, P. A. Hunt, S. Ehrlich, R. Hauser, V. Padmanabhan, H. S. Taylor, S. H. Swan, C. A. Vandeoort, J. A. Flaws, *Environ. Health Perspect.* **122** (2014) 775–786 (<https://doi.org/10.1289/ehp.1307728>)
125. I. B. D. Law, W. B. Bunn, T. W. Hesterberg, *Solubility of polymeric organic fibers and manmade vitreous fibers in gambles solution*, 1990 (<https://www.tandfonline.com/doi/abs/10.3109/08958379009145261>)
126. A. Sridhar, D. Kannan, A. Kapoor, S. Prabhakar, *Chemosphere* **286** (2022) 131653 (<https://doi.org/10.1016/J.CHEMOSPHERE.2021.131653>)
127. G. A. Elizalde-Velázquez, L. M. Gómez-Oliván, *Sci. Total Environ.* **780** (2021) 146551 (<https://doi.org/10.1016/J.SCITOTENV.2021.146551>)
128. K. D. Cox, G. A. Covernton, H. L. Davies, J. F. Dower, F. Juanes, S. E. Dudas, *Environ. Sci. Technol.* **53** (2019) 7068 (<https://doi.org/10.1021/acs.est.9b01517>)
129. L. G. A. Barboza, A. Cózar, B. C. G. Gimenez, T. L. Barros, P. J. Kershaw, L. Guilhermino, *Macroplastics pollution in the marine environment*, second ed., Elsevier Ltd., Amsterdam, 2018 (<https://doi.org/10.1016/B978-0-12-805052-1.00019-X>)
130. M. Forte, G. Iachetta, M. Tussellino, R. Carotenuto, M. Prisco, M. De Falco, V. Laforgia, S. Valiante, *Toxicol. Vitr.* **31** (2016) 126 (<https://doi.org/10.1016/J.TIV.2015.11.006>)
131. F. Stock, C. Kochleus, B. Bänsch-Baltruschat, N. Brennholt, G. Reifferscheid, *TrAC – Trends Anal. Chem.* **113** (2019) 84 (<https://doi.org/10.1016/j.trac.2019.01.014>)
132. N. H. Mohamed Nor, M. Kooi, N. J. Diepens, A. A. Koelmans, *Environ. Sci. Technol.* **55** (2021) 5084 (<https://dx.doi.org/10.1021/acs.est.0c07384>)
133. V. Paget, S. Dekali, T. Kortulewski, R. Grall, C. Gamez, K. Blazy, O. Aguerre-Chariol, S. Chevillard, A. Braun, P. Rat, G. Lacroix, *PLoS One* **10** (2015) (<https://doi.org/10.1371/journal.pone.0123297>)
134. M. Xu, G. Halimu, Q. Zhang, Y. Song, X. Fu, Y. Li, Y. Li, H. Zhang, *Sci. Total Environ.* **694** (2019) 133794 (<https://doi.org/10.1016/J.SCITOTENV.2019.133794>)
135. G. F. Schirinzi, I. Pérez-Pomeda, J. Sanchís, C. Rossini, M. Farré, D. Barceló, *Environ. Res.* **159** (2017) 579 (<https://doi.org/10.1016/J.ENVRRES.2017.08.043>)
136. S. Grafmueller, P. Manser, L. Diener, P. A. Diener, X. Maeder-Althaus, L. Maurizi, W. Jochum, H. F. Krug, T. Buerki-Thurnherr, U. von Mandach, P. Wick, *Environ. Health Perspect.* **123** (2015) 1280 (<https://doi.org/10.1289/ehp.1409271>)
137. D. Lithner, A. Larsson, G. Dave, *Sci. Total Environ.* **409** (2011) 3309 (<https://doi.org/10.1016/J.SCITOTENV.2011.04.038>)
138. B. Gewert, M. M. Plassmann, M. Macleod, *Environ. Sci. Process. Impacts* **17** (2015) 1513 (<https://doi.org/10.1039/c5em00207a>)
139. A. L. Andrade, *Mar. Pollut. Bull.* **62** (2011) 1596 (<https://doi.org/10.1016/j.marpolbul.2011.05.030>)
140. J. Kim, S. V. Chankeshwara, F. Thielbeer, J. Jeong, K. Donaldson, M. Bradley, W. S. Cho, *Nanotoxicology* **10** (2016) 94 (<https://doi.org/10.3109/17435390.2015.1022887>)
141. E. Miller, M. Sedlak, D. Lin, C. Box, C. Holleman, C. M. Rochman, R. Sutton, *J. Hazard. Mater.* **409** (2021) 124770 (<https://doi.org/10.1016/J.JHAZMAT.2020.124770>)
142. A. Tirkey, L. S. B. Upadhyay, *Mar. Pollut. Bull.* **170** (2021) 112604 (<https://doi.org/10.1016/j.marpolbul.2021.112604>)
143. B. Shi, M. Patel, D. Yu, J. Yan, Z. Li, D. Petriw, T. Pruyn, K. Smyth, E. Passeport, R. J. D. Miller, & J. Y. Howe, *Sci. Total Environ.* **825** (2022) 153903 (<https://doi.org/10.1016/J.SCITOTENV.2022.153903>)
144. Q. T. Birch, P. M. Potter, P. X. Pinto, D. D. Dionysiou, S. R. Al-Abed, *Talanta* **224** (2021) 121743 (<https://doi.org/10.1016/J.TALANTA.2020.121743>)

145. W. Fu, J. Min, W. Jiang, Y. Li, W. Zhang, *Sci. Total Environ.* **721** (2020) 137561 (<https://doi.org/10.1016/J.SCITOTENV.2020.137561>)
146. M. Parolini, M. A. Ortenzi, C. Morelli, V. Gianotti, *Curr. Opin. Toxicol.* **28** (2021) 38 (<https://doi.org/10.1016/J.COTOX.2021.09.007>)
147. N. A. Yaranal, S. Subbiah, K. Mohanty, *Environ. Technol. Innov.* **21** (2021) 101253 (<https://doi.org/10.1016/J.ETI.2020.101253>)
148. S. Piarulli, C. Malegori, F. Grasselli, L. Airolidi, S. Prati, R. Mazzeo, G. Sciuotto, P. Oliveri, *Chemosphere* **286** (2022) 131861 (<https://doi.org/10.1016/J.CHEMOSPHERE.2021.131861>)
149. Y. Zhou, M. Kumar, S. Sarsaiya, R. Sirohi, S. K. Awasthi, R. Sindhu, P. Binod, A. Pandey, N. S. Bolan, Z. Zhang, L. Singh, S. Kumar, M. K. Awasthi, *Sci. Total Environ.* **802** (2022) 149823 (<https://doi.org/10.1016/J.SCITOTENV.2021.149823>).



Development of 2D and 3D QSAR models of pyrazole derivatives as acetylcholine esterase inhibitors

PUJA MISHRA^{1*}, SUMIT NANDI¹, ANKIT CHATTERJEE¹, TRIDIB NAYEK¹,
SOUVIK BASAK¹, AMIT KUMAR HALDER^{1,2} and ARUP MUKHERJEE³

¹Dr. B.C. Roy College of Pharmacy and Allied Health Sciences, Durgapur, WB, India,

²LAQV@REQUIMTE/Department of Chemistry and Biochemistry, Faculty of Sciences,
University of Porto, Porto, Portugal and ³Department of Biotechnology, Maulana Abul
Kalam Azad University of Technology, WB, India

(Received 21 February, revised 2 August 2023, accepted 31 March 2024)

Abstract: The drugs that are the most useful in all stages of Alzheimer's disease (AD) are acetylcholinesterase (AChE) inhibitors. The objectives of this work are to generate various QSAR models for such drugs and to select a robust predictive models from the corresponding models. Studies were then focused on finding a range of pyrazole-like AChE inhibitors by 2D and 3D QSAR analysis. The genetic algorithm-based multiple linear regression (GA-MLR) provided the statistically robust 2D QSAR model that depicted the significance of the molecular volume and the number of multiple bonds along with the presence/absence of specific atom-centred fragments and topological distance between 2D pharmacophoric features. Furthermore, these results were correlated well with the electrostatic and steric contour maps retrieved from the 3D QSAR (*i.e.*, alignment-dependent molecular field analysis). The 2D QSAR analysis developed a highly statistical and reliable model, which was compared with the mechanistic interpretation of 3D structures and their electrostatic and steric field contributions leading to a predictive 3D QSAR model. The molecule-protein interactions, elicited by molecular docking, corroborated with the field interactions, as revealed by 2D QSAR. Thus, the developed computational models and simulation analyses in the current work provide valuable information for the future design of pyrazole and spiropyrazoline analogs, as potent AChE inhibitors.

Keywords: acetylcholinesterase; QSAR analysis; GA-MLR; contour maps; molecular docking.

*Corresponding authors. E-mail: pujam.phe15@itbhu.ac.in
<https://doi.org/10.2298/JSC230221039M>

INTRODUCTION

Alzheimer's disease (AD) was defined as a progressive neurodegenerative disorder, characterized by the gradual loss of cholinergic neurons and accumulation of β -amyloid protein in the brain areas like cortex and hippocampus. AD is manifested by successive impairment of activities of daily living, cognitive and memory deterioration, and a variety of neuropsychiatric symptoms and disturbances. Loss of memory, cognitive decline, impaired performance of activities of daily life, and behavioural changes are the main characteristics of the disease. Every 20 years the cases were estimated to double thus leading to a figure of over 120 million affected from AD in Asia by 2050. The World Health Organization (WHO) projects that by 2025, about 3/4 of the estimated 1.2 billion people aged 60 years and older, affected by this disease, will reside in developing countries. AD onset starts with short-term memory impairment that gradually progresses to a complete loss of cognitive function, weak performance of activities of daily life, and ultimately to death. Research in this area will be beneficial to AD patients.^{1–3}

AD has no proper cure to date thus a molecule that provides symptomatic relief by inhibiting acetylcholinesterase (AChE) enzyme within the brain is studied. Almost 40 such inhibitors were collected from the literature survey and divided into a test set (20 % of total compounds and a training set (80 % of total compounds). The validated and predictive quantitative structure–activity relationship (QSAR) models were generated based on various feature selection methods. In addition, molecular docking⁴ was also employed in order to reveal that the ionization state of the compounds had an impact on their interaction with AChE.^{2,4–7}

EXPERIMENTAL

A dataset containing forty pyrazole and spiro pyrazoline analogs with AChE inhibitors was collected from the report of Gutti *et al.*⁷ For the development of the QSAR model, the software such as ChemDraw ultra 8.0, April 23, 2003 (ChembridgeSoft Corporation, 100 Cambridge Park Drive, Cambridge, MA 02140, USA), Discovery Studio Visualizer, ver. 21.1.0.20298, Marvin View tool (Marvin View, ver. 18.18.0; ChemAxon: Budapest, Hungary, 2010), alvaDesc, ver. 2.0.4 under OCHEM web server,^{8,9} MLR plus Validation, ver. 1.3 (<https://sites.google.com/site/mlrplusvalidation>), DTC-QSAR, ver. 1.0.6¹⁰ and Open3DQSAR (<http://www.softsea.com/review/Open3DQSAR.html>) were used.¹¹

Construction of chemical structures

The simplified molecular input line entry system (SMILES) notations of 40 compounds (Table I) were first converted to 2D structures by Marvin View tool, and these structures were subsequently saved as 3D structures (in .sdf file).

TABLE I. Library of compounds SMILES along with biological activity⁷

No.	SMILES	R/R'	pIC ₅₀
			AChE
43	O=C(Nc1cccc(-c2cc(-c3cccc3)n[nH]2)c1)c1cccc1	H	5.393
44	O=C(Nc1cccc(-c2cc(-c3ccc(Cl)cc3)n[nH]2)c1)c1cccc1	4-Cl	5.713
45	O=C(Nc1cccc(-c2cc(-c3cccc3Cl)n[nH]2)c1)c1cccc1	2-Cl	5.517
46	O=C(Nc1cccc(-c2cc(-c3ccc(Cl)cc3)n[nH]2)c1)c1cccc1	2,4-diCl	5.711
47	O=C(Nc1cccc(-c2cc(-c3ccc(Br)cc3)n[nH]2)c1)c1cccc1	4-Br	5.665
48	O=C(Nc1cccc(-c2cc(-c3cccc(Br)c3)n[nH]2)c1)c1cccc1	3-Br	5.521
49	O=C(Nc1cccc(-c2cc(-c3ccc(F)cc3)n[nH]2)c1)c1cccc1	4-F	5.68
50	O=C(Nc1cccc(-c2cc(-c3cccc(F)c3)n[nH]2)c1)c1cccc1	3-F	5.589
51	COc1ccc(-c2cc(-c3cccc(NC(=O)c4cccc4)c3)[nH]n2)cc1	4-OMe	5.073
52	COc1cccc(-c2cc(-c3cccc(NC(=O)c4cccc4)c3)[nH]n2)c1	3-OMe	5.06
53	COc1ccc(-c2cc(-c3cccc(NC(=O)c4cccc4)c3)[nH]n2)cc1OC	3,4-diOMe	4.818
54	O=C(Nc1cccc(-c2cc(-c3ccc(C(F)(F)F)cc3)n[nH]2)c1)c1cccc1	4-CF3	5.627
55	O=C(Nc1cccc(-c2cc(-c3cccc(C(F)(F)F)c3)n[nH]2)c1)c1cccc1	3-CF3	5.495
56	O=C(Nc1cccc(-c2cc(-c3ccc(OC(F)(F)F)cc3)n[nH]2)c1)c1cccc1	4-OCF3	5.215
57	N#Cc1ccc(-c2cc(-c3cccc(NC(=O)c4cccc4)c3)[nH]n2)cc1	4-CN	5.417
58	N#Cc1cccc(-c2cc(-c3cccc(NC(=O)c4cccc4)c3)[nH]n2)c1	3-CN	5.405
59	Cc1ccc(-c2cc(-c3cccc(NC(=O)c4cccc4)c3)[nH]n2)cc1	4-Me	4.828
60	Cc1cccc1-c1cc(-c2cccc(NC(=O)c3cccc3)c2)[nH]n1	2-Me	4.771
61	CC(C)c1ccc(-c2cc(-c3cccc(NC(=O)c4cccc4)c3)[nH]n2)cc1	4-iPr	4.81
62	O=C(Nc1cccc(-c2cc(-c3cccc4cccc4)n[nH]2)c1)c1cccc1	α-Naphthyl	4.556
66	O=C(Nc1cccc(C(=O)C2=NNC3(CCCCCC3)C2c2cccc2)c1)c1cccc1	H	5.705
67	O=C(Nc1cccc(C(=O)C2=NNC3(CCCCCC3)C2c2ccc(Cl)cc2)c1)c1cccc1	4-Cl	6.333
68	O=C(Nc1cccc(C(=O)C2=NNC3(CCCCCC3)C2c2cccc2Cl)c1)c1cccc1	2-Cl	5.706
69	O=C(Nc1cccc(C(=O)C2=NNC3(CCCCCC3)C2c2ccc(Cl)cc2Cl)c1)c1cccc1	2,4-diCl	5.877
70	O=C(Nc1cccc(C(=O)C2=NNC3(CCCCCC3)C2c2ccc(Br)cc2)c1)c1cccc1	4-Br	5.943
71	O=C(Nc1cccc(C(=O)C2=NNC3(CCCCCC3)C2c2cccc(Br)c2)c1)c1cccc1	3-Br	5.752
72	O=C(Nc1cccc(C(=O)C2=NNC3(CCCCCC3)C2c2ccc(F)cc2)c1)c1cccc1	4-F	6.023
73	O=C(Nc1cccc(C(=O)C2=NNC3(CCCCCC3)C2c2cccc(F)c2)c1)c1cccc1	3-F	5.789
74	COc1ccc(C2C(C(=O)c3cccc(NC(=O)c4cccc4)c3)=NNC23CCCCC3)cc1	4-OMe	5.635
75	COc1cccc(C2C(C(=O)c3cccc(NC(=O)c4cccc4)c3)=NNC23CCCCC3)c1	3-OMe	5.548
76	COc1ccc(C2C(C(=O)c3cccc(NC(=O)c4cccc4)c3)=NNC23CCCCC3)cc1OC	3,4-diOMe	5.521
77	O=C(Nc1cccc(C(=O)C2=NNC3(CCCCCC3)C2c2ccc(C(F)(F)F)cc2)c1)c1cccc1	4-CF3	5.838
78	O=C(Nc1cccc(C(=O)C2=NNC3(CCCCCC3)C2c2cccc(C(F)(F)F)cc2)c1)c1cccc1	3-CF3	5.716
79	O=C(Nc1cccc(C(=O)C2=NNC3(CCCCCC3)C2c2ccc(OC(F)(F)F)cc2)c1)c1cccc1	4-OCF3	5.65
80	N#Cc1ccc(C2C(C(=O)c3cccc(NC(=O)c4cccc4)c3)=NNC23CCCCC3)cc1	4-CN	5.75
81	N#Cc1cccc(C2C(C(=O)c3cccc(NC(=O)c4cccc4)c3)=NNC23CCCCC3)c1	3-CN	5.707
82	Cc1cccc1C1C(C(=O)c2cccc(NC(=O)c3cccc3)c2)=NNC23CCCCC3)cc1	4-Me	5.329
83	Cc1cccc1C1C(C(=O)c2cccc(NC(=O)c3cccc3)c2)=NNC12CCCCC2	2-Me	5.23
84	CC(C)c1ccc(C2C(C(=O)c3cccc(NC(=O)c4cccc4)c3)=NNC23CCCCC3)cc1	4-iPr	5.146
85	O=C(Nc1cccc(C(=O)C2=NNC3(CCCCCC3)C2c2cccc3cccc23)c1)c1cccc1	α-Naphthyl	4.535

Descriptors generation

The 3D chemical structures of 40 AChE inhibitors were subjected to descriptors calculation using alvaDesc v.2.0.4 (<https://www.alvascience.com/alvadesc/>) under OCHEM web server. The 3D descriptors were calculated after the geometrical optimization performed separately with Corina (molecular mechanical) and ULYSSES (quantum chemical PM67¹²). The calculated descriptors for the dataset compounds were combined with their respective pIC_{50} values in order to generate a data-matrix for 2D QSAR model generation.

Model generation

To initiate the model development procedure the data set ($n = 40$) was divided into a training set (consisting of 80 % of the total number of compounds) and a test set (20 % of the total number of compounds) using a Java-based platform DTC-QSAR^{8,10,13-15} tool (<https://dtclab.webs.com/software-tools>) using random division technique with multiple random state values (*i.e.*, by applying different seed values like 5, 10, 14, *etc.*). Since the major objective of the current investigation is to generate interpretable 2D-QSAR models, we employed selected categories of alvaDesc descriptors and these belong to constitutional descriptors, functional group counts, 2D-atom pairs, drug-like indices, ring descriptors, atom-centred fragments, pharmacophore descriptors and molecular properties. The linear interpretable 2D QSAR models were also generated using the DTC-QSAR tool, freely accessed from http://teqip.jdvu.ac.in/QSAR_Tools/. The genetic algorithm-multiple linear regression (GA-MLR) method, implemented in DTC-QSAR-tool, was employed for the regression-based 2D-QSAR model generation. The data treatment was carried out by setting a variance cut-off of 0.001 (to remove constant and near-constant descriptors) and a correlation cut-off of 0.99 (to eliminate highly inter-correlated descriptors). During the model development, a maximum of 5 descriptors were allowed.

Model validation procedures

The model validation was performed using both external and internal validation parameters, which included leave-one-out (LOO) cross-validated determination coefficient (Q^2_{LOO}) and predicted R^2 (R^2_{pred}) as well as the related parameters which have been described in detail in the Supplementary material to this paper.

3D QSAR modelling

The 3D QSAR is used to explore the relationship between three-dimensional molecular structures and their measured biological activity. The 3D-QSAR depends mainly on the biologically active conformers of the ligands (the compound **67**) and their structural alignments.¹⁹ The atom-based alignment or unsupervised rigid-body molecular alignment method¹⁶ was used for aligning the dataset compounds. The 3D structures of the ligands were first minimized using the OpenBabel “obminimize” tool by the steepest descent method with a maximum of 10000 runs. After the minimization, the structures were eventually allowed to generate 100 conformations by superimpositions, followed by the alignment rdMolAlign.GetCrippenO3A program of Rdkit. The Python scripts used for the atom-based alignment are provided in the GitHub repository (<https://github.com/rdkit/rdkit/blob/master/Code/GraphMol/MolAlign/Wrap/testMolAlign.py>)

Model development

Open 3D QSAR¹⁶ is an open software used for model development. This open software calculates electrostatic fields using a volume less positively (+1) charged probe of the query chemicals, whereas steric fields were calculated using a sp³ carbon probe. The steric and elec-

trostatic energies were considered as independent CoMFA variables. The comparative molecular field analysis (CoMFA) is an alignment-dependent and molecular field-based method used for developing a quantitative structural activity relationship, with the response of steric and electrostatic fields. A generalized smart region definition (SRD) cut-off of 2 was set by removing the N-level variables. This SRD was based on the closeness of variables in 3D space. The Open3DQSAR uses two different variable selection algorithms, uninformative variable elimination partial least square (UVE-PLS) and fractional factorial design-based variable selection (FFD-SEL). The contour maps were visualized with iso-contour values at PLS coefficients of +0.005 (green) and -0.005 (yellow) for the steric field and +0.003 (blue) and -0.003 (red) for the electrostatic field.

The dataset was randomly divided into a training set ($n_{Tr} = 33$) and a test set ($n_{Ts} = 7$) for 3D QSAR model generation. The 3D QSAR-PLS models were generated for the best fit or active compound and low active compound. The statistical values generated from the compounds were examined using the $R^2/SDEC$ which is the coefficient R^2 and its standardized errors of calibration ($SDEC$), F -test results, $Q_{LOO}^2/SDEP$ (leave-one-out Q_{LOO}^2), $Q_{LTO}^2/SDEP$ (leave-two-out Q_{LTO}^2), $Q_{LMO}^2/SDEP$ (leave-many-out Q_{LMO}^2) with associated standardized errors of prediction ($SDEP$) values. However, the R_{pred}^2 values obtained from 3D QSAR can be compared with a 2D QSAR model to generate the predictivity of the model. In addition, the uniqueness of the model was justified by the progressive scrambling methods, and the following criteria were followed: critical value: 0.80, type: LMO groups = 5, runs = 20 and scrambling = 20. The robustness of the model is justified by Q_{LMO}^2 .

Molecular docking analyses

The X-ray crystal structure of human AChE (PDB ID: 4EY7)⁷ was retrieved from the Protein Data Bank (<https://www.rcsb.org/>). The protein structure was prepared by removing all water molecules and ligands. Subsequently, the hydrogen atoms were added. The partial atomic charges were assigned using the Gasteiger–Marsili method. Initially, a blind docking analysis was carried out using the Autodock Vina tool¹⁷ locating the grid at the centre of the macromolecule and extending the grid to cover the whole protein structure. After ensuring that the ligands can bind at the catalytic site of the enzyme, defined by the location-bound ligand donepezil, the Autodock 4.2 tool was employed for final docking.¹⁸ A grid size of 40 Å × 40 Å × 40 Å with a grid-point spacing of 0.375 Å was defined at $X = -11.14$, $Y = -45.85$, $Z = 23.65$. The 3D structures of the input ligands were protonated at pH 7.4 and were subsequently minimized using the OpenBabel “obminimize” tool by the steepest descent method with a maximum of 10,000 runs. A genetic algorithm-based conformational search was carried out for the semi-rigid docking setting the maximum number of evaluations as 2,500,000. The other important genetic algorithm parameters employed for docking are as follows: a) number of runs: 10, b) population size: 150, c) maximum number of generations: 27,000, d) rate of gene mutation: 0.02, e) rate of cross-over: 0.8. Default docking parameter settings found in Autodock 4.2 were used. The analysis of the 2D ligand protein interactions was conducted using the Discovery Studio Visualizer 2017 R2.

RESULTS AND DISCUSSION

Collection of dataset and dataset preparation

The compounds of the dataset consisted of pyrazole derivatives⁷ (compounds **43–62**) and spiropyrazolines derivatives⁷ (compounds **66–85**, Table I). The GA-MLR generates the most predictive 2D QSAR model based on inter-

pretable descriptors. A summary of the obtained statistical result of the model is presented in Eq. (1) whereas the observed *vs.* the predicted activity plot of the model is depicted in Fig. 1:

$$\begin{aligned} pIC_{50} = & (-0.275 \pm 0.022) \times nBM - (0.416 \pm 0.061) \times C\text{-}001 + \\ & +(13.255 \pm 1.579) \times Mv + (0.232 \pm 0.061) \times CATS2D_08_DL - \\ & -(0.325 \pm 0.091) \times C\text{-}014 + (2.019 \pm 0.827) \end{aligned} \quad (1)$$

The model was based on five molecular descriptors, namely *nBM*, *C-001*, *Mv*, *CATS2D_08_DL* and *C-014*. The descriptors belong to constitutional descriptors (*nBM*, *Mv*), atom-centred fragments (*C-001*, *C-014*), and pharmacophore descriptors (*CATS2D_08_DL*). We initially developed this GA-MLR model with the Corina (molecular mechanical) optimized structures. It is noteworthy that all these five descriptors are 2D in nature and therefore, the values of these are not dependent on the 3D structures of the compounds. Nevertheless, we calculated the alvaDesc descriptors after optimizing these structures with the semi-empirical method ULYSSES (quantum chemical PM6)⁷ but GA-MLR failed to develop any better model. The relative significance of these five descriptors was estimated based on the standardized coefficients that are presented in Fig. 1. The *Mv* has the maximum relative significance on the model. The value of *Mv* or the mean atomic van der Waals volume (scaled on carbon atom) depends on the formula:

$$V_{vdw} = \sum \text{All-Atom contributions} - 5.92N_B - 14.7R_A - 3.8R_{NA} \quad (2)$$

Where V_{vdW} is the mean atomic van der Waals volume, N_B is the number of bonds, R_A is the number of aromatic rings, and R_{NA} is the number of non-aromatic rings). The formula describes that the contribution of aromatic ring, or R_A , decreases the van der Waals volume as it is observed in our QSAR results. The low active compound **85** exhibits mean atomic van der Waals volume (scaled on carbon atom), *Mv* of 0.6567 due to the presence of a large aromatic group naphthalene. However, *nBM* is decisive in distinguishing the most active and the least active substances. The presence of polycyclic aromatic rings like naphthalene is responsible for the decreased *Mv*. However, as shown in Table II, the highly active compound (*compound 67*) exhibits a greater value of 0.6607 than that of compound **85**. The structural features of both the compounds are presented in Fig. 2. The compound **67** has an additional chlorophenyl group which is replaced by naphthalene in the compound **85**. The chlorophenyl group contributes less to the V_{vdW} value when compared to naphthalene. The least contributing descriptor also gets correlated to our results. The compound **67** has less *nBM* value than the compound **85**. The chlorophenyl group has a smaller number of multiple bonds (*nBM* value of 21 in the compound **67**) in comparison to a greater number of

multiple bonds as in naphthalene (*nBM* value of 26 in the compound **85**). Furthermore, two atom-centred fragments *C-001* and *C-014* (which refer to CH₃R/CH₄ and CX₄, respectively) contributed unfavourably to the biological activity. Indeed, in some lower active compounds such as **59**, **60** and **82–84**, the substitution of phenyl ring with methyl or isopropyl groups was found to be detrimental to the biological activity. Similarly, the substitution of benzene with trifluoromethoxy group in the compounds like **56** and **79** was also found to have a negative influence on the biological activity. Finally, *CATS2D_08_DL* stands for hydrogen bond donor and lipophilic features, located at a topological distance of 8. Two (*Mv*, *CATS2D_08_DL*) out of five selected descriptors influence the predicted *IC*₅₀ value positively as illustrated in the Eq. (1). The *CATS2D_08_DL* is responsible for the increase in *IC*₅₀ whereas *nBM*, *C-001* and *C-014* are negatively correlated to the above equation.

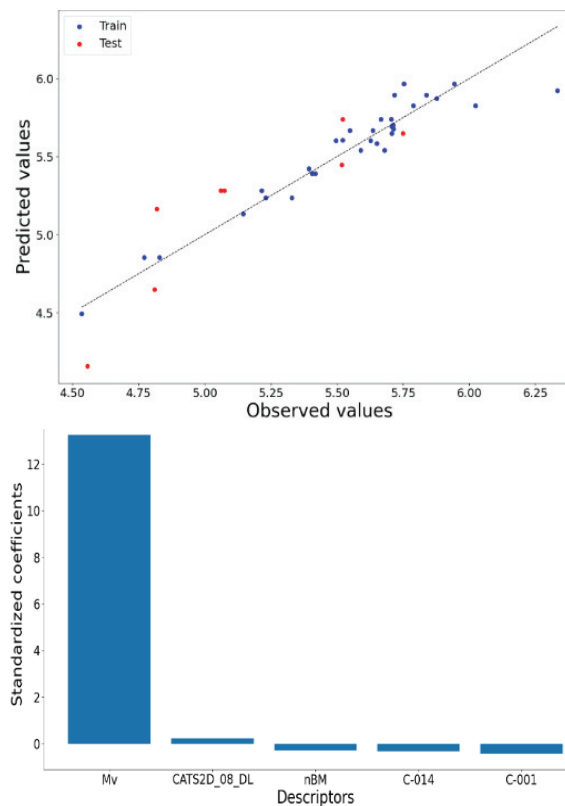


Fig. 1. Observed vs. predicted biological activity plot (left) and relative significance of the descriptors of the most predictive 2D QSAR model.

Based on the pIC_{50} value, the highly active compound and the lowest active compound were selected for the comparison with the molecular descriptor as depicted in Fig. 2. The highly active compound **67** with pIC_{50} values of 6.333 is our best lead and the values of each descriptor are compared to the lowest active compound **85**, with pIC_{50} values of 4.535. The maximum contributing descriptors in both high and low active compounds show no difference as observed in Table II. Similarly, the second major descriptor also plays no role in their activity. However, the third highest contributing factor Mv influences the IC_{50} value.

TABLE II. Comparison of high and low active compounds

Compound No.	Observed pIC_{50}	Predicted pIC_{50}	Mv	nBM
67	6.333	5.923	0.6607	21
85	4.535	4.492	0.6567	26

Both the compounds have a structural resemblance with the marketed drug donepezil (as depicted in Fig. 2). Donepezil¹⁹ is an N-benzyl piperidine derivative with Indanone (Site I), piperidine (Site II) and benzyl segments (Site III). All three segments of donepezil interact with AChE in such an orientation that finds a pattern for all AChE interacting agents.²⁰

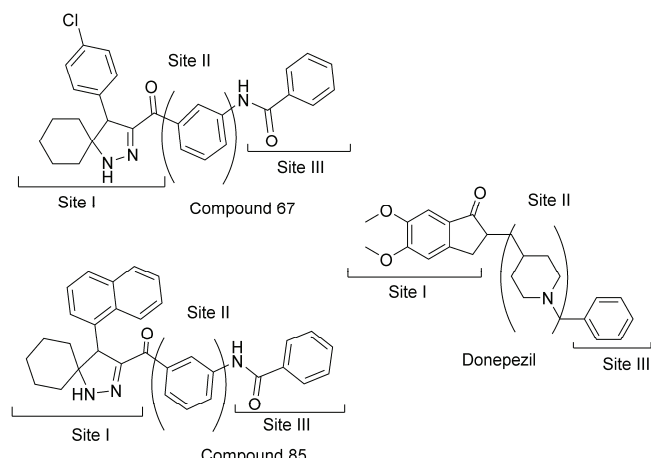


Fig. 2. Structural correlation of three sites of compound **67** and compound **85** with donepezil.

Model validation procedures: Leave-one-out method

The overall statistical quality of each model was justified by the internal validation parameter Q^2 and the external validation parameter R_{pred}^2 . The best model was generated with a random division-based training set and test set using the seed value 10.

The GA-MLR generated the most predictive model based on the interpretable descriptors. The best model was generated with 32 training sets and 8 test set compounds. The results obtained for the training set (Table III) and test set (Table IV) are presented below. A good QSAR model is represented by a minimal coefficient of determination (R^2), and an adjusted R^2 (R_A^2) of nearly one (obtained values are $R^2 = 0.906$, $R_A^2 = 0.888$). The mean absolute error (MAE) was used to generate the goodness fit of the model (obtained values of (obtained values of MAE are 0.074). Thus the QSAR model can be described as a good fit for the model. The internal cross-validation coefficient Q_{LOO}^2 was obtained when all the descriptors were used for the model development and to check the robustness and internal predictivity. The Q_{LOO}^2 of 0.876 exhibits that the model is not over-fitted for the training set. A high Q^2 value that is $Q^2 > 0.5$ is considered proof of the high predictive ability of the model (here, $Q^2 = 0.876$, $r_m^2 = 0.825$). Furthermore, the values of r_m^2 are 0.825 and $r_{m,LOO}^2$ is 0.042 are the internal validation parameters and suggests that the training set is validated.

Table III. Training set: Statistical results

No.	R^2	R^2_{adj}	Q_{LOO}^2	MAE	MSE	$R_{m,Train}^2$	$\Delta R_{m,Train}^2$
32	0.906	0.888	0.876	0.074	0.11	0.825	0.042

Maximum inter-correlation (Pearson r) between two descriptors: 0.766.

TABLE IV. Test set: Statistical results

No.	R_{pred}^2/Q_{F1}^2	Q_{F2}^2	$RMSEP$	$R_{m,Test}^2$	$\Delta R_{m,Test}^2$
8	0.821	0.628	0.24	0.668	0.161

The maximum inter-correlation (Pearson r) between two descriptors is 0.766, which suggests that the descriptors of the regression model are devoid of high inter-co linearity and each descriptor of the model is thus unique.

External Validation: Calculation of R_{pred}^2

The R_{pred}^2 was calculated by fitting the test set descriptors into the developed 2D QSAR model equation and thereafter comparing the predicted bioactivity of the compounds with their observed bioactivity. As far as the external validation is concerned, a satisfactory R_{pred}^2 of 0.821. The value of $R_{pred}^2 > 0.6$ indicates a good external predictability of a model. The GA-MLR model yields a highly predictive QSAR model with a Q_{LOO}^2 value greater than 0.5 and an R_{pred}^2 value greater than 0.6. The satisfactory internal and external predictivity of the model was demonstrated. Furthermore, the maximum inter-correlation (Pearson r) between two descriptors is 0.766, which suggests that the descriptors of each model are independent of each other.

The applicability domain of the model

The applicability domain of the model was found by availing the Williams plot (generated with one of our tools named SFS-QSAR-tools_v2, https://github.com/ncordeirfcup/SFS-QSAR-tool_v2) which is a plot drawn between the standardized residuals in the *y*-axis and the leverage values in the *x*-axis. If the leverage value of any compound is more than the hat value (h^*) which is calculated by the formula: $h^* = 3p'/n$ (where, p' is several model descriptors +1, whereas n is several data in the training set), then the compound is assumed to be a structural outlier. However, if the standardized residuals are greater than ± 3.0 then it is considered a response outlier.

It is known that if the leverage value of any compound is more than the hat value (h^*), here 0.55, then the compound is assumed to be a structural outlier. Similarly, if the standardized residuals are greater than ± 3 , as here, then it is considered a response outlier. Two structural outliers (one in the training set and one in the test set) and one response outlier were found (Fig. 3). The relative significance of the descriptors could be described, as most of the data remains within the standardized residuals.

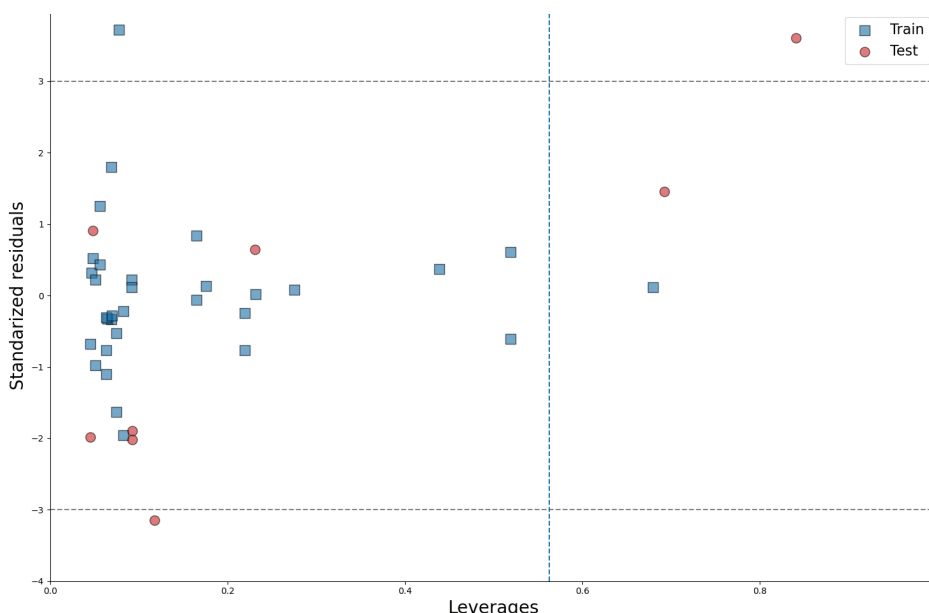


Fig. 3. Applicability domain of the 2D QSAR model.

3D QSAR: Alignment method

The Open3DQSAR model was generated by two methods namely, the fractional factorial design based variable SELECTION (FFD-SEL) and the uninf-

ormative variable elimination based partial least square (UVE-PLS). The statistical results of both the FFD-SEL and UVE-PLS models are presented in Table V. The results of 3D QSAR analysis infer that the UVE-PLS model as compared to FFD-SEL is more helpful in drawing a successful conclusion. The UVE-PLS model exhibits a Q_{LOO}^2 of 0.693 and an R_{pred}^2 value of 0.692. The uniqueness of the model was suggested by Q_{LMO}^2 values, which happen to be 0.662. Thus, it can be concluded that the current 3D QSAR model can explain the structural requirements of these dataset compounds.

TABLE V. 3D QSAR Statistical results in FFD-SEL and UVE-PLS

Parameter	FFD-SEL	UVE-PLS
N_{training}	33	33
N_C	4	4
$R^2/SDEC$	0.898/0.134	0.920/0.119
F	61.41	80.23
$Q^2_{\text{LOO}}/SDEP$	0.718/0.222	0.693/0.232
$Q^2_{\text{LTO}}/SDEP$	0.711/0.225	0.687/0.234
$Q^2_{\text{LMO}}/SDEP$	0.679/0.237	0.662/0.243
N_{test}	7	7
R^2_{Pred}	0.658/0.184	0.692/0.175

The above results were also confirmed from alignment-dependent molecular field analysis which correlates with the results obtained from 2D QSAR analysis.²⁰ The contour maps were visualized with iso-contour values at steric (green and yellow regions) and electrostatic field (blue and red regions), at PLS coefficients as depicted in Fig. 4. The electrostatic and steric fields of the two compounds (the best active compound **67** and the least active compound **85**) were elucidated in Fig. 4. The steric contribution was 43 % whereas the electrostatic contribution was 57 %. The steric regions of the best active compound **67** contain a bulky chlorobenzene moiety inserted into the steric favourable field (Fig. 4a). The bulky naphthalene group is found close to the steric unfavourable field which also confirms the results obtained from that of 2D QSAR analysis (Fig. 4c). The van der Waals volume of the compound **67** was 0.661 due to the presence of less number of aromatic groups as compared to the compound **85** which consists of the bulky poly aromatic naphthalene group. The steric effects of the compound **67** mainly contribute to the model development. The steric favourable group was found near the positive field which happens to lead to greater biological activity. Fig. 4a and c depict that the side chain variation in the steric fields leads to a change in biological activity. The electrostatic contribution mainly supports the model development, when compared to steric field contributions. The electrostatic contribution of the best active compound **67** elucidates that the electron-deficient moiety is inserted into the electropositive field (Fig. 4b). The electron-rich naphthalene moiety is inserted in the electropositive field,

thus explaining the reason for the decreased biological activity of the compound **85** (Fig. 4d). The naphthalene ring being highly electron-rich gets embedded into the electropositive field. The electron-rich moieties favour lower potency.

To gain a more complete scientific significance, a molecular docking study should be performed on the AChE with the two analysed compounds **67** and **85**. AChE was selected and downloaded from Protein Data Bank (www.rcsb.org, PDB ID: 4EY7). The two compounds were docked using AutoDock v4.2 (The Scripps Research Institute, La Jolla, California). The docking poses are shown in Fig. 5.

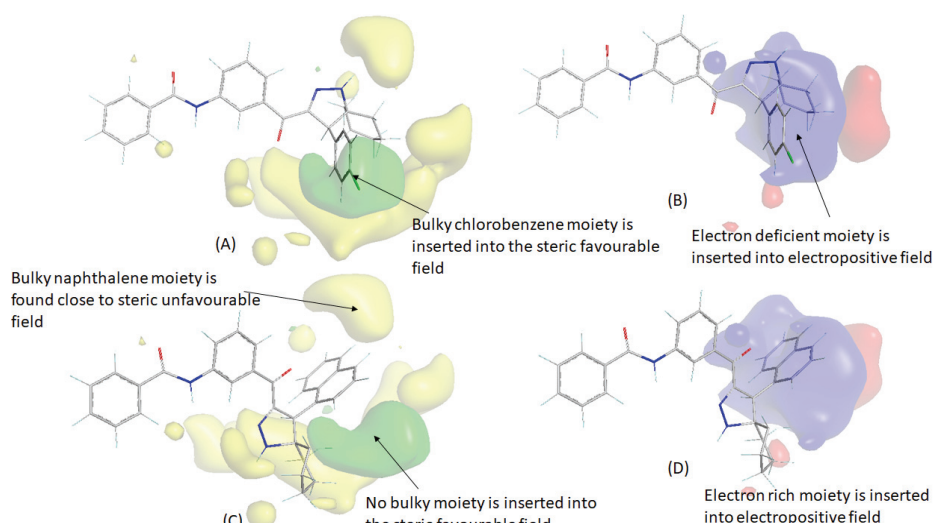


Fig. 4. Contour maps visualized with PLS coefficients: a) steric regions of best active compound **67**, b) electrostatic region of the best active compound **67**, c) steric regions of least active compound **85** and d) electrostatic region of the least active compound **85** (green: steric favorable, yellow: steric unfavorable blue: electropositive favorable; red: electronegative favorable).

First of both **67** and **85** were docked at the same binding site, though there is a large difference between their binding affinities. The best poses of the compounds **67** and **85** were found to have binding affinities of -5.64 and -0.62 kcal*/mol, respectively. Both 2D and 3D QSAR analyses highlighted the importance of the chlorobenzene residue of **67** for higher activity when compared to the naphthalene moiety of **85**. The 3D-QSAR highlighted that the unfavourable steric and electrostatic interactions with the naphthalene moiety of **85** are responsible for the significantly low activity of **85**. Now, from docking analyses, it is evident that similar to the chlorobenzene residue of **67**, the naphthalene residue forms a

* 1 kcal = 4184 J

$\pi-\pi$ interaction with Phe338. However, the former is more effective as its chlorine is associated with π -alkyl interactions with Phe295 and Phe297. Noticeably, the possibility of such interactions was highlighted in 3D-QSAR analyses. However, it is more interesting that the docking analyses revealed that the $\pi-\pi$ interactions between the naphthalene residue of **85** and Phe338 caused an unfavourable interaction clash between **85** and Tyr124. Therefore, it may be inferred that the interpretations obtained from our 2D QSAR and 3D QSAR analyses are consistent with the docking results.

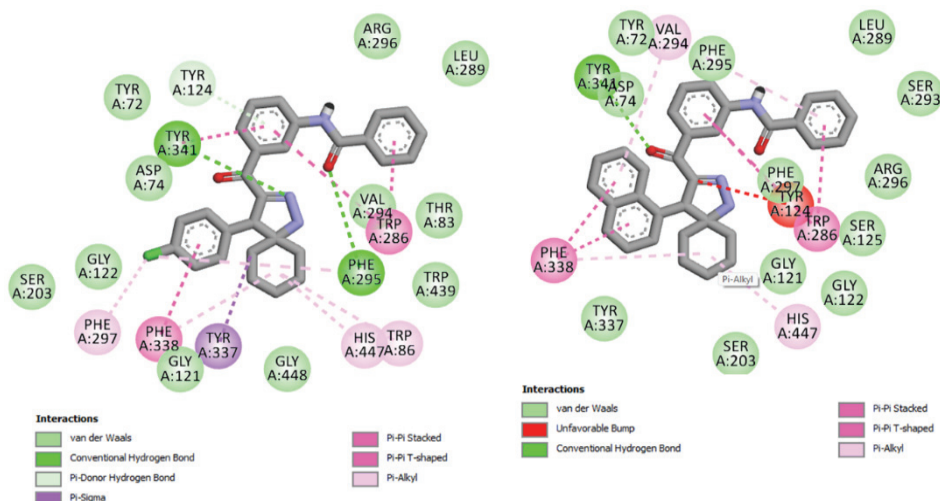


Fig. 5. The docking poses of **67** (left) and **85** (right).

CONCLUSION

The current work investigates the structural requirements of a series of pyrazole and spiropyrazoline analogs for higher AChE inhibitory potential. We performed 2D QSAR and 3D QSAR analyses in a systematic manner to find out the most crucial structural attributes. The 2D QSAR model was constructed with selected interpretable alvaDesc descriptors and the most predictive and evaluative GA-MLR model was developed with the satisfactory statistical predictivity. The 2D QSAR model highlighted that molecular volume and number of multiple bonds along with presence/absence of specific atom centred fragments and topological distance between 2D pharmacophoric features determine the potency of these compounds against this enzyme. The 3D QSAR model, on the other hand, depicted the importance of specific electrostatic and steric contours regions which favourably or unfavourably influence the activity of the compounds. We compared the most potent (**67**, *N*-(3-(4-(4-chlorophenyl)-1,2-diazaspiro[4.5]dec-2-ene-3-carbonyl)phenyl)benzamide) and the least potent compound **85** of the dataset. In spite of having high structural similarity, their biological activities

varied to a considerable extent. The 3D QSAR model was able to explain this phenomenon by showing the importance of chlorophenyl moiety of **67** for higher activity as compared to naphthyl moiety of **85**. More importantly, the inference was largely supported by the molecular docking methodology performed with these. The current work provides valuable information for the future design of pyrazole and spiropyrazoline analogues as potent AChE inhibitors.

SUPPLEMENTARY MATERIAL

Additional data and information are available electronically at the pages of journal website: <https://www.shd-pub.org.rs/index.php/JSCS/article/view/12286>, or from the corresponding author on request.

Acknowledgment. The Authors are thankful to Dr. B.C. Roy College of Pharmacy & Allied Health Sciences, Durgapur, WB, India, for providing all the support for the execution of the work.

ИЗВОД РАЗВОЈ 2D И 3D QSAR МОДЕЛА ПИРАЗОЛСКИХ ДЕРИВАТА КАО ИНХИБИТОРА АЦЕТИЛХОЛИН-ЕСТЕРАЗЕ

PUJA MISHRA¹, SUMIT NANDI¹, ANKIT CHATTERJEE¹, TRIDIB NAYEK¹, SOUVIK BASAK¹,
AMIT KUMAR HALDER^{1,2} и ARUP MUKHERJEE³

¹Dr. B.C. Roy College of Pharmacy & Allied Health Sciences, Durgapur, WB, India, ²LAQV@REQUIMTE/
Department of Chemistry and Biochemistry, Faculty of Sciences, University of Porto, Porto, Portugal и

³Department of Biotechnology, Maulana Abul Kalam Azad University of Technology, WB, India

Инхибитори ацетилхолинестеразе (AChE) су лекови који су најкориснији за лечење Алцхајмерове болести (AD) у свим стадијумима. Циљеви овог рада су генерисање различитих QSAR модела и одабир робусних предиктивних модела. Фокус даљег истраживања је на проналажењу низа AChE инхибитора сличних пиразолу помоћу 2D и 3D QSAR анализе. Вишеструка линеарна регресија заснована на генетском алгоритму (GA-MLR) обезбедила је статистички робустан 2D QSAR модел који је приказао значај запремине молекула волумена и броја вишеструких веза заједно са присуством/одсуством специфичних фрагмената центрираних на атому и тополошке удаљености између 2D фармакофора. Штавише, ови резултати су у доброј корелацији са електростатичким и стерним малама контура преузетим из 3D QSAR (тј. анализа молекуларног поља зависна од поравнања). 2D QSAR анализа развила је високо статистички и поуздан модел који је упоређен са механичком интерпретацијом 3D структура и њиховим доприносима електростатичком и стеричном пољу што је довело до предиктивног 3D QSAR модела. Интеракције молекул-протеин изазване молекуларним спајањем поткрепиле су интеракције поља које је открио 2D QSAR. Према томе, развијени рачунарски модели и симулационе анализе у овом раду дају драгоцене информације за будући дизајн аналога пиразола и спиропиразолина као моћних инхибитора AChE.

(Примљено 21. фебруара, ревидирано 2. августа 2023, прихваћено 31. марта 2024)

REFERENCES

- M. Hernández-Rodríguez, J. Correa-Basurto, F. Martínez-Ramos, I. I. Padilla-Martínez, C. G. Benítez-Cardoza, E. Mera-Jiménez, M. C. Rosales-Hernández, *J. Alzheimer's Dis.* **41** (2014) 1073 (<https://doi.org/10.3233/JAD-140471>)

2. S. Habtemariam, *Molecules* **24** (2019) 1519 (<https://doi.org/10.3390/molecules24081519>)
3. Y. Yamaguchi, H. Miyashita, H. Tsunekawa, A. Mouri, H. C. Kim, K. Saito, T. Matsuno, S. Kawashima, T. Nabeshima, *J. Pharmacol. Exp. Ther.* **317** (2006) 1079 (<https://doi.org/10.1124/jpet.105.098640>)
4. P. Mishra, S. Basak, A. Mukherjee, A. Basu, *Lett. Drug Des. Discov.* **19** (2021) 192 (<https://doi.org/10.2174/1570180818666210813120444>)
5. L. Lecanu, V. Papadopoulos, *Recent Pat. CNS Drug Discov.* **2** (2007) 113 (<https://doi.org/10.2174/157488907780832715>)
6. R. Chawla, A. Arora, M. K. Parameswaran, P. Chan, D. Sharma, S. Michael, T. K. Ravi, *Acta Pol. Pharm.* **67** (2010) 247 (https://www.ptfarm.pl/pub/File/acta_pol_2010/3_2010/247-253.pdf)
7. G. Gutti, D. Kumar, P. Paliwal, A. Ganeshpurkar, K. Lahre, A. Kumar, S. Krishnamurthy, S. K. Singh, *Bioorg. Chem.* **90** (2019) 103080 (<https://doi.org/10.1016/j.bioorg.2019.103080>)
8. *Ecotoxicological QSARs*, K. Roy Ed., Springer 2020, ISBN 978-1071601495
9. I. Sushko, A. K. Pandey, S. Novotarskyi, R. Körner, M. Rupp, W. Teetz, S. Brandmaier, A. Abdelaziz, V. V. Prokopenko, V. Y. Tanchuk, R. Todeschini, A. Varnek, G. Marcou, P. Ertl, V. Potemkin, M. Grishina, J. Gasteiger, I. I. Baskin, V. A. Palyulin, E. V. Radchenko, W. J. Welsh, V. Kholodovych, D. Chekmarev, A. Cherkasov, J. Aires-De-Sousa, Q. Y. Zhang, A. Bender, F. Nigsch, L. Patiny, A. Williams, V. Tkachenko, I. V. Tetko, *J. Cheminform.* **3** (Suppl. 1) (2011) P20 (<https://doi.org/10.1186/1758-2946-3-S1-P20>)
10. P. Ambure, R. B. Aher, A. Gajewicz, T. Puzyn, K. Roy, *Chemom. Intell. Lab. Syst.* **147** (2015) 1 (<https://doi.org/10.1016/j.chemolab.2015.07.007>)
11. P. Tosco, T. Balle, *J. Mol. Model.* **17** (2011) 201 (<https://doi.org/10.1007/s00894-010-0684-x>)
12. J. Sadowski, J. Gasteiger, G. Klebe, *J. Chem. Inf. Comp. Sci.* **54** (1994) 1000 (<https://pubs.acs.org/doi/10.1021/ci00020a039>)
13. A. K. Halder, M. N. D. S. Cordeiro, *Biomolecules* **11** (2021) 1670 (<https://doi.org/10.3390/biom1111670>)
14. G. Kryger, I. Silman, J. L. Sussman, *Structure* **7** (1999) 297 ([https://doi.org/10.1016/S0969-2126\(99\)80040-9](https://doi.org/10.1016/S0969-2126(99)80040-9))
15. H. Safarizadeh, Z. Garkani-Nejad, *J. Mol. Graph. Model.* **87** (2019) 129 (<https://doi.org/10.1016/j.jmgm.2018.11.019>)
16. T. K. Shameera Ahmed, V. K. Rajan, K. Muraleedharan, *Food Sci. Hum. Wellness* **8** (2019) 53 (<https://doi.org/10.1016/j.fshw.2019.02.001>)
17. O. Trott, A. J. Olson, *J. Comput. Chem.* **31** (2009) 455 (<https://doi.org/10.1002/jcc.21334>)
18. G. M. Morris, H. Ruth, W. Lindstrom, M. F. Sanner, R. K. Belew, D. S. Goodsell, A. J. Olson, *J. Comput. Chem.* **30** (2009) 2785 (<https://doi.org/10.1002/jcc.21256>)
19. H. Sugimoto, *Pure Appl. Chem.* **71** (2009) 2031 (<https://doi.org/10.1351/pac199971112031>)
20. P. Mishra, P. Sharma, P. N. Tripathi, S. K. Gupta, P. Srivastava, A. Seth, A. Tripathi, S. Krishnamurthy, S. K. Shrivastava, *Bioorg. Chem.* **89** (2019) 103025 (<https://doi.org/10.1016/j.bioorg.2019.103025>).



SUPPLEMENTARY MATERIAL TO
**Development of 2D and 3D QSAR models of pyrazole derivatives as
acetylcholine esterase inhibitors**

PUJA MISHRA^{1*}, SUMIT NANDI¹, ANKIT CHATTERJEE¹, TRIDIB NAYEK¹, SOUVIK
BASAK¹, AMIT KUMAR HALDER^{1,2} and ARUP MUKHERJEE³

¹Dr. B.C. Roy College of Pharmacy & Allied Health Sciences, Durgapur, WB, India,

²LAQV@REQUIMTE/Department of Chemistry and Biochemistry, Faculty of Sciences,
University of Porto, Porto, Portugal and ³Department of Biotechnology, Maulana Abul
Kalam Azad University of Technology, WB, India

J. Serb. Chem. Soc. 89 (7–8) (2024) 981–995

TEXT S1. MODEL VALIDATION PROCEDURES

Leave-one-out method

Leave-one-out (LOO), one of the popular cross-validation methods was implemented. The cross-validated R² is the result from the cross-validation method which is used as a condition of robustness and predictive capability of the model. The cross-validated determination coefficient R² that is LOO-Q² is calculated using the following formula

$$Q^2 = 1 - \frac{\sum(Y_{obs} - Y_{pred})^2}{\sum(Y_{obs} - \bar{Y})^2}$$

In this equation, \bar{Y} denotes average activity value of the training set, Y_{obs} and Y_{pred} signify the values of observed and predicted activity respectively. A high Q² value ($Q^2 > 0.5$) is considered as parameter of the high predictive capability of the model.

External validation

Calculation of R²_{pred} from test set

In this study, the original dataset was divided into training set and test set. Based on the training set compounds, 2D QSAR model (MLR equation) was developed. The predictive ability of the models was determined by the statistical parameter, like the predictive R² (R^2_{pred}) values, which was derived by the following equation

$$R^2_{pred} = 1 - \frac{\sum(Y_{pred(test)} - Y_{test})^2}{\sum(Y_{test} - \bar{Y}_{Training})^2}$$

* Corresponding author. E-mail: pujam.phe15@itbhu.ac.in

In this equation, $Y_{pred\ (Test)}$ and $Y_{(Test)}$ represents the predicted and the observed activity values of a certain test set of compounds, respectively, and $\bar{Y}_{training}$ denotes the mean activity value of the training set. The value of $R^2_{pred} > 0.6$ indicates a good external predictability of a model.

Here, the multiple linear regression model generated from trainee set was used for the prediction purpose of bioactivity of the test set compounds by forming an equation as

$$\log \text{Predicted activity (y)} = m_1x_1 + m_2x_2 + m_3x_3 + \dots + m_nx_n + C$$

where $m_1, m_2, m_3, \dots, m_n$ are respective coefficients of descriptors such as $x_1, x_2, x_3, \dots, x_n$

A well-known statistical method (metrics) was used to determine the goodness of the fit, the robustness and the internal predictivity of the final QSAR model. The coefficient of determination (R^2), adjusted R^2 (R^2_A) and the MAE (mean absolute error) were used to generate the goodness fit of the model and the internal cross validation coefficient Q^2_{LOO} was used to check the robustness and the internal predictivity. Further, the metrics such as r_m^2 and $r_m^2_{LOO}$ are used as the internal validation parameters. The external validation parameter R^2_{Pred} is essential to judge the external predictivity of the molecule. The best QSAR model was validated by the inter-correlation (Pearson r) between the two descriptors. A correlation matrix was generated to check the correlation matrix of different descriptors.

TEXT S2. ENERGY OPTIMIZATION OF SELECTED MOLECULES

The results of Auto energy optimization of the compounds using Avogadro give values, such as 260.085 KJ/mol which is confirmed using Orca (the semi empirical method). The structural optimization using both the software exhibits that there is no significant change in geometry after the various geometry optimization cycle.

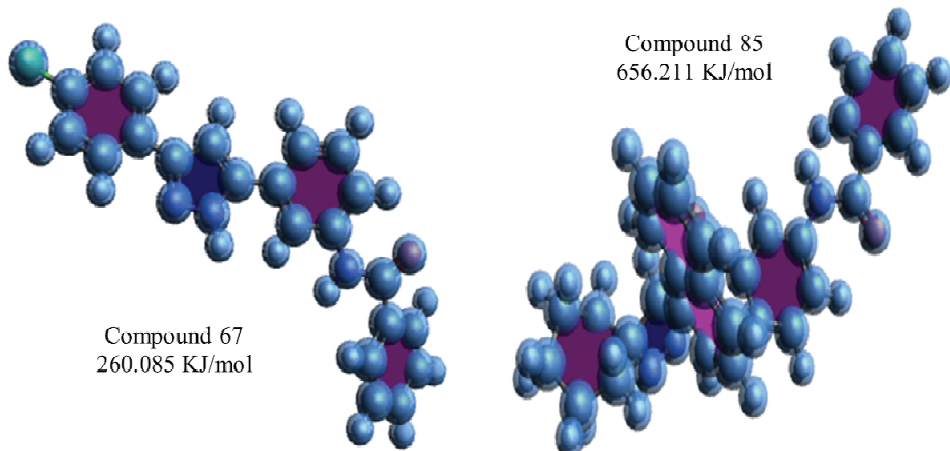


Fig. S1. Geometry optimization using Avogadro by using MM force fields.

QM optimized structures (eventually with a semi-empirical method)

Energy change	-0.0004823076	0.0000050000	(No significant energy change after 24 geometry optimization cycle)
RMS gradient	0.0004785364	0.0001000000	
MAX gradient	0.0034948286	0.0003000000	
RMS step	0.0034607630	0.0020000000	
MAX step	0.0320313071	0.0040000000	

Diagonalization of the overlap matrix:

Smallest eigenvalue	... 2.478e-04
Time for diagonalization	0.275 sec
Threshold for overlap eigenvalues	1.000e-08
Number of eigenvalues below threshold	0
Time for construction of square roots	0.112 sec
Total time needed	0.395 sec

Table SI. Trainee set with chosen descriptors of 2D-QSAR

Sr. No.	Experimental pIC ₅₀	Predicted pIC ₅₀	nB M	C- 001	Mv	CATS2D_08_ DL	C- 014
43	5.393	5.713	24	0	0.6853	4	0
44	5.713	5.517	24	0	0.7045	4	0
46	5.711	5.665	24	0	0.7238	3	0
47	5.665	5.521	24	0	0.7091	4	0
49	5.68	5.68	24	0	0.6942	4	0
50	5.589	5.589	24	0	0.6942	4	0
54	5.627	5.073	24	0	0.6988	4	0
55	5.495	5.06	24	0	0.6988	4	0
56	5.215	5.627	24	0	0.6991	4	1
57	5.417	5.495	25	0	0.7037	4	0
58	5.405	5.215	25	0	0.7037	4	0
59	4.828	5.417	24	1	0.6738	4	0
60	4.771	5.405	24	1	0.6738	4	0
66	5.705	4.828	21	0	0.6469	4	0
67	6.333	4.81	21	0	0.6607	4	0
68	5.706	7.721	21	0	0.6607	3	0
69	5.877	5.705	21	0	0.6745	3	0
70	5.943	6.333	21	0	0.664	4	0
71	5.752	5.877	21	0	0.664	4	0
72	6.023	5.943	21	0	0.6533	4	0
73	5.789	5.752	21	0	0.6533	4	0
74	5.635	6.023	21	0	0.6415	4	0
75	5.548	5.789	21	0	0.6415	4	0
76	5.521	5.635	21	0	0.6367	4	0
77	5.838	5.548	21	0	0.6586	4	0
78	5.716	5.521	21	0	0.6586	4	0
79	5.65	5.716	21	0	0.6595	4	1
81	5.707	5.65	22	0	0.6608	4	0
82	5.329	5.75	21	1	0.6403	4	0
83	5.23	5.707	21	1	0.6403	4	0
84	5.146	5.23	21	2	0.6289	6	0
85	4.535	5.146	26	0	0.6567	4	0

Table SII. Test set with chosen descriptors (arranged in descending order of pIC₅₀ values)

Sr. No.	Experimental 1pIC ₅₀	Predicted pIC ₅₀	C-001	Mv	CATS2D_08_- DL		C-014
	45	5.517	5.393	24	0	0.7045	3
48	5.521	5.711	24	0	0.7091		4
51	5.073	4.818	24	0	0.6746		4
52	5.06	4.771	24	0	0.6746		4
53	4.818	4.556	24	0	0.6657		4
61	4.81	5.706	24	2	0.6547		6
62	4.556	5.838	29	0	0.6937		4
80	5.75	5.329	22	0	0.6608		4

Table III. Elaboration on chosen descriptors

Sr.No.	Descriptors	Class	Description
1.	nBM	constitutional descriptors	number of multiple bond
2.	C-001	atom centred fragments	CH ₃ R/CH ₄
3.	Mv	constitutional descriptors	mean atomic vander waals volume (scaled on carbon atom)
4.	CATS2D_08_DL	pharmacophore descriptors	CATS2D donor-lipophilic at lag 8
5.	C-014	atom centred fragments	CX4



In silico studies of phycobilins as potential candidates for inhibitors of viral proteins associated with COVID-19

VESNA B. JOVANOVIĆ¹, MILAN R. NIKOLIĆ^{1#} and SRĐAN Đ. STOJANOVIĆ^{2*}

¹University of Belgrade, Faculty of Chemistry, Department of Biochemistry and Centre of Excellence for Molecular Food Sciences, Belgrade, Serbia and ²University of Belgrade, Institute of Chemistry, Technology and Metallurgy – National institute of the Republic of Serbia, Department of Chemistry, Belgrade, Serbia

(Received 26 March, revised 17 April, accepted 8 May 2024)

Abstract: In this *in silico* study, it was investigated whether phycobilins (phycocyanobilin, phycoerythrobilin and phycourobilin) could be inhibitors of the activity of the main proteins of the SARS-CoV-2 virus. All chromophores exhibited a binding energy value of $\geq -37 \text{ kJ mol}^{-1}$ for PLpro-WT, PLpro-C111S, helicase-ANP binding site, Nsp3-macrodomain, Nsp3-MES site and Nsp10/14-N7-Mtase. Phycocyanobilin showed the highest binding energy of $-44.77 \text{ kJ mol}^{-1}$ against the target protein PLpro-C111S. It was found that, apart from the hydrogen bonds and hydrophobic interactions, phycobilins also form electrostatic interactions with the SARS-CoV-2 proteins. The network of non-covalent interactions was found to be important for the stability of the examined virus proteins. All phycobilins have good pharmacokinetic and drug-likeness properties. This study's results suggest that the screened phycobilins could serve as promising drugs for the treatment of COVID-19 with further rigorous validation studies.

Keywords: phycobilins; COVID-19; inhibitors; proteins; *in silico* studies.

INTRODUCTION

The SARS-CoV-2 infection has spread around the world at an extremely high speed, causing a severe medical and humanitarian crisis in almost every region of the world. This virus has been officially linked to severe acute respiratory syndrome coronaviruses (SARS-CoVs) and named severe acute respiratory syndrome coronavirus 2 (SARS-CoV-2) by the International Committee on Taxonomy of Viruses.¹ Coronavirus Disease 2019 (COVID-19) is an infectious respiratory disease caused by SARS-CoV-2, a recently discovered coronavirus strain. Despite advances in vaccine and drug research, there is still a lack of

* Corresponding author. E-mail: srdjanst@chem.bg.ac.rs

Serbian Chemical Society member.

<https://doi.org/10.2298/JSC240326052J>

prophylactic vaccinations and effective antiviral drugs for many viral diseases, including coronavirus infections.^{2,3} Finding effective therapeutic strategies for treating COVID-19 patients has thus become a crucial and urgent task. Different methods can be used for antiviral research to act against SARS-CoV-2. For example, target structural proteins in view to inhibit virus entry in human host cells, looking for functional internal viral protein inhibitors to block its replication or target human receptor for virus entry prevention.^{4–6} Computation docking is an effective strategy and widely used technique for understanding the molecular aspects of proteins and protein–ligand interactions in the drug discovery.^{5,7} Interactions between SARS-CoV-2 proteins have been extensively studied from a biothermodynamic perspective. For example, binding affinities of the spike glycoprotein of various variants of SARS-CoV-2 to the ACE2 receptor have been discussed.^{8–10}

Natural products with antimicrobial and antiviral properties are of great interest to scientists to study their effectiveness in combating COVID-19.¹¹ Medicines based on natural phytochemicals are gaining traction in modern healthcare due to their lower toxicity, effective health benefits and potential use in connection with existing therapies becoming increasingly important. Marine products are known to serve as a seemingly limitless bioresource to combat pathogenic microbes and cancers.¹² Several literature studies have reported the antiviral properties of phytochemicals against CoVs and other viruses.^{13,14} Kumar *et al.*¹⁵ used molecular docking and molecular dynamics simulations to screen effective compounds from purple nutsedge (*Cyperus rotundus*) against the main protease (Mpro) of SARS-CoV-2. Silva *et al.*¹⁶ investigated the pharma-cokinetic and toxicological properties of molecules in a natural product data-base of the Brazilian semiarid region and performed location prediction and drug-ability analysis on SARS-CoV-2 Mpro. Gupta *et al.*¹⁷ screened more than 53,500 bioactive natural molecules from six different natural product databases to identify effective molecules against Mpro. Li *et al.*¹⁸ used ensemble and cooperative docking and molecular simulations to investigate possible interactions of more than 600 compounds from a herbal drug with eight SARS-CoV-2 proteins, including spike protein, nucleocapsid protein, Mpro and papain-like protease, RNA-dependent RNA polymerase (RdRp), nonstructural protein 3 (Nsp3), and cat/human angiotensin-converting enzyme 2. Pendyala and Patras¹⁹ showed that phycocyanobilins showed high binding affinity for the SARS-CoV-2 Mpro and RdRp *in silico* molecular docking studies. Despite the challenges, it is clear that marine organisms represent a promising avenue for future pharmacological interventions.²⁰

The results of our study prompted us to take further steps, primarily examining all proteins and binding profiles with phycobilins available in the COVID-19 docking server. Phycobilins are open-chain light-trapping tetrapyrrole pigments found in cyanobacteria (blue phycocyanobilin) and red algae (red phycoerythron-

bilin and orange phycourobilin). They are covalently bound to phycobiliproteins via a thioether bond and are carriers of the powerful biological activities of these fluorescent water-soluble proteins with new pharmaceutical potential.²¹

The present study aimed to identify the most relevant antiviral SARS-CoV-2 phycobilin molecules through docking and *in silico* toxicity assessment. We report natural phycobilins as potent broad-spectrum natural inhibitory compounds against major SARS-CoV-2-associated proteins *via* an *in silico* approach.

EXPERIMENTAL

Molecular docking and visualization

To investigate the affinity of phycobilins toward SARS-CoV-2 virus' receptors, molecular docking calculations were carried out using COVID-19 Docking Server 2.0 (nCoVDock2).²² A new docking server, nCoVDock2 was constructed to predict the binding modes between the wild type and mutants of SARS-CoV-2 therapeutic targets and their potential ligands. AutoDock Vina²³ is used as the docking engine for small molecule docking. AutoDock Vina is upgraded to the latest version 1.2.0,²⁴ on the new server. Open Babel was used for format transformation or 3D coordinate generation for the uploaded files.²⁵ The docking box is defined as the center of native ligand coordinates with dimensions of 30 Å×30 Å×30 Å to include residues of the entire cavity. Homology-modeled structures are defined according to the information of active sites or binding sites of its homologs of SARS-CoV. The MGLTools was used to add hydrogens and prepare pdbqt files for proteins and ligands. All the parameters were set as default, and we chose the exhaustiveness value option as 12. The higher level of exhaustiveness parameter is considered to provide more precise docking results and longer computational time. We used all proteins provided by this server (Table I). The input 3D sdf ligand files of selected phycobilins (phycocyanobilin, phycoerythrobilin and phycourobilin) were retrieved from PubChem²⁶ database (<https://pubchem.ncbi.nlm.nih.gov/>) and uploaded to COVID-19 Docking Server 2.0. The docked receptor and ligand interactions were visualized using Biovia Discovery Studio Visualizer.²⁷

Non-covalent interaction analysis

The docked receptor and ligand interactions were analyzed and visualized using Biovia Discovery Studio Visualizer²⁷ with default-specific criteria and geometrical feature settings (these criteria and settings are provided in the Supplementary material to this paper).

Physicochemical, pharmacokinetic, drug-likeness and medicinal chemistry properties

Physicochemical, pharmacokinetic, drug-likeness and medicinal chemistry properties were predicted for the phycobilins using the SwissADME server.²⁸ The SMILES format of the phycobilins was retrieved from the PubChem database and used as input for the SwissADME server.

RESULTS AND DISCUSSION

The first part of this work focuses on evaluating anti-SARS-CoV-2 activity by docking phycobilin compounds. The second part of the article deals with an *in silico* study on the toxicity of the selected molecules.

Molecular docking studies

Molecular docking simulations were performed to determine the binding affinities between the phycobilins and the target SARS-CoV-2 protein sites and to identify the molecular interactions that play a key role in binding. COVID-19 Docking Server, an online meta server, was built to elaborate on the SARS-CoV-2 target–ligand interactions. Structures of proteins involved in the virus life cycle were established based on the homologs of coronavirus. The binding mode and affinity between estimated molecules and target protein can be deduced through this server. Based on the above, all the phycobilins were submitted to the COVID-19 Docking Server to unveil their interfering capacity in the life cycle of the SARS-CoV-2 virus. Docking results of all compounds in difference proteins expressing as score value (kJ mol^{-1}) and RF score value are presented in Table I. They are associated with the top-ranked poses (best models of studied complexes). Score value below or equal to -33 kJ mol^{-1} demonstrates a significant strength of interactions between small molecules and proteins; the lower the score value, the stronger the interaction. The distribution frequency of binding energy score among the phycobilins and SARS-CoV-2 proteins varies between -21 and -45 kJ mol^{-1} .

In all the simulated ligand–protein docking model, among all targets, PLpro-^{-WT}, PLpro-C111S, Helicase-ANP binding site, Nsp3-macrodomain, Nsp3-MES site and Nsp10/14-N7-Mtase displayed higher score than all other proteins. Papain-like protease (PLpro) is an interesting antiviral target because it is essential for replicating coronaviruses.²⁹ In addition, as a consequence of the alterations present in the genome of SARS-CoV-2, the PLpro is now well-equipped to cleave the ubiquitin-like interferon-stimulated gene 15 protein,²⁹ thereby evading the host's innate immune responses. The docking scores of the other proteins, except for Nsp10-nsp10-14 and Nsp10-nsp10-16, were lower than -30 kJ mol^{-1} and also exhibited notable affinities, implying these proteins may be potent targets for inhibition of SARS-CoV-2. Among the phycobilins, the results revealed that the affinities of phycocyanobilin for PLpro-C111S, Helicase-ANP binding site, RdRp-RTP site and Nsp3-macrodomain, Nsp10/14-N7-Mtase was highest, indicating that phycocyanobilin was the main antiviral active component. The results show phycocyanobilin docked with the best score with a binding energy of $-44.77 \text{ kJ mol}^{-1}$. It is interesting to note that phycoerythrobilin showed higher affinity for non-structural proteins: Nsp10/16-MGP site, Nsp10/16-SAM site, Nsp10/16-GTA site, Nsp10/14-N7-Mtase and Nsp10/14-chaps site than other phycobilins and the origin ligands. The difference arises from the higher number of non-covalent interactions in phycoerythrobilin–non-structural protein interfaces; the interplay between interactions may exist. This should also be taken into account when determining binding affinity. Therefore, these phycobilins could be potent inhibitors of SARS-CoV-2 targets. Non-structural proteins (Nsp10-nsp10-

-14 and Nsp10-nsp10-16) have shown the weakest binding energy among the proteins studied, possibly due to the dominance of hydrophobic residues involved in the binding pocket with phycobilins. The results of molecular docking scoring were consistent with those of Mpro and PLpro target proteins previously reported.¹⁹

TABLE I. Covid-19 docking server results of phycobilins; *SV* – score value; *RF SV* – RF score value

Protein	Phycoerythrobilin		Phycourobilin		Phycocyanobilin	
	<i>SV</i> kJ mol ⁻¹	<i>RF SV</i> pKd	<i>SV</i> kJ mol ⁻¹	<i>RF SV</i> pKd	<i>SV</i> kJ mol ⁻¹	<i>RF SV</i> pKd
Nsp3-macrodomain (5RSF)	-37.24	7.37	-36.82	7.05	-39.33	7.51
Nsp3-ADP ribose phosphatase (6W6Y)	-33.05	7.00	-32.22	6.65	-34.73	7.30
Nsp3-MES site (6W6Y)	-34.73	6.79	-39.33	7.34	-39.33	7.62
PLpro-WT (7RZC)	-39.75	7.97	-43.93	7.86	-43.10	7.90
PLpro-C111S (7SQE)	-42.26	7.82	-39.33	7.84	-44.77	8.09
Mpro-WT (7SI9)	-33.89	7.12	-34.31	7.15	-35.15	7.14
Nsp9-FR6 bound (7KRI)	-29.71	6.30	-28.87	6.09	-29.71	6.26
Nsp9-oridonin bound (7N3K)	-37.24	7.81	-37.66	7.64	-38.49	7.52
Nsp10-nsp10-14 (7ORR)	-27.61	6.08	-23.85	5.76	-25.94	5.77
Nsp10-nsp10-16 (7ORU)	-24.69	6.09	-20.82	5.76	-26.78	6.05
RdRp-RTP site (7BV2)	-40.58	7.88	-40.17	7.93	-41.00	7.90
RdRp-RNA site (7D4F)	-31.79	6.76	-29.71	6.74	-28.45	6.40
Helicase-ANP binding site (7NN0)	-37.66	7.33	-38.07	7.77	-41.00	7.43
Helicase-fragment binding site (5RML)	-36.82	7.29	-35.15	7.08	-28.45	7.37
Nsp10/14-chapsO site (7N0D)	-38.91	7.26	-35.56	7.15	-36.82	7.30
Nsp10/14-ExoN (7N0D)	-30.54	6.81	-32.22	6.87	-30.54	7.62
Nsp10/14-N7-Mtase (7N0D)	-43.51	7.79	-40.58	8.02	-41.00	7.64
Nsp15-WT (7K1L)	-30.96	6.53	-30.54	6.33	-32.22	6.44
Nsp10/16-MGP site (6WVN)	-39.33	7.45	-36.41	6.96	-36.82	7.43
Nsp10/16-SAM site (6W4H)	-39.33	7.49	-36.82	7.10	-36.82	7.46
Nsp10/16-GTA site (6WVN)	-38.91	7.34	-36.82	7.09	-35.98	7.44
Nprotein-NCB site (MODEL)	-34.73	7.24	-35.15	7.26	-33.05	7.54

Binding profile of SARS-CoV-2 associated proteins with the phycobilins

To better understand binding affinity, we also listed the binding profile of the SARS-CoV-2 associated proteins with the relevant phycobilins mentioned above, molecular interaction types, and their properties in Table II.

The interaction prediction using Discovery Studio Visualizer software revealed that phycobilins could have various interactions. While analyzing the interaction profile, it was found that, apart from the hydrogen bonds and hydrophobic

interactions, which were considered the most common type of protein–ligand interactions,³⁰ phycobilins also form electrostatic interactions with the SARS-CoV-2 proteins. Ion pairs play an important role in the stabilization of protein structures. Electrostatic interactions are infrequent among protein–ligand interfaces (Table II). Many of interfaces did not form electrostatic interactions, while the largest number of electrostatic interactions in an interface was five (Phycocyanobilin–PLpro-C111S). From Fig. 1, the types of molecular interactions and the interacting residues of the PLpro-C111S chains can be clearly seen.

TABLE II. Interaction profiles between SARS-CoV-2 associated proteins and the tested phycobilins

Protein	Phycobilin											
	Phycoerythrobilin				Phycourobilin				Phycocyanobilin			
	N _{HB} ^a	N _{ES} ^b	N _{HP} ^c	N _O ^d	N _{HB}	N _{ES}	N _{HP}	N _O	N _{HB}	N _{ES}	N _{HP}	N _O
Nsp3-macrodomain (5RSF)	3	—	7	—	4	—	4	—	2	—	8	—
Nsp3-ADP ribose phosphatase (6W6Y)	4	—	8	—	2	—	3	—	8	—	7	—
Nsp3-MES site (6W6Y)	4	—	6	—	4	—	6	—	5	—	8	—
PLpro-WT (7RZC)	7	1	5	—	2	1	7	—	3	3	4	—
PLpro-C111S (7SQE)	7	1	3	—	5	2	2	—	5	5	3	—
Mpro-WT (7SI9)	5	—	—	2	2	—	2	1	6	4	2	—
Nsp9-FR6 bound (7KRI)	6	—	4	—	3	—	6	—	5	—	3	—
Nsp9-ordinonin bound (7N3K)	5	1	5	—	4	1	2	—	2	1	4	—
Nsp10-nsp10-14 (7ORR)	4	—	3	—	2	—	4	—	3	—	3	—
Nsp10-nsp10-16 (7ORU)	4	—	3	—	4	1	—	—	6	1	—	—
RdRp-RTP site (7BV2)	4	—	3	—	7	—	4	—	6	4	3	—
RdRp-RNA site (7D4F)	7	—	4	—	2	—	3	—	5	—	3	—
Helicase-ANP binding site (7NN0)	8	—	5	—	8	—	3	—	6	2	1	—
Helicase-Fragment binding site (5RML)	6	1	6	—	5	1	5	—	9	1	5	—
Nsp10/14-chapso site (7N0D)	2	—	8	—	1	—	4	—	2	—	4	—
Nsp10/14-ExoN (7N0D)	5	—	2	1	6	1	—	1	3	5	3	2
Nsp10/14-N7-Mtase (7N0D)	7	—	3	—	9	—	3	—	6	1	5	—
Nsp15-WT (7K1L)	7	1	5	—	2	1	4	—	7	2	4	—
Nsp10/16-MGP site (6WVN)	6	—	4	—	10	—	2	—	6	2	3	—
Nsp10/16-SAM site (6W4H)	5	—	4	—	9	—	2	—	8	—	3	—
Nsp10/16-GTA site (6WVN)	7	—	3	—	11	—	2	—	6	—	3	—
Nprotein-NCB site (MODEL)	2	—	5	—	4	1	6	—	3	3	7	—

^aNumber of hydrogen bonds; ^bnumber of electrostatic interactions; ^cnumber of hydrophobic interactions;
^dnumber of other interactions

As shown, phycocyanobilin interacts with the papain-like protease (PLpro-C111S) through B:Arg166:NH2, B:Glu167:OE1, C:Asp164:OD1, C:Glu167:OE1 and C:Tyr264 via electrostatic interactions. Additionally, phycocyanobilin makes

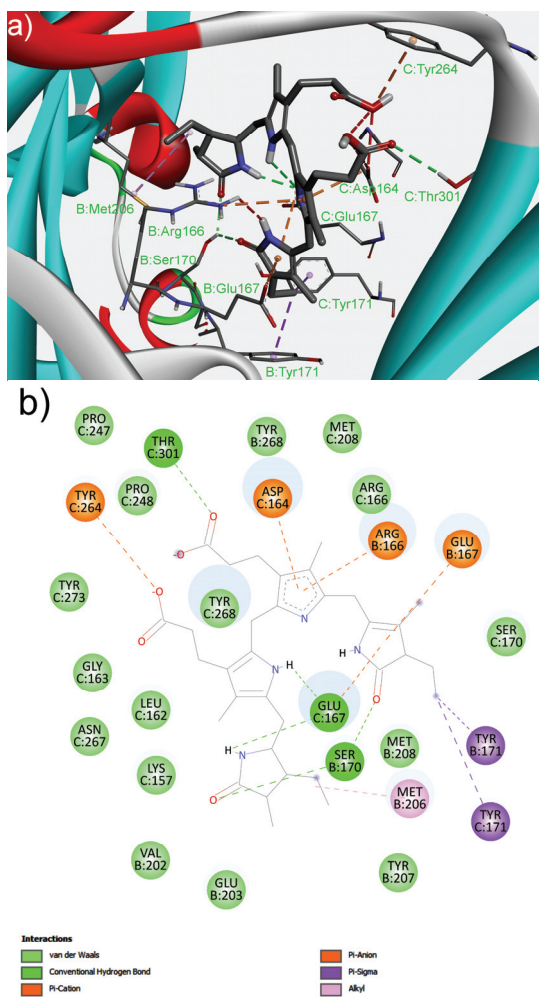


Fig. 1. Details of the strongest binding affinity; $-44.77 \text{ kJ mol}^{-1}$ (phycocyanobilin-PLpro-C111S (7SQE)): a) 3D view and b) 2D view of interaction profile.

five hydrogen bonds (B:Ser170:HG, C:Glu167:OE1 and C:Thr301:HG1) and three hydrophobic interactions (B:Tyr171, B:Met206 and C:Tyr171). The specific arrangement or connectivity of protein clusters could significantly influence their structural stability.³¹ A donor group (HG) from B:Ser170 (PLpro-C111S) interact with two acceptor groups of phycocyanobilin simultaneously. In addition, C:Glu167 makes two hydrogen bonds as an acceptor with phycocyanobilin. This result indicates that these residues are crucial in binding phycocyanobilin and the PLpro enzyme. Hydrogen bonds with multiple donors (acceptor furcation) and multiple acceptors (donor furcation) are common in protein structures. These arrangements might add more stability and play an important role in understanding the 3D structure of protein-ligand complexes.³¹ Here, although RdRp-RNA site has such a large number of hydrogen bond interactions (non-

-multiple), the low binding affinity of the RdRp-RNA site can be attributed to the relatively lower electrostatic and hydrophobic interactions of the RdRp-RNA site compared to other proteins.

The analysis shows that around 45 % of the dataset's total interactions are involved in forming multiple non-covalent interactions. An illustrative example is shown in Fig. 1 that B:Ser170, C:Aasp164 and C:Glu167 form multiple interactions. Another additional feature is the observed additive property of these interactions, showing an effect on the strength of the host-guest system.³¹ As for the non-structural proteins (Nsp10-nsp10-14 and Nsp10-nsp10-16), docking results show the lowest scores between -21 and -27 kJ mol⁻¹, possibly due to the dominance of hydrophobic residues involved in the binding pocket with phycobilins (Fig. 2a). While analyzing the interaction profile of phycourobilin–Nsp10-nsp10-14 complex (Fig. 2b), it was found that five amino acids such as A:Phe16, A:Ala20, A:Lys25, A:Ala26 and A:Tyr30 were involved in the formation of two hydrogen bonds and four hydrophobic interactions.

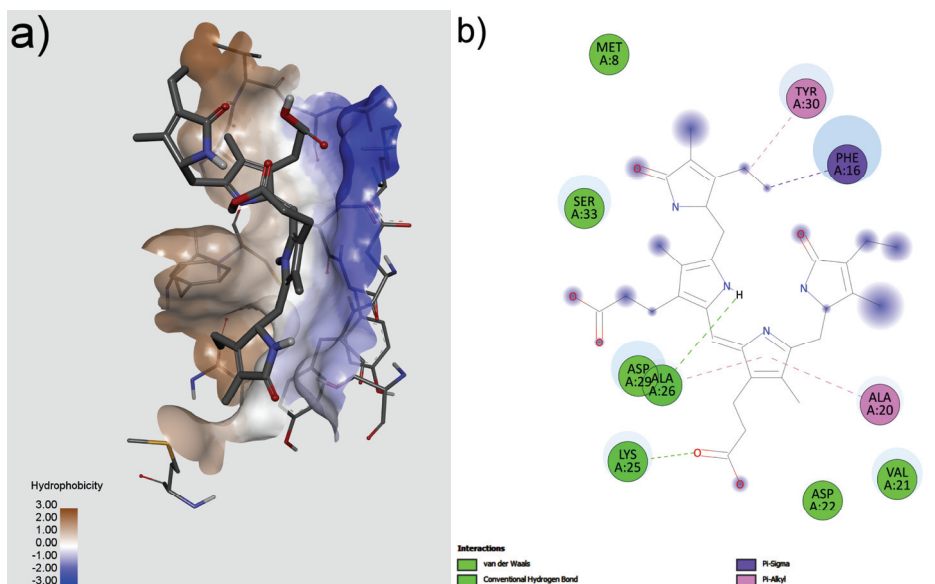


Fig. 2. Details of the weakest binding affinity; -23.85 kJ mol⁻¹ (phycourobilin–Nsp10-nsp10-14 (70RR)): a) 3D hydrophobicity view of binding pocket and b) 2D view of interaction profile.

Physiochemical, pharmacokinetic and drug-likeness properties of phycobilins

The ADME (absorption, distribution, metabolism, and excretion) properties of the compounds allow drug developers to understand the reliability and efficacy of a drug candidate compound, accelerating the timeline for the new drug submission process to the Food and Drug Administration (FDA). Therefore, after

docking assays and binding interaction analysis, an *in silico* toxicity study was conducted on the phycobilins with the SwissADME tool (Table III).

TABLE III. Drug-likeness analysis of the phycobilins obtained with SwissADME

Physicochemical property	Phycoerythrobilin	Phycourobilin	Phycocyanobilin
<i>MW</i> / g mol ⁻¹	586.68	590.71	586.68
H-bond acceptors	7	7	7
H-bond donors	5	5	5
<i>TPSA</i> / Å ²	164.71	160.95	164.71
Lipophilicity			
iLOGP	3.81	3.98	3.52
Water solubility			
Log <i>S</i> (ESOL)	-4.38	-3.71	-4.55
Solubility, mg mL ⁻¹	2.45e-02	1.16e-01	1.67e-02
Solubility, mol L ⁻¹	4.18e-05	1.96e-04	2.85e-05
Class	Moderately soluble	Soluble	Moderately soluble
Pharmacokinetics			
GI absorption	Low	Low	Low
BBB permeability	No	No	No
Druglikeness			
Lipinski #violations	1: <i>MW</i> > 500	1: <i>MW</i> > 500	1: <i>MW</i> > 500
Veber #violations	2: Rotors > 10, <i>TPSA</i> > 140	2: Rotors > 10, <i>TPSA</i> > 140	1: <i>TPSA</i> > 140
Bioavailability Score	0.11	0.11	0.11
Medicinal chemistry			
PAINS #alerts	0 alert	0 alert	0 alert
Brenk #alerts	0 alert	0 alert	0 alert
Leadlikeness	No; 2 violations: <i>MW</i> > 350, Rotors > 7	No; 2 violations: <i>MW</i> > 350, Rotors > 7	No; 2 violations: <i>MW</i> > 350, Rotors > 7
Synthetic accessibility	6.09	6.25	6.11

All the screened phycobilins were found to have little violation in the Lipinski rule of 5 (1 violation: *MW* > 500), and it was believed to be effective despite of a few violations. Out of the three compounds, phycourobilin is water soluble, while the others are moderately soluble. While checking the pharmacokinetic profile, it was noted that all compounds were ineffective in crossing the blood brain barrier, so no toxic chemicals crossed it. All the candidates were predicted to be absorbed by the gastrointestinal tract but at a low level. While analyzing medicinal chemistry, it was noted that all phycobilins do not present any resemblance to PAINS and Brenk alerts. It was compelling to note that all the compounds screened were safe as they were non-carcinogenic and non-toxic by nature. Other properties, such as pharmacokinetic, physicochemical and drug-

-likeness properties, are mentioned in Table III. Combined with their docking results, these candidates seem strongly relevant to the search for natural agents to fight against SARS-CoV-2, similar to other marine-derived antiviral compounds.³²

CONCLUSION

The present study considered molecular docking on selected phycobilins submitted to SARS-CoV-2 docking server. The primary purpose of the present paper was to test their ability to inhibit SARS-CoV-2 associated main proteins *via* an *in silico* approach. In the second part, an *in silico* toxicity analysis was conducted to assess the safety of selected compounds. This study finding revealed that phycobilins had shown high binding energy against PLpro-WT, PLpro-C111S, helicase-ANP binding site, Nsp3-macrodomain, Nsp3-MES site and Nsp10/14-N7-Mtase in the range from -37 to -45 kJ mol $^{-1}$. The interaction profile revealed that phycobilins could have various interactions (electrostatic, hydrophobic and hydrogen bonds). The strong binding affinity can be attributed to phycobilins' relatively higher electrostatic and hydrophobic interactions with some SARS-CoV-2 proteins. From the results, it can be underlined that around 45 % of the total interacting residues in the dataset are involved in forming of multiple interactions, which might add more stability to the phycobilin–SARS-CoV-2 complex. All phycobilins have good pharmacokinetic and drug-likeness properties. Therefore, all the compounds screened were safe as they were naturally non-carcinogenic and non-toxic. Based on the results obtained, phycobilins can be considered inhibitors against the important viral proteins of SARS-CoV-2. They could serve as potential drugs to treat COVID-19 with further validation studies.

SUPPLEMENTARY MATERIAL

Additional data and information are available electronically at the pages of journal website: <https://www.shd-pub.org.rs/index.php/JSCS/article/view/12867>, or from the corresponding author on request.

Acknowledgement. This research has been financially supported by the Ministry of Science, Technological Development and Innovation of Republic of Serbia (Contract No: 451-03-66/2024-03/200026 and 451-03-66/2024-03/200168).

ИЗВОД

IN SILICO СТУДИЈЕ ФИКОБИЛИНА КАО МОГУЋИХ КАНДИДАТА ЗА ИНХИБИТОРЕ
ВИРУСНИХ ПРОТЕИНА ПОВЕЗАНИХ СА COVID-19

ВЕСНА Б. ЈОВАНОВИЋ¹, МИЛАН Р. НИКОЛИЋ¹ И СРЂАН Ђ. СТОЈАНОВИЋ²

¹Универзитет у Београду, Хемијски факултет, Кафедра за биохемију и Центар изузетних вредности за молекуларне науке о храни, Београд и ²Универзитет у Београду, Институт за хемију, технологију и мешавине, Центар за хемију, Институт ог националној значају за Републику Србију, Београд

У овој *in silico* студији испитано је да ли би фикобилини (фикоцијанобилин, фикоеритробилин и фикоуробилин) могли бити инхибитори активности главних протеина SARS-CoV-2 вируса. Све хромофоре су показале вредност енергије везивања $\geq -37 \text{ kJ mol}^{-1}$ према PLpro-WT, PLpro-C111S, хеликаза-ANP везујућем месту, Nsp3-макродомену, Nsp3-MES месту и Nsp10/14-N7-Mt-ази. Фикоцијанобилин је показао највећу енергију везивања, од $-44,77 \text{ kJ mol}^{-1}$, за циљни протеин PLpro-C111S. Утврђено је да, осим водоничних веза и хидрофобних интеракција, фикобилини формирају и електростатичке интеракције са SARS-CoV-2 протеинима. Пронађена је мрежа нековалентних интеракција важна за стабилност испитаних вирусних протеина. Сви фикобилини су показали обећавајућа фармакокинетичка својства и карактеристике сличне лековима. Резултати ове студије сугеришу да би, уз додатна ригорозна валидациона испитивања, анализирани фикобилини могли да послуже као обећавајући лекови за COVID-19.

(Примљено 26. марта, ревидирано 17. априла, прихваћено 8. маја 2024)

REFERENCES

1. A. E. Gorbatenko, S. C. Baker, R. S. Baric, R. J. de Groot, C. Drosten, A. A. Gulyaeva, B. L. Haagmans, C. Lauber, A. M. Leontovich, B. W. Neuman, D. Penzar, S. Perlman, L. L. M. Poon, D. V. Samborskiy, I. A. Sidorov, I. Sola, J. Ziebuhr, *Nat. Microbiol.* **5** (2020) 536 (<https://doi.org/10.1038/s41564-020-0695-z>)
2. S. Aboul-Fotouh, A. N. Mahmoud, E. M. Elnahas, M. Z. Habib, S. M. Abdelraouf, *Virol. J.* **20** (2023) 241 (<https://doi.org/10.1186/s12985-023-02210-z>)
3. A. von Delft, M. D. Hall, A. D. Kwong, L. A. Purcell, K. S. Saikatendu, U. Schmitz, J. A. Tallarico, A. A. Lee, *Nat. Rev. Drug Discov.* **22** (2023) 585 (<https://doi.org/10.1038/s41573-023-00692-8>)
4. T. F. Aiello, C. Garcia-Vidal, A. Soriano, *Rev. Esp. Quimioter.* **35** (2022) 10 (<https://doi.org/10.37201/req/s03.03.2022>)
5. C. C. Chang, H. J. Hsu, T. Y. Wu, J. W. Liou, *Tzu Chi Med. J.* **34** (2022) 276 (https://doi.org/10.4103/tcmj.tcmj_318_21)
6. D. Saxena, L. Batra, S. K. Verma, *Pathogens* **12** (2023) 823 (<https://doi.org/10.3390/pathogens12060823>)
7. M. S. Murugaitio, M. Bermudez, J. Mortier, G. Wolber, *Drug Discov. Today Technol.* **9** (2012) e219 (<https://doi.org/10.1016/j.ddtec.2012.07.009>)
8. P. Gale, *Microb. Risk Anal.* **21** (2022) 100198 (<https://doi.org/10.1016/j.mran.2020.100140>)
9. M. E. Popović, G. Šekularac, M. Popović, *Microb. Risk Anal.* **26** (2024) 100290 (<https://doi.org/10.1016/j.mran.2024.100290>)
10. M. Popović, M. Stevanović, M. Mihailović, *J. Serb. Chem. Soc.* **89** (2024) 305 (<https://doi.org/10.2298/JSC240119019P>)

11. C. H. Kim, *Front. Pharmacol.* **12** (2021) 590509 (<https://doi.org/10.3389/fphar.2021.590509>)
12. M. M. Rahman, M. R. Islam, S. Shohag, M. E. Hossain, M. Shah, S. K. Shuvo, H. Khan, M. A. R. Chowdhury, I. J. Bulbul, M. S. Hossain, S. Sultana, M. Ahmed, M. F. Akhtar, A. Saleem, M. H. Rahman, *Environ. Sci. Pollut. Res. Int.* **29** (2022) 46527 (<https://doi.org/10.1007/s11356-022-20328-5>)
13. R. Ghildiyal, V. Prakash, V. K. Chaudhary, V. Gupta, R. Gabrani, Phytochemicals as Antiviral Agents: Recent Updates. in M. K. Swamy (eds) *Plant-derived Bioactives: Production, Properties and Therapeutic Applications*. Singapore: Springer Singapore, 2020:279 (https://doi.org/10.1007/978-981-15-1761-7_12)
14. J. S. Mani, J. B. Johnson, J. C. Steel, D. A. Broszczak, P. M. Neilsen, K. B. Walsh, M. Naiker, *Virus Res.* **284** (2020) 197989 (<https://doi.org/10.1016/j.virusres.2020.197989>)
15. S. B. Kumar, S. Krishna, S. Pradeep, D. E. Mathews, R. Pattabiraman, M. Murahari, T. P. K. Murthy, *Comput. Biol. Med.* **134** (2021) 104524 (<https://doi.org/10.1016/j.combiomed.2021.104524>)
16. R. C. Silva, H. F. Freitas, J. n. M. Campos, N. M. Kimani, C. H. T. P. Silva, R. S. Borges, S. S. R. Pita, C. B. R. Santos, *Int. J. Mol. Sci.* **22** (2021) 11739 (<https://doi.org/10.3390/ijms22111739>)
17. S. S. Gupta, A. Kumar, R. Shankar, U. Sharma, *J. Mol. Graph. Model.* **106** (2021) 107916 (<https://doi.org/10.1016%2Fj.jmgm.2021.107916>)
18. J. Li, K. T. McKay, J. M. Remington, S. T. Schneebeli, *Sci. Rep.* **11** (2021) 16307 (<https://doi.org/10.1038/s41598-021-95826-6>)
19. B. Pendyala, A. Patras, C. Dash, *Front Microbiol.* **12** (2021) 645713 (<https://doi.org/10.3389/fmicb.2021.645713>)
20. S. Geahchan, H. Ehrlich, M. A. Rahman, *Marine Drugs* **19** (2021) 409 (<https://doi.org/10.3390/md19080409>)
21. L. Tounsi, H. B. Hlima, F. Bentati, O. Bentati, H. Derbel, P. Michaud, S. Abdelkafi, *Mar. Drugs* **21** (2023) 440 (<https://doi.org/10.3390/md21080440>)
22. K. Liu, X. Lu, H. Shi, X. Xu, R. Kong, S. Chang, *Nucleic Acids Res.* **51** (2023) W365 (<https://doi.org/10.1093/nar/gkad414>)
23. O. Trott, A. J. Olson, *J. Comput. Chem.* **31** (2010) 455 (<https://doi.org/10.1002/jcc.21334>)
24. J. Eberhardt, D. Santos-Martins, A. F. Tillack, S. Forli, *J. Chem. Inf. Model.* **61** (2021) 3891 (<https://doi.org/10.1021/acs.jcim.1c00203>)
25. N. M. O'Boyle, M. Banck, C. A. James, C. Morley, T. Vandermeersch, G. R. Hutchison, *J. Cheminformatics.* **3** (2011) 33 (<https://doi.org/10.1186/1758-2946-3-33>)
26. S. Kim, J. Chen, T. Cheng, A. Gindulyte, J. He, S. He, Q. Li, B. A. Shoemaker, P. A. Thiessen, B. Yu, L. Zaslavsky, J. Zhang, E. E. Bolton, *Nucleic Acids Res.* **51** (2023) D1373-D1380 (<https://doi.org/10.1093/nar/gkac956>)
27. Biovia, D.S. (2021) Discovery Studio Visualizer. San Diego.
28. A. Daina, O. Michielin, V. Zoete, *Sci. Rep.* **7** (2017) 42717 (<https://doi.org/10.1038/srep42717>)
29. D. Shin, R. Mukherjee, D. Grawe, D. Bojkova, K. Baek, A. Bhattacharya, L. Schulz, M. Widera, A. R. Mehdipour, G. Tascher, P. P. Geurink, A. Wilhelm, G. van der Heden van Noort, H. Ovaa, S. Müller, K. P. Knobeloch, K. Rajalingam, B. A. Schulman, J. Cinatl, G. Hummer, S. Ciesek, I. Dikic, *Nature* **587** (2020) 657 (<https://doi.org/10.1038/s41586-020-2601-5>)

30. R. Ferreira de Freitas, M. Schapira, *Med. Chem. Commun.* **8** (2017) 1970
(<https://doi.org/10.1039/C7MD00381A>)
31. A. S. Mahadevi, G. N. Sastry, *Chem. Rev.* **116** (2016) 2775
(<https://doi.org/10.1021/cr500344e>)
32. R. Singh, N. Chauhan, M. Kuddus, *Environ. Sci. Pollut. Res. Int.* **28** (2021) 52798
(<https://doi.org/10.1007/s11356-021-16104-6>).



SUPPLEMENTARY MATERIAL TO

***In silico* studies of phycobilins as potential candidates for inhibitors of viral proteins associated with COVID-19**

VESNA B. JOVANOVIĆ¹, MILAN R. NIKOLIĆ¹ and SRĐAN Đ. STOJANOVIĆ^{2*}

¹University of Belgrade, Faculty of Chemistry, Department of Biochemistry and Centre of Excellence for Molecular Food Sciences, Belgrade, Serbia and ²University of Belgrade, Institute of Chemistry, Technology and Metallurgy – National institute of the Republic of Serbia, Department of Chemistry, Belgrade, Serbia

J. Serb. Chem. Soc. 89 (7–8) (2024) 997–1009

HYDROGEN BONDS

Classical^l

Conventional hydrogen bond interactions between a hydrogen bond donor atom and an acceptor atom can exist. Atoms of element types N, O, P, and S are considered as classical hydrogen bond donor atoms, and hydrogen atoms are considered as hydrogen bond donors if connected to such atoms. In this case, the heavy atom is no longer considered as a hydrogen bond donor. Atoms of element types N, O, P, and S are also hydrogen bond acceptor atoms if at least one electron lone pair is present (for example, NH₃ but not NH₄⁺). However, an sp²-hybridized N atom with at least one electron lone pair is not considered a hydrogen bond acceptor atom if it is connected by a single bond to another sp²-hybridized atom. Additionally, atoms of element type F, Cl, Br, and I are also considered hydrogen bond acceptor atoms.

If both atoms are N or O, the distance criterion d between the heavy donor and acceptor atoms is 3.4 Å by default (*Strong H-bond D(H)...A (max dist)*). Otherwise the distance criterion is 3.8 Å (*Weak H-bond D(H)...A (max dist)*). If there is an explicit hydrogen atom, the distance dh between the hydrogen atom and the acceptor atom must be less than the specified distance criterion -0.7 Å (that is, 2.7 Å or 3.1 Å). See Fig. 1-S and Fig. 2-S.

*Corresponding author. E-mail: srdjanst@chem.bg.ac.rs

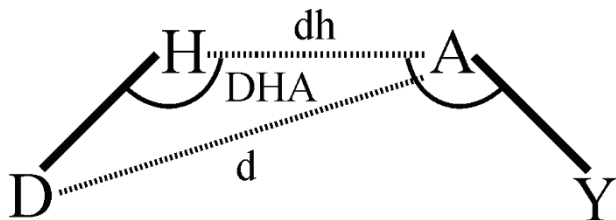


Fig. 1-S. Hydrogen bond when an explicit hydrogen exists. The angles and distances used to determine if an interaction exists are shown.

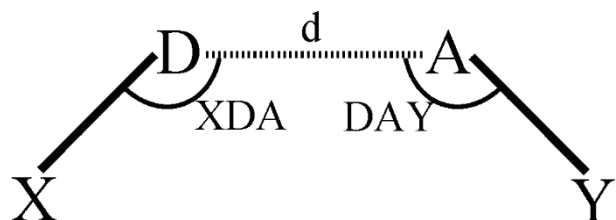


Fig. 2-S. Hydrogen bond when an explicit hydrogen does not exist. The angles and distances used to determine if an interaction exists are shown.

By default, angle constraints are checked to determine whether a hydrogen bond is present. For a general hydrogen bond $X\text{-D}\text{-H...A-Y}$, where D is the hydrogen bond donor heavy atom, H is the explicit donor hydrogen if present, A is the hydrogen bond acceptor atom, X is any non-hydrogen atom attached to the donor atom, and Y is any atom attached to the acceptor atom. The angles that can be constrained are $X\text{-D-A}$, $D\text{-H-A}$, $D\text{-A-Y}$, and $H\text{-A-Y}$. These must all lie within the minimum (90° by default) and maximum (180° by default) values of the following angle parameters: *Hydrogen-bond X-D-A angle*, *Hydrogen-bond D-H-A angle*, *Hydrogen-bond D-A-Y angle*, and *Hydrogen-bond H-A-Y angle*.

In the case of an sp hybridized donor atom, its hydrogen atom will be colinear with the D-X bond, so any interaction should lie closer to this vector. Therefore, a stricter minimum angle constraint *Hydrogen Bond with Sp donor X-DA* (135° by default) is applied.

Non Classical¹

Carbon hydrogen bond interactions are considered weaker hydrogen bonds where the donor is a polarized carbon atom. A carbon atom is considered to be a donor if it is either in an acetylene group or if it is adjacent to an oxygen or nitrogen atom.

These interactions are determined using the same geometric criteria used for classical hydrogen bonds with the exception of the default distance criterion being 3.8 Å (*Weak H-bond D(H)...A (max dist)*).

Pi-Donor hydrogen bond interactions are hydrogen bonds that occur between hydrogen bond donor atoms and a Pi ring that functions as a hydrogen bond acceptor. The following tests are performed to find these interactions:

1. Hydrogen bond donor atoms are found.
2. C-H donors are excluded because they form Pi-Sigma interactions.
3. The distance between each donor heavy atom and the centroid of each Pi ring is tested to find those within the *Pi-Donor (max dist)* cutoff (4.2 Å by default).
4. The angle between the donor heavy atom-centroid vector and the normal to the ring plane should be less than the *Pi-Donor* angle (40° by default).
5. The positions of each of the donor's explicit or implicit hydrogen atoms are found. A heavy-H-centroid angle must exist that deviates from linearity by no more than the *Pi-Donor deviation angle* (40.0° by default).

*Water*¹

The Water monitor is useful for identifying bridging water molecules (when a water molecule is hydrogen bonded to two different molecules such as a protein and a ligand or two domains of a protein) and visualize water networks. After all hydrogen bonds have been determined, the bonds that bridge chains are classified as *Water Mediated Hydrogen Bonds* and colored mid-blue. Other hydrogen bonds involving at least one water molecule are classified as *Water Hydrogen Bonds* and colored light-blue.

*Salt Bridge*¹

Salt Bridge interactions are relatively strong non-bonded interactions between pairs of oppositely charged groups where hydrogen bonding also occurs. These interactions can be observed at a longer range than uncharged hydrogen bonds. Interactions are classified as salt bridges for pairs of atoms closer than 4.0 Å (*Salt bridge D(H)...A (max dist)*), where one atom is positively charged, one is negatively charged, and there is a hydrogen bond between them.

ELECTROSTATIC

*Charge*²

Attractive Charge interactions exist between atoms bearing opposite whole or fractional formal charges that are within the *Charge-charge (max dist)* cutoff (5.6 Å by default).

Salt Bridge interactions are also listed in the Electrostatic and Hydrogen bond categories since they can be considered members of both.

Pi-Charge^{3,4}

Pi-Cation interactions can exist between a positively charged atom and the electrons of a delocalized Pi system. The following tests are performed to find them:

1. Cations are considered to be atoms that have a formal charge of at least +0.5. This allows the inclusion of delocalized cationic species such as lysine and arginine side chains.
2. The distance between a cation and the centroid of a Pi ring should be less than the *Pi-Cation* (*max dist*) cutoff (5.0 Å by default, see R in Fig. 3-S).
3. The angle between the cation-centroid vector and the normal to the ring plane should be less than the *Pi-Cation* maximum angle (40° by default, see θ in Fig. 3-S).

Pi-Anion interactions are calculated similarly to *Pi-Cation* interactions, but only atoms with charges of -0.5 or less are considered.

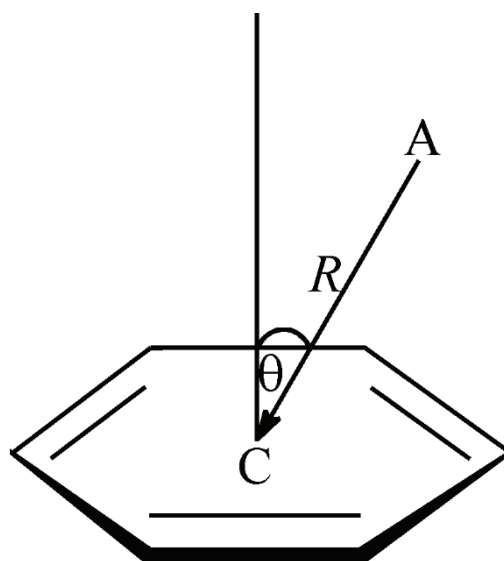


Fig. 3-S. Example of a Pi-atom interaction (for example, Pi-cation, Pi-anion, and so on). The important measurements are the angle θ and the distance R.

HYDROPHOBIC

Pi-Hydrophobic^{5,6}

Pi rings are defined as planar ring systems composed of sp^2 hybridized atoms. They include (but are not confined to) aromatic rings.

Pi-Pi stacked interactions are determined following the methodology of McGaughey et al.⁵ Stacked and staggered Pi-Pi interactions are determined by the following tests:

1. The distance between the centroid of each Pi ring pair is determined to find those which fall within the cutoff distance (*Pi-Pi centroid (max dist)*, 6 Å by default, see R_{cen} , Fig. 4-S).
2. For these interactions, an atom from each ring must be within the (*Pi-Pi closest atom (max dist)*) cutoff, 4.5 Å by default, see R_{clo} , Fig. 4-S).
3. The angle θ between the normal of one or both rings and the centroid-centroid vector must be between 0° and \pm the *Stacked Pi-Pi theta* angle cutoff (50° by default), and the angle γ between the normal to each ring must be between 0° and \pm the *Stacked Pi-Pi gamma* cutoff angle (35° by default).

Pi-Pi T-shaped interactions occur if the following conditions are met:

1. The distance between the centroid of each pair of Pi rings is determined to find those which fall within the *Pi-Pi centroid (max dist)* cutoff distance (6 Å by default).
2. An atom from each ring should be within the *Pi-Pi closest atom (max dist)* cutoff (4.5 Å by default).

The angle ω between the normal of one or both rings and the centroid-centroid vector must be between 0° and \pm the *T-Shaped Pi-Pi theta* angle cutoff (30° by default), and the angle γ between the normal to each ring must be within the *T-Shaped Pi-Pi gamma* angle cutoff (55° by default) or greater.

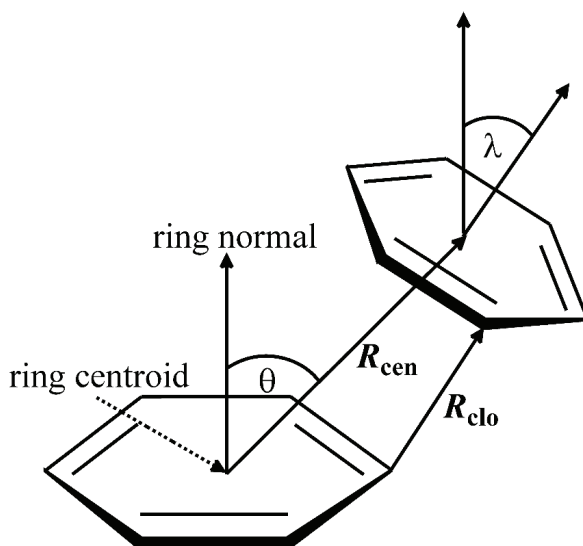


Fig. 4-S. Example of a Pi-Pi interaction. The distances and angles needed for an interaction are labeled.

Amide-Pi Stacked interactions occur between an amide group and a Pi ring if the following criteria are met:

1. The distance between the centroid of the amide group and the Pi rings falls within the *Pi-Pi centroid (max dist)* (6 Å by default).
2. An atom from each group should be within the *Pi-Pi closest atom (max dist)* (4.5 Å by default).

The angle ω between the normal of one or both groups and the centroid-centroid vector must be between 0° and \pm the *Stacked Pi-Amide theta* angle cutoff distance (40° by default), and the angle γ between the normal to each must be between 0° and \pm the *Stacked Pi-Amide gamma* angle cutoff (20° by default).

*Alkyl Hydrophobic*²

Alkyl groups are defined as the following non-polarized, non-Pi systems:

Predominantly aliphatic amino acid side-chains: These include Alanine, Valine, Leucine, Isoleucine, Methionine, Selenomethionine, Cysteine, Proline, atoms CB, CG, and CD of Lysine, and atoms CB and CG of Arginine.

Hydrophobic groups on ligands are coniguous sets of atoms that are not adjacent to concentrations of charge (charged atoms or electronegative atoms). A group of atoms is considered hydrophobic if its surface area is equal or greater than the area of a methyl group multiplied by the *Surface area scale factor* (default 0.65), which corresponds to the surface area of a chlorine atom.

The criteria for this type of interaction are met when if the groups' centroids are within the *Alkyl centroid (max dist)* cutoff (5.5 Å by default) and they have at least one pair of atoms within the same *Pi-Pi closest atom (max dist)* cutoff used for Pi-Pi interactions.

*Mixed Pi/Alkyl Hydrophobic*⁷

Pi-Sigma interactions (sometimes referred to as CH- π interactions) are weak interactions between a hydrogen and a Pi ring system. An interaction of this type must meet the following conditions:

1. The hydrogens acting as the donor can be implicit or explicit hydrogens. They must be connected to a nonaromatic carbon atom.
2. The distances between the hydrogen and the center of the Pi ring must be within the *Pi-Sigma (max dist)* cutoff (4.1 Å by default, see R in Fig. 5-S).
3. The C-H-centroid angle cannot deviate from linearity by more than the *Pi-Sigma deviation* angle (20° by default, see δ in Fig. 5-S) and the angle between the C-centroid vector and the normal to the ring plane is not more than the *Pi-Sigma* angle (45° by default, see θ in Fig. 5-S).

Pi-Alkyl interactions exist where the centroids of a Pi ring and an alkyl group are within the *Alkyl centroid (max dist)* cutoff (5.5 Å by default) and they

have at least one pair of atoms within the same *Pi-Pi closest atom (max dist)* cutoff as used for Pi-Pi interactions.

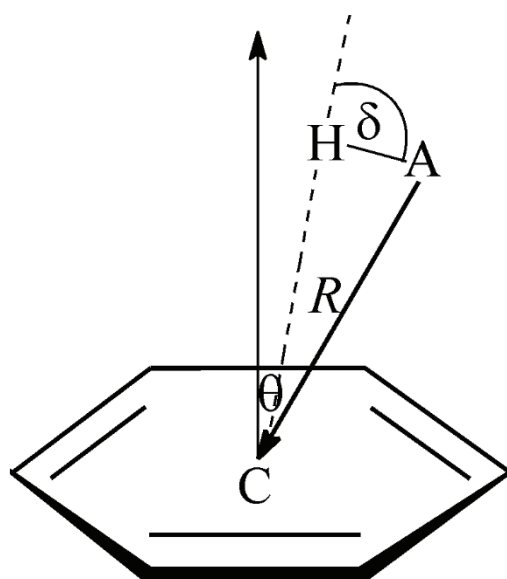


Fig. 5-S. Illustration of a Pi-Sigma interaction.

HALOGEN

Fluorine^{1,8}

Halogen (Fluorine) interactions are carbon-bound halogen interactions (C-X...B-Y) with structural significance to weak hydrogen bonds. Interactions with carbon-bound fluorine are monitored and identified separately from those involving Cl, Br, and I. Additionally, halogen interactions (including F) with hydrogen donors are identified separately.

Fluorine interactions (C-F...B-Y) are identified and monitored with all hydrogen donors and the specific case where B is carbon, nitrogen, and oxygen. In all cases, a maximum distance criterion (*Fluorine non-bond (max dist)*) is 3.7 Å by default) is used. When the interaction is with a hydrogen donor, the hydrogen bond angle criteria are used and the interaction is identified as both a fluorine and a hydrogen bond interaction.

Fluorine interactions with carbon and oxygen are limited to C=O moieties. Nitrogen interactions are limited to nucleophilic nitrogen. These interactions are also limited by the same maximum distance criterion (3.7 Å by default). However, no angle constraints are applied.

Cl, Br, I^{l,8}

Halogen (Cl, Br, I) interactions have distance criteria defined as a fraction of the sum of the atoms' van der Waals radii (controlled by *Halogen (Cl, Br, I) VDW fraction (max)*). The default fraction is 1, using the full van der Waals distance as the cutoff. As with fluorine interactions with a hydrogen donor, halogen interactions with hydrogen donors use the hydrogen bond angle criteria to identify interactions.

Non-fluorine halogen interactions to carbon and oxygen are also limited to C=O moieties. Additionally, interactions with (B-Y) N-C, N-S, N-P, S-C, S-S and S-P are considered. A separate set of angle criteria are used in these cases (*Halogen (Cl, Br, I) bond X-B-Y angle* with a default between 75° and 180° and *Halogen (Cl, Br, I) bond C-X-B angle* with a default between 120° and 180°).

REFERENCES

1. C. Bissantz, B. Kuhn, M. Stahl, *J. Med. Chem.* **53** (2010) 5061 (<https://doi.org/10.1021/jm100112j>)
2. G. Wolber, T. Langer, *J. Chem. Inf. Model.* **45** (2005) 160 (<https://doi.org/10.1021/ci049885e>)
3. J. P. Gallivan, D. A. Dougherty, *Proc. Natl. Acad. Sci. USA* **96** (1998) 9459 (<https://doi.org/10.1073/pnas.96.17.9459>)
4. A. Frontera, P. Gamez, M. Mascal, T. J. Mooibroek, J. Reedijk, *Angew. Chem. Int. Ed.* **50** (2011) 9564 (<https://doi.org/10.1002/anie.201100208>)
5. G. B. McGaughey, M. Gagné, A. K. Rappé, *J. Biol. Chem.* **273** (1998) 15458 (<https://doi.org/10.1074/jbc.273.25.15458>)
6. J. B. O. Mitchell, C. L. Nandi, I. K. McDonald, J. M. Thornton, S. L. Price, *J. Mol. Biol.* **239** (1994) 315 (<https://doi.org/10.1006/jmbi.1994.1370>)
7. T. Ozawa, E. Tsuji, M. Ozawa, C. Handa, H. Mukaiyama, T. Nishimura, S. Kobayashi, K. Okazaki, *Bioorg. Med. Chem.* **16** (2008) 10311 (<https://doi.org/10.1016/j.bmc.2008.10.041>)
8. P. Auffinger, F. A. Hays, E. Westhof, P. S. Ho, *Proc. Natl. Acad. Sci. USA* **101** (2004) 16789 (<https://doi.org/10.1073/pnas.0407607101>).



Introducing a novel crystal form of pyruvic acid thiosemicarbazone and its sodium salt

SVETLANA K. BELOŠEVIĆ^{1#}, SLAĐANA B. NOVAKOVIĆ^{2*}, MARKO V. RODIĆ^{3#},
VUKADIN M. LEOVAC^{3#}, LJILJANA S. VOJINOVIĆ-JEŠIĆ^{3#}, GORAN A.
BOGDANOVIĆ² and MIRJANA M. RADANOVIĆ^{3***#}

¹Faculty of Technical Sciences, University of Priština, Knjaza Miloša 7, 38220 Kosovska Mitrovica, Serbia, ²"Vinča" Institute of Nuclear Sciences - National Institute of the Republic of Serbia, University of Belgrade, P. O. Box 522, 11001 Belgrade, Serbia and ³University of Novi Sad, Faculty of Sciences, Trg Dositeja Obradovića 3, 21000, Novi Sad

(Received 17 April, revised 26 April, accepted 8 May 2024)

Abstract: The reaction of thiosemicarbazide and sodium pyruvate has been thoroughly studied and the novel crystal form of pyruvic acid thiosemicarbazone (H_2pt) and its sodium salt was obtained. Compounds were characterized by IR spectra, melting points, elemental analysis, conductometric measurements and single-crystal X-ray analysis. A detailed comparative analysis of crystal structures of these compounds is given, as well as comparison with some of the earlier known complexes containing H_2pt . The two novel crystal structures exhibit notably different hydrogen bonding patterns, mutually and in comparison with previously reported crystal form of H_2pt . All crystal structures are stabilized by extensive network of N–H···O, O–H···O and N–H···S hydrogen bonds. The cyclic hydrogen bonding motif involving the thioureido moieties of the ligand is the only one which repeats in each structure.

Keywords: thiosemicarbazone; crystal structure; physicochemical properties; metal complexes; hydrogen bonding.

INTRODUCTION

Thiosemicarbazones are a versatile class of compounds with a very wide range of biological activities and numerous potential applications in pharmacology and medicine,^{1–5} as well as analytical chemistry^{6–8} and industry.^{9,10} The majority of these remarkable features arise from the ability of thiosemicarbazones [$R_1R_2C=N^1N^2(H)C(S)N^3H_2$] to strongly coordinate the transition metal ions. The coordination usually occurs through the hydrazine N1 and thioamide S donors, while other coordination modes are also available due to several potential

* Corresponding authors. E-mail: (*)snovak@vin.bg.ac.rs; (**)mirjana.lalovic@dh.uns.ac.rs

Serbian Chemical Society member.

<https://doi.org/10.2298/JSC240417050B>

donor atoms in the thiosemicarbazone moiety.^{11,12} Another very important feature of thiosemicarbazones is their great structural variety achieved by the variation of residues attached to the NNCS system. Thus, the thiosemicarbazone ligands, which are generally obtained in the condensation reaction of thiosemicarbazide and different aldehydes and ketones, also incorporate additional coordination and/or interaction sites available at the carbonyl residues.^{11–13} Equally important as the coordination and structural variety is the ability of thiosemicarbazones to form extensive hydrogen bonding with the closest environment. This is of primary importance for biologically active molecules where the non-covalent interactions lead the molecule recognition processes with the biological systems.^{14–16}

As the properties of thiosemicarbazones are dependable on their carbonyl residues, a vast number of carbonyl compounds have been used in their synthesis, including the keto-acids. Among the ligands of the latter type, particular attention has been paid to the pyruvic acid thiosemicarbazone and its complex compounds due to their evident biological activity.^{17–21} Pyruvic acid is the simplest of the alpha-keto acids, known as an important component in several metabolic processes within the living cell. Apart from incorporating biologically relevant fragment, the corresponding pyruvic acid thiosemicarbazone gains additional coordination sites in the form of two oxygen donors from the carboxylic group. Moreover, the pyruvic acid thiosemicarbazone, a relatively small size molecule, joins together three very interactive fragments, *viz.* hydrazine, thioamide, and carboxylate, all with exceptional hydrogen bonding ability. This feature certainly increases the ability for intermolecular interactions, as well as the possibility for polymorphic crystallization.

This paper presents a novel synthetic route for the pyruvic acid thiosemicarbazone ligand. The structural analysis of the obtained compound revealed that this is actually a new crystal form of the pyruvic acid thiosemicarbazone (H_2pt), dissimilar to the previously reported crystal structure²² (CSD refcode:²³ YEBBUC). In addition, the study includes novel crystal structure of the sodium salt of pyruvic acid thiosemicarbazone, which is one of very rare crystal structures of the alkali and earth-alkali compounds with the thiosemicarbazone ligands in general. Considering the significance of different crystal forms and dissimilar intermolecular arrangements for properties such as biological activity and solubility, in the present study we aim to compare remarkable hydrogen bonding features in different crystal forms of H_2pt and its sodium salt.

EXPERIMENTAL

Materials and physical measurements

All starting materials and solvents were purchased from Sigma–Aldrich and were used without further purification. C, H, N and S elemental analyses were performed by standard micro-methods in the Center for Instrumental Analysis, ICTM, Belgrade, Serbia. Melting

points were measured with a Nagema PHMT 05 hot-stage microscope. IR spectra were carried out in a range of 400–4000 cm⁻¹ using Nicolet Nexus 670 FTIR (Thermo Scientific) spectrophotometer. The molar conductivity measurements of freshly prepared solutions ($c = 1 \text{ mmol L}^{-1}$) were performed on a Jenway 4510 conductivity meter.

Preparation of H₂pt·0.5H₂O (1)

The initial solution of H₂pt was obtained in the reaction of a mildly heated aqueous solution (5 cm³) of thiosemicarbazide hydrochloride (0.64 g, 5 mM) and an aqueous solution (5 cm³) of sodium pyruvate (0.55 g, 5 mM). The mixture was mildly heated for about 3 min. The obtained white microcrystalline product was filtered off after 24 h and washed with water. Yield: 55 %. A few single crystals suitable for X-ray analysis were obtained from the mixture of CaCO₃ (10 mg) and the obtained ligand (32 mg) in water (5 cm³) heated at 60 °C for 15 min and then cooled to room temperature.

Preparation of sodium pyruvate thiosemicarbazone {[Na(Hpt)(H₂O)₃]·H₂O} (2)

The aqueous solution (5 cm³) of equimolar amounts of sodium pyruvate (0.55 g, 5 mM) and thiosemicarbazide (0.46 g, 5 mM), was heated at 50 °C for about 1.5 h. After solvent evaporation at room temperature, obtained white single crystals were washed with EtOH–H₂O (1:1). Yield: 47 %.

Analytical and spectral data of the synthesized compounds are given in Supplementary material to this paper.

Crystal structure determination

The single-crystal X-ray diffraction data for **1** and **2** were collected using an Oxford Diffraction Gemini S diffractometer. The reflection integration and data reduction were performed with the CrysAlisPro.²⁴ The crystal structures were solved by direct methods and refined using full-matrix least-squares against F^2 with the SHELX programs.²⁵ The H atoms bonded to N and O atoms were located from difference Fourier maps and refined isotropically, or by applying DFIX restraints, with O–H and N–H distances restrained to 0.82(1) and 0.87(1) Å, respectively, and $U_{\text{iso}}(\text{H}) = 1.2U_{\text{eq}}(\text{O,N})$. H atoms bonded to C atoms were introduced in idealized positions and treated with a riding model. Crystallographic and refinement details are given in Table S-I of the Supplementary material. Mercury software²⁶ was used to analyze and graphically present the crystal structures. The CrystalExplorer²⁷ was employed to calculate intermolecular interaction energies at the B3LYP-D2/6-31G(d,p) level of theory using the crystal geometry. Crystallographic data associated with this publication are deposited with the Cambridge Crystallographic Data Centre under the CCDC Numbers 2347833 and 2347834. The data are available free of charge at <https://www.ccdc.cam.ac.uk/structures>.

RESULTS AND DISCUSSION

Syntheses and characterization

In Fig. 1 the synthesis of both known ligand forms and the sodium salt is presented. According to the previously described synthetic procedure,^{28,29} the pyruvic acid thiosemicarbazone could be obtained from the aqueous solution of thiosemicarbazide hydrochloride and pyruvic acid. The same compound was obtained here, by the reaction of aqueous solution of thiosemicarbazide hydrochloride and sodium-pyruvate. Interestingly, by heating the aqueous solution of the pyruvic acid thiosemicarbazone and CaCO₃, instead of the expected calcium salt,

single crystals of a new crystal form of the initial ligand were obtained ($\text{H}_2\text{pt}\cdot 0.5\text{H}_2\text{O}$, **1**). On the other hand, the reaction of the warm aqueous solution of neutral thiosemicarbazide and sodium pyruvate resulted in the sodium salt of pyruvic acid thiosemicarbazone $\{\text{Na}(\text{Hpt})(\text{H}_2\text{O})_3\}\cdot \text{H}_2\text{O}$ (**2**). The molar conductivity of water and methanolic solutions of **2** corresponds to a 1:1 type of electrolyte.

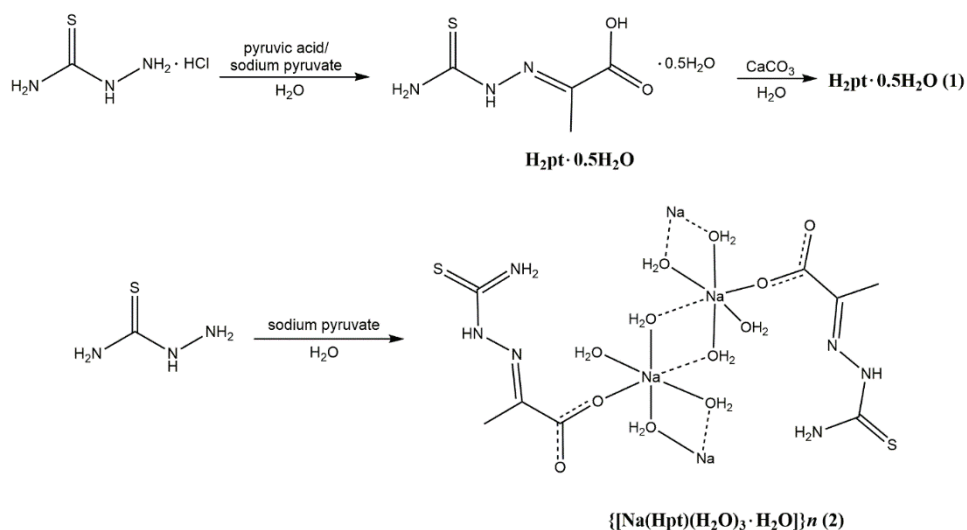


Fig. 1. Reaction scheme for obtaining H_2pt and its sodium salt.

In most structures of metal complexes containing H_2pt , it is coordinated as a monoanionic or dianionic tridentate *ONS* ligand through the oxygen atom of the carboxyl group, the azomethine nitrogen atom, and the sulfur atom.^{29,30} However, in pentacoordinate $[\text{Zn}(\text{H}_2\text{pt})(\text{Hpt})\text{Cl}]$,³⁰ aside from the tridentate coordination of Hpt^- , monodentate coordination of neutral H_2pt through the sulfur atom is found. In **2**, another mode of monodentate coordination of this ligand is found, *i.e.*, coordination via the oxygen atom of the deprotonated carboxyl group (vide infra). Thus, in the IR spectra of **1** and **2** (Figs. S-1 and S-2, of the Supplementary material), $\nu(\text{C}=\text{N})$ and $\nu(\text{C}=\text{S})$ bands are found at nearly the same wavenumbers. A significant difference can be observed in the positioning of carboxyl bands, found at 1727 and 1699 cm^{-1} in the spectrum of **1**, and 1571 cm^{-1} , $\nu_{\text{a}}(\text{CO}_2^-)$, and 1381 cm^{-1} , $\nu_{\text{s}}(\text{CO}_2^-)$ in the spectrum of **2**.

*Molecular structures of $\text{H}_2\text{pt}\cdot 0.5\text{H}_2\text{O}$ (**1**) and $\{\text{Na}(\text{Hpt})(\text{H}_2\text{O})_3\}\cdot \text{H}_2\text{O}$ (**2**)*

Crystal structures of **1** and **2** have been determined by single crystal X-ray analysis. The molecular structures of these compounds are presented in Fig. 2, while selected geometrical parameters are compared in Table I. Both compounds crystallize in the triclinic crystal system in space group $P\bar{1}$. The asymmetric unit

of **1** contains two crystallographically independent molecules (denoted A and B) and a molecule of crystal water (Fig. 2a), dissimilar to its previously reported crystal form containing the three independent H₂pt molecules.²² The compound **2** crystallizes as a coordination polymer with Hpt⁻ neutralized by the solvated sodium counterions (Fig. 2b).

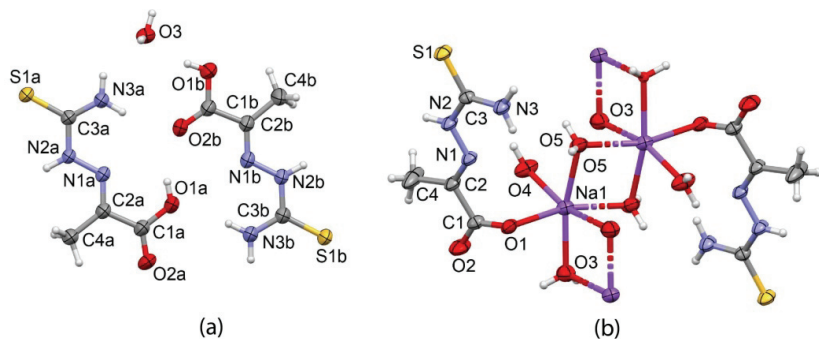


Fig. 2. Molecular structure of: a) **1** and b) fragment of **2**.

TABLE I. Selected geometric parameters

Bond	1_A	1_B	2
	Length, Å		
N1–N2	1.361(2)	1.361(2)	1.376(2)
N1–C2	1.283(2)	1.280(2)	1.272(2)
N2–C3	1.361(2)	1.320(2)	1.347(2)
N3–C3	1.312(2)	1.357(2)	1.312(2)
C3–S1	1.685(2)	1.686(2)	1.699(2)
C1–O1	1.329(2)	1.310(2)	1.258(2)
C1–O2	1.203(2)	1.212(2)	1.242(2)
Na1–O1	—	—	2.457(2)
<Na1–Ow>	—	—	2.314
	Angle, °		
N1–N2–C3	118.6(2)	119.0(2)	118.3(2)
N2–C3–N3	117.3(2)	117.6(2)	117.9(2)
N2–C3–S1	119.3(2)	119.5(2)	119.2(2)
O1–C1–O2	119.0(2)	123.9(2)	125.4(2)

At the molecular level, the neutral H₂pt ligand and its anion, Hpt⁻, show little differences. The main structural feature of these molecules is their approximately planar form resulting from the intrinsic planarity of the pyruvate and thiosemicarbazide components. The dihedral angles between the best planes formed by the non-H atoms of two components are 4.21(8) and 5.02(8)^o in independent molecules H₂pt_A and H₂pt_B, respectively and 1.6(1)^o in the Hpt⁻ of the salt. Also, all molecules adopt the *E* configuration with respect to the C2–N1 and the C3–N2 bond. This arrangement places the N1 and S ligators on mutually

opposite sides of the molecule, as typical for most uncoordinated thiosemicarbazone ligands (Fig. 2).

The bond lengths and angles of the three molecules, compared in Table I, confirm their close geometrical similarity. The bond distances are intermediate between those of single and double bonds, indicating the electron delocalization, as consistent with the molecular planarity. Among the three C–N bonds present in each molecule, the C2–N1, at the junction of two fragments, has the highest double bond character. A more significant bond length differences involve C–O bonds, which obviously differ in H₂pt molecules due to protonated O1 while having similar lengths in the anion. It is interesting to mention that intra-ligand bond lengths in **2** are in accordance with those found in the tridentate coordinated Hpt[−] in [Zn(H₂pt)(Hpt)Cl].³⁰ The C–C bonds are single bonds allowing for free fragment rotation; indeed, the two independent molecules of H₂pt show different orientation of their carboxyl residues, with N1–C2–C1–O1 torsion angle of 179.0(1) and 4.8(2)[°] in molecules A and B, respectively.

In the crystal structure of **2**, the sodium ion is six-coordinated by one carboxylic oxygen atom from the thiosemicarbazone ligand and five oxygen atoms from the water molecules (Fig. 2b). Four of these water ligands have the role of the bridging ligands connecting the molecules into the one-dimensional chain, running along the *a* crystallographic axis. The Na–O bond distance involving the Hpt[−] is 2.457(2) Å, while those to water molecules are 2.314 Å on average. The central part of the formed coordination polymer is composed of Na₂O₂ four-membered rings arranged at the dihedral angle of 77.7(1)[°]. The thiosemicarbazone ligand occupies the lateral sides of this chain and has a crucial role in the interconnection of chains by intermolecular interactions.

Comparison of crystal packing features

The crystal structures of **1** and **2** are both stabilized by the extensive network of N–H···O, O–H···O and N–H···S interactions. Deprotonation of H₂pt ligand and the presence of additional water molecules in the sodium complex significantly change the hydrogen bonding pattern of pyruvate thiosemicarbazone relative to its neutral (acidic) form, despite the pronounced structural similarity of ligands at the molecular level. Nevertheless, even the two crystallographically independent molecules in the crystal structure of **1** (Fig. 2a) have notably different hydrogen bonding patterns, mainly related to the different orientations of their carboxylic groups. Thus, in molecule A, the carboxylic proton is oriented towards the hydrazine N1 atom to form an intramolecular O1a–H1a···N1a hydrogen bond, while in molecule B, the equivalent proton points out of the molecule to engage in short O1b–H1b···O3 interaction with the crystal water of the asymmetric unit (Fig. 2a).

There are two strong and directional N3–H \cdots O hydrogen bonds (Table II) joining the pair of independent molecules within the asymmetric unit of **1**. Although the molecules A and B employ the equivalent thioamide N3–H donors, the dissimilar carboxylic oxygen atoms, *i.e.*, O1 and O2, serve as their acceptors (Fig. 3a). Viewed in terms of these N3–H \cdots O interactions, the cyclic hydrogen bonding motif that links two independent molecules within the asymmetric unit of **1** can be described in Etter's graph-set notation³¹ as R²₂(16), Fig 3a. In addition to the pair of N3–H \cdots O interactions the O1a–H donor, already engaged in the intramolecular O1a–H \cdots N1a, also engages in O1a–H \cdots O2b interaction reinforcing the binding between the independent molecules. This is the only interaction in the crystal structure of **1** which directly links the two carboxyl groups. In combination with the above N3–H \cdots O hydrogen bonds, the O1a–H \cdots O2b gives rise to two smaller ring patterns R¹₂(10) and R²₂(10), Fig. 3a.

TABLE II. Hydrogen bonding geometry ($^{\circ}$, Å)

Bond	H \cdots A	D \cdots A	D–H \cdots A	Symmetry codes
	Bond length, Å	Bond angle, $^{\circ}$		
1				
N3a–H3a \cdots O2b	2.13(2)	2.98(2)	172(2)	<i>x, y, z</i>
N3b–H3d \cdots O1a	2.13(2)	2.98(2)	172(2)	<i>x, y, z</i>
O1b–H \cdots O3w	1.85(2)	2.65(2)	166(2)	<i>x, y, z</i>
O1a–H \cdots O2b	2.02(2)	2.79(2)	155(2)	<i>x, y, z</i>
N3b–H3c \cdots O2a	2.11(2)	3.00(2)	177(2)	$-x+2, -y, -z+1$
N2b–H \cdots S1a	2.67(2)	3.54(2)	174(2)	<i>x, y, z+1</i>
N2a–H \cdots S1b	2.62(2)	3.50(2)	174(2)	<i>x, y, z-1</i>
O3–H3 \cdots S1a	2.36(2)	3.176(2)	176(2)	$-x+1, -y+2, -z$
O3–H4 \cdots S1b	2.45(2)	3.246(2)	166(2)	$-x+1, -y+1, -z+1$
2				
O5–H6 \cdots O1	1.90(2)	2.736(2)	174(2)	<i>x+1, y, z</i>
O4–H4a \cdots O2	1.87(2)	2.731(2)	171(2)	<i>x+1, y, z</i>
O4–H4b \cdots O2	2.23(2)	2.933(2)	148(2)	$-x+1, -y, -z+1$
N3–H3a \cdots O6	2.24(2)	3.070(2)	166(2)	<i>x, y, z</i>
O6–H6 \cdots N2	2.65(2)	3.182(2)	127(2)	<i>x, y, z</i>
N2–H2 \cdots S1	2.76(2)	3.584 (2)	173(2)	$-x+2, -y, -z$
N3–H3b \cdots S1	2.59(2)	3.445 (2)	167(2)	$-x+2, -y+1, -z$

From an energy standpoint (Table III) this molecular pair exhibits the highest binding affinity ($E = -64 \text{ kJ mol}^{-1}$) with electrostatic interactions notably prevailing. This dominance is anticipated due to the mediation of two robust hydrogen bonds.

The remaining N3–H donor of molecule A interacts with the crystal water ($E = -27 \text{ kJ mol}^{-1}$), while the equivalent N3–H donor of molecule B serves to connect the molecular pairs from the neighbouring asymmetric units through N3b–H3c \cdots O2a interaction ($E = -30 \text{ kJ mol}^{-1}$). Employing this latter interact-

ion, the pairs of AB molecules arrange into tetramers, generating the cyclic hydrogen bonding motif R⁴(12), Fig. 3a.

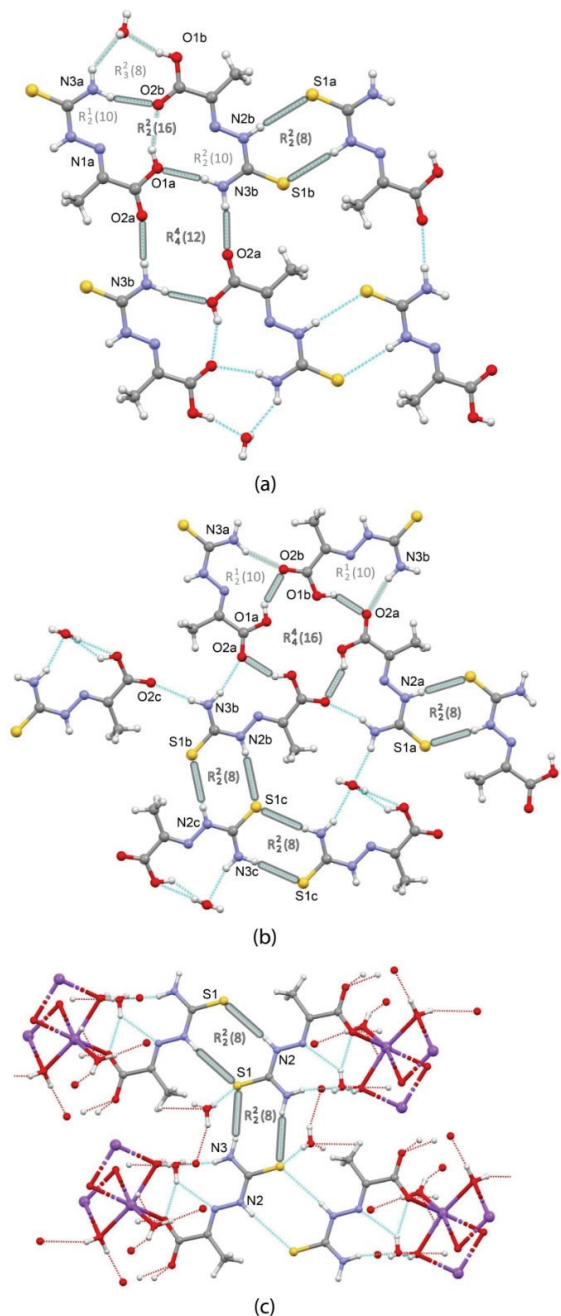


Fig. 3. Hydrogen bonding patterns in:
 a) H₂Pt·0.5H₂O (**1**),
 b) H₂Pt^Y·0.33H₂O²² and
 c) {[Na(Hpt)(H₂O)₃]·H₂O}_n (**2**).
 The ring patterns composed of one type of hydrogen bond are marked with thicker lines.

By contrast to present crystal structure **1**, the previously reported crystal form of H₂pt (CSD refcode YEBBUC, in further text H₂pt^Y) contains three symmetry independent molecules in the asymmetric unit, together with one molecule of crystal water. Though generally of the same types, the intermolecular interactions that stabilize the crystal structure of H₂pt^Y lead to notably different molecular arrangements in comparison to **1** (Fig. 3b). Firstly, all three molecules of H₂pt^Y have an equivalent orientation of the carboxylic moiety with H donor engaged in intramolecular O1–H···N1 hydrogen bond. There are two hydrogen bonds mutually connecting the independent molecules A^Y and B^Y, the O1–H···O2 and N3–H···O2, both utilizing the O2 acceptor. The ring pattern R¹₂(10) formed in this way is the only one based on N–H···O and O–H···O interactions that is common for **1** and H₂pt^Y (Fig. 3a and b). Contrary to **1**, the O1 of H₂pt^Y does not serve as an acceptor but only as an H-donor. Thus, two equivalent O1a–H···O2b and O1b–H···O2a interactions associate the pairs of independent molecules A^Y and B^Y into a tetramer, generating the ring motif R⁴₄(16) composed only of carboxylic residues (Fig. 3b). As regards the independent molecule C^Y, the both of its donor sites N1–H and O1–H are captured by the molecule of crystal water. The molecule C^Y links to the A^YB^Y-tetramer *via* the N3b–H···O2c interaction, where it provides the acceptor, Fig. 3b.

All molecules belonging to crystal structures of **1** and H₂pt^Y utilize their thiourea moieties to mutually connect by cyclic N–H···S hydrogen bonds (Fig. 3). In the structure of **1**, energy of this molecular dimer is estimated to −43 kJ mol^{−1}, mediated by N2a–H2a...S1b hydrogen bond. The R²₂(8) ring motif formed by these interactions frequently appears in thiosemicarbazide-based crystal structures in general.³² In **1** and H₂pt^Y, all molecules form the R²₂(8) motif by the pairs of N2–H···S interactions. The exception is molecule C^Y, which, besides this one, forms the additional R²₂(8) motif utilizing centrosymmetric N3–H···S interaction (Fig. 3b).

Apart from the described interactions facilitated by hydrogen bonds, which orient molecules of **1** to form a sheet approximately parallel to the (940) crystallographic plane, three energetically comparable interactions emerge that are not reliant on specific atom-to-atom contacts. These interactions occur between stacked molecules. Unlike the electrostatically dominated interactions mediated by hydrogen bonds, these stacking interactions exhibit a comparable contribution from the dispersion component (Table III). These interactions, characterized by cohesion energies ranging from −20 to −30 kJ mol^{−1}, are the driving force behind the stacking of hydrogen-bonded layers, as opposed to the O–H···S hydrogen bond with an estimated energy of −12 kJ mol^{−1}.

In the crystal structure of **2**, there are five water molecules in the coordination environment of the sodium ion and the molecule of crystal water (Fig. 2b). Therefore, the O–H···O hydrogen bonds interconnecting the water molecules

within the coordination polymer seem to dominate this crystal structure (Table II). In the dense network of O–H···O interactions, Hpt[−] participates with both oxygen acceptors of the deprotonated carboxyl group (Fig 3c). The coordination of Hpt[−] to solvated sodium cation reduces the number of direct interactions between the thiosemicarbazone units. Nevertheless, the thiourea moieties of Hpt[−] again self-associate using the N–H···S interactions to form a well-known R₂(8) ring motif (Fig 3c). Similarly to C^Y from H₂pt^Y, Hpt[−] can form two of these motifs, one by N2–H···S and the other by N3–H···S interaction. In the crystal structure of **2**, these hydrogen bonds have the role of connecting the neighboring polymeric chains.

TABLE III. Summary of relevant intermolecular interaction energies molecular pairs for **1**; X, Y are two molecules in interaction; R is the distance between molecular centroids. $E_{\text{tot}} = k_{\text{ele}}E_{\text{ele}} + k_{\text{pol}}E_{\text{pol}} + k_{\text{dis}}E_{\text{dis}} + k_{\text{rep}}E_{\text{rep}}$, where $k_{\text{ele}} = 1.057$, $k_{\text{pol}} = 0.740$, $k_{\text{dis}} = 0.871$, and $k_{\text{rep}} = 0.618$ for the B3LYP/6-31G(d,p) energy model used. Only intermolecular energies with $-E > 25 \text{ kJ mol}^{-1}$ are listed

X···Y	Symmetry operation on Y	Interactions involved	R / Å	E / kJ mol ^{−1}				
				E_{ele}	E_{pol}	E_{dis}	E_{rep}	E_{tot}
A···B	x, y, z	N3a–H3a···O2b	5.82	−80.59	−20.57	−20.44	87.91	−63.92
		O1a···H3d–N3b						
		O1a–H1a···O2b						
A···B	$x, y, z−1$	N2a–H2a···S1b	6.51	−56.96	−9.80	−19.57	66.65	−43.35
B···H ₂ O	x, y, z	O1b–H1b···O3	6.17	−62.64	−15.68	−5.59	64.64	−42.77
B···B	$−x+1, −y+1, −z+1$	Stacking	4.42	−14.21	−2.35	−27.30	10.85	−33.84
B···A	$−x+2, −y, −z+1$	N3b–H3c···O2a	8.89	−35.70	−6.52	−8.85	32.39	−30.27
A...A	$−x+1, −y+1, −z$	stacking	5.20	−18.14	−5.46	−23.67	24.59	−28.64
A···H ₂ O	x, y, z	N3a–H2b···O3	5.21	−28.07	−5.26	−4.70	16.82	−27.27
A···B	$−x+2, −y+1, −z+1$	Offset stacking	5.88	−14.47	−3.60	−13.63	7.90	−24.96

Apart from the extensive hydrogen bonding network and persistent R₂(8) motif formed by thiourea moieties, the common feature of three crystal structures is their layered three-dimensional crystal packing. Fig. 4 displays 3D structure

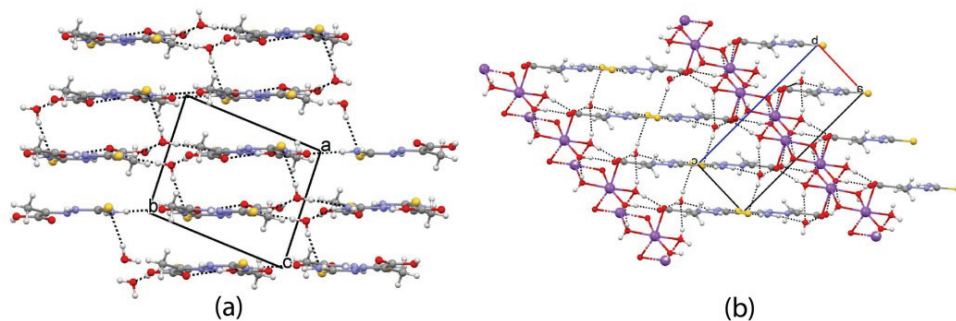


Fig. 4. Packing diagram of (a) **1** and (b) **2**.

for compounds **1** and **2**. The layered structure is not surprising considering the planar form of the pyruvate thiosemicarbazone unit and the coplanarity of its hydrogen bonding sites, with the exception of methyl H atoms. The distance between two successive layers of ligands is 3.46, 3.34, and 3.64 Å in **1**, $\text{H}_2\text{Pt}^{\text{Y}}\cdot 0.33\text{H}_2\text{O}$, and **2**. The layers are interconnected by the hydrogen bonds involving water molecules (Fig. 4).

CONCLUSION

By exploring novel synthetic routes for thiosemicarbazones with keto acids, and their complex salts with alkali and earth-alkali metals, we were able to isolate novel crystal form of pyruvic acid thiosemicarbazone, dissimilar to the previously reported crystal structure of this ligand. The sodium pyruvate thiosemicarbazone was also obtained in the form of a single crystal. Here presented crystal structure of the sodium complex is one of very rare crystal structures of alkali and earth-alkali complexes of thiosemicarbazone ligands in general.

The thiosemicarbazone molecules display rather consistent planar form, due to overall electron delocalization. The allowed rotation of carboxylic fragment and its deprotonation particularly affect the hydrogen bonding pattern. A detailed comparison has been made regarding the remarkable diversity of hydrogen bonding in novel and previously reported crystal form of pyruvic acid thiosemicarbazone. The comparison to sodium salt is also performed. Among the number of structural patterns formed by N–H…O, O–H…O and N–H…S interactions the cyclic hydrogen bonding motif involving thioureido moieties is the only one common for three crystal structures.

SUPPLEMENTARY MATERIAL

Additional data and information are available electronically at the pages of journal website: <https://www.shd-pub.org.rs/index.php/JSCS/article/view/12896>, or from the corresponding author on request.

Acknowledgement. This work was supported by the Ministry of Science, Technological Development and Innovation of the Republic of Serbia (Grant Nos. 451-03-66/2024-03/200017; 451-03-66/2024-03/200125 and 451-03-65/2024-03/200125).

И З В О Д

НОВА КРИСТАЛНА ФОРМА ТИОСЕМИКАРБАЗОНА ПИРОГРОЖЂАНЕ КИСЕЛИНЕ И
ЊЕГОВЕ СОЛИ НАТРИЈУМА

СВЕТЛАНА К. БЕЛОШЕВИЋ¹, СЛАЂАНА Б. НОВАКОВИЋ², МАРКО В. РОДИЋ³, ВУКАДИН М. ЛЕОВАЦ³,
ЉИЉАНА С. ВОЈИНОВИЋ-ЈЕШИЋ³, ГОРАН А. БОГДАНОВИЋ² И МИРЈАНА М. РАДАНОВИЋ³

¹Факултет техничких наука, Универзитет у Приштини, Књаза Милоша 7, 38220 Косовска
Митровица, ²Институција за нуклеарне науке „Винча“ – Институција од националног значаја за
Републику Србију, Универзитет у Београду, Лабораторија за теоријску физику и физику кондензоване
материје, 11001 Београд и ³Универзитет у Новом Саду, Природно-математички факултет,
Трг Д. Обрадовића 3, 21000 Нови Сад

Детаљно је анализирана реакција тиосемикарбазида и натријум-пирувата, као и нова кристална форма добијеног тиосемикарбазона пирогрожђане киселине (H_2pt) и његове соли натријума. Једињења су охарактерисана IR спектроскопијом, елементалном анализом, кондуктометријом и рентгенском структурном анализом. Дата је упоредна анализа кристалних структура нових једињења, и њихова својства су упоређена са претходно описаним комплексима који садрже H_2pt . Две нове кристалне структуре показују значајне разлике у обрасцима водоничних веза, како међусобно тако и у поређењу са претходно описаном кристалном формом H_2pt . Све кристалне структуре су стабилизоване разгранатом мрежом N–H···O, O–H···O и N–H···S водоничних веза. Циклични мотив водоничних веза који укључује тиоамидне фрагменте лиганда је једини структурни мотив који се понавља у три упоређене кристалне структуре.

(Примљено 17. априла, ревидирано 26. априла, прихваћено 8. маја 2024)

REFERENCES

1. A. Gómez Quiroga, C. Navarro Ranninger, *Coord. Chem. Rev.* **248** (2004) 119
(<https://doi.org/10.1016/j.cct.2003.11.004>)
2. G. L. Parrilha, R. G. dos Santos, H. Beraldo, *Coord. Chem. Rev.* **458** (2022) 214418
(<https://doi.org/10.1016/j.ccr.2022.214418>)
3. H. Beraldo, D. Gambino, *Mini-Rev. Med. Chem.* **4** (2004) 31
(<https://doi.org/10.2174/1389557043487484>)
4. D.S. Kalinowski D. R.Richardson, *Pharmacol. Rev.* **57** (2005) 547
(<https://doi.org/10.1124/pr.57.4.2>)
5. A. Mushtaq, P. Wu, M. M. Naseer, *Pharmacol. Ther.* **254** (2024) 108579
(<https://doi.org/10.1016/j.pharmthera.2023.108579>)
6. O. Özbek, C. Berkel, *Polyhedron* **238** (2023) 116426
(<https://doi.org/10.1016/j.poly.2023.116426>)
7. L. Feng, W. Shi, J. Ma, Y. Chen, F. Kui, Y. Hui, Z. Xie, *Sens. Actuators, B* **237** (2016)
563 (<https://doi.org/10.1016/j.snb.2016.06.129>)
8. R. Basri, N. Ahmed, M. Khalid, M. Usman Khan, M. Abdullah, A. Syed, A. M. Elgorban,
S. S.Al-Rejaie, A. A. C. Braga, Z. Shafiq, *Sci. Rep.* **12** (2022) 4927
(<https://doi.org/10.1038/s41598-022-08860-3>)
9. E. Khamis, M. A. Ameer, N. M. AlAndis, G. Al-Senani, *Corrosion* **56** (2000) 127
(<https://doi.org/10.5006/1.3280528>)
10. Q. A. Jawad, D. S. Zinad, R. D. Salim,A. A Al-Amiry,T. S. Gaaz,M. S. Takriff, A. A. H.
Kadhum, *Coatings* **9** (2019) 729 (<https://doi.org/10.3390/coatings9110729>)
11. T. S. Lobana, R. Sharma, G. Bawa, S. Khanna, *Coord. Chem. Rev.* **253** (2009) 977
(<https://doi.org/10.1016/j.ccr.2008.07.004>)

12. J.S. Casas, M.S. Garcia-Tasende, J. Sordo, *Coord. Chem. Rev.* **209** (2000) 197 ([https://doi.org/10.1016/S0010-8545\(00\)00363-5](https://doi.org/10.1016/S0010-8545(00)00363-5))
13. D. X. West, S. B. Padhye, P. B. Sonawane, *Struct. Bond.* **76** (1991) 1 (https://doi.org/10.1007/3-540-53499-7_1)
14. J. Haribabu, K. Jeyalakshmi, Y. Arun, N. S. P. Bhuvanesh, P. T. Perumal, R. Karvembu, *RSC Adv.* **5** (2015) 46031 (<https://doi.org/10.1039/C5RA04498G>)
15. L. R. P. de Siqueira, P. A. T. de Moraes Gomes, L. P. de Lima Ferreira, M. J. B. de Melo Rêgo, A. C. L. Leite, *Eur. J. Med. Chem.* **170** (2019) 237 (<https://doi.org/10.1016/j.ejmech.2019.03.024>)
16. H. Dong, J. Liu, X. Liu, Y. Yu, S. Cao, *Bioorg. Chem.* **75** (2017) 106 (<https://doi.org/10.1016/j.bioorg.2017.07.002>)
17. J. Wiecek, V. Dokorou, Z. Ciunik, D. Kovala-Demertzi, *Polyhedron* **28** (2009) 3298 (<https://doi.org/10.1016/j.poly.2009.05.012>)
18. M. B. Ferrari, F. Bisceglie, G. Pelosi, P. Tarasconi, R. Albertini, S. Pinelli, *J. Inorg. Bioch.* **87** (2001) 137 ([https://doi.org/10.1016/S0162-0134\(01\)00321-X](https://doi.org/10.1016/S0162-0134(01)00321-X))
19. I. Graur, T. Bespalova, V. Graur, V. Tsapkov, O. Garbuz, E. Melnic, P. Bourosh, A. Gulea, *J. Chem. Res.* **47** (2023) 6 (<https://doi.org/10.1177/17475198231216422>)
20. T.A. Yousef, G.A. El-Reash, O.A. El-Gammal, R. A. Bedier, *J Mol Struct.* **1035** (2013) 307 (<https://doi.org/10.1016/j.molstruc.2012.10.058>)
21. N. I. Dodoff, D. Kovala-Demertzi, M. Kubiak, J. Kuduk-Jaworska, A. Kochel, G. A. Gorneva, *Z. Naturforsch., B* **61** (2006) 1110 (<https://doi.org/10.1515/znb-2006-0909>)
22. B. Ya. Antosyak, V. N. Biyushkin, L. F. Chapurina, T. I. Malinovsky, *Dokl. Akad. Nauk SSSR* **327** (1992) 219
23. C. R. Groom, I. J. Bruno, M. P. Lightfoot, S. C. Ward, *Acta Cryst., B* **72** (2016) 171. (<https://dx.doi.org/10.1107/S2052520616003954>)
24. Rigaku Oxford Diffraction, *CrysAlisPro Software system, version 1.171.42*, Rigaku Corporation, Wroclaw, 2022
25. G. M. Sheldrick, *Acta Cryst., C* **71** (2015) 3 (<https://doi.org/10.1107/S2053229614024218>)
26. C. F. Macrae, I. Sovago, S. J. Cottrell, P. T. Galek, P. McCabe, E. Pidcock, P. A. Wood, *J. Appl. Cryst.* **53** (2020) 226 (<https://doi.org/10.1107/S1600576719014092>)
27. P. R. Spackman, M. J. Turner, J. J. McKinnon, S. K. Wolff, D. J. Grimwood, D. Jayatilaka, M. A. Spackman, *J. Appl. Cryst.* **54** (2021) 1006 (<https://doi.org/10.1107/S1600576721002910>)
28. G. L. Sawhney, J. S. Baijal, S. Chandra, K. B. Pandeya, *Acta Chim. Acad. Sci. Hung.* **108** (1981) 325
29. M. D. Timken, S. R. Wilson, D. N. Hendrickson, *Inorg. Chem.* **24** (1985) 3450 (<https://dx.doi.org/10.1021/ic00215a030>)
30. M. Belicchi Ferrari, Giovanna Gasparri Fava, G. Pelosi, P. Tarasconi, *Polyhedron* **19** (2000) 1895 ([https://doi.org/10.1016/S0277-5387\(00\)00454-X](https://doi.org/10.1016/S0277-5387(00)00454-X))
31. M C Etter, J C MacDonald, J Bernstein, *Acta Cryst., B* **46** (1990) 256 (<https://doi.org/10.1107/S0108768189012929>)
32. S. B. Novaković, B. Fraisse, G. A. Bogdanović, A. Spasojević-de Biré, *Cryst. Growth Des.* **17** (2007) 2993 (<https://doi.org/10.1021/cg060497>).



SUPPLEMENTARY MATERIAL TO
**Introducing a novel crystal form of pyruvic acid
thiosemicarbazone and its sodium salt**

SVETLANA K. BELOŠEVIĆ¹, SLAĐANA B. NOVAKOVIĆ^{2*}, MARKO V. RODIĆ³,
VUKADIN M. LEOVAC³, LJILJANA S. VOJINOVIĆ-JEŠIĆ³, GORAN A.
BOGDANOVIĆ² and MIRJANA M. RADANOVIĆ^{3**}

¹Faculty of Technical Sciences, University of Priština, Knjaza Miloša 7, 38220 Kosovska Mitrovica, Serbia, ²"Vinča" Institute of Nuclear Sciences - National Institute of the Republic of Serbia, University of Belgrade, P. O. Box 522, 11001 Belgrade, Serbia and ³University of Novi Sad, Faculty of Sciences, Trg Dositeja Obradovića 3, 21000, Novi Sad

J. Serb. Chem. Soc. 89 (7–8) (2024) 1011–1023

ANALYTICAL AND SPECTRAL DATA

H₂pt·0.5H₂O (1)

Anal. Calc. for C₄H₇N₃O₂S·0.5H₂O (H₂pt·0.5H₂O): C, 28.23; H, 4.71; N, 24.71; S, 18.82 %. Found: C, 28.52; H, 4.60; N, 24.58; S, 18.74 %. M. p. 216 °C. Selected IR bands (cm⁻¹): 3414_m, v_a(H₂O); 3293_m, 3182_m, v_s(NH₂/NH); 1727_s, 1699_{vs}, v(CO) of COOH; 1614_{vs}, v(CN); 802_m, v(CS).

Sodium pyruvate thiosemicarbazone {[Na(Hpt)(H₂O)₃]·H₂O}_n (2)

Anal. Calc. for NaC₄H₈N₃O₃S·3H₂O: C, 20.70; H, 6.03; N, 18.10 %. Found: C, 20.55; H, 5.89; N, 18.01 %. M. p. 208 °C; λ_M [Scm²mol⁻¹]: 87 (H₂O), 98 (MeOH). Selected IR bands (cm⁻¹): 3458_m v(H₂O); 3366_m, 3315_m, 3141_m, v(NH₂/NH); 1622_m, v(CN); 1571_{vs}, v_a(CO₂⁻); 1381_{vs}, v_s(CO₂⁻); 789_m, v(CS).

Corresponding authors. E-mail: ()snovak@vin.bg.ac.rs; (**)mirjana.lalovic@dh.uns.ac.rs

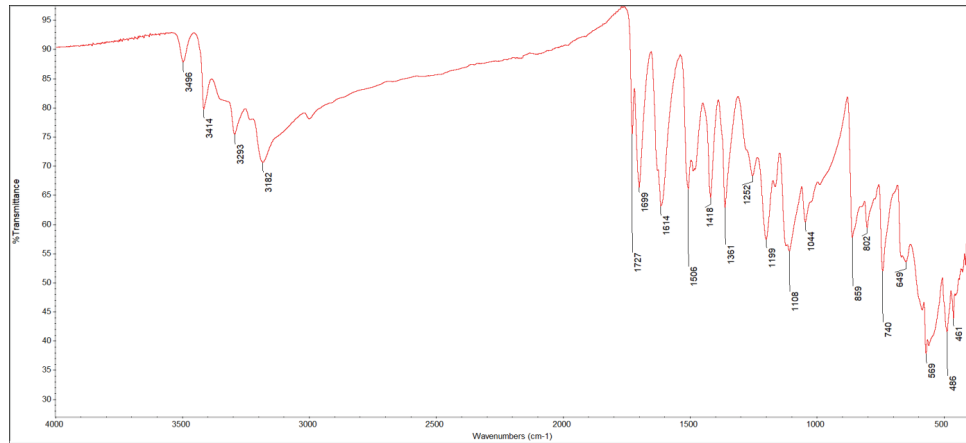


Fig. S-1. IR spectra of compound 1.

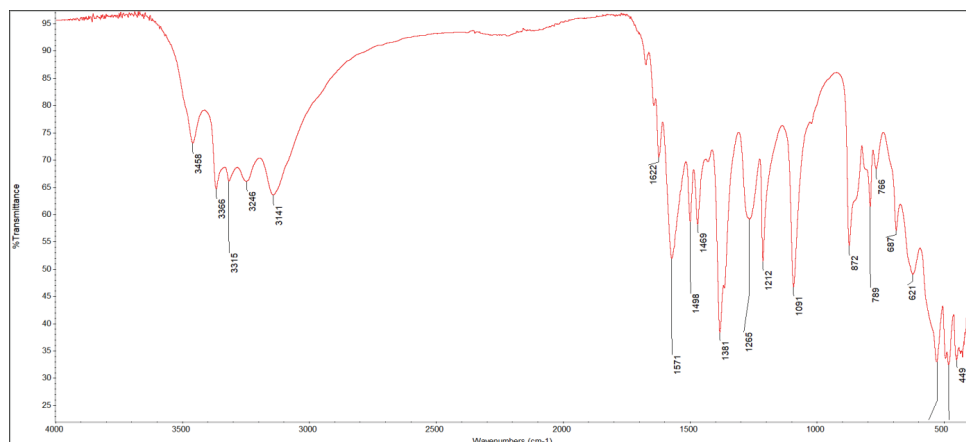


Fig. S-2. IR spectra of compound 2.

TABLE S-I. Crystallographic data

	1	2
Empirical formula	C ₈ H ₁₆ N ₆ O ₅ S ₂	C ₄ H ₁₄ N ₃ NaO ₆ S
Formula weight	340.39	255.23
Temperature (K)	293(2)	293(2)
Wavelength (Å)	0.71073	0.71073
Crystal system	Triclinic	Triclinic
Space group	<i>P</i> 	<i>P</i> 
Unit cell dimensions		
<i>a</i> (Å)	7.3991(6)	5.2792(5)
<i>b</i> (Å)	8.8745(5)	8.5201(7)
<i>c</i> (Å)	12.2109(7)	13.1342(10)
α (°)	75.274(5)	86.131(6)
β (°)	79.180(6)	87.338(7)
γ (°)	82.915(6)	74.253(8)
<i>V</i> (Å ³)	759.27(9)	567.06(9)
<i>Z</i>	2	2
<i>D</i> _{calc} (Mg/m ³)	1.489	1.495
μ (mm ⁻¹)	0.381	0.337
θ range for data collection (°)	2.6–29.1	2.5–29.1
Reflections collected	13178	4043
Independent reflections, <i>R</i> _{int}	3584, 0.0215	2557, 0.0162
Data / restraints/parameters	3584/10/225	2557/0/181
Goodness-of-fit	1.028	1.040
Final <i>R</i> ₁ / <i>wR</i> ₂ indices [<i>I</i> > 2 σ (<i>I</i>)]	0.035/0.089	0.034/0.083
Final <i>R</i> ₁ / <i>wR</i> ₂ indices (all data)	0.046/0.096	0.044/0.089
Largest diff. peak and hole (e Å ⁻³)	0.27/−0.24	0.22/−0.23



New pyrene and fluorene-based π -conjugated Schiff bases: Theoretical and experimental investigation of optical properties

YUNUSCAN SİVRİKAYA¹, HANDAN CAN SAKARYA^{2*}, GÖKHAN KILIÇ³,
SULTAN FUNDA EKTİ⁴ and MERVE YANDIMOĞLU²

¹*Graduate School of Natural and Applied Sciences, Eskişehir Osmangazi University,*

²*Department of Chemistry, Faculty of Science, Eskişehir Osmangazi*

University, Eskişehir, Turkey, ³Department of Physics, Faculty of Science, Eskişehir Osmangazi University, Eskişehir, Turkey and ⁴Department of Chemistry, Faculty of Science, Eskişehir Technical University, Eskişehir, Turkey

(Received 31 August, revised 16 December, accepted 20 December 2023)

Abstract: The new Schiff bases with D- π -A system were synthesized by the reaction of polycyclic aldehydes and substituted benzothiazoles. The structures of the synthesized Schiff bases (**7a** and **9a**) were determined by FT-IR, ¹H-NMR, ¹³C-NMR, ESI-Mass and elemental analyses. The optical properties of the new compounds were investigated and the optical band gaps (E_g) were calculated by the Tauc method using the UV–Vis absorption spectra. Density functional theory (DFT/B3LYP/6-31G(d,p)) calculations were conducted to get more insight on the structural and electronic properties of novel Schiff bases. The optimized molecular geometry, UV–Vis spectroscopic parameters and HOMO–LUMO energies were examined and the calculated results were compared with experimental data.

Keywords: imine; UV–Vis; optical bandgap; Tauc method; DFT.

INTRODUCTION

Schiff bases are compounds that are formed by the nucleophilic addition reaction of aldehydes or ketones and amines and contain the $-\text{CH}=\text{N}-$ group in their structure. Schiff base was firstly synthesized by the chemist Hugo Schiff in Germany in 1894.¹ They are stable in the presence of aryl groups attached to imine group of the Schiff base.² It is known that Schiff base complexes containing aromatic rings are used in many different fields today. Since the imine group has strong bonds, Schiff bases are effectively used in the development of chemo-sensors.³ At the same time, their complexes are versatile compounds used in qualitative and quantitative analyses, dyestuff, pharmaceutical and plastics indus-

* Corresponding author. E-mail: hsakarya@ogu.edu.tr
<https://doi.org/10.2298/JSC230815097S>

tries, synthesis of bioactive compounds, cycloaddition reactions and nucleophilic addition with organometallic reagents.^{4–6} Schiff bases are used in pharmacological chemistry, pharmaceutical chemistry and especially in antibacterial,⁷ anti-fungal⁸ and antitumor⁹ activity applications. Schiff bases have been investigated in recent years as functional material interesting optoelectronic properties due to their easily prepared and purified π -conjugated organic compounds.¹⁰ New conjugated organic compounds with favorable optoelectronic properties offer significant advantages over carbon analogs as they can be easily prepared, purified¹¹ and synthesized without expensive catalysts. In previous studies, Schiff bases were used as optical molecular switches,¹² luminescence, pH indicators,¹³ electrochromic and photochromic materials.¹⁴ Schiff bases, which are iso electronic with their vinyl bond, are a π -conjugated organic semiconductor material and form a kind of hole-transporting material.¹⁵ The azomethine nitrogen of the Schiff base can be protonated with unshared electron pairs and organic and inorganic acids. In this way, the optical and electrooptical properties of azomethine compounds can be adjusted.¹⁶ Organic materials play very important role in the field of nonlinear optics due to their delocalized electronic structure and are usually formed by bonding electron-donating and withdrawing groups from a π -electronic bridge with a large D- π -A conjugated system. The electron push-pull system helps to improve the molecular polarity so that larger nonlinear optical (NLO) materials can be obtained.¹⁷ The electron-donating part in this system usually has been chosen as aromatic and heteroaromatic rings. These rings are great components for making tertiary NLO materials. In recent years, many studies have been conducted on the development of conjugated organic compounds.¹⁸ Among π -conjugated organic compounds, especially Schiff base derivatives have emerged as promising compounds for NLO materials due to the π -electron bridge in carbon-nitrogen double bonds.¹⁹ These compounds have very mobile clouds of π -electrons in the large molecular structures and can be easily polarized.²⁰

In this study, we synthesized two new Schiff bases and their structures have been elucidated by various techniques such as $^1\text{H-NMR}$, $^{13}\text{C-NMR}$, ESI-Mass, and elemental analyses. The optical properties of these compounds have been investigated by UV-Vis spectroscopy. The band gap energies of the compounds have been determined by the UV-Vis absorption spectra using the Tauc method. Calculations of density functional theory (DFT) were performed using the Gaussian 09 program to investigate the optical properties of the compounds, and compare them for experimental data. DFT has been employed in theoretical studies to determine the vibrational frequencies, geometrical shapes and electrochemical characteristics of the molecule. In Schiff bases, the basic functional set of B3LYP/6-31G(d,p) was mostly preferred,^{21,22} to explore the nature and type of UV-Vis shifts, a modified computation study time-dependent DFT was done.²³

EXPERIMENTAL

General information

All chemicals and solvents were purchased from Sigma Aldrich. 2-Amino-4-methyl benzothiazole (97 %), pyrene-1-carbaldehyde (98 %), fluorene-2-carbaldehyde (99 %) and hydrochloric acid (99.7 %) were used without further purification. The organic solvents (ethanol (EtOH, 99.8 %), dichloromethane (DCM, 99 %) and petroleum ether (90 %)) were used of HPLC grade or purified by a standard procedure. Melting points of synthesized compounds were determined by the Gallenkamp melting point apparatus using capillary tubes. FT-IR and UV-Vis absorption spectroscopy were taken at Eskisehir Osmangazi University Inorganic Chemistry Research Laboratory. FT-IR spectra were recorded with Bruker FT-IR spectrometer in the range of 4000–400 cm⁻¹ wavelengths. UV-Vis absorption spectra were recorded with a Shimadzu UV-2600 spectrometer and the optical band gap was determined using Tauc methods and evaluated using UV Probe Software. ¹H-NMR (500 MHz, DMSO-*d*₆, TMS internal standard) and ¹³C-NMR (125 MHz, DMSO-*d*₆, TMS internal standard) spectroscopic analyses were carried out on using Jeol ECZ500R (11.75 Tesla) NMR equipment at Eskisehir Osmangazi University Central Research Laboratory Application and Research Center (ARUM). ESI-Mass and elemental analyses were recorded by Waters Alliance HPLC, 2Q micromass spectrometer, and Leco CHNS 932 elemental analyzer, respectively, at Ankara University Central Research Laboratory. Thin layer chromatography (TLC) plates were purchased as ready-coated from Merck and used to control the reactions. With the help of the hybrid functional (B3LYP) and a specific basis set of 6-31G(d,p), a Gaussian 09 program was successfully operated. For extended electrochemical analyses of synthesized moieties, the energy gaps between their HOMO and LUMO states were determined using the readily available tool Gauss View 6.0.

*General method for 4-methyl-N-(pyren-1-yl-methylene)benzo[d]thiazol-2-amine (**7a**) and N-(9H-fluoren-3-yl-methylene)-4-methylbenzo[d]thiazol-2-amine (**9a**)*

A solution of 4-methyl-2-amino benzothiazole (1 eq.) in ethyl alcohol was added to appropriate aldehyde (0.8 eq), 2–3 drops of 5 % HCl solution were added to the reaction medium and refluxed in a nitrogen atmosphere at 75 °C for 4 h. The reaction was terminated with TLC control (1:10 petroleum ether/DCM). After cooling the solution at room temperature overnight, the precipitates were filtered and extracted with DCM and then recrystallized from ethyl alcohol. **7a** was obtained as orange crystals and **9a** as yellow crystals. The protocol followed for the synthesis of the **7a** and **9a** Schiff bases and the numbering of the protons in the molecule is summarized in Scheme S-1 of the Supplementary material to this paper.

Analytical and spectral data of the synthesized compounds are given in Supplementary material.

RESULTS AND DISCUSSION

Chemistry

In the FT-IR spectra of compounds **7a** and **9a**, peaks at 3400 cm⁻¹ belonging to the amino group of 4-methyl-2-amino benzothiazole, and at 1720 cm⁻¹ belonging to the C=O group of aldehyde have not been observed. The imine group of compound **7a** is marked at 1593 cm⁻¹. The other peaks have been observed at 3038 cm⁻¹ (for aromatic C–H), 2965–2918 cm⁻¹ (for aliphatic C–H), 1576, 1537 and 1478 cm⁻¹ (for C=C peaks). Aromatic C–H, aliphatic C–H, aro-

matic C=C peaks have been observed at 3038, 2965–2918, 1576, 1537 and 1478 cm⁻¹, respectively (Fig. S-1 of the Supplementary material). The FT-IR spectrum of compound **9a** showed similar signals to the FT-IR spectrum of compound **7a** (Fig. S-3 of the Supplementary material).

According to ¹H-NMR spectrum compound **7a**, signals of 3 non-identical protons of the benzothiazole ring and 9 protons of the pyrene ring have been observed in the δ range of 8.15–9.28 ppm. Since the π -electrons in the pyrene ring of compound **7a** are conjugated with the imine group and are a donor group, the ring electrons are resonantly directed towards the benzothiazole ring (Fig. 1).

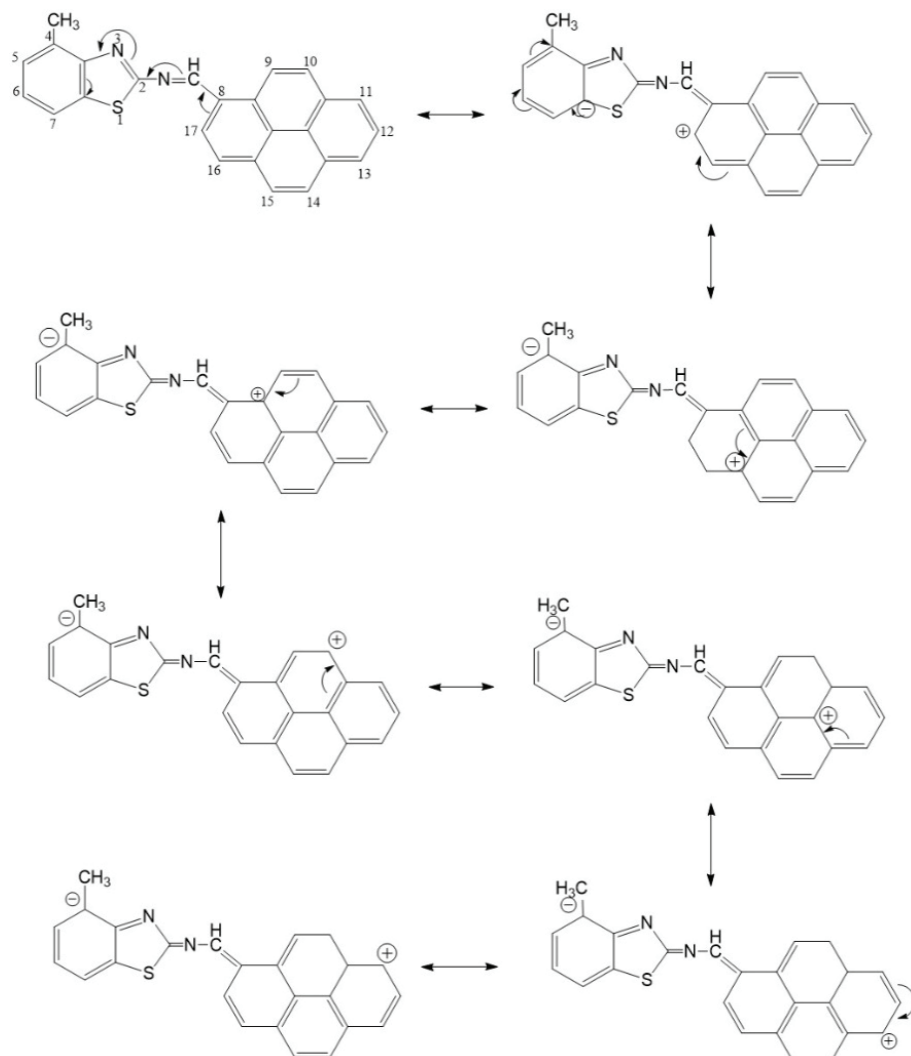


Fig. 1. Resonance forms of compound **7a**.

Therefore, considering the resonance structures of the compound **7a**, the protons in the pyrene ring have been observed, as expected, in the low field compared to the protons in the benzothiazole ring. As seen in Fig. S-2 of the Supplementary material, since the electron density around the H17 and H10 protons decreases with resonance, these protons resonate in the lower field due to the distance to the imine group ($-\text{CH}=\text{N}-$) compared to the other protons of pyrene ring. One proton doublets at δ 9.28 and 8.84 ppm have been observed as H17 and H10 protons, respectively. Other pyrene protons are marked at δ 8.44 ppm (*m*, 5H, H11, H16, H14, H15 and H9). One doublet at δ 8.28 ppm and one triplet at δ 8.15 ppm were observed belonging to H13 and H12 protons, respectively. On the other hand, the H5 and H7 protons of the acceptor benzothiazole ring are labeled as doublet at δ 7.31 ppm. Generally, the Schiff base imine proton resonates at δ 8–9 ppm, while the resonance delocalization of the π -electrons from the pyrene ring increases the polarization of the imine bond, and therefore the imine signal resonates at δ 9.98 ppm. In the ^{13}C -NMR of compound **7a**, 18 signals were observed instead of 23 signals of carbons in the aromatic region due to the identical carbons in the pyrene ring. In the ^1H -NMR spectrum of compound **9a**, it has been observed that the protons in the fluorene ring resonate at the higher field than substance **7a**, depending on the resonance structure (Fig. 2).

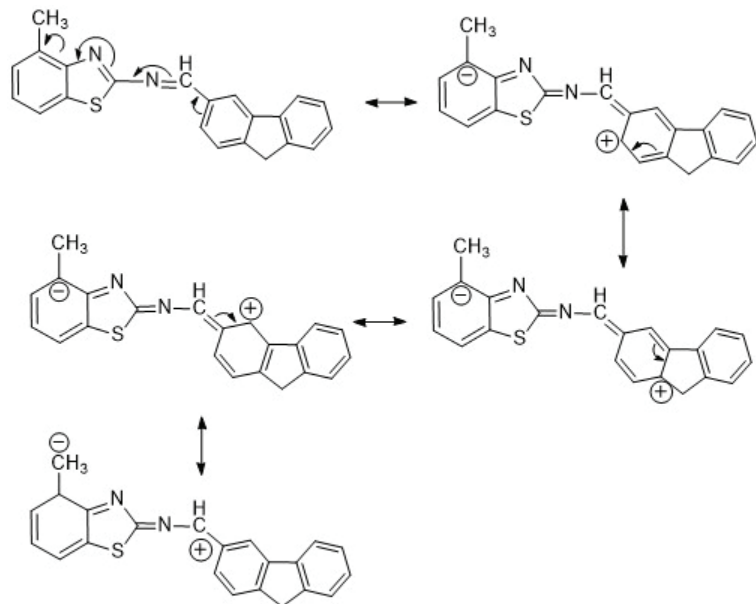


Fig. 2. Resonance forms of compound **9a**.

The ^1H -NMR of compound **9a** shows similar properties to compound **7a**. However, the increase in electron density around the protons in the fluorine ring

of compound **9a** lead these protons to resonate in the higher field, so the fluorene protons in compound **9a** resonate in higher field than the protons in the pyrene ring of compound **7a**. Therefore, the signal of the imine proton has been observed in the higher field at 9.14 ppm (Fig. S-4 of the Supplementary material).

In the ESI-MS spectrum of compound **7a**, the signal at m/z 377.68 (M^+) is the peak of the molecular mass; m/z 165.15 and 245.48 are the signals of molecular masses of 4-methyl-2-amino benzothiazole and pyrenecarbaldehyde, respectively. M^++1 , M^++2 peaks have been observed at m/z 378.71 and 379.77. In the ESI-MS spectrum of **9a**, the main peak of the compound has been observed at m/z 341.63 (M^+). The peaks at m/z 342.63 and 343.65 belong to M^++1 and M^++2 , respectively. The peaks of fluorene and benzothiazole ions have been observed at m/z 209 and 165.1, respectively.

The UV–Vis spectrum of material provides important structural information and a good way to study the properties of semiconductors, as it involves boosting an electron from the ground state from σ - and π -orbitals to the higher energy state.²⁴ It also gives information about the optical bandgap energy of the material. The forbidden energy gap of insulators is higher than 4 eV, whereas for semiconductors it is less than 3 eV.²⁵ In this study, solutions of Schiff bases **7a** and **9a** in different solvents, *n*-hexane, THF, DCM, DMF and DMSO have been prepared at 10^{-5} M concentrations and absorbance spectra has been recorded to clarify their optical properties. Two types of transitions, $n-\pi^*$ and $\pi-\pi^*$, belonging to the imine group ($-\text{CH}=\text{N}-$), have been observed, as expected, in the UV–Vis spectrum of Schiff bases **7a** and **9a** (Fig. 3).

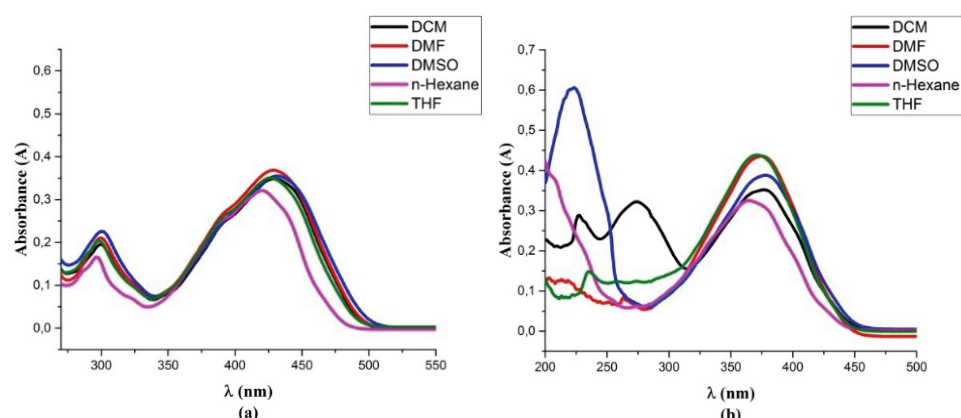


Fig. 3. a) UV–Vis spectra of compound **9a** in various solvents (1×10^{-5} M).

The short wavelength band results from electron conjugation on the backbone molecule and is known as the $\pi-\pi^*$ electronic transition. Long wavelength transitions are known as $n-\pi^*$ transitions as shown in Table I. This transition

occurs as a result of solute-solvent interaction *via* lone electron pair for compounds **7a** and **9a** (Figs. S-5 and S-6 of the Supplementary material).

TABLE I. The λ_{\max} values (nm) of the n– π^* and π – π^* transitions of compounds **7a** and **9a** in different solvents

Compound	Transition type	<i>n</i> -Hexane	DCM	THF	DMF	DMSO
7a	n– π^*	420	429	426	429	431
	π – π^*	297	300	299	301	302
9a	n– π^*	363	376	371	374	379
	π – π^*	209	274	234	265	225

In the UV–Vis spectrum of compounds **7a** and **9a**, π – π^* and n– π^* transitions were observed to be red-shifted by solvent effect in five solvents with different polarities: *n*-hexane, THF, DCM, DMF and DMSO. This situation, as seen in Figs. 1 and 2, is due to the increased stability of the excited state by the conjugation effect. For the increase in the polarity of the solvent, the absorption band of the π – π^* and n– π^* transitions of compound **7a** was observed in the range of 297–302 nm and 420–431 nm, respectively. This situation is explained by increased stability of the excited state caused by conjugation, decrease of the energy of the excited state especially due to interaction with polar solvents, and a red shift of the π – π^* transition as well as n– π^* transition absorption band since the ground state energy does not change. Similarly, π – π^* and n– π^* transitions of compound **9a** are observed at 209–274 nm and 363–379 nm, respectively. With increasing solvent polarity, the n– π^* transition of the imine of compound **9a** displays a red shift. However, a shift to a shorter wavelength has been observed due to decreasing conjugation in compound **9a** compared to compound **7a**. This red shift and high absorption in the UV–Vis regions is a desirable property in organic electronics.

Calculation of optical bandgap

Optical bandgaps in synthesized materials were calculated by the Tauc method.²⁶ Tauc describes the absorption coefficient dependence on photon energy as:

$$\alpha h\nu = A(h\nu - E_g)^n \quad (1)$$

Here, A is a constant, $h\nu$ is the photon energy, E_g is the optical bandgap. The value of n takes the value of 1/2 for direct transitions and 2 for indirect transitions. For direct transitions, the equation is given as:

$$\alpha n_0 h\nu \approx (h\nu - E_0)^{1/2} \quad (2)$$

This approach is valid for direct transitions. Here, $n = 1/2$ corresponds to the allowed direct transition. For indirect transitions, the equation is given as:

$$\alpha n_0 h\nu \approx (h\nu - E_0)^2 \quad (3)$$

Here, $n = 2$ corresponds to possible allowed indirect transitions. Indirect transitions are generally valid for amorphous structures. Photon energies belonging to the wavelengths corresponding to the linear part of the curve in the absorption spectrum were calculated with the help of the $E = h\nu$ equation, and using these values, $(\alpha h\nu)^2 - h\nu$ Tauc curves were drawn for each Schiff base separately for the direct allowed transition. The direct transition optical bandgaps of the Schiff bases is calculated from the value $(\alpha h\nu)^2 = 0$ of the line passing through the maximum number of points on the absorption edge of these curves. For a direct bandgap semiconductor, the optical bandgap is equal to the electronic bandgap. The graphs of $(\alpha h\nu)^2 - h\nu$ of novel benzothiazole derived Schiff bases **7a** and **9a** are given in Figs. 4 and 5.

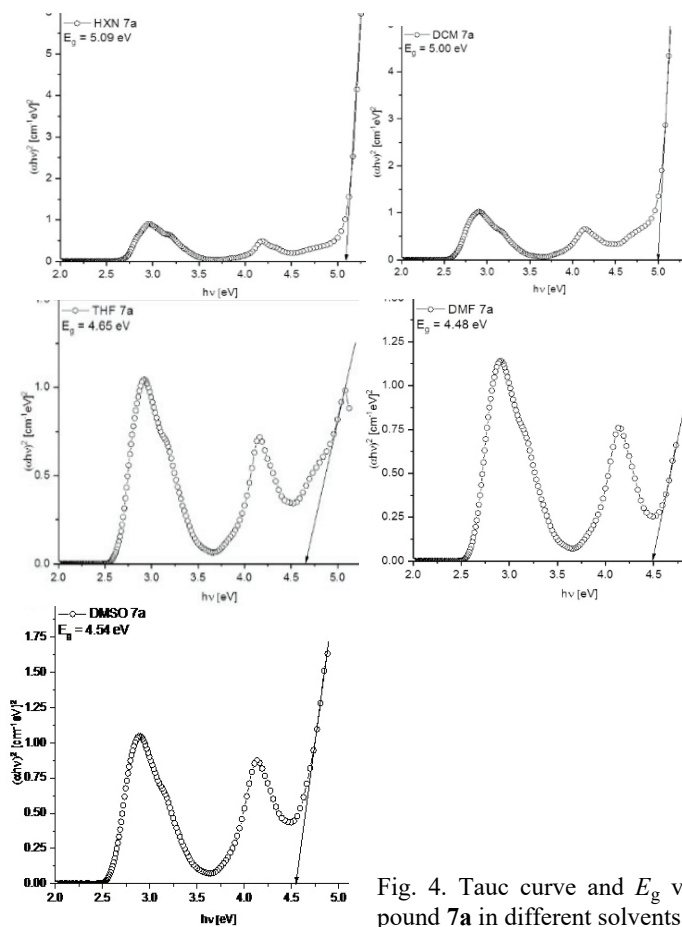


Fig. 4. Tauc curve and E_g values of compound **7a** in different solvents.

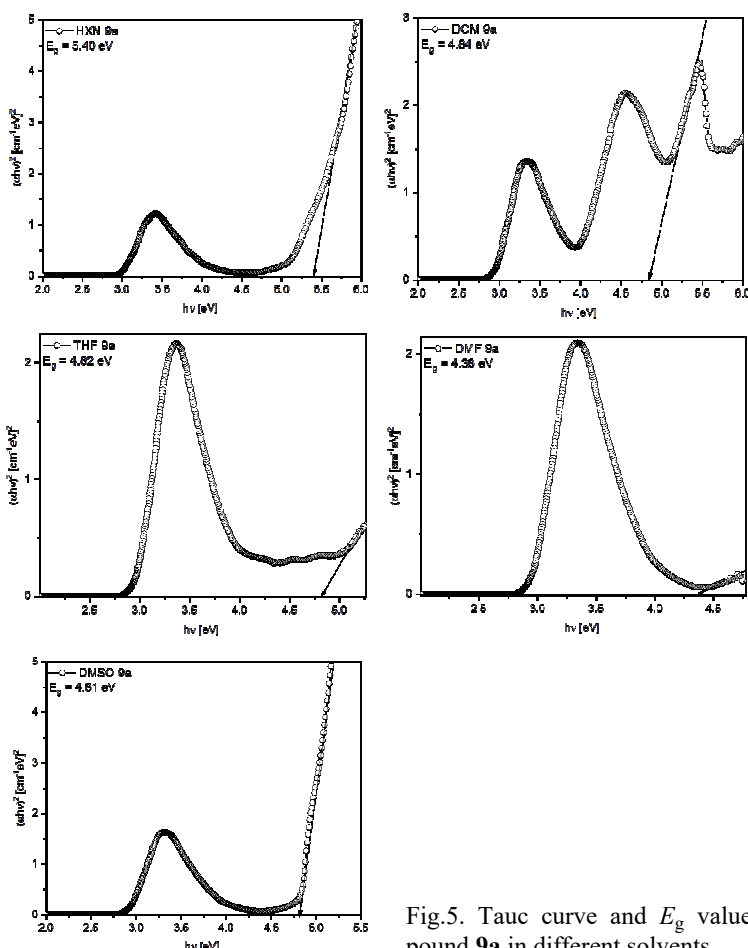


Fig.5. Tauc curve and E_g values of compound **9a** in different solvents.

The bandgap energy of organic π -conjugated semiconductors is related to the electronic structure of their molecules.^{21,22,27,28} The effect, which increases the conjugation of organic compounds and solvent polarity, decreases the energy bandgap. Similarly, the difference in optical band gap E_g values of compounds **7a** and **9a** is due to their different resonance structures (Figs. 1 and 2). Due to the conjugation of the pyrene ring in compound **7a**, the optical bandgap energy (E_g) is smaller than in compound **9a**. The high bandgap energy of compound **9a** is due to the fluorene ring. The E_g values of Schiff base **7a** and **9a** showed variable values in solvents of different polarity (Table II).

The E_g of compound **7a** was decreased in polar solvents, particularly DMSO (4.54 eV) and DMF (4.48 eV) solvents. Although DMSO is more polar than DMF, the high E_g value was measured to be greater in the DMSO solvent. DMSO and DMF solvents are aprotic polar solvents, so there is no hydrogen

bond interaction with compound **7a**. This increase in the optical bandgap energy E_g value was explained by the increase in the molecular mass of DMSO. Due to the trapping of electrons and holes, the bandgap energy between the valence band and conduction band increases as the particle size decreases. The optical bandgap energy E_g decreases gradually with chain length. Therefore, when the E_g values of **7a** and **9a** are compared, the decrease in the E_g values of **9a** is due to the smaller particle size.

TABLE II. Optical bandgap energy (E_g / eV) of compound **7a** and **9a**

Compound	<i>n</i> -Hexane	DCM	THF	DMF	DMSO
7a	5.09	5.00	4.65	4.48	4.54
9a	5.40	4.84	4.82	4.38	4.81

Computational study

An extensive body of research supports the idea that DFT calculation shed light on the structural and electronic properties of conjugated molecules.^{21,22} In Schiff bases, the B3LYP/6-31G(d,p) basis functional set was mostly preferred to investigate the nature and type of UV–Vis shifts, and a modified computational study of time-dependent DFT (TD-DFT) was conducted. This function, particularly adept at accurately calculating electron distribution and energy levels in conjugated systems, facilitates the reliable modeling of molecular structures and spectroscopic properties.^{21–23} In this way, the ground state optimization of compound **7a** and **9a** were performed at the B3LYP/6-31G(d,p) level in the gas phase and DMSO without any symmetry constraints employing the Gaussian09 package program.^{29,30} Optimization was first performed by scanning the potential energy surface (PES) and selecting the geometry around zero. Following the optimization with B3LYP, vibration frequency calculations were performed at the same level of theory and the minima of the calculated structures were verified by analyzing the harmonic vibrational frequencies using analytical second derivatives, which have $NIMAG = 0$. The conductor-like polarizable continuum model (CPCM) was implemented to discern the solvent effect in DMSO.^{27,31} The construction of frontier molecular orbitals (FMO) was completed using Gausview²⁸ while the dihedral angle between benzothiazole and the pyrene ring is 174° in compound **7a**, the dihedral angle between benzothiazole plane and fluorene is 180° in compound **9a**. The angles indicated that pyrene and fluorene rings are planar with the benzotiazole plane in **7a** and **9a**. The dihedral angles of the related atoms are given in detail in the supporting information.

To reach more insight into intramolecular charge transfer (ICT) characters of the compounds frontier molecular orbitals (FMO) were calculated. The HOMOs were found to be, in both **7a** and **9a**, localized on benzothiazole, azomethine bonds and the rings (pyrene in **7a**, fluorene in **9a**). Concerning the LUMOs, they

were localized on the azomethine bonds, pyrene (**7a**) and fluorene (**9a**) rings spreading slightly over benzothiazole. As demonstrated in Fig. 6, the azomethine bond is a π -bridge between the benzothiazole and the rings in compound **7a** and **9a**. λ_{\max} values and vertical excitation energies of the compounds were predicted by a time-dependent DFT (TD-DFT) method.

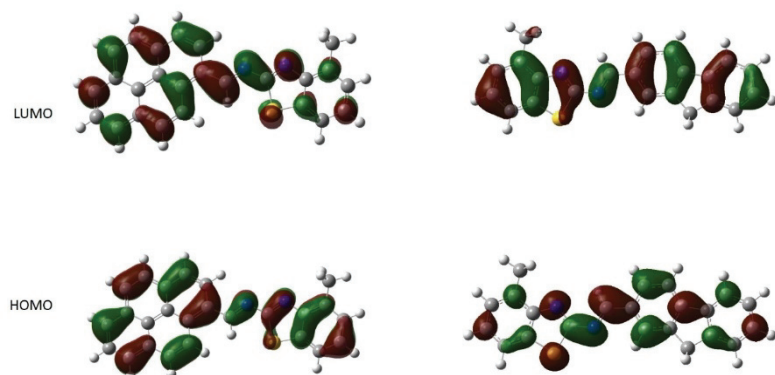


Fig. 6. HOMOs and LUMOs of **7a** (left) and **9a** (right) estimated at the B3LYP/6-31G(d,p) level in the gas phase.

In order to receive absorption bands, N states of 50 for singlets were computed. The λ_{\max} values of compounds **7a** and **9a** are predicted to be 431.8 and 388.56 nm in DMSO, which shows low energy transitions resulting from HOMO–LUMO (95–98 %). The calculated excitation and absorption energies agree well with the experimental results.

In parallel with all calculations performed, a dispersion component was added to the B3LYP 6-31G(d,p) level of theory used in DFT calculations, and re-optimization and frequency calculations of the investigated **7a** and **9a** molecules were completed. First, there is no difference in the dihedral angles and therefore the geometry of the optimized structures by using the dispersion component.

Excited energy calculations were rerun with the freshly optimized geometries, and results were compared with previously obtained theoretical results. When the HOMO–LUMO band gap energies of **7a** and **9a** were examined, narrower band gap energies were detected compared to the calculations conducted without using this dispersion component. The band gap energy values obtained both without and using the dispersion component tend to decrease or increase in the same way as the experimental study. However, it is seen that the band gap value obtained by adding the dispersion component deviates further from the experimental data. The results of the calculations with and without the dispersion component are given in supporting information.

CONCLUSION

In this study, we have synthesized and characterized two novel Schiff bases **7a** and **9a**. Optical properties have been investigated by UV–Vis spectra. The optical bandgap has been calculated by the Tauc method and DFT calculation. The optical band gap of compounds **7a** and **9a** in the DMF solvent is 4.48 and 4.38 eV, respectively. Experimental results showed that the optical band gap of compounds **7a** and **9a** decreases with increasing optical absorption, red-shift, π -electronic system, solvent polarity and particle size. Finally, the increased optical absorption and reduced energy gap make the optimized samples suitable materials for solar applications.

Since pyrene contributes more to conjugation than fluorene, the experimental band gap energy of compound **7a** is expected to be lower than that of compound **9a**. This difference was observed as 2.87 eV for **7a** and 3.19 eV for **9a** in calculated data conducted in DMSO by B3LYP 6-31G(d,p). Considering the optical band gap energy obtained by the Tauc method from the experimental absorbance graphs recorded in DMSO (4.54 eV for **7a** and 4.81 eV for **9a**), the trends in the calculated band gap energies are in agreement with the experimental data. In addition, when the frontier molecular orbital is examined, it is clearly seen that the electrons are not located in only one region, but that these electrons are homogeneously distributed throughout the molecule. The fact that the charge transport in the molecule can continue unhindered throughout the molecule can be explained by the fact that compounds **7a** and **9a** have almost planar structures. For future studies, molecules with narrow band gap energies can be designed and synthesized by increasing the conjugated groups attached to compounds **7a** and **9a**.

SUPPLEMENTARY MATERIAL

Additional data are available electronically at the pages of journal website: <https://www.shd-pub.org.rs/index.php/JSCS/article/view/12546>, or from the corresponding author on request.

Acknowledgment. The authors would like to thank the Eskişehir Osmangazi University Scientific Research Projects Council for financial support (Project No 202019059).

ИЗВОД

НОВЕ π -КОЊУГОВАНЕ ШИФОВЕ БАЗА ЗАСНОВАНЕ НА ПИРЕНУ И ФЛУОРЕНУ:
ТЕОРИЈСКО И ЕКСПЕРИМЕНТАЛНО ИСТРАЖИВАЊЕ ОПТИЧКИХ СВОЈСТАВА

YUNUSCAN SIVRİKAYA¹, HANDAN CAN SAKARYA², GÖKHAN KILIÇ³, SULTAN FUNDA EKTİ⁴
и MERVE YANDIMOĞLU²

¹Graduate School of Natural and Applied Sciences, Eskişehir Osmangazi University, Eskişehir, Turkey,

²Department of Chemistry, Faculty of Science, Eskişehir Osmangazi University, Eskişehir, Turkey,

³Department of Physics, Faculty of Science, Eskişehir Osmangazi University, Eskişehir, Turkey и

⁴Department of Chemistry, Faculty of Science, Eskişehir Technical University, Eskişehir, Turkey

Реакцијом полицикличних алдехида и супституисаних бензотиазола, синтетисане су нове Шифове базе са D- π -A системом. Структуре синтетисаних Шифових база (**7a** и

9a) одређене су помоћу FT-IR, ^1H -NMR, ^{13}C -NMR, ESI-Mass и елементалном анализом. Истражене су оптичке особине нових једињења и оптички јаз између трака (E_g) је израчунат Тауковом методом користећи UV–Vis апсорpcione спектре. Да би се добио бољи увид у структурне и електронске особине нових база урађена су израчунавања теоријом функционала густине (DFT/B3LYP/6-31G(d,p)). Оптимизоване молекулске геометрије, UV–Vis спектроскопски параметри и HOMO–LUMO енергије су испитане и резултати израчунавања су упоређени са експерименталним подацима.

(Примљено 31. августа, ревидирано 16. децембра, прихваћено 20. децембра 2023)

REFERENCES

1. H. Schiff, *Justus Liebigs Ann. Chem.* **150** (1869) 193
2. N. Öztürk, *MSc Thesis*, Istanbul University, 1998
3. C. Sasaki, K. Nakajima, M. Kojima, J. Fujita, *Bull. Chem. Soc. Jpn.* **64** (1991) 1318 (<https://doi.org/10.1246/bcsj.64.1318>)
4. S. Kanemasa, M. Yoshioka, O. Tsuge, *Bull. Chem. Soc. Jpn.* **62** (1989) 869 (<https://doi.org/10.1246/bcsj.62.869>)
5. M. F. Aly, M. I. Younes, S. A. Metwally, *Tetrahedron* **50** (1994) 3159 ([https://doi.org/10.1016/S0040-4020\(01\)81114-5](https://doi.org/10.1016/S0040-4020(01)81114-5))
6. A. E. Taggi, A. M. Hafez, H. Wack, B. Young, D. Ferraris, T. Lectka, *J. Am. Chem. Soc.* **124** (2002) 6626 (<https://doi.org/10.1021/ja0258226>)
7. K. Singh, M. S. Barwa, P. Tyagi, *Eur. J. Med. Chem.* **41** (2006) 147 (<https://doi.org/10.1016/j.ejmec.2005.06.006>)
8. S. K. Sridhar, M. Saravanan, A. Ramesh, *Eur. J. Med. Chem.* **36** (2001) 615 ([https://doi.org/10.1016/S0223-5234\(01\)01255-7](https://doi.org/10.1016/S0223-5234(01)01255-7))
9. R. Mladenova, M. Ignatova, N. Manolova, T. Petrova, I. Rashkov, *Eur. Polym. J.* **38** (2002) 989 ([https://doi.org/10.1016/S0014-3057\(01\)00260-9](https://doi.org/10.1016/S0014-3057(01)00260-9))
10. M. Koole, R. Frisenda, M. L. Petrus, M. L. Perrin, H. S. van der Zant, T. J. Dingemans, *Org. Electron.* **34** (2016) 38 (<https://doi.org/10.1016/j.orgel.2016.03.043>)
11. N. Bouguerra, A. Růžička, C. Ulbricht, C. Enengl, S. Enengl, V. Pokorná, D. Výprachtický, E. Tordin, R. Aitout, V. Cimrová, D. A. M. Egbe, *Macromolecules* **49** (2016) 455 (<https://doi.org/10.1021/acs.macromol.5b02267>)
12. J. Jankowska, M. F. Rode, J. Sadlej, A. L. Sobolewski, *ChemPhysChem* **13** (2012) 4287 (<https://doi.org/10.1002/cphc.201200560>)
13. K. Haupt, K. Mosbach, *Chem. Rev.* **100** (2000) 2495 (<https://doi.org/10.1021/cr990099w>)
14. S. Pu, Z. Tong, G. Liu, R. Wang, *J. Mater. Chem. C* **1** (2013) 4726 (<https://doi.org/10.1039/C3TC30804A>)
15. M. Petrus, R. Bouwer, U. Lafont, S. Athanasopoulos, N. Greenham, T. Dingemans, *J. Mater. Chem. A* **2** (2014) 9474 (<https://doi.org/10.1039/C4TA01629G>)
16. A. Bolduc, L. Rivier, S. Dufresne, W. Skene, *Mater. Chem. Phys.* **132** (2012) 722 (<https://doi.org/10.1016/j.matchemphys.2011.12.002>)
17. U. H. A. Azeez, D. Ayyappan, S. G. Chidambaram T, R. Singh, J. Subbiah, A. Sambandam, *J. Mol. Struct.* **1294** (2023) 136315 (<https://doi.org/10.1016/j.molstruc.2023.136315>)
18. S. Mukhopadhyay, C. Risko, S. R. Marder, J.-L. Brédas, *Chem. Sci.* **3** (2012) 3103 (<https://doi.org/10.1039/C2SC20861J>)
19. Z. Fatima, H. A. Basha, S. A. Khan, *J. Mol. Struct.* **1292** (2023) 136062 (<https://doi.org/10.1016/j.molstruc.2023.136062>)

20. W. Xu, Z. Shao, Y. Han, W. Wang, Y. Song, H. Hou, *Dyes Pigm.* **152** (2018) 171179 (<https://doi.org/10.1016/j.dyepig.2018.01.056>)
21. G. Turkoglu, M. Cinar, A. Buyruk, E. Tekin, S. Mucur, K. Kaya, T. Ozturk, *J. Mater. Chem. C* **4** (2016) 6045 (<https://doi.org/10.1039/C6TC01285J>)
22. M. Wałęsa-Chorab, M. H. Tremblay, W. G. Skene, *Chem. Eur. J.* **22** (2016) 11382 (<https://doi.org/10.1002/chem.201600859>)
23. K. S. M. Salih, *J. Mol. Struct.* **1244** (2021) 131267 (<https://doi.org/10.1016/j.molstruc.2021.131267>)
24. K. Mangaiyarkarasi, A. Ravichandran, K. Anitha, A. Manivel, *J. Mol. Struct.* **1155** (2018) 758 (<https://doi.org/10.1016/j.molstruc.2017.11.065>)
25. G. A. Evingür, Ö. Pekcan, *Compos. Struct.* **183** (2018) 212 (<https://doi.org/10.1016/j.compstruct.2017.02.058>)
26. J. Singh, K. Shimakawa, in *Advances in Amorphous Semiconductors*, J. Singh, K. Shimakawa, Eds., Taylor and Francis New York, 2003 (ISBN 9780415287708)
27. M. Cossi, N. Rega, G. Scalmani, V. Barone, *J. Comput. Chem.* **24** (2003) 669 (<https://doi.org/10.1002/jcc.10189>)
28. R. Dennington, T. Keith, J. Millam, *J.GaussView, version 5*, Semichem Inc., Shawnee Mission, KS, 2009
29. C. Lee, W. Yang, R.G. Parr, *Phys. Rev. B* **37** (1988) 785 (<https://doi.org/10.1103/PhysRevB.37.785>)
30. *Gaussian 09, Rev. A*, Gaussian Inc, Wallingford, CT, 2009
31. V. Barone, M. Cossi, *J. Phys. Chem., A* **102** (1998) 1995. (<https://doi.org/10.1021/jp9716997>).

SUPPLEMENTARY MATERIAL TO

**New pyrene and fluorene-based π -conjugated Schiff bases:
Theoretical and experimental investigation of optical properties**

YUNUSCAN SİVRİKAYA¹, HANDAN CAN SAKARYA^{2*}, GÖKHAN KILIÇ³,
SULTAN FUNDA EKTİ⁴ and MERVE YANDIMOĞLU²

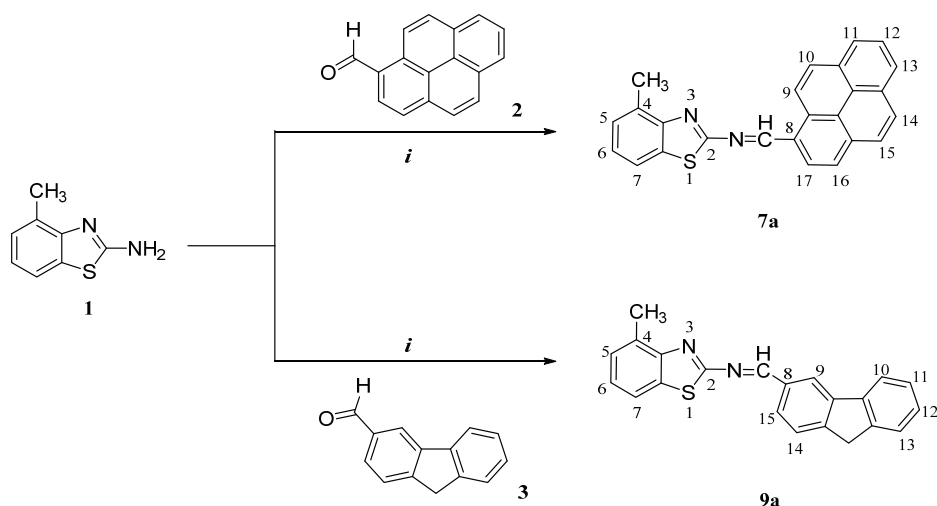
¹Graduate School of Natural and Applied Sciences, Eskişehir Osmangazi University,

Eskişehir, Turkey, ²Department of Chemistry, Faculty of Science, Eskişehir Osmangazi

University, Eskişehir, Turkey, ³Department of Physics, Faculty of Science, Eskişehir Osmangazi University, Eskişehir, Turkey and ⁴Department of Chemistry, Faculty of Science, Eskişehir Technical University, Eskişehir, Turkey.

J. Serb. Chem. Soc. 89 (7–8) (2024) 1025–1038

EXPERIMENTAL



i: EtOH, 75 °C, reflux, %5 HCl, N₂(g)

Scheme S-1. Synthesis method and numbers of protons.

SPECTROSCOPIC DATA OF MAIN COMPOUNDS

N-(pyren-1-ylmethylene)-4-methylbenzo[d]thiazol-2-amine (7a) Yield: 50 %, mp. 212–216 °C. FT-IR (KBr, cm⁻¹): 3038 (Aromatic C-H), 2965–2918 (Aliphatic C-H), 1593 (CH=N),

*Corresponding author. E-mail: hsakarya@ogu.edu.tr

-1576, 1537 and 1478 (C=C) (Fig.S1). ^1H NMR (500 MHz, DMSO- d_6 , δ ppm): 9.98 (s, 1H, CH=N), 9.28 (d, 1H, J=9 Hz, H17), 8.84 (d, 1H, J= 7 Hz, H10), 8.44 (m, 5H, H9, H11, H14, H15, H16), 8.28 (d, 1H, J= 8.9 Hz, H13), 8.15 (t, 1H, J= 8.6 Hz, H12), 7.88 (dd, 1H, H6), 7.31 (d, 2H, H5 ve H7), 2.45 (s, 3H) (Fig.S2). ^{13}C NMR (125 MHz, DMSO- d_6 , δ ppm): 135.0 (CH=N), 134.36, 132.80, 131.74, 131.21, 130.86, 130.61, 130.53, 129.08, 127.09, 127.67, 127.59, 127.50, 127.41, 125.83, 124.51, 123.93, 123.28, 120.25. ESI-MS (m/z): 377.68 (M^+), 378.71 (M^++1), 379.77 (M^++2), 245.48 ($M^+ - \text{C}_8\text{H}_8\text{N}_2\text{S}$), 165.15 ($M^+ - \text{C}_{17}\text{H}_{19}$). Anal. Calcd. for $\text{C}_{25}\text{H}_{16}\text{N}_2\text{S}$: C, 79.76; H, 4.28; N, 7.44; S, 8.52. Found: C, 79.52; H, 4.44; N, 7.37; S, 8.40.

N-(9H-fluoren-3-ylmethylene)-4-methylbenzo[d]thiazol-2-amine (9a) Yield: 60 %, mp. 180-183 °C. FT-IR (KBr, cm^{-1}): 3046 (Aromatic C-H), 2957, 2910 (Aliphatic C-H), 1620 (CH=N), 1586, 1549 and 1518 (C=C) (Fig.S3). ^1H NMR (500 MHz, DMSO- d_6 , δ ppm): 9.14 (s, 1H, -CH=N-), 8.26 (s, 1H, H9), 8.07 (d, 2H, J=1.5 Hz H14 and H15), 7.99 (d, 1H, J= 7.0 Hz, H7), 7.80 (dd, 1H, J=2.5 Hz, J=8 Hz, H10), 7.62 (d, 1H, J=8.0 Hz, H5), 7.39 (t, 1H, J=7.5 Hz, H6 and dt, 1H, J=8 Hz, H12), 7.28 (d, 1H, J=8.0 Hz, H13 and t, 1H J=7 Hz, H11), 4.00 (s, 2H, Fluorene -CH₂), 2.60 (s, 3H, -CH₃) (Fig.S4). ESI-MS (m/z): 341.63 (M^+), 342.63 (M^++1), 343.65 (M^++2), 209 ($M^+ - \text{C}_7\text{H}_5\text{N}_2\text{S}$), 165.1 ($M^+ - \text{fluorine}$). Anal. Calcd. for $\text{C}_{22}\text{H}_{16}\text{N}_2\text{S}$: C, 77.62; H, 4.74; N, 8.23; S, 9.42. Found: C, 79.90; H, 4.98; N, 8.23; S, 9.40.

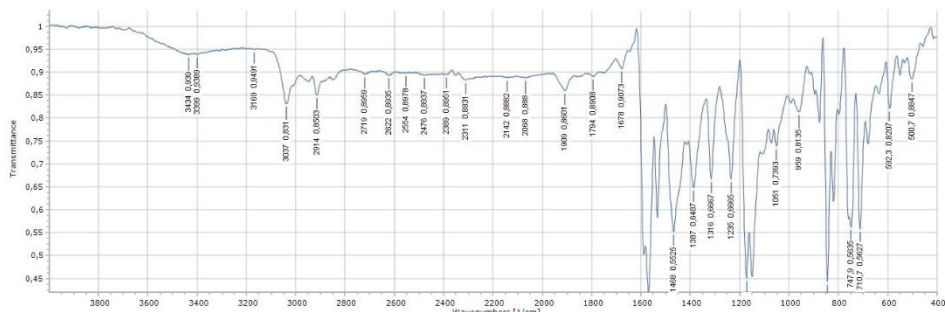


Fig. S-1. FT-IR spectrum of 7a.

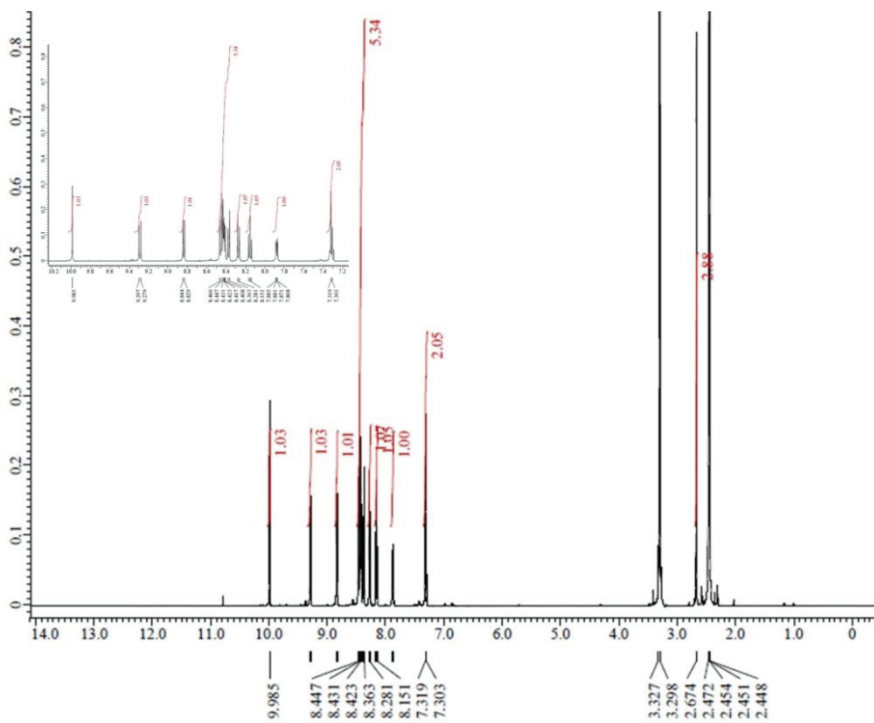
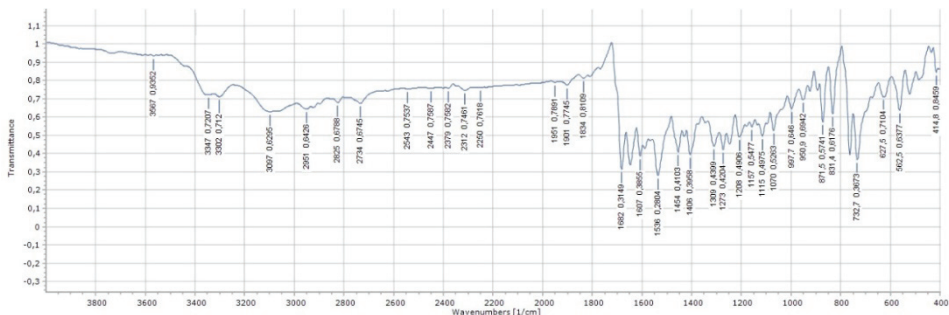
Fig. S-2. ^1H NMR spectrum of compound 7a.

Fig. S-3. FT-IR spectrum of 9a.

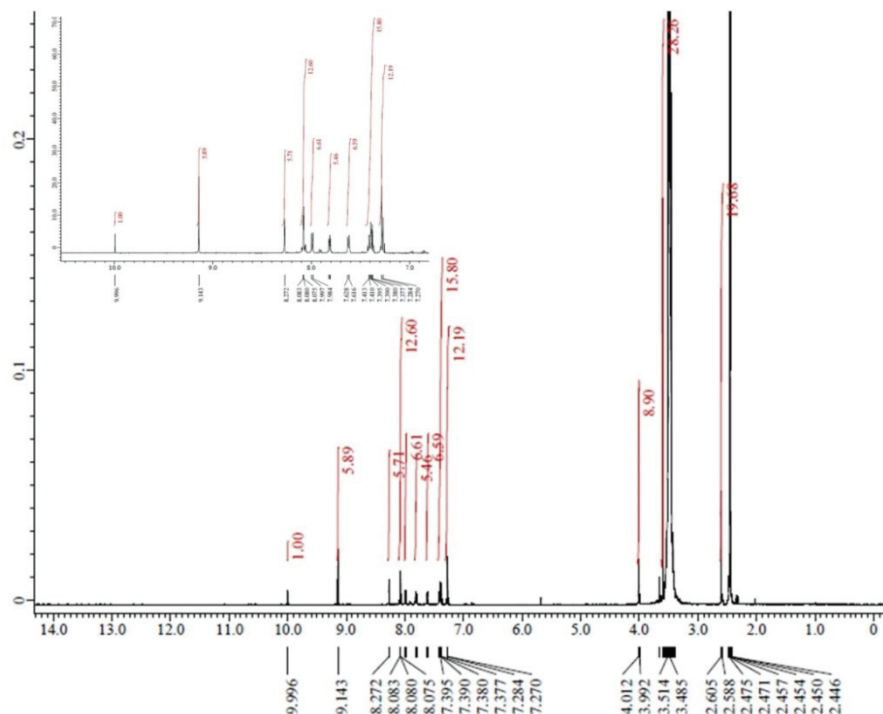


Fig. S-4. ^1H NMR spectrum of compound 9a.

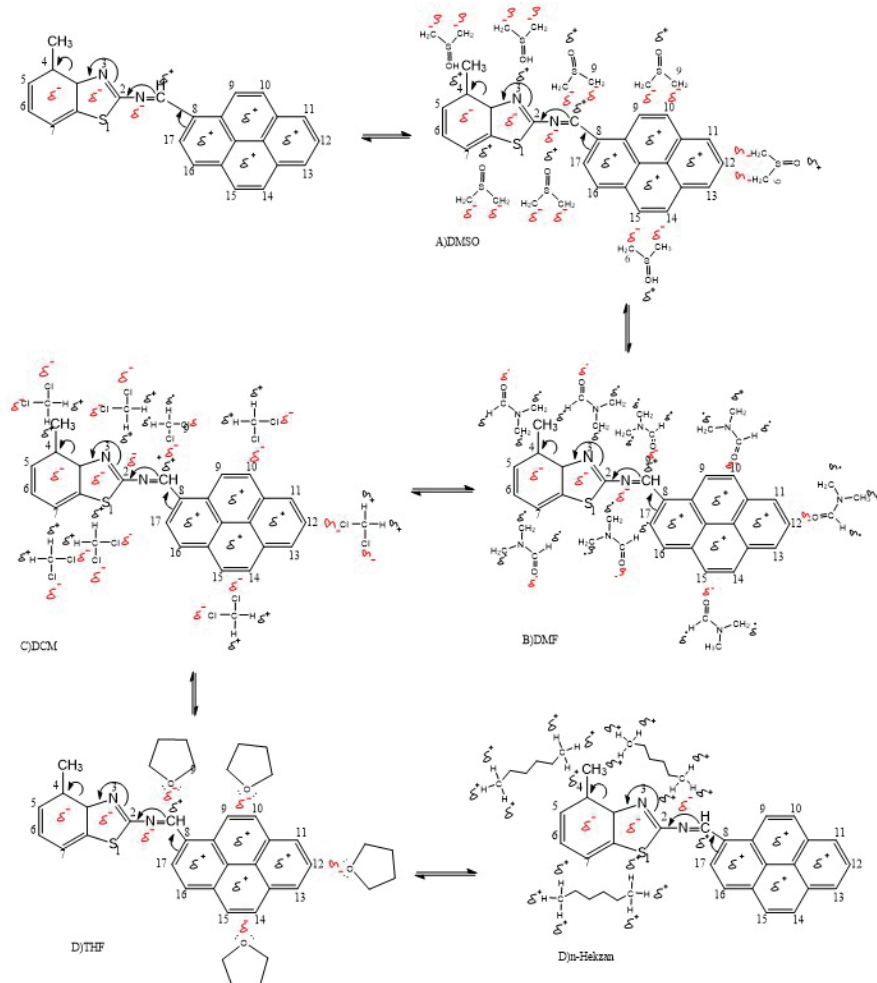


Fig. S-5. Resonance structures in different solvents for compound 7a.

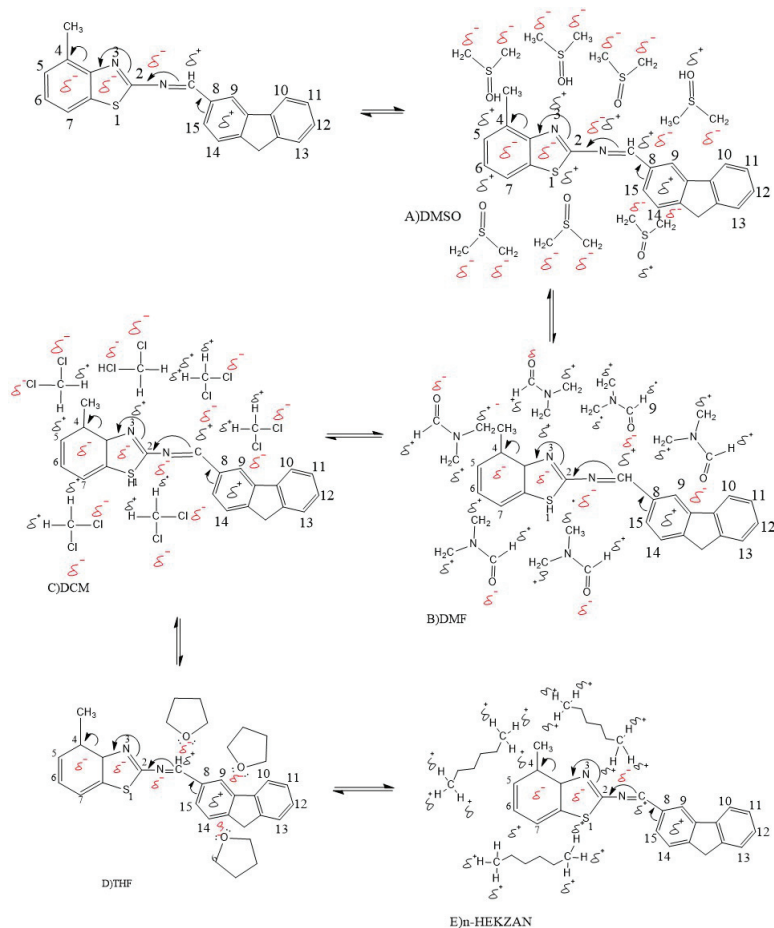


Fig. S-6. Resonance structures in different solvents for compound 9a.

COMPUTATIONAL STUDY

*Optimized Geometries
7a*

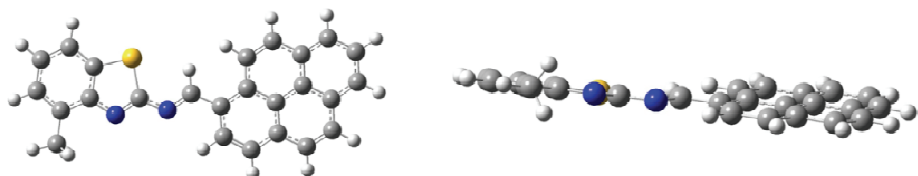


Fig. S-7. Front (left) and side (right) view of the optimized structure of compound 7a.

Sum of electronic and thermal Free Energies (Hartree)= -1469.786060
 Thermal correction to Gibbs Free Energy (Hartree)= 0.287006

C	-5.7557	-4.0026	0.0403
C	-4.8025	-4.9499	0.0676
C	-3.5033	-4.6125	0.1156
C	-3.1932	-3.3093	0.1353
C	-4.1457	-2.3685	0.108
C	-5.4488	-2.6917	0.0598
S	-1.8702	-2.6883	0.1863
C	-2.3634	-1.2992	0.1789
N	-3.6308	-1.2171	0.1341
N	-1.7306	-0.1971	0.2101
C	-0.4709	-0.0485	0.2569
C	-0.5637	2.2588	0.2734
C	-0.0138	3.4781	0.3045
C	1.319	3.6125	0.3545
C	2.0969	2.5118	0.3727
C	1.5341	1.2785	0.3408
C	0.1837	1.1368	0.2906
C	3.4378	2.6806	0.4232
C	4.2568	1.6119	0.4431
C	3.7152	0.3861	0.4118
C	2.3851	0.232	0.3617
C	3.9861	3.9133	0.4547
C	5.3219	4.0657	0.5046
C	6.1272	2.995	0.5239
C	5.5916	1.7674	0.4931
C	1.8605	4.8418	0.3857
C	3.1895	4.994	0.4357
C	-6.5436	-1.6528	0.0288
H	-6.8147	-4.3086	0.001
H	-5.089	-6.0151	0.0506
H	-2.7287	-5.3977	0.1378
H	0.1072	-0.9805	0.2704
H	-1.666	2.2343	0.2333
H	-0.6762	4.361	0.2885
H	4.3565	-0.5126	0.4267
H	2.0557	-0.8168	0.3395
H	5.7816	5.0685	0.5307
H	7.2219	3.123	0.5648
H	6.2682	0.8959	0.5096
H	1.2281	5.7462	0.371
H	3.607	6.0151	0.4605
H	-6.157	-0.6105	0.0607
H	-7.1454	-1.7565	-0.9027
H	-7.2219	-1.7825	0.9027

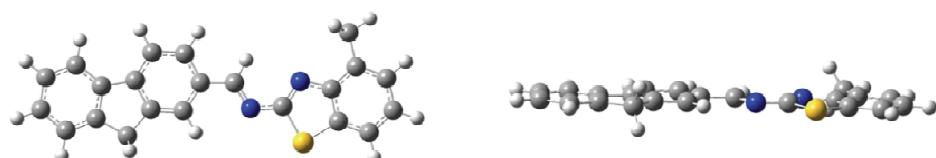
9a

Fig. S-7. Front (left) and side (right) view of the optimized structure of compound **9a**.

Sum of electronic and thermal Free Energies (Hartree)= -1355.461210
Thermal correction to Gibbs Free Energy (Hartree)= 0.268929

C	7.0316	0.69762	0.24052
C	7.26734	-0.65893	-0.0043
C	6.22069	-1.54738	-0.19256
C	4.91385	-1.06566	-0.13392
C	4.67582	0.30957	0.11157
C	5.73912	1.20826	0.30349
S	3.41762	-1.94978	-0.32722
C	2.5349	-0.41676	-0.07801
N	3.29832	0.64939	0.13484
N	1.12015	-0.39232	-0.05995
C	0.42027	0.68441	-0.25694
C	-1.04407	0.63639	-0.20738
C	-1.74033	-0.55218	0.06513
C	-3.12127	-0.51314	0.09489
C	-3.81911	0.69399	-0.14285
C	-3.13384	1.86797	-0.41156
C	-1.74169	1.82843	-0.44165
C	-4.09047	-1.63175	0.35997
C	-5.42491	-0.94853	0.25127
C	-5.25135	0.42454	-0.04592
C	-6.69227	-1.48005	0.39949
C	-7.79082	-0.62966	0.24879
C	-7.61911	0.71905	-0.04313
C	-6.34252	1.26387	-0.19443
C	5.49993	2.649	0.56448
H	7.88589	1.36978	0.38561
H	8.29958	-1.02318	-0.04675
H	6.41233	-2.60878	-0.38288
H	0.87647	1.6678	-0.4669
H	-1.2047	-1.49079	0.25044
H	-3.67581	2.80149	-0.59496
H	-1.18593	2.75032	-0.65236
H	-3.98584	-2.44856	-0.3778
H	-3.93785	-2.07827	1.35986
H	-6.83293	-2.54066	0.62927
H	-8.80209	-1.03412	0.36289
H	-8.49628	1.3647	-0.1563
H	-6.20451	2.3253	-0.42418
H	4.94652	3.11196	-0.26377
H	4.90548	2.78929	1.4775
H	6.43807	3.20643	0.68978

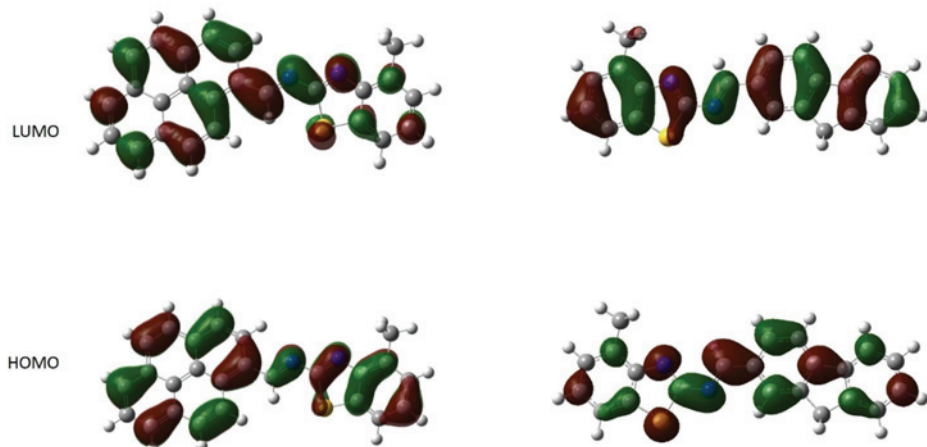


Fig. S-9. HOMOs and LUMOs of **7a** (left) and **9a** (right) estimated at the B3LYP/6-31G(d,p) level in the gas phase.

A dispersion component was added to the B3LYP 6-31 G (d,p) level of theory used in DFT calculations, and re-optimization and frequency calculations of the investigated **7a** and **9a** molecules were completed. The command line for frequency calculations with added dispersion component is given below:

```
freq=noraman      b3lyp/6-31g(d,p)      scrf=(cpcm,solvent=dmso)      guess=save
geom=connectivity EmpiricalDispersion=GD3BJ
```

First, there is no difference in the dihedral angles and therefore the geometry of the optimized structures by using the dispersion component.

Then, excited energy calculations were rerun with the freshly optimized geometries, and results were compared with previously obtained theoretical results.

When the HOMO-LUMO band gap energies of **7a** and **9a** were examined, narrower band gap energies were detected compared to the calculations done without using this dispersion component. The band gap energy values obtained both without and using the dispersion component tend to decrease or increase in the same way as the experimental study. However, it is seen that the band gap value obtained by adding the dispersion component deviates further from the experimental data.

Table S-I. The results of the calculations with and without the dispersion component

Compound	Phase	Calculation with dispersion component		Calculation without dispersion component	
		The sum of thermal and free energy (Hartree)	Band gap energy (eV)	The sum of thermal and free energy (Hartree)	Band gap energy (eV)
7a	Gas	-1469.9010	2.85	-1469.7861	2.85
	DMSO	-1469.9125	2.66	-1469.7974	2.87
9a	Gas	-1355.5595	3.22	-1355.4612	3.20
	DMSO	-1355.5644	3.04	-1355.4801	3.19



Computational exploration of flavonoids from the genus *Knema* with anti-inflammatory potential

ABUBAKAR SIDDIQ SALIHU^{1,2}, WAN MOHD NUZUL HAKIMI WAN SALLEH^{1*}
and TOMISIN HAPPY OGUNWA^{3,4}

¹Department of Chemistry, Faculty of Science and Mathematics, Universiti Pendidikan Sultan Idris, 35900 Tanjung Malim, Perak, Malaysia, ²Department of Pure and Industrial Chemistry, Faculty of Natural and Applied Sciences, Umaru Musa Yar'adua University, Katsina, Nigeria, ³Centre for Biocomputing and Drug Design, Adekunle Ajasin University, Akungba-Akoko, Ondo State, Nigeria and ⁴Department of Biochemistry, Adekunle Ajasin University, Akungba-Akoko, Ondo State, Nigeria

(Received 4 September, revised 25 October, accepted 11 December 2023)

Abstract: Inflammation, a widespread biological process linked to various diseases, poses a significant global health challenge. Recent research targeting the development of new anti-inflammatory drugs has prioritized plant-derived compounds due to their cost-effectiveness and minimal side effects compared to synthetic drugs. Flavonoids, polyphenolic compounds in plants, show potential for treating inflammation-related diseases. This study evaluates the anti-inflammatory activity of flavonoids from the *Knema* genus, a member of the Myristicaceae family. We focused on inhibiting two pro-inflammatory proteins, human and murine interleukin-1B (IL-1) and human interleukin-6 (IL-6). Molecular docking and ADMET prediction identified sulfuretin and (−)-catechin with high binding affinity to IL-6, whereas 4'-hydroxy-7-methoxyflavanone and 7,2'-dihydroxy-6,8-dimethyl-4',5'-methylenedioxyflavan stably bind IL-6. Molecular interaction analyses revealed that hydrogen and π–σ bonds contribute to the interaction. Notably, these flavonoids exhibited affinities comparable to celecoxib. Our computational predictions support the suitability of these flavonoids as drug candidates, indicating their promise as natural anti-inflammatory agents capable of modulating pro-inflammatory signaling pathways.

Keywords: 4'-hydroxy-7-methoxyflavanone; molecular docking; Myristicaceae; interleukin, sulfuretin.

INTRODUCTION

Inflammation is a complex biological response activated by the immune system to injury, infection or foreign substances.¹ It is a protective mechanism that

* Corresponding author. E-mail: wmn hakimi@fsmt.upsi.edu.my
<https://doi.org/10.2298/JSC230904094S>

helps to remove harmful stimuli and initiate tissue repair.² Signs of acute inflammation include redness, warmth, swelling and pain caused by increased blood flow to the affected area. These bring white blood cells that fight infection and remove damaged tissue.³ Chronic inflammation, on the other hand, is a long-term response that can last for months or even years and is associated with various diseases such as rheumatoid arthritis, asthma and cancer.^{4–6} Chronic inflammation can result from several factors, including poor diet, lack of exercise, exposure to toxins and certain medical conditions.^{7–9} Anti-inflammatory medications such as celecoxib, ibuprofen, aspirin and corticosteroids can be used to reduce inflammation, but also have side effects.^{10–12}

In recent years, natural products have gained significant attention as potential sources of new drugs for various diseases, including those associated with inflammation.¹³ The growing interest in natural products is driven by the need for safe and effective alternatives to synthetic drugs, which often have undesirable side effects.¹⁴ Additionally, natural products have evolved over millions of years to interact specifically with biological systems, making them more likely to be effective as drugs.¹⁵ Plants have been used in traditional medicine for years and remain an essential therapeutic agent source. In particular, flavonoids, a large class of natural compounds widely distributed in plants, have diverse biological activities, including anti-inflammatory activity.¹⁶ Flavonoids inhibit the activity of pro-inflammatory enzymes such as cyclooxygenase and lipoxygenases, and modulate the production of pro-inflammatory cytokines such as TNF-alpha, IL6 and IL-1.¹⁷ Furthermore, flavonoids suppress the activation of inflammatory signalling pathways such as the nuclear factor-kappa B (NF- κ B) pathway.¹⁸

The Myristicaceae is a large family of flowering plants that includes over 1000 species. It is widely distributed in tropical regions and has a long history of medicinal use in traditional medicine. Extracts and compounds isolated from Myristicaceae species exhibit various medicinal properties, including anti-inflammatory activity.¹⁹ For example, studies have shown that malabaricone C, isolated from *Myristica fragrans* have shown antioxidant (IC_{50} value 6.56 μ g/mL) and anti-inflammatory activities (IC_{50} value 2.06 μ g/mL).²⁰ Similarly, compounds isolated from other species of *M. dactyloides*, *M. malabarica* and *M. cinnamomea* possess anti-inflammatory, antioxidant and analgesic properties.²⁰

The genus *Knema*, in particular, is a member of the Myristicaceae family with anti-inflammatory, antioxidant, antinematodal and anticancer properties.^{21,22} In this study, we investigated thirty-five flavonoids isolated from the genus *Knema* for their anti-inflammatory activity. Two pro-inflammatory proteins, human and murine interleukin-1B (IL-1) and human interleukin-6 (IL-6), were targeted for potential inhibition using the *Knema* flavonoids. Our findings provide insights into the ability of natural compounds from the Myristicaceae family, particularly those of the genus *Knema*, as possible alternatives to reduce inf-

lammation and prevent the development of chronic diseases associated with excessive or prolonged inflammation.

EXPERIMENTAL

Preparation of ligands

Thirty-five flavonoids isolated from the genus *Knema* were retrieved from the PubChem database (<https://pubchem.ncbi.nlm.nih.gov/>) as SDF files. The standard drug, celecoxib, was also included in the study as a benchmark for comparison. The openbabel tool²³ embedded in PyRx²⁴ was used to perform energy minimization for each ligand separately using the default parameters of steepest descent steps 100 with step size 0.02 (Å) and conjugate gradient steps 100 with step size 0.02 (Å), whereas the update interval was fixed at 10.²⁵

Preparation of the target protein

The crystal structures of IL-1 and IL-6 with PDB ID 5I1B and 1ALU, respectively, were accessed from the Protein Data Bank (PDB) (<http://www.rcsb.org>). Before docking, water molecules, other atoms and ligands cocrystallized with the protein were removed with the Biovia Discovery Studio 2021 Client.²⁶ The protein structure was minimized by using the conjugate gradient algorithm and the AMBER force field with UCSF Chimera 1.10.1.²⁷

Molecular docking

AutoDock 4.2²⁸ in PyRx virtual screening tool was used for the molecular docking experiment to dock the ligands to the pro-inflammatory receptors. The center and size were adjusted to contain the residue in the binding pocket as reported by,²⁹ and allow the ligands to move freely. The exhaustiveness value was set to 8 to maximize the binding conformational analysis, and the docked compounds were evaluated based on their lowest binding energy (kJ/mol). The binding energy (ΔG) in kJ/mol and the inhibition constants (K_i) of isolated ligands and standard drugs were determined by duplicating the docking experiments. The 2D and 3D depictions of the docking complexes were generated using Discovery Studio 2021.²⁵

Evaluation of pharmacokinetics and toxicity

Drug candidates are expected to have minimal toxicity and a high pharmacokinetic profile. Therefore, using AdmetLab2 (<https://admetmesh.scbdd.com>) and SwissADME (<http://www.swissadme.ch>), the pharmacokinetic profile and toxicity of selected flavonoids were determined.³⁰

RESULTS AND DISCUSSION

Cytokine formation is a critical aspect of responding to stimuli that trigger inflammation. Many cytokines and growth factors come from macrophages, which are essential cells in the immune response. However, an uncontrolled inflammatory response can lead to chronic inflammation and further tissue damage. To regulate the inflammation process, macrophages secrete various inflammatory mediators such as nitric oxide (NO), tumor necrosis factor- α (TNF- α), interleukin-1 β (IL-1), prostaglandins and IL-6.²⁹ In addition, suppression of macrophages or their secretions can help repair damages caused by inflammation. Many medicinal plants have been used in traditional medicine to modulate inflammation.²⁹ Traditional medicine utilizes both steroidal and non-steroidal anti-inflammatory drugs that suppress cyclooxygenase (COX) in treating acute inf-

lammation. However, these treatments are ineffective in persistent inflammatory disorders like rheumatoid arthritis or osteoarthritis.⁴ As a result, there is a desire for alternative therapies with potent and less toxic agents.

Molecular docking is an indispensable tool to investigate bioactive compounds' conformation and binding mechanisms to the catalytic domain of proteins in drug discovery.³¹ In the current study, we adopted this method to predict the inhibitory potential of 35 natural flavonoids from the genus *Knema* against interleukin-1(IL-1) and interleukin-6 (IL-6) by evaluating the high binding conformation and affinity. The results of the docking experiment are shown in Table I, demonstrating that a higher binding affinity correlates with a higher docking score. The binding energies of the docked flavonoids against human IL-6 (1ALU; Fig. 1a) and human and murine IL-1 (5I1B; Fig. 1b) ranged from -28.79 to -10.38 kJ/mol and from -26.11 to -14.64 kJ/mol, respectively. Among the flavonoids, sulfuretin had the highest score (-26.11 kJ/mol) against IL-6, followed by (-)-catechin whereas 4'-hydroxy-7-methoxyflavanone (-28.79 kJ/mol) and 7,2'-dihydroxy-6,8-dimethyl-4',5'-methylenedioxyflavan (-28.33 kJ/mol) displayed highest docking score against IL-1. These four compounds from *Knema* species were identified as potential inhibitors of pro-inflammatory proteins, with a binding affinity comparable to celecoxib (Table I).

TABLE I. Docking score and inhibition constant (*Ki*) of interactions between *Knema* flavonoids and pro-inflammatory proteins; LBE: ligand binding energy; *Ki*: inhibition constant; *nHb*: number of hydrogen bonds formed

Compound	PubChem ID	1ALU			5I1B		
		LBE kJ/mol	<i>Ki</i> μM	<i>nHb</i>	LBE kJ/mol	<i>Ki</i> μM	<i>nHb</i>
Naringenin	932	-23.22	85.33	4	-24.69	46.95	3
(+)-Catechin	9064	-21.97	141.73	6	-25.65	32.24	3
(-)-Catechin	73160	-25.61	32.69	5	-22.89	97.57	4
Sakuranetin	73571	-23.97	62.63	2	-23.05	92.06	3
Butin	92775	-18.54	570.37	4	-24.48	51.22	4
Dihydrokaempferol	122850	-23.10	90.45	3	-22.09	134.59	3
(S)-2-(3,4-Dihydroxy-phenyl)-5,7-di-hydroxy-chroman-4-one	440735	-23.93	63.82	2	-25.44	35.09	5
Fisetinidol	442397	-20.59	248.63	3	-26.15	26.26	5
Myristinin D	497362	-16.95	1.07	3	-17.66	805.35	2
2-(3,4-Dihydroxy-phenyl)-3,5,7-tri-hydroxy-chromen-4-one	5280343	-21.92	144.53	4	-22.34	121.44	5
Biochanin A	5280373	-22.51	114.33	3	-24.98	42.27	2
Formononetin	5280378	-25.10	39.75	3	-24.84	44.14	2
Luteolin	5280445	-21.05	204.36	3	-22.09	134.05	3
Isoquercitrin	5280804	-18.49	572.12	4	-10.38	15.21	3
3-Methylkaempferol	5280862	-23.51	69.66	4	-22.55	111.24	3
Kaempferol	5280863	-22.93	96.30	3	-26.78	20.40	4

TABLE I. Continued

Compound	PubChem ID	1ALU			5I1B		
		LBE kJ/mol	Ki μM	nHb	LBE kJ/mol	Ki μM	nHb
Genistein	5280961	-24.02	62.02	3	-25.56	32.98	4
Sulfuretin	5281295	-26.11	25.37	2	-23.35	81.72	2
4',5,7-Trihydroxy-6-methoxyisoflavanone	5281811	-23.43	78.96	3	-25.48	34.09	3
2'-Hydroxybiochanin A	5282075	-21.97	140.98	3	-25.48	56.90	2
Astragalin	5282102	-18.24	637.53	5	-16.61	1.23	4
5,7,4'-Trihydroxy-3'-methoxyisoflavanone	5319744	-21.88	145.77	1	-22.55	112.69	3
8-O-Methylretusin	5319771	-21.06	207.20	1	-23.81	67.48	1
Proanthocyanidin A1	9872976	-19.62	362.89	2	-22.47	116.56	5
4'-Hydroxy-7-methoxyflavanone	10265122	-22.97	94.38	2	-28.79	9.09	3
4-[3-(2-hydroxy-4-methoxyphenyl)-propyl]-2-methoxyphenol	14017333	-19.16	436.07	1	-20.50	257.86	3
7,4'-Dihydroxy-3'-methoxyflavan	14157887	-24.43	52.55	2	-22.89	97.87	2
5,7,3'-Trihydroxy-4'-methoxyflavan	20315197	-21.97	141.21	3	-25.31	36.64	3
Virolane	21722171	-24.10	60.23	1	-24.60	48.90	2
2',7-Dihydroxy-4',5'-methylenedioxy-isoflavone	23724666	-24.81	44.76	2	-26.04	27.37	3
7-Hydroxy-3',4'-methylenedioxyflavan 7-O-β-D-glucopyranoside	44257175	-23.22	85.47	2	-23.01	93.07	3
7,2'-Dihydroxy-6,8-dimethyl-4',5'-methylenedioxyflavan	44257181	-23.93	64.01	2	-28.33	10.89	3
2'-Hydroxy-7-methoxy-4',5'-methylene-dioxyflavan	44257183	-24.06	61.39	2	-26.53	22.36	2
3,4',7-Trihydroxy-flavone 7-O-rutin-oxide	101422354	-14.90	2.46	2	-17.74	776.69	4
Dehydrocatechin	132582811	-22.43	116.83	3	-25.73	31.07	7
Celecoxib	2662	-25.06	40.58	5	-18.70	527.29	3

Further analyses were performed, including drug-likeness, absorption, distribution, metabolism, excretion and toxicity (ADMET). These additional steps provide a comprehensive drug-like assessment of the potential of these compounds.

Molecular interaction analysis of the sulfuretin-IL-6 complex showed two hydrogen bonds formed by Pro65 and Glu172 of IL-6 with sulfuretin at the binding site. This interaction is crucial in regulating the activity of the protein. A π-donor hydrogen bond observed between sulfuretin and Met67 may contribute to the stability of the protein-sulfuretin complex. In addition, two π-alkyl bonds were found between sulfuretin and Lys66 residues through ring B and ring C. van der Waals interactions with six amino acid residues of IL-6 play a role in the overall stability of the complex (Fig. 2b). Furthermore, the bioactivity of sulfur-

etin from *Rhus verniciflua* (Anacardiaceae) cannot be overstated. Sulfuretin, a major flavonoid component isolated from *R. verniciflua*, has demonstrated potent anti-inflammatory effects in macrophage.³² As in the work³² who investigated the effect of sulfuretin on the LPS-induced iNOS and COX-2 expression in RAW264.7 macrophages. They challenged macrophages with LPS (1 µg/mL) in the presence or absence of sulfuretin at non-cytotoxic concentrations ranging from 5 to 40 µM. The results showed that sulfuretin effectively suppressed LPS-induced iNOS and COX-2 protein expression in a dose-dependent manner. Additionally, sulfuretin reduced LPS-induced mRNA expression levels of iNOS and COX-2 in a dose-dependent manner, as assessed by RT-PCR analysis. These findings underscore the remarkable anti-inflammatory potential of sulfuretin and its ability to modulate key inflammatory mediators, providing valuable insights into its therapeutic applications in inflammation-related conditions.

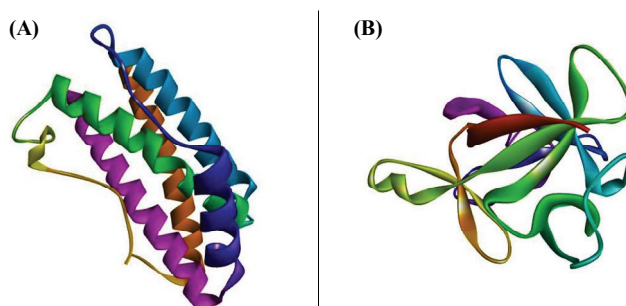


Fig. 1. Crystal structure of: A) human interleukin-6 (PDB ID: 1ALU) and B) human and murine interleukin-1B (PDB ID: 5I1B).

Catechin interacts with human IL-6 with binding energy -25.61 kJ/mol and establishes five hydrogen bonds through residues Pro65, Lys66, Met67, Glu172 and Arg179 which is among the key active residues as described in the work.³³ These hydrogen bonds, formed between the positively charged hydrogen atom of catechin and negatively charged atoms of the residues, help stabilize the catechin-IL-6 complex. In addition, a pi-donor hydrogen bond was observed between Met67 and catechin, while a π -alkyl bond was formed with Phe74. van der Waals interactions were seen between catechin and amino acid residues of IL-6 (Fig. 2a). The structure of catechin plays a critical role in its interaction with human IL-6 residues. Catechin, being a flavonoid, has a unique molecular structure that allows it to form various interactions with proteins, including hydrogen bonding, π - π stacking and van der Waals interactions. These interactions enhance the stability and specificity of the interaction between catechin and IL-6, which in turn contributes to its efficacy as an anti-inflammatory agent. Catechin has demonstrated significant bioactivity in the context of inflammation, as supported by the research.³⁴ The findings reveal that catechin plays a crucial role in attenuat-

ing inflammation induced by TNF- α in mature adipocytes through the activation of the AMPK/SIRT1 pathway. Celecoxib interacts with human IL-6, forming hydrogen bonds with Cys73, Lys66, Gln75 and Arg179 residues. Carbon–hydrogen bonds, π -alkyl and halogen bonds were also observed. However, an unfavourable interaction was also detected with Gln183 (Fig. 2c). Notably, celecoxib formed fewer hydrogen bonds and favourable interactions with IL-6. Catechin and sulfuretin showed a more extensive network of interactions including π -alkyl bonding and van der Waals interaction. This suggests that they may have a stronger ability to regulate the inflammatory response compared to celecoxib.

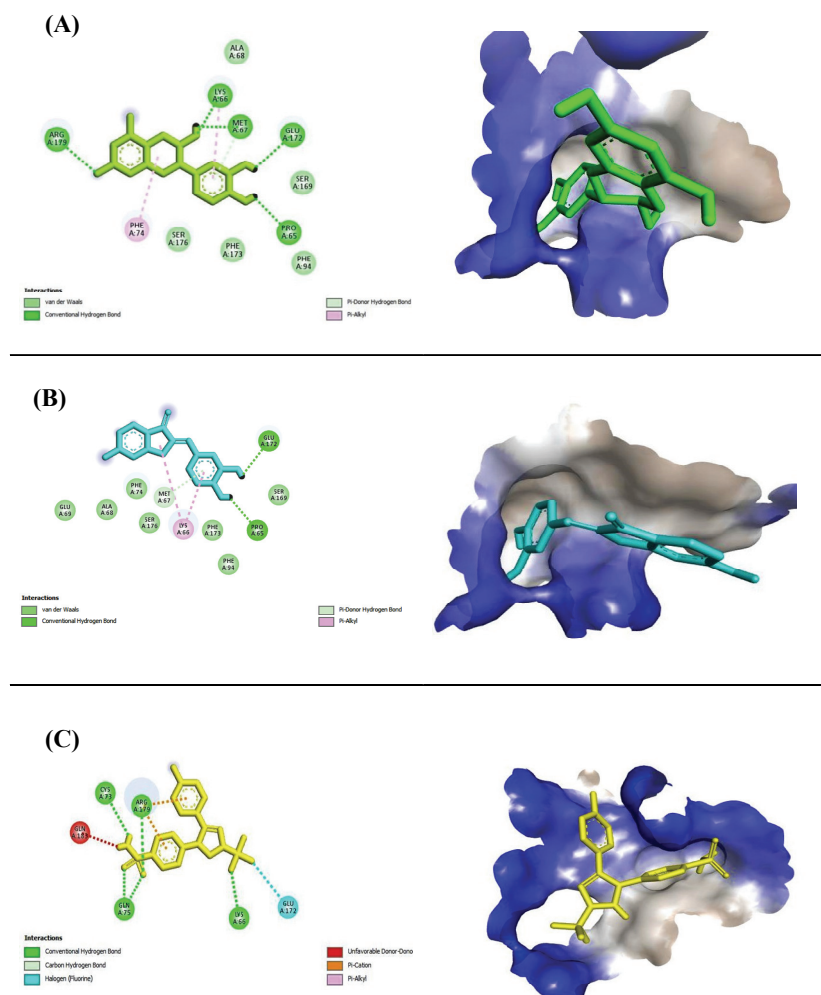


Fig. 2. 2D and 3D interaction map of: A) (-)-catechin, B) sulfuretin and C) celecoxib with IL-1. The protein binding pocket is shown as surface representation and the ligands are presented as stick; (-)-catechin (green), sulfuretin (blue) and celecoxib (yellow).

Analysis of 4'-hydroxy-7-methoxyflavanone interaction with IL-1B revealed three hydrogen bonds *via* Leu134, Val132 and Phe133. The compound also formed a π -donor hydrogen bond with Leu134 and a π -alkyl interaction with Leu80. Additionally, three alkyl interactions were observed with Val132, Leu26 and Leu80. 4'-hydroxy-7-methoxyflavanone also formed a π -anion interaction and a π -sigma interaction with Glu25. Furthermore, eight amino acid residues of IL-1B in the binding pocket displayed van der Waals interaction with 4'-hydroxy-7-methoxyflavanone (Fig. 3a). Alkyl interactions between the ligand and Val40,

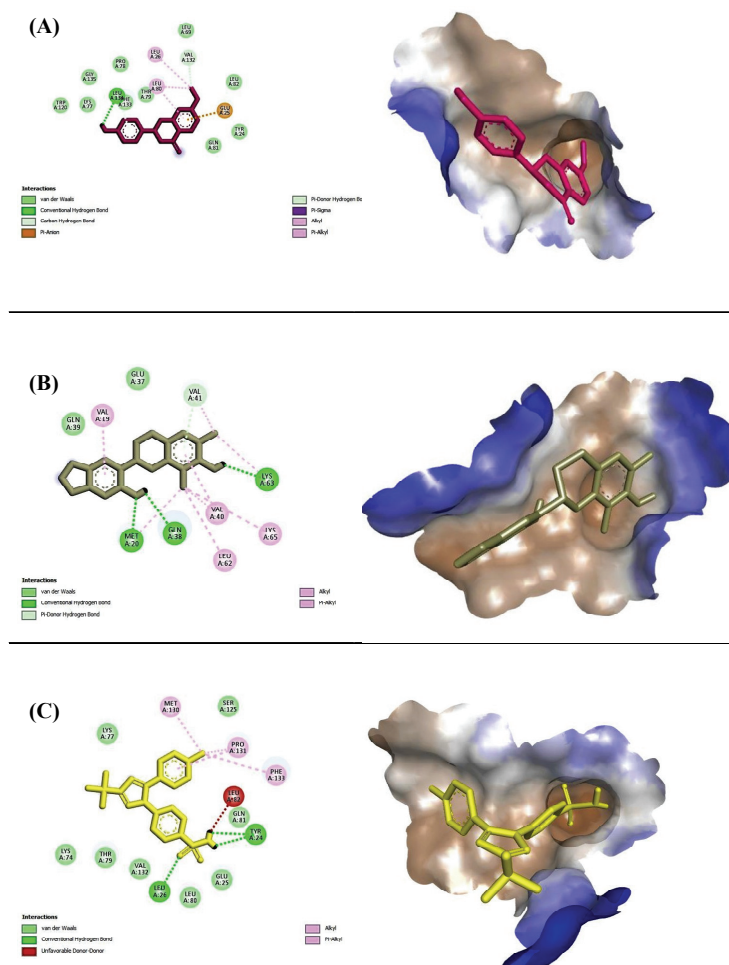


Fig 3. 2D and 3D interaction map of: A) 4'-hydroxy-7-methoxyflavanone; B) 7,2'-dihydroxy-6,8-dimethyl-4',5'-methylenedioxyflavan; C) celecoxib. The protein binding pocket is shown as a surface representation and the ligands are presented as sticks; 4'-hydroxy-7-methoxyflavanone (red), 7,2'-dihydroxy-6,8-dimethyl-4',5'-methylenedioxyflavan (green) and celecoxib (yellow).

Leu62, Lys65 and Met20 were observed (Fig. 3b). Similarly, 7,2'-dihydroxy-6,8-dimethyl-4',5'-methylenedioxyflavan exhibited hydrogen bonds with residues Met20, Gln38 and Lys63 as well as a π -donor hydrogen bond with Val41 whereas π -alkyl interactions were seen with Val19 and Val40. Additionally, it's worth noting that an earlier study³⁵ reported the cytotoxic potential of 4'-hydroxy-7-methoxyflavanone, isolated from the leaves of *M. calabura*, in inhibiting the growth of HT-29 (colon cancer) cell lines.

Celecoxib, an anti-inflammatory drug used as a control in this study, established hydrogen bonds with Leu20 and Tyr24. Additionally, π -alkyl interactions with Pro131 and Phe133 and hydrophobic bonds with Pro131 and Met130 were observed. An unfavorable donor-donor interaction was found with Leu82 and van der Waals interactions with residues such as Glu25 and Leu80 (Fig. 3c). Comparing the binding affinities and inhibition constants, celecoxib (-18.70 kJ/mol and $527.29\text{ }\mu\text{M}$) had the best binding affinity and inhibition constant than 4'-hydroxy-7-methoxyflavanone (-28.79 kJ/mol and $9.09\text{ }\mu\text{M}$), followed by 7,2'-dihydroxy-6,8-dimethyl-4',5'-methylenedioxyflavan (-28.33 kJ/mol and $10.89\text{ }\mu\text{M}$). However, celecoxib is a small molecule and does not have similar chemical structure like catechin and sulfuretin. The structure of the flavonoids allows them to form various interactions with proteins. However, celecoxib can tightly bind IL-1B and IL-6 to effectively regulate the body's inflammatory response.

Evaluating the pharmacokinetics profile of natural compounds plays a crucial role in predicting their biological activity, as these properties are often the reason for failure of drugs in clinical trials. Several rules have been proposed to determine the suitability of small molecules as therapeutic agents, with the Lipinski rule of five (*RO5*) being the most widely used.³⁶ *RO5* states that for a compound to be a good candidate for drug development, it should not violate more than one of the following criteria: molecular weight less than 500 Da, octane–water partition coefficient less than 5, hydrogen bond donor less than or equal to 5, hydrogen bond acceptor less than or equal to 10.³⁷ This study evaluated the selected flavonoids from *Knema* species for their adsorption, distribution, metabolism, excretion (ADME) properties and drug likeness potential on Swissadme server.

The results show that all selected compounds fulfilled the Lipinski rule (Table II), indicating that they have potential as therapeutic agents. Furthermore, the pharmacokinetic profile was evaluated using human intestinal absorption (HIA), blood/brain barrier (BBB), P-glycoprotein substrate (P-gp-sub), P-glycoprotein inhibitor (P-gp inh) clearance and human colon adenocarcinoma cell line permeability (Caco-2). The results presented in Table III indicate that all phytochemicals fall within the recommended range for these parameters. An effective prediction of human intestinal absorption of drug molecules has been demonstrated using Caco-2 cell lines, and the blood/brain partition coefficient is crucial in

evaluating drugs for the central nervous system.³¹ In addition, organ toxicological evaluation for each compound was also carried out, and the results are presented in Table IV.

TABLE II. Drug-likeness properties of the selected *Knema* flavonoids and standard drug were calculated using Swissadme online webtool; *MW*: molecular weight (130.0–725.0); *HBd*: hydrogen bond donor (0.0–6.0); *HBa*: hydrogen bond acceptor (2.0–20.0); *TPSA*: topological polar surface area (7.0 to 200.0); *RO5*: rule of five (Maximum violation: 2)

Phytochemical	<i>MW</i>	<i>WLOGP</i>	<i>TPSA</i>	<i>HBa</i>	<i>HBd</i>	<i>RO5</i>
(–)-Catechin	290.27	1.22	110.38	6	5	0
Sulfuretin	270.24	2.31	86.99	5	3	0
7,2'-Dihydroxy-6,8-dimethyl-4',5'-methyl-enedioxyflavan	314.33	3.19	68.15	5	2	0
4'-Hydroxy-7-methoxyflavanone	270.28	2.78	55.76	4	1	0
Celecoxib	381.37	5.75	86.36	7	1	0

TABLE III. Pharmacokinetic profiles of the selected *Knema* flavonoids and standard drugs calculated using AdmetLab2 online webtool; *Pgp-inh*: P-glycoprotein inhibition; *Pgp-sub*: P-glycoprotein substrate; *HIA* – human intestinal absorption; *Caco-2* – human colon adenocarcinoma cell line permeability; *BBB* – blood/brain barrier; *CL*: clearance

Phytochemical	<i>Pgp-inh</i>	<i>Pgp-sub</i>	<i>HIA</i>	<i>Caco-2</i>	<i>BBB</i>	<i>CL</i>
(–)-Catechin	0.008	0.032	0.016	–5.846	0.018	17.07
Sulfuretin	0.007	0.002	0.01	–5.011	0.039	11.10
7,2'-Dihydroxy-6,8-dimethyl-4',5'-methyl-enedioxyflavan	0.017	0.007	0.002	–4.85	0.078	19.86
4'-Hydroxy-7-methoxyflavanone	0.206	0.001	0.005	–4.583	0.175	14.7
Celecoxib	0.084	0.005	0.003	–4.767	0.586	0.99

TABLE IV. Organ toxicity prediction of the selected *Knema* flavonoids and standard drug was calculated using AdmetLab2 (online webtool); *Carc*: carcinogenicity; *EC*: eye corrosion; *AM*: Ames mutagenesis; *HT*: hepatotoxicity

Phytochemical	<i>Carc</i>	<i>EC</i>	<i>AM</i>	<i>HT</i>
(–)-Catechin	0.136	0.004	0.531	0.111
Sulfuretin	0.782	0.004	0.804	0.251
7,2'-Dihydroxy-6,8-dimethyl-4',5'-methylenedioxyflavan	0.885	0.003	0.027	0.245
4'-Hydroxy-7-methoxyflavanone	0.799	0.034	0.59	0.386
Celecoxib	0.139	0.003	0.016	0.641

Most of the compounds were found to be negative for carcinogenesis, Ames toxicity, hepatotoxicity and eye corrosion, indicating their less toxicity. These findings highlight the importance of comprehensively evaluating pharmacokinetics and toxicity for developing natural compounds as novel pharmaceutical agents.

CONCLUSION

This study investigated the anti-inflammatory potential of 35 flavonoids isolated from the *Knema* genus using molecular docking against two pro-inflammatory proteins, human and murine interleukin-1B and human interleukin-6. The findings suggest that sulfuretin and (–)-catechin have high binding affinities against human interleukin-6. Moreover, 4'-hydroxy-7-methoxyflavanone and 7,2'-dihydroxy-6,8-dimethyl-4',5'-methylenedioxyflavan displayed high binding affinities against human and murine interleukin-1B and may act as promising natural anti-inflammatory agents by modulating pro-inflammatory signalling pathways. The significance of this study extends beyond the identification of specific flavonoids. It contributes to the growing body of evidence supporting the utilization of flavonoids as therapeutic agents for inflammatory diseases. Moreover, the highlighted compounds offer potential leads for future drug development in the quest for effective anti-inflammatory treatments. As a stepping stone, future investigations, including rigorous *in vitro* and *in vivo* experiments, are warranted to validate and expand upon the findings presented here, ultimately advancing the translational potential of these natural compounds in the realm of anti-inflammatory drug development.

Acknowledgements. This research was supported by the Fundamental University Research Grant (GPUF2022, 2022-0130-102-01). The authors would like to thank the Department of Chemistry, Faculty of Science and Mathematics, UPSI, for its research facilities.

ИЗВОД

РАЧУНАРСКО ИСТРАЖИВАЊЕ ФЛАВАНОИДА ИЗ РОДА *Knema* КОЈИ ИМАЈУ АНТИИНФЛАМАТОРНИ ПОТЕНЦИЈАЛ

ABUBAKAR SIDDIQ SALIHU^{1,2}, WAN MOHD NUZUL HAKIMI WAN SALLEH¹ и TOMISIN HAPPY OGUNWA^{3,4}

¹Department of Chemistry, Faculty of Science and Mathematics, Universiti Pendidikan Sultan Idris, 35900 Tanjong Malim, Perak, Malaysia, ²Department of Pure and Industrial Chemistry, Faculty of Natural and Applied Sciences, Umara Musa Yar'adua University, Katsina, Nigeria, ³Centre for Biocomputing and Drug Design, Adekunle Ajasin University, Akungba-Akoko, Ondo State, Nigeria и ⁴Department of Biochemistry, Adekunle Ajasin University, Akungba-Akoko, Ondo State, Nigeria

Запаљење је раширени биолошки процес повезан са разним болестима, и представља значајан изазов за здравље у свету. Скорија истраживања која циљају нове антиинфламаторне лекове дају предност једињењима добијеним из биљака због њихове исплативости и минималних споредних ефеката у поређењу са синтетичким лековима. Флавоноиди, полифенолна једињења у биљкама, показују потенцијал за третирање болести повезаних са запаљењима. Овај рад процењује антиинфламаторну активност флавоноида из рода *Knema*, из породице Myristicaceae. Фокусирали смо се на инхибирање два проинфламаторна протеина, хуманог и мишјег интерлеукина-1Б (IL-1) и хуманог интерлеукина-6 (IL-6). Молекулски докинг и ADMET предвиђање су идентификовали сулфуретин и (–)-катехин са високим везивним афинитетом за IL-6, док 4'-хидрокси-7-метоксифлаванон и 7,2'-дихирокси-6,8-диметил-4',5'-метилендиокси-флаван стабилно везују IL-6. Анализе молекулских интеракција откривају да водоничне и π-σ везе доприносе ин-

еракцији. Посебно, ови флаваноиди испољавају афинитете упоредиве са селеко-ксибом. Наша рачунарска предвиђања подржавају прикладност ових флаваноида као кандидата за лекове, указујући да су они обећавајући природни противупални агенси способни да модулирају проинфламаторне сигналне путеве.

(Примљено 4. септембра, ревидирано 25. октобра, прихваћено 11. децембра 2023)

REFERENCES

1. A. M Soliman, D. R. Barreda, *Int. J. Mol. Sci.* **24** (2023) 641 (<https://doi.org/10.3390/ijms24010641>)
2. M. A. Santos, F. N. Franco, C. A. Caldeira, G. R. de Araujo, A. Vieira, M. M. Chaves, *Arch. Gerontol. Geriatr.* **107** (2023) 104895 (<https://doi.org/10.1016/j.archger.2022.104895>)
3. R. Tyszkowski, R. Mehrzad, *Inflamm. Obes.* (2023) 19 (<https://doi.org/10.1016/B978-0-323-90960-0.00009-6>)
4. C. Balchin, A. L. Tan, O. J. Wilson, J. McKenna, A. Stavropoulos-Kalinoglou, *Rheumatol. Adv. Pract.* **7** (2022) 1 (<https://doi.org/10.1093/rap/rkac110>)
5. C. Lu, Q. Liu, M. Deng, H. Liao, X. Yang, P. Ma, *Sci. Total Environ.* **869** (2023) 161760 (<https://doi.org/10.1016/j.scitotenv.2023.161760>)
6. L. Falkowski, J. Buddenkotte, A. Datsi, *Semin. Cell Dev. Biol.* (2023) (<https://doi.org/10.1016/j.semcedb.2023.01.008>)
7. M. Sun, L. Wang, X. Wang, L. Tong, J. Fang, Y. Wang, Y. Yang, B. Li, *Food Funct.* **14** (2023) 1003 (<https://doi.org/10.1039/D2FO01832B>)
8. A. Y. Arikawa, D. Kraft, M. Harris, D. Perez, M. Bednarzyk, J. M. Ross, *J. Nutr. Health* (2023) (<https://doi.org/10.1177/02601060231151263>)
9. T. Powolny, R. Scheifler, F. Raoul, M. C. Clémentine Fritsch, *Environ. Pollut.* **317** (2022) 120675 (<https://doi.org/10.1016/j.envpol.2022.120675>)
10. C. Russo, A. Maugeri, L. Musumeci, G. De Sarro, S. Cirmi, M. Navarra, *Int. J. Mol. Sci.* **24** (2023) 2899 (<https://doi.org/10.3390/ijms24032899>)
11. S. J. More, S. S. Tandulwadkar, A. R. Balap, S. Lohidasan, A. Sinnathambi, K. R. Mahadik, *Future J. Pharm. Sci.* **9** (2023) 1 (<https://doi.org/10.1186/s43094-022-00450-4>)
12. D. Minhas, A. Nidhaan, M. E. Husni, *Rheum. Dis. Clin. North Am.* **49** (2023) 179 ([https://www.rheumatic.theclinics.com/article/S0889-857X\(22\)00075-8/pdf](https://www.rheumatic.theclinics.com/article/S0889-857X(22)00075-8/pdf))
13. A. P. Das, S. M. Agarwal, *Mol. Divers.* (2023) 1 (<https://doi.org/10.1007/s11030-022-10590-7>)
14. D. K. Mahapatra, S. K. Bharti, *Biologically Active Small Molecules*, CRC Press, Boca Raton, FL, 2023, pp. 17–44 (<https://www.routledge.com/Biologically-Active-Small-Molecules-Modern-Applications-and-Therapeutic/Mahapatra-Bharti/p/book/9781774910689>)
15. I. A. Oreagba, K. A. Oshikoya, *Med. Entrepren.* (2023) 325 (https://doi.org/10.1007/978-981-19-6696-5_21)
16. S. E. Bianchi, L. A. Frank, I. A. Alves, M. R. Serafini, *Drug Discovery from Natural Products: An Approach Using Recent Patents*, CRC Press, Boca Raton, FL, 2022, pp. 1–14 (<https://doi.org/10.1201/9781003231745-1>)
17. S. S. Rabidas, C. Prakash, J. Tyagi, J. Suryavanshi, P. Kumar, J. Bhattacharya, D. Sharma, *Brain Sci.* **13** (2023) 102 (<https://doi.org/10.3390/brainsci13010102>)

18. X. Yang, Y. Liu, C. Zhong, J. Hu, S. Xu, P. Zhang, L. He, *BMC Complement. Med. Ther.* **23** (2023) 23 (<https://doi.org/10.1186/s12906-023-03851-x>)
19. T. Malik, R. Sharma, P. S. Panesar, R. Gehlot, O. Tokusoglu, S. B. Dhull, H. Vural, A. Singh, *J. Food Proces. Preserv.* (2021) e15848 (<https://doi.org/10.1111/jfpp.15848>)
20. A. Kadukkattil Ramanunny, S. Wadhwa, S. Kumar Singh, J. Nambukulangara Vijayan, *Herbs, Spices and Their Roles in Nutraceuticals and Functional Foods*, Academic Press, Cambridge, MA, 2023, pp. 279–307 (<https://doi.org/10.1016/B978-0-323-90794-1.12001-0>)
21. W. M. N. H. W. Salleh, F. Ahmad, *Pharm. Sci.* **23** (2017) 249 (<https://doi.org/10.15171/PS.2017.37>)
22. A. S. Salihu, W. M. N. H. W. Salleh, *Vietnam J. Chem.* **61** (2023) 397 (<https://onlinelibrary.wiley.com/doi/full/10.1002/vjch.202200224>)
23. N. M. O’Boyle, M. Banck, C. A. James, C. Morley, T. Vandermeersch, G. R. Hutchison, *J. Cheminformatics* **3** (2011) (<https://doi.org/10.1186/1758-2946-3-33>)
24. S. Dallakyan, A. J. Olson, *Methods Mol. Biol.* **1263** (2014) 243 (https://doi.org/10.1007/978-1-4939-2269-7_19)
25. N. Inandiklioglu, A. Tas, T. Agbektas, Z. Tunçbilek, K. Y. Raheem, G. Cinar, Y. Silig, *J. Mol. Struct.* **1273** (2023) 134346 (<https://doi.org/10.1016/j.molstruc.2022.134346>)
26. B. Dassault, *Systèmes, Discovery Studio client*, San Diego, CA, 2021 (<https://discover.3ds.com/discovery-studio-visualizer-download>)
27. T. D. Goddard, C. C. Huang, E. C. Meng, E. F. Pettersen, G. S. Couch, J. H. Morris, T. E. Ferrin, *Prot. Sci.* **27** (2017) 14 (<https://doi.org/10.1002/pro.3235>)
28. G. M. Morris, R. Huey, W. Lindstrom, M. F. Sanner, R. K. Belew, D. S. Goodsell, A. J. Olson, *J. Comput. Chem.* **30** (2009) 2785 (<https://doi.org/10.1002/jcc.21256>)
29. H. A. Salman, A. S. Yaakop, S. Aladaileh, M. Mustafa, M. Gharaibeh, U. M. Kahar, *Heliyon* **9** (2023) e12730 (<https://doi.org/10.1016/j.heliyon.2022.e12730>)
30. S. Şahin, N. N. Can, *Polycycl. Arom. Comp.* (2023) 1 (<https://doi.org/10.1080/10406638.2022.2161585>)
31. D. A. Omoboyowa, M. N. Iqbal, T. A. Balogun, D. S. Bodun, J. O. Fatoki, O. E. Oyeneyin, *Comput. Toxicol.* **23** (2022) 100235 (<https://doi.org/10.1016/j.comtox.2022.100235>)
32. D.S. Lee, G.-S. Jeong, B. Li, H. Park, Y.C. Kim, *Int. Immunopharmacol.* **10** (2010) 850 (<http://dx.doi.org/10.1016/j.intimp.2010.04.019>)
33. A.W. Cheng, X. Tan, J.Y. Sun, C.M. Gu, C. Liu, X. Guo, *Plos One* **14** (2019) e0217090 (<https://doi.org/10.1371/journal.pone.0217090>)
34. E. Gligoric, R. Ilic, B. Teofilovic, N. Grujic-Letic, *Int. J. Mol. Sci.* **24** (2023) 11848 (<https://doi.org/10.3390/ijms241411848>)
35. N. D. Mahmood, N. L. M. Nasir, M. S. Rofiee, S. F. M. Tohid, S. M. Ching, L. K. Teh, M. Z. Salleh, Z. A. Zakaria, *Pharm. Biol.* **52** (2014) 1598 (<https://doi.org/10.3109/13880209.2014.908397>)
36. D. A. Omoboyowa, O. M. Omomule, T. A. Balogun, O. A. Saibu, D. S. Metibemu, *Phytomed. Plus* **1** (2021) 100145 (<https://doi.org/10.1016/j.phyplu.2021.100145>)
37. C. A. Lipinski, F. Lombardo, B. W. Dominy, P. J. Feeney, *Adv. Drug Deliv. Rev.* **23** (1997) 3 ([https://doi.org/10.1016/S0169-409X\(96\)00423-1](https://doi.org/10.1016/S0169-409X(96)00423-1)).



Co-pyrolysis of various plastic waste components as an environmentally sustainable source of alternative fuels

IVANA JOVANČIĆEVIĆ¹, MALIŠA ANTIĆ², GORDANA GAJICA³
and JAN SCHWARZBAUER^{1*}

¹RWTH Aachen University, Institute of Organic Biochemistry in Geo-Systems, Lochnerstrasse 4–20, 52056, Aachen, Germany, ²University of Belgrade, Faculty of Agriculture, Nemanjina 6, 11 080, Zemun, Belgrade, Serbia and ³University of Belgrade, Institute of Chemistry, Technology and Metallurgy, Njegoševa 12, 11000 Belgrade, Serbia

(Received 7 February, revised 1 March, accepted 12 April 2024)

Abstract: In this study, pyrolysis and co-pyrolysis of commonly used plastic materials (polyethylene terephthalate – PET, high density polyethylene – HDPE, and polystyrene – PS) were conducted to analyse the chemical composition of the corresponding pyrolyzates. Different ratios of plastic materials were applied to obtain a composition of aliphatic and aromatic degradation products that closely resemble those of conventional fossil fuels. The systematic chemical variations can act as base for evaluating this approach as a sustainable source of alternative fuels. HDPE revealed an aliphatic composition of degradation products, while PS and PET produced only aromatic compounds. Quantitative analysis of the obtained pyrolyzates revealed a clear correlation of initial proportion with the resulting quantitative product composition. The generation of individual pyrolysis products gave a high reproducibility. However, it became evident that the decomposition products of PS consistently emerged as the most prominent among all tested HDPE/PS mixtures. The ratio of HDPE:PS = 1:3 showed 96 % of the aromatic compounds as PS decomposition products. PET revealed a oxygen containing structure of the products, contributing to 83 % of the HDPE:PET = 1:3 mixture. These results gain insights into the potential of plastic waste as a sustainable source for alternative fuels and valuable chemicals.

Keywords: co-pyrolysis; synthetic polymers; plastic-derived-fuel; GC–MS; sustainability.

INTRODUCTION

Over the past few decades, plastic materials have gained attention in various contexts. They offer exceptional versatility, functionality and economic efficiency. Yet, the increase in their use and production lead to massive waste gener-

* Corresponding author. E-mail: jan.schwarzauer@emr.rwth-aachen.de
<https://doi.org/10.2298/JSC240207046J>

ation, posing a significant environmental threat. Furthermore, environmental concerns go beyond plastic waste to include additives added to plastic production to improve their properties. These additives include antioxidants and UV stabilizers for heat, aging and light resistance, pigments and dye stuffs to modify color and functional agents such as plasticizers, surfactants and flame retardants. In Germany, 18.9 million tons (228 kg per capita) of packaging waste were generated in 2019, which significantly exceeds the EU average of 177 kg per capita.¹ Therefore, it is crucial to explore alternatives that have the potential to prevent undesirable landfilling and mitigate the unacceptable littering of the environment.

Pyrolysis of synthetic polymers is one efficient approach to reduce waste, while also allowing for the recovery of monomers and other valuable materials.² Given the high carbon and hydrogen content of synthetic polymers, pyrolysis of these materials can produce high-quality liquid oils, with a high calorific value and a high proportion of compounds similar and compatible with fossil fuels.³ This expands the options for plastic waste management and reduces reliance on petroleum-based resources. In this sense, Rehan *et al.* (2016) investigated the potential of pyrolysis technology for thermal conversion of municipal plastic waste from Makkah city, to obtain liquid fuel. The energy content of 40 MJ kg⁻¹ of this waste derived fuel was found to be similar to conventional diesel.⁴ Further on, Achilias *et al.* (2007) reported a series of alkanes and alkenes recovered by pyrolyzing raw materials made out of polypropylene (PP) in a laboratory fixed bed reactor.⁵

Co-pyrolysis of different feedstocks has recently gained significant attention as a promising approach to enhance both the yields and quality of biofuels. Plastic materials have demonstrated high potential as catalysts in the fuel production through biomass pyrolysis.^{6–8} Furthermore, co-pyrolysis of different plastic materials has gained considerable attention as a promising approach to enhance plastic-derived fuel yields and quality, overcoming the problems associated with heterogeneous plastic waste and contributing to a more efficient and sustainable recycling process. Combining various plastics during pyrolysis can lead to synergistic effects, resulting in increased oil yield and improved fuel properties compared to individual plastic pyrolysis.^{9,10} Therefore, it is important to evaluate the degree of pyrolytic interactions between different feedstocks and to determine whether the additivity rule can be applied to predict the product yields from co-pyrolysis experiments.

In this study, pyrolysis and co-pyrolysis of commonly used plastic materials (PET, HDPE and PS) were conducted to analyse the chemical composition of the corresponding pyrolysates. These characterisations gain insights into the potential of plastic waste pyrolysis as a sustainable source for alternative fuels and valuable chemicals. In more detail, the experiments in this study involved the use of different ratios of plastic materials to produce a composition of aliphatic and

aromatic degradation products that closely resemble those of conventional fossil fuels. Hence, a comparison between the composition of the plastic derived oils and diesel fuel was conducted to assess their similarity and potential viability as a substitute. Furthermore, the study aimed to investigate any cross-reaction effects arising from the interactions between different polymers during co-pyrolysis. Additionally, the study also examined the presence of additives in plastic waste to gain insights into their potential influence on the pyrolysis process and the resulting plastic-derived oil composition.

EXPERIMENTAL

Chemicals and reference compounds

Standard reference materials of PE, PS and PET were purchased from Geyer Th. GmbH & Co. KG. Acetone and hexane used for offline pyrolysis were purchased from Geyer Th. GmbH & Co. KG as well.

Plastic waste material such as food packaging, food and cosmetic containers, plastic furniture, plastic bottles, *etc.*, have been collected from several households in Aachen, Germany. The collected material consists of different synthetic polymers such as: HDPE, PS and PET. The collected plastic waste was selected for this study due to its high production and utilization rate as well as its chemical recycling potential.

Continuous flow off-line pyrolysis

Off-line pyrolysis experiments were performed on a MTF 10/15/130 model Carbolite tube furnace. The samples were placed in aluminum-foil vessels in the middle of a quartz tube (150 mm in length and 15 mm in diameter) that was set within the furnace. On one side, the quartz tube was connected to a continuous stream of nitrogen, while the other side was connected to a flask tube filled with 4 mL of acetone and cooled with dry ice and ethanol. Pyrolysis experiments were performed under the following conditions: temperature of 450 °C, no heating rate, duration time 30 min and constant nitrogen flow of 50 mL min⁻¹. After pyrolysis, the volume of the pyrolysates sampled in the cold trap was reduced to approximately 2 mL and dried over anhydrous sodium sulphate. For qualitative and quantitative analysis, pyrolysates were measured by gas chromatography/mass spectrometry (GC/MS). Furthermore, GC/MS analysis was also applied for the identification of additives present in plastic waste.

The described procedure was applied to pyrolysis and co-pyrolysis of HDPE, PS and PET standard reference materials and corresponding municipal plastic waste. Co-pyrolysis experiments were performed with compositions of the following ratios:

1. HDPE:PS = 1:1; 1:3; 3:1; 9:1;
2. HDPE:PET = 1:1; 1:3; 3:1; 9:1;
3. HDPE:PS:PET = 1:1:1; 8:1:1.

The maximum sample weight for co-pyrolysis experiments was 100 mg.

Sample preparation

The collected plastic waste samples were categorized according to their specific product labels. The material was first washed and air-dried, cut into smaller particles (approx. 2 cm) with scissors and then shredded into particles smaller than 5 mm. Shredding was carried out under a high flow of nitrogen gas, which was used to cool the samples and prevent them from melting.

GC/MS analysis

Qualitative and quantitative analysis of the obtained pyrolyzates were performed on an Thermo Quest Trace GC gas chromatograph connected to Thermo Quest Trace MS single quadrupole mass spectrometer, equipped with a ZB-5 capillary column (30 mm×0.25 mm ID 0.25 µm film). The chromatograph conditions were the following: 1 µL splitless injection (splitless time 60 s; injector temperature 270 °C), oven temperature heated from 80 °C (held 3 min) at 4 °C min⁻¹ to 310 °C (held 20 min) and helium carrier gas flow of 1.5 mL min⁻¹. The mass spectrometer was operated in an electron impact ionization mode (EI⁺, 70 eV) with a source temperature of 200 °C and an interface temperature of 270 °C scanning from *m/z* 35 to 500 in full scan mode with a scan rate of 0.67 scan s⁻¹.

The identification was based on a detailed interpretation of the mass spectra and comparison with the NIST Mass Spectral Library, as well as comparison with literature data. Calculation of relative quantitative compositions was based on integration of ion chromatograms and corresponding peak areas. A surrogate standard solution containing the reference compounds fluoroacetophenone (5.8 ng µL⁻¹), benzophenone-d10 (6.3 ng µL⁻¹), and hexadecane-d34 (6.0 ng µL⁻¹) was used for quantitative analysis of the obtained pyrolysates.

RESULTS AND DISCUSSION

The development and utilization of plastic-derived oils from pyrolysis processes require comprehensive qualitative and quantitative chemical characterization of the pyrolysis products to ensure desired technical specification. This study employs an analytical approach to analyze and quantify compounds present in co-pyrolysis products of common polymers, emphasizing the principal composition of aliphatic and aromatic hydrocarbons as well as functionalized compounds, similar to characterizing crude oil and related fossil matter.

For the pyrolysis experiments, HDPE, PS and PET in varying compositions have been used. The selection of these particular polymers was based on their distinct chemical characteristics, as PE is composed of a long aliphatic chain, in contrast to the aromatic constituents of PS and PET. Furthermore, chemical composition of the pyrolysis resulting oils was investigated (additional data are given in the Supplementary material to this paper).

Pyrolysis of synthetic polymers

As a preliminary step, offline pyrolysis experiments were performed on reference material as well as raw waste samples consisting of PE, PET, and PS, to analyze accurately the pattern of their degradation products. Further on, the samples have been analyzed for potential impurities that can remarkably affect the chemical composition of the pyrolysates.

Pyrolysis of both PE reference material, and HDPE waste samples, resulted in the formation of white insoluble flocks forming wax as one of the pyrolysis products. The obtained wax was insoluble in common solvents like acetone, dichloromethane and hexane. The formation of wax during pyrolysis of low-density polyethylene (LDPE) was observed already by Wiliams and Wiliams (1997) who reported that the obtained wax product was comprised of long chain ali-

phatic compounds of up to 57 carbon atoms.¹¹ For a technical usage, the obtained wax was proposed to be utilized as a chemical feedstock in the petrochemical industry, where a wide range of high carbon olefins is highly demanded.⁹ Wax was isolated from the acetone fraction and was not discussed in further work.

HDPE, PS and PET

Offline pyrolysis of both PE reference material and the corresponding waste material (HDPE) revealed a pattern composed of a sequence of triplets, each consisting of *n*-alkadienes, *n*-alkenes and *n*-alkanes forming a homologues series of increasing chain lengths (see Fig. 1). Generally, the resulting pyrolysate was composed of 47.5 % of *n*-alkanes, followed by 44 % *n*-alkenes and 8.5 % *n*-alkadienes. Based on three measurements, the three compound groups exhibited a relative standard deviation in the range of 30 %.

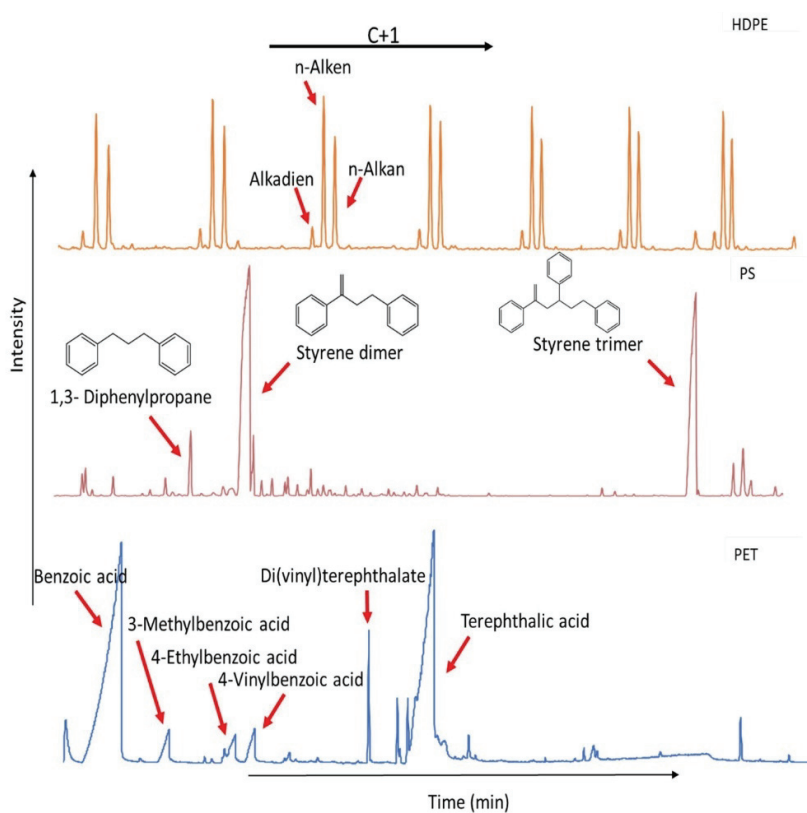


Fig. 1. TIC of pyrolysis experiments conducted on HDPE, PET; and PS.

Pyrolysis experiments on PET manifested a diverse range of monocyclic aromatic degradation products, with benzoic acid, and terephthalic acid identified

as the most prominent products (see Fig. 1) constituting 32 and 56 % of the resulting pyrolysis products, respectively. Notably, multiple repetitions of the experiments revealed variations in their proportions of less than 10 %. These products are in accordance with the on-line degradation products identified, *e.g.*, by Dziwiński *et al.*¹²

When subjected to off-line pyrolysis, PS decomposed to form dark viscous oil. As expected, GC/MS analysis of this oil revealed a more aromatic composition of the pyrolysis products, with three main degradation products identified as 1,3-diphenylpropane, 2,4-diphenylbutene and 2,4,6-triphenylhexene (see Fig. 1). They constituted 4, 40 and 54 % of the resulting pyrolysis products, respectively, with variations in their proportions approximately around 20 %. These products represent the group of styrene oligomers, or more precisely, dimers and trimers of the styrene monomer.¹³ In addition to these main product groups, pyrolysis of PS revealed numerous compounds with significantly lower intensities. Some of them were identified as: 1,2-diphenylethylene, bibenzyl, 1,2-diphenylpropane, 1,2-diphenylpropane, 1,2,3,4-tetrahydro-1-phenylnaphthalene, 1,4-diphenyl-1,3-butadiene and 1-phenylnaphthalene. Each of these products accounted for less than 0.5 % of the total pyrolisate and, therefore, were not included in further quantitative analysis. Finally, compared to pyrolysis experiments applied on reference material samples, pyrolysis of plastic waste samples HDPE, PS and PET revealed no visible changes regarding the chemical composition of the degradation products.

Co-pyrolysis experiments

Co-pyrolysis experiments on defined plastic mixtures produced a blend of all compounds already identified in the single pyrolysis experiments. Noteworthy, no further or new degradation products were observed (as illustrated in Fig. 2) pointing to the absence of cross reaction between the different components during pyrolysis. Both, HDPE/PS and HDPE/PET mixtures revealed an aliphatic pattern within the C₁₂–C₂₇ range as HDPE contribution. The obtained range of aliphatic compounds is very valuable, since these chain length fits the C₁₈–C₂₂ range in the production of important raw materials in the detergent industry such as sodium lauryl ether sulphate and alkyl benzene sulphonate.⁹ In the HDPE/PS experiments, the main aromatic products result directly from the pyrolysis of PS, namely 1,3-diphenylpropane, 2,4-diphenylbutene and 2,4,6-triphenylhexene. Within the range of preselected mixture rates from 1:3 to 9:1 a clear dominance of aromatic products was observed, whereby, a decrease in the initial amount of PS resulted in a proportional decrease of these aromatic products. Fig. 3a illustrates this relationship, indicating that a 1:1 ratio of HDPE to PS yielded nearly 90 % aromatic compounds and only 10 % aliphatic compounds consisting in detail of 4.4 % *n*-alkanes, 4.5 % *n*-alkenes, and 1 % *n*-alkadienes.

Pyrolysis applied to a 3:1 mixture yielded approximately 22.7 % aliphatic hydrocarbons and 77.3 % aromatic hydrocarbons. Only in the case of a 9:1 ratio, a similar proportion of aliphatic hydrocarbons as compared to aromatic compounds was observed with 26 % *n*-alkenes, 22 % *n*-alkanes and 3 % *n*-alkadienes. These quantitative observations clearly point to: *i*) a higher relative pyrolysis yield of the aliphatic polymer HDPE and *ii*) a clear correlation of initial proportion with the resulting quantitative product composition.

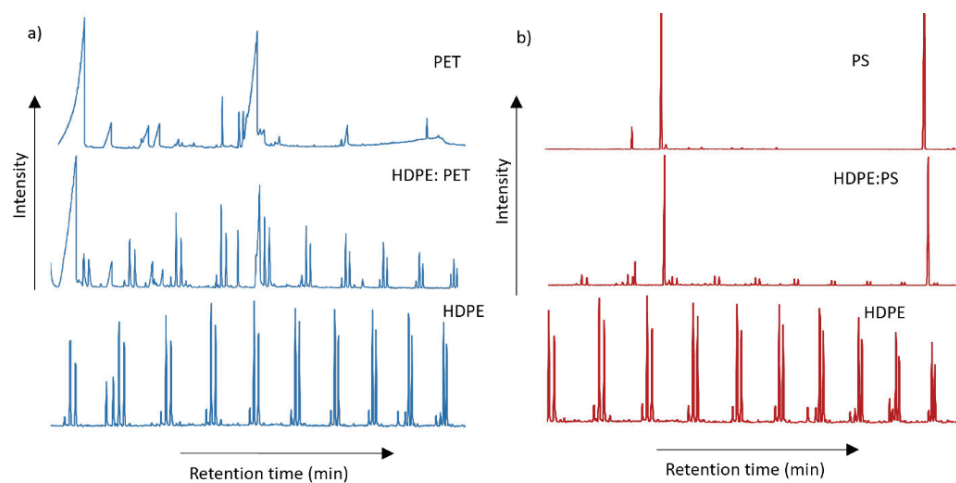


Fig. 2. TIC of the pyrolysis and co-pyrolysis experiments on: a) PET, HDPE:PET and HDPE and b) PS, HDPE:PS and HDPE experiments.

The quantitative results of the pyrolysis products derived from HDPE:PET mixtures are illustrated in Fig. 3b. These findings indicate that oxygen-containing aromatic hydrocarbons represent the most prominent group, accounting for nearly 62 % of the pyrolysis products in the HDPE:PET = 1:1 experiments. Here, benzoic acid was the most abundant oxygen-containing compound identified in the co-pyrolysis experiments. In the case of HDPE:PET = 3:1 ratio, the pyrolysis products were predominantly composed of aliphatic compounds, comprising approximately 60 % of the total amount of the detected pyrolysis products. In the HDPE:PET = 9:1 approach, this predominance of aliphatic compounds reached nearly 76 %. Noteworthy, based on the presented results, the individual products demonstrated high reproducibility. As shown in Fig. 3, the homologous series of aliphatic compounds maintains a consistent order in the sequence of the obtained products.

As a final approach, the co-pyrolysis of all three polymers have been systematically studied. In the co-pyrolysis experiments involving equimolar ratios of all three polymers, no novel degradation products were detected pointing once again to the absence of cross reaction of all components during the pyrolysis process.

Aromatic and oxygen containing compounds derived from PS and PET, dominated with a significant majority (89.3 %) of the pyrolysis products. Within the group of aromatic compounds, approximately 52 % were identified as oxygen-containing aromatic compounds. Only 11.7 % of the pyrolysates were attributed to aliphatic compounds, as depicted in Fig. 3c.

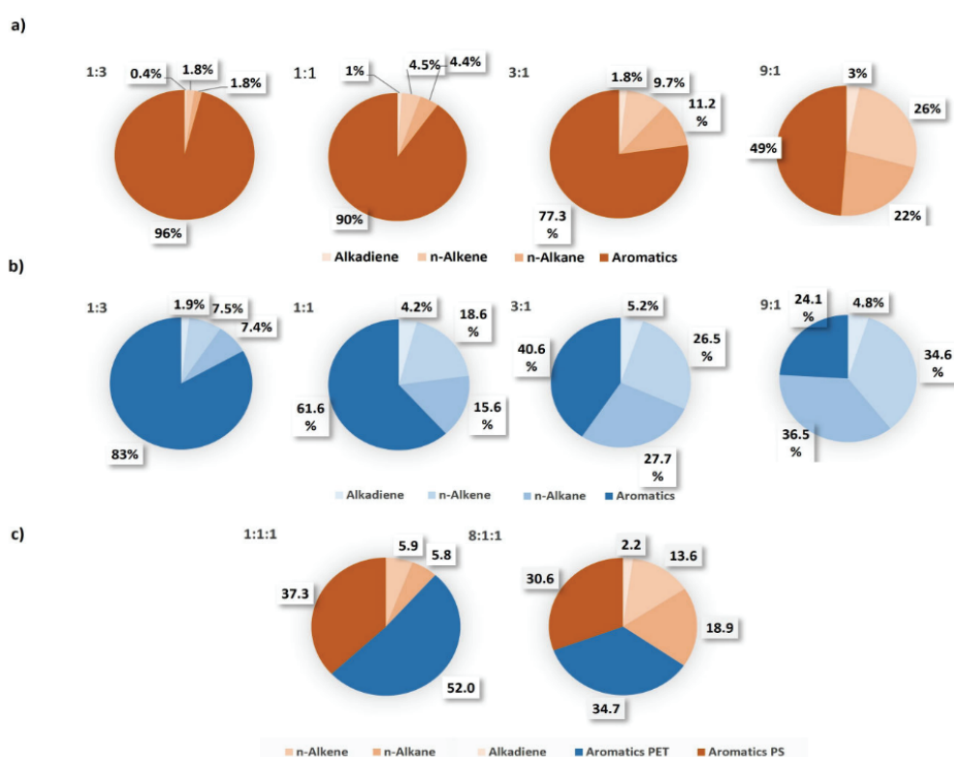


Fig. 3. Pyrolysis product groups of: a) HDPE:PS; b) HDPE:PET; c) HDPE:PS:PET co-pyrolysis experiments given in %. Only compounds constituting 1 % or more of the pyrolysis products composition are highlighted in the figure.

The quantities are presented as percentages.

Based on these results, an experimental set-up with a significant higher proportion of HDPE was applied. This pyrolysis of a mixture of HDPE:PET:PS = 8:1:1 yielded a higher amount of aliphatic products (34.7 %), along with oxygenated compounds (34.7 %) and aromatic products resulting from the degradation of PS (30.6 %).

Additives

Plastic materials benefit from the addition of substances known as additives, which serve to enhance or alter their properties. These substances are introduced

during the manufacturing process to enhance properties like strength, flexibility, and colour, including plasticizers, UV stabilizers, flame retardants, and colorants.¹⁴ However, some additives may pose risks to health and the environment.^{14,15} During plastic-derived fuel production via pyrolysis, some additives may not fully degrade, potentially persisting in the resulting oil. In addition to the characteristic pyrolysis products various polymer additives present in the samples were also noticed and it is important to acknowledge these with respect to the proposed production of plastic-derived fuels. The identified additives are listed in Table I.

TABLE I. The identified additives in the obtained pyrolyzates

Additive	IUPAC name	Polymer	Uses	Safety hazards	CAS registry number
2,4-DTBP	2,4-Di-tert-butylphenol	HDPE	Intermediate in the production of UV stabilizers and antioxidants. ¹⁶	Causes skin, eye and respiratory irritation. Very toxic to aquatic life. ¹⁶	96-76-4
Bumetizole UV326	2-(3-tert-butyl-2-hydroxy-5-methylphenyl)-5-chlorobenzotriazole	HDPE	UV stabilizer, enhances the light resistance of polymers. ¹⁷	May lead to metabolic imbalance; toxic to aquatic life. ¹⁷	3896-11-5
α -Hexyl-cinnamaldehyde	2-(Phenylmethylene)-octanal	HDPE, PET	Fragrance, odor agents. ¹⁸	Causes an allergic skin reaction; toxic to aquatic life with long lasting effects. ¹⁸	101-86-0
Isopropyl myristate	1-Methylethyl ester-tetradecanoic acid	HDPE, PET	Thickener and a lubricant in beauty products. ¹⁹	Can cause skin irritation. ¹⁹	110-27-0
Terphenyl	Diphenylbenzene	HDPE, PET, PS	Terphenyl mixtures are used as textile dye carriers and as intermediates for lubricants. ²⁰	Can cause skin and eyes irritation; may affect the liver and kidneys. ²⁰	26140-60-3

Aspects of application for plastic-derived fuel production

For an efficient technical usage of plastic-derived fuels resulting from plastic pyrolysis, the chemical composition needs to be compared to established fossil fuel products, since the basic properties of such fossil fuels are based on their chemical constitution. Diesel fuel typically consists of around 75 % aliphatic hydrocarbons within the C₉–C₂₅ range, while approximately 25 % of its compos-

ition comprises aromatic hydrocarbons like benzene, styrene, phenanthrene, fluoranthene, pyrene, benz(a)anthracene, chrysene and benzo(a)pyrene.^{21–23} However, the chemical composition of diesel fuel can vary depending on its origin or source. The findings of this study revealed a striking similarity in the chemical composition between the plastic oils obtained and diesel. These similarities are visualized in Fig. 4, where the chromatograms of one diesel derived from the Caspian Sea is compared with those of the HDPE:PS and HDPE:PET experiments. The chemical composition of the obtained plastic-derived oil shows similarities to diesel especially in terms of its aliphatic composition, mainly in the range of C₁₂ to C₂₇ *n*-alkanes. Noteworthy, in the refining process of crude oil, alkenes are generated through the cracking of heavier fractions, but they are not typically found in diesel. Alkenes generally exist in lower concentrations, ranging from 0 to 10 %, and within a narrower carbon number range.^{24,25} Unsaturated hydrocarbons prove less suitable for fuel combustion due to their tendency to result in incomplete combustion, thereby generating higher levels of carbon monoxide.²⁶ To address this limitation, additional improvements in the composition of plastic-pyrolysis oil are necessary, specifically targeting the presence of *n*-alkenes and alkadienes. One possibility is an additional hydrogenation of the double bond. Prior research has demonstrated that this transformative process effectively converts the alkene products present in pyrolysis oil into alkanes.^{26–29}

An essential parameter in plastic-derived fuel production is the octane number, which measures a fuel's resistance to auto-ignition and explosive combustion in internal combustion engines. Higher octane numbers indicate greater resistance to auto-ignition under increased pressure and temperature before ignition by the engine spark plug. While straight chain aliphatic compounds exhibit lower octane ratings, aromatic compounds are valued for their higher-octane values. Therefore, the inclusion of aromatic compounds is important in fuel formulations.^{30,31} On the other hand, these aromatic constituents are the predominant source of particulate matter (PM) emissions and in that way represent the major air pollutants affecting human health.³² In this work, the co-pyrolysis mixtures of HDPE:PS and HDPE:PET in ratios of 1:1, 1:3 and 3:1, as well as the pyrolysis of all three polymers in ratios of 1:1:1 and 8:1:1 were found to generate a significant quantity of aromatic compounds, which makes these ratios unsuitable for fuel production.

While conventional fuels typically contain oxygen, sulfur and nitrogen compounds (NSO fraction) within specific ranges,^{33,34} plastic-derived oils offer potential advantages in minimizing these elements. While some research has noted high sulfur content in plastic waste pyrolysis,³⁵ this study did not identify sulfur or nitrogen compounds in the pyrolysates examined. This absence suggests a potential environmental advantage of plastic-derived oils over conventional fuels, particularly regarding emissions of sulfur oxides and other pollutants.

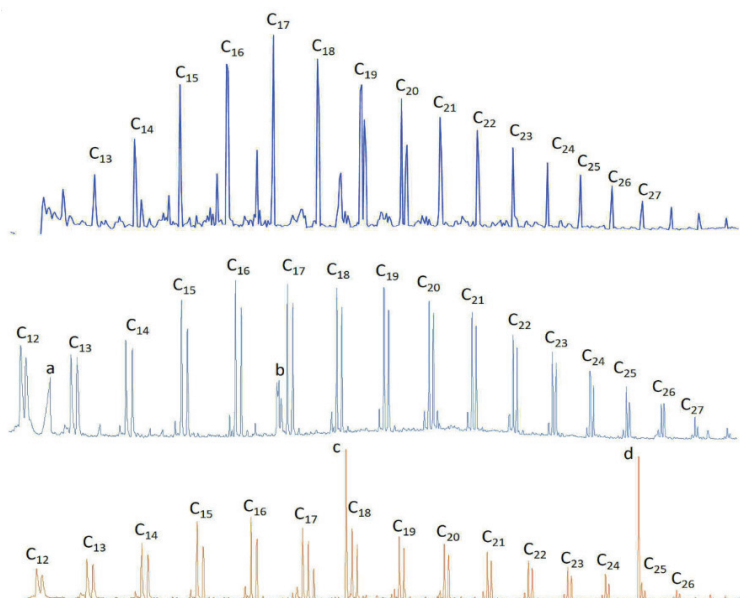


Fig. 4. Top: Total ion chromatogram (TIC) of pure diesel fuel (Caspian Sea). Middle: TIC of co-pyrolysis experiments using a 9:1 mixture of HDPE : PET. C₁₂–C₂₇ represent the carbon numbers of the aliphatic compounds in the pyrolysis product; a – benzoic acid; b – terephthalic acid. Bottom: TIC of co-pyrolysis experiment using a 9:1 mixture of HDPE:PS (C₁₂–C₂₇ represent the carbon numbers of the aliphatic compounds in the pyrolysis product; c – styrene dimer; d – styrene trimer).

The production of fuel through pyrolysis using plastic waste entails numerous technical and environmental factors to consider, including the handling of waste and the effectiveness of the pyrolysis process. Based on the findings obtained in the present study, it's essential to consider the proportions and types of plastics used. Additionally, increasing the proportion of HDPE plastic waste in pyrolysis feedstock can align the chemical composition with desired specifications. Given the high production volume of PE like plastic materials,³⁶ directing more PE waste towards recycling and sustainable practices would promote environmental benefits and align with industry sustainability goals.

CONCLUSION

The findings of this study do not only contribute to the understanding of polymer waste management but also hold promise for environmentally sustainable plastic-derived fuel production. Through systematic pyrolysis experiments of plastic waste samples composed of HDPE, PS, and PET and following chemical characterisation of the pyrolyzates by GC/MS analysis, valuable insights have been gained into the composition of degradation products. These systematic chemical variations can act as base for evaluating this approach as a sustainable

source of alternative fuels. The study highlights distinct behaviors of polymers during pyrolysis with HDPE revealing aliphatic compounds, PS aromatic compounds and PET contributing to oxygen-containing structures. However, an essential observation from the investigation is the substantial influence of PS and PET decomposition in HDPE:PS and HDPE:PET mixtures. This influence accounts for 90 % of the pyrolysate obtained from the HDPE:PS 1:1 mixture and 62 % from the HDPE:PET 1:1 mixture. Increasing the HDPE proportion in the pyrolysis feedstock holds promise for high-quality plastic-derived oil production aligning with conventional fossil fuel constituents.

It is important to emphasize that this approach is a proposition, representing a preliminary step in the pursuit of plastic-derived fuel development. Further comprehensive characterization and optimization of the obtained fuel are likely necessary to fine-tune its properties and performance. In this pursuit, the exploration of various additives may become instrumental, offering opportunities to enhance the fuel's quality and customize it to specific applications.

SUPPLEMENTARY MATERIAL

Additional data and information are available electronically at the pages of journal website: <https://www.shd-pub.org.rs/index.php/JSCS/article/view/12806>, or from the corresponding author on request.

Acknowledgement. The authors acknowledge the Federal Ministry of Education and Research (Bundesministerium für Bildung und Forschung) for the support.

ИЗВОД

КОПИРОЛИЗА РАЗЛИЧИТИХ КОМПОНЕНТИ ПЛАСТИЧНОГ ОТПАДА КАО ЕКОЛОШКИ ОДРЖИВ ИЗВОР АЛТЕРНАТИВНИХ ГОРИВА

ИВАНА ЈОВАНЧИЋЕВИЋ¹, МАЛИША АНТИЋ², ГОРДАНА ГАЈИЦА³ и JAN SCHWARZBAUER¹

¹RWTH Aachen University, Institute of Organic Biochemistry in Geo-Systems, Lochnerstrasse 4–20, 52056, Aachen, Germany, ²Универзитет у Београду, Повојног ратног факултета, Немањина 6, 11080, Земун, Београд и ³ Универзитет у Београду, Институт за хемију, технолођију и међалуприју, Његошева 12, 11000 Београд

У овој студији, пиролиза и ко-пиролиза најчешће коришћених пластичних материјала (полиетилен-терефталат – PET, полиетилен високе густине – HDPE и полистирен – PS) су спроведене ради анализе хемијског састава одговарајућих пиролизата. Примењени су различити односи пластичних материјала да би се добио састав алифатичних и ароматичних производа разградње који су веома слични онима код конвенционалних фосилних горива. Систематске хемијске варијације могу послужити као основа за процену овог приступа као одрживог извора алтернативних горива. HDPE је дао алифатичне производе разградње, док су PS и PET производили само ароматична јединења. Квантитативна анализа добијених пиролизата показала је јасну корелацију почетног односа са добијеним квантитативним саставом производа. Генерисање појединачних производа пиролизе показало је високу поновљивост. Међутим, било је очигледно да су се производи разлагања PS доследно појављивали као најистакнутији међу свим тестираним смешама HDPE:PS. Однос HDPE:PS = 1:3 дао је 96 % ароматичних јединења, која су продукти распадања PS. PET је продуковао производе који углавном садрже

кисеоник, и који доприносе са 86 % пиролизату смеше HDPE:PS = 1:3. Ови резултати дају увид у потенцијал пластичног отпада као одрживог извора алтернативних горива и вредних хемикалија.

(Примљено 7. фебруара, ревидирано 1. марта, прихваћено 12. априла 2024)

REFERENCES

1. <https://www.eea.europa.eu/publications/many-eu-member-states/germany>
2. L. Dai, N. Zhou, Y. Lv, Y. Cheng, R. Ruan, Y. Liu, K. Cobb, P. Chen, H. Lei, R. Ruan, *Progr. Energy Combust. Sci.* **93** (2022) 101021 (<https://doi.org/10.1016/j.pecs.2022.101021>)
3. J. Scheirs, W. Kaminsky, *Feedstock recycling and pyrolysis of waste plastics: Converting waste plastics into Diesel and other fuels*, Wiley Pol. Sci., 2006 (ISBN: 0-470-02152-7)
4. M. Rehan, A.-S. Nizami, K. Shahzad, O. K. M. Ouda, I. M. I. Ismail, T. Almeelbi, T. Iqbal, A. Demirbaş, *En. Source, A* **38** (2016) 2598 (<https://doi.org/10.1080/15567036.2016.1153753>)
5. D. S. Achilias, C. Roupakias, P. Megalokonomos, A. A. Lappas, E. V. Antonakou, *J. Hazard. Mater.* **149** (2007) 536 (<https://doi.org/10.1016/j.jhazmat.2007.06.076>)
6. P. Rutkowski, A. Kubacki, *En. Con. Manage.* **47**(6) (2006) 716 (<https://doi.org/10.1016/j.enconman.2005.05.017>)
7. M. Brebu, S. Uçar, C. Vasile, J. Yanik, *Fuel* **89** (2010) 1911 (<https://doi.org/10.1016/j.fuel.2010.01.029>)
8. B. B. Uzoejinwa, X. He, S. Wang, A. E. Abomohra, Y. Hu, Q. Wang, *En. Con. Manage.* **163** (2018) 468 (<https://doi.org/10.1016/j.enconman.2018.02.004>)
9. J. A. Onwudili, N. Insura, P. T. Williams, *J. Anal. Appl. Pyrolysis* **86**(2) (2009) 293 (<https://doi.org/10.1016/j.jaat.2009.07.008>)
10. R. U. Henneberg, R. P. Nielsen, M. E. Simonsen, *J. Anal. Appl. Pyrolysis* **173** (2023) 106037 (<https://doi.org/10.1016/j.jaat.2023.106037>)
11. E. A. Williams, P. T. Williams, *J. Anal. Appl. Pyrolysis* **40–41** (1997) 347 ([https://doi.org/10.1016/s0165-2370\(97\)00048-x](https://doi.org/10.1016/s0165-2370(97)00048-x))
12. E. Dziwiński, J. Howska, J. Gniady, *Pol. Test.* **65** (2018) 111 (<https://doi.org/10.1016/j.polymertesting.2017.11.009>)
13. J. Choi, F. Jitsunari, F. Asakawa, D. S. Lee, *Food Addit. Contam.* **22**(7) (2005) 693 (<https://doi.org/10.1080/02652030500160050>)
14. R. Pfaendner, *Pol. Deg. Stab.* **91** (2006) 2249 (<https://doi.org/10.1016/j.polymdegradstab.2005.10.017>)
15. S. Al-Malaika, F. H. Axtell, R. Rothon, M. Gilbert, in *Brydson's Plastics Materials*, VIII ed., M. Gilbert, Ed., Elsevier, Amsterdam, 2017, pp. 127 (<https://doi.org/10.1016/b978-0-323-35824-8.00007-4>)
16. X. Ren, R. Chang, Y. Huang, A. A. Amato, C. Carivenc, M. Grimaldi, Y. Kuo, P. Balaguer, W. Bourguet, B. Blumberg, *Endocrinology* **164** (2023) 1 (<https://doi.org/10.1210/endocr/bqad021>)
17. C. Apel, J. Tang, R. Ebinghaus, *Env. Poll.* **235** (2018) 85 (<https://doi.org/10.1016/j.envpol.2017.12.051>)
18. *Material Safety Data Sheet*, <https://datasheets.scbt.com/sc-223762.pdf>
19. Z. Wen, L. Fang, H. Zhang, *Drug Deliv.* **16**(4) (2009) 214 (<https://doi.org/10.1080/10717540902836715>)
20. I. Y. R. Adamson, J. Weeks, *Arch. Env. Health* **27** (1973) 69 (<https://doi.org/10.1080/00039896.1973.10666320>)

21. C. A. Baldrich, *Diesel characterization by high resolution mass spectrometry-gas chromatography*, C.T.F Cienc. Tecnol. Futuro [online], vol. 1, n. 4, 1998, pp. 65 (ISSN 0122-5383)
22. S. C. Gad, Diesel fuel, in *Encyclopedia of Toxicology*, Elsevier eBooks, Amstrdam, 2005, pp. 19 (<https://doi.org/10.1016/b0-12-369400-0/00320-3>)
23. M. Huth, A. Heilos, in *Modern Gas Turbine Systems*, P. Jansohn, Ed., Woodhead Publishing Ltd., Sawston, 2013, pp. 635 (<https://doi.org/10.1533/9780857096067.3.635>)
24. *Diesel fuel and exhaust emissions*, (Environmental Health Criteria, 171), World Health Organization, Geneva, 1996 (ISBN 92-4-157171-3, <https://www.inchem.org/documents/ehc/ehc/ehc171.htm>)
25. C. Zhou, A. Farooq, L. Yang, A. M. Mebel, *Prog. Energy Combust. Sci.* **90** (2022) 100983 (<https://doi.org/10.1016/j.pecs.2021.100983>)
26. V V. L. Mangesh, S. Padmanabhan, P. Tamizhdurai, S. S. Narayanan, R. Arumugam, *J. Hazard. Mater.* **386** (2020) 121453 (<https://doi.org/10.1016/j.jhazmat.2019.121453>)
27. A. Çakıcı, J. Yanık, S. Uçar, T. Karayıldırım, H. Anıl, *J. Mater. Cycles Waste Manage.* **6** (2004) 20 (<https://doi.org/10.1007/s10163-003-0101-y>)
28. A A. R. Ardiyanti, C. A. Хромова, R. H. Venderbosch, V. A. Yakovlev, H. J. Heeres, *Appl. Catal., B* **117–118** (2012) 105 (<https://doi.org/10.1016/j.apcatb.2011.12.032>)
29. I. Hita, A. Gutiérrez, M. Olazar, J. Bilbao, J. M. Arandes, P. Castaño, *Fuel* **145** (2015) 158 (<https://doi.org/10.1016/j.fuel.2014.12.055>)
30. CONCAWE Review **11**(2) (2002) 10 (<https://www.concawe.eu/wp-content/uploads/cr112-aromatics-2003-01897-01-e.pdf>)
31. M. J. DeWitt, E. Corporan, J. Graham, D. K. Minus, *Energy Fuels* **22** (2008) 2411 (<https://doi.org/10.1021/ef8001179>)
32. S. Sharma, P. Singh, C. Bhardwaj, B. Khandelwal, S. Kumar, *Energy Fuels* **35** (2021) 3150 (<https://doi.org/10.1021/acs.energyfuels.0c03511>)
33. E. B. Strel'nikova, I. V. Goncharov, O. B. Серебренникова, *Pet. Chem.* **52** (2012) 278 (<https://doi.org/10.1134/S096554411204010X>)
34. A. G. A. Jameel, Y. Han, O. Brignoli, S. Telalović, A. M. Elbaz, H. G. Im, W. L. Roberts, *J. Anal. Appl. Pyrolysis* **127** (2017) 183 (<https://doi.org/10.1016/j.jaap.2017.08.008>)
35. M. Z. H. Khan, M. Sultana, Md. R. Al-Mamun, Md. R. Hasan, *J. Env. Pub. Health* **2016** (2016) 7869080 (<https://doi.org/10.1155/2016/7869080>)
36. Wilke, S. (n.d.). Kunststoffabfälle. *Umweltbundesamt* (<https://www.umweltbundesamt.de/daten/ressourcen-abfall/verwertung-entsorgung-ausgewaehler-abfallarten/kunststoffabfaelle#kunststoffvielfalt>).

SUPPLEMENTARY MATERIAL TO
Co-pyrolysis of various plastic waste components as an environmentally sustainable source of alternative fuels

IVANA JOVANIĆEVIĆ¹, MALIŠA ANTIĆ², GORDANA GAJICA³ and JAN SCHWARZBAUER^{1*}

¹RWTH Aachen University, Institute of Organic Biochemistry in Geo-Systems, Lochnerstrasse 4–20, 52056, Aachen, Germany, ²University of Belgrade, Faculty of Agriculture, Nemanjina 6, 11 080, Zemun, Belgrade, Serbia and ³University of Belgrade, Institute of Chemistry, Technology and Metallurgy, Njegoševa 12, 11000 Belgrade, Serbia

J. Serb. Chem. Soc. 89 (7–8) (2024) 1053–1066

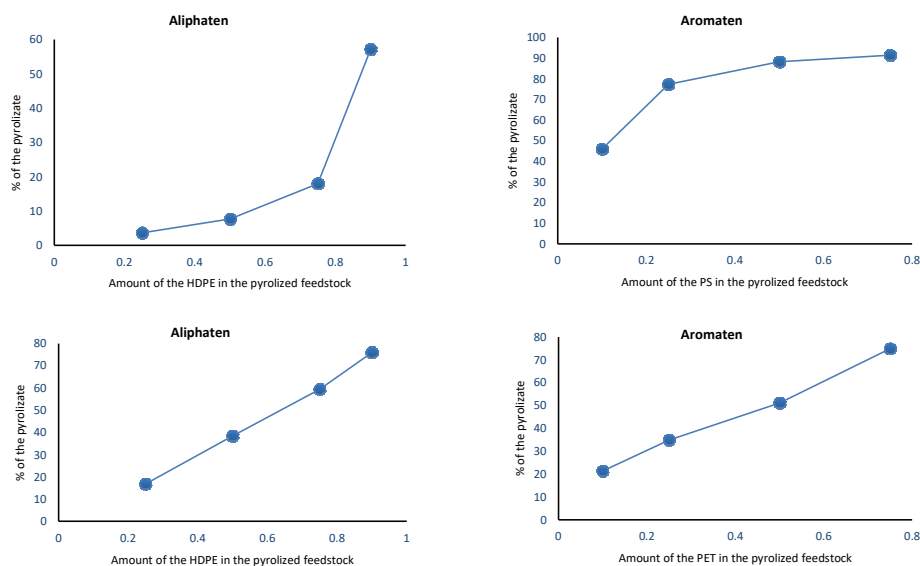


Fig. S-1. Quantitative analysis of the most abundant degradation products in the co-pyrolysis experiments of: a) Correlation between the pyrolyzed feedstock in the HDPE/PS mixture and the % of the pyrolysis products in the obtained pyrolyzate; and b) Correlation between the pyrolyzed feedstock in the HDPE/PET mixture and the % of the pyrolysis products in the obtained pyrolyzate.

*Corresponding author. E-mail: jan.schwarzbauer@emr.rwth-aachen.de

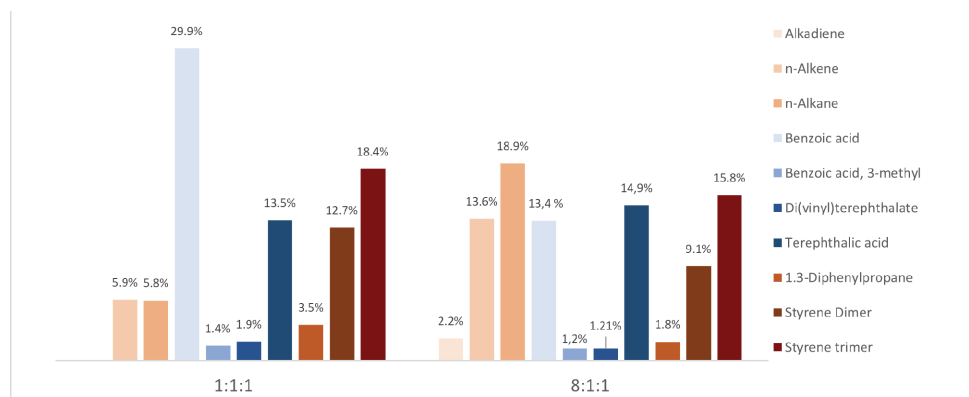


Fig. S-2. Distribution of the most abundant degradation products obtained from co-pyrolysis experiments on HDPE/PS/PET mixtures (%).

Table S-I. The identified pyrolysis products from the co-pyrolysis experiments of the HDPE:PS:PET mixture

Nr.	Compound
1	Aliphatic compounds C ₁₇ -C ₂₇
2	Benzoic acid
3	3-Methyl-benzoic acid
4	Diphenyl
5	4-Ethylbenzoic acid
6	4-Vinylbenzoic acid
7	Di(vinyl)terephthalate
8	Ethyl vinyl terephthalate
9	Terephthalic acid
10	Ethyl-4-ethoxybenzoate
11	Monomethyl terephthalate
12	Ethan-1,2-diyldibenzene
13	2-(Benzoyloxy)ethyl vinyl terephthalate
14	Diphenylmethane
15	1,2-Diphenylethylene
16	Bibenzyl
17	1,2-Diphenylpropane -
18	13-Diphenylpropane
19	2,4-Diphenyl-1-butene
20	1,2,3,4-Tetrahydro-1-phenylnaphthalene -
21	1,3-Diphenylbutene
22	1,4-Diphenylbutene
23	Unknown
24	1,5-Diphenyl-1,5-hexadiene
25	2,4,6-Triphenyl-1-hexene
26	1-Phenyl-4-(10-phenylethyl) tetralin isomer



The influence of conversion creatine and guanidinoacetic acid from zwitterionic to cationic form on their solubility in water – A thermodynamic study

MILAN B. VRANES[#] and JOVANA J. PANIĆ^{#*}

Faculty of Sciences, Department of Chemistry, Biochemistry and Environmental Protection,
University of Novi Sad, Trg Dositeja Obradovića 3, 21000 Novi Sad, Serbia

(Received 10 June, revised 19 July 2023, accepted 4 April 2024)

Abstract: In this work, the solubility of creatine, creatinine, guanidinoacetic acid and their hydrochlorides in water at atmospheric pressure and in the temperature range T 293.15–313.15 K was determined by the gravimetric method. The thermodynamic parameters of dissolution in water for the mentioned compounds were calculated. The solubility increases significantly by converting the zwitterionic structures of creatine and guanidinoacetic acid into a cationic form, *i.e.*, hydrochloride salt. The effect of increasing solubility is more pronounced for guanidinoacetic acid and decreases with temperature for both compounds. A simple process of transforming the electrically neutral zwitterionic structures into cations represents a good way to increase the solubility in water and bioavailability of biologically active compounds.

Keywords: solubility; creatine hydrochloride; guanidinoacetate hydrochloride; creatinine.

INTRODUCTION

Creatine (CR) is an endogenous amino acid that the human body naturally produces as a source of muscle energy. It promotes the renewal of ATP used during muscle work, and with its supplementation, “extended work” is achieved, *i.e.*, greater strength and better endurance.¹ There are various forms of creatine, but the most studied and commonly used form is creatine monohydrate. Due to its disadvantages, such as low solubility in water, spontaneous cyclization into creatinine, and the possibility of entering the cell only through specific transporters,² it is necessary to find new forms that will try to overcome these drawbacks.

* Corresponding author. E-mail: jovanap@dh.uns.ac.rs

[#] Serbian Chemical Society member.
<https://doi.org/10.2298/230610041V>

Guanidinoacetic acid (GAA) is a natural metabolic precursor of creatine. GAA is biologically converted into creatine in the liver through a methylation reaction. Many recent scientific papers indicate that the combination of creatine and GAA is more effective in increasing the amount of creatine in serum, muscle tissue and brain compared to pure creatine.^{3–5} However, both creatine and GAA are relatively poorly soluble in water, so their conversion to more soluble hydrochloride salts is desirable. Several formulations on the sports supplement market, described as advanced, contain creatine hydrochloride salts. However, the solubility of creatine, as well as creatine and GAA hydrochloride salts, has not been systematically investigated, however the solubility of GAA in water was determined in our previous work.⁶

Therefore, this research deals with the conversion of creatine and GAA into hydrochloride salts and then the determination of their solubility of creatine, creatinine, creatine hydrochloride and GAA hydrochloride in water at atmospheric pressure and in the temperature range $T = 293.15\text{--}313.15\text{ K}$. Based on the 78 solubility results, the thermodynamics of the dissolution of the studied compounds will be analysed.

EXPERIMENTAL

Materials, apparatus and procedure

Commercial creatine monohydrate (Scitech Nutrition), anhydrous creatine (Sigma–Aldrich, purity ≥ 0.99), anhydrous creatinine (Sigma–Aldrich, purity ≥ 0.98), guanidinoacetic acid (Sigma–Aldrich, purity ≥ 0.99), 37% water solution of hydrochloric acid (Sigma–Aldrich) and ultrapure water were used in the experimental work.

To synthesize the hydrochloride salts of creatine and guanidinoacetic acid (Fig. 1), the appropriate mass of CR or GAA was measured and dissolved in distilled water. Then, an equimolar amount of standardized hydrochloric acid was added. The solutions were mixed at room temperature for 30 min. Water was removed using a rotary vacuum evaporator at $T = 353.15\text{ K}$.

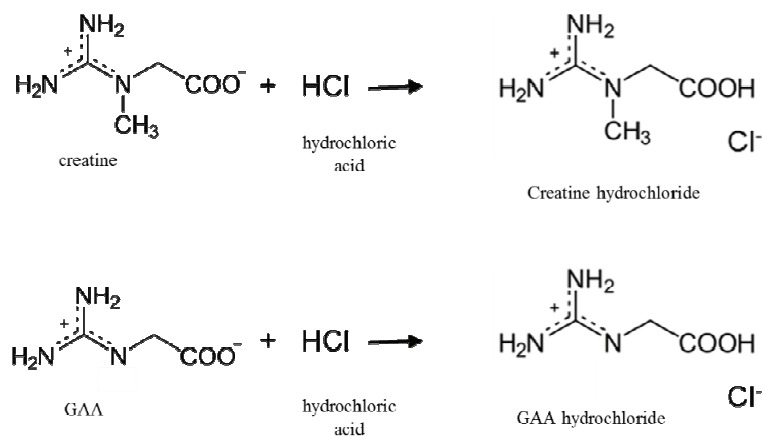


Fig. 1. Synthesis scheme of creatine hydrochloride and GAA hydrochloride.

Both salts, creatine hydrochloride (CR-HCl) and guanidinoacetate hydrochloride (GAA-HCl) remained as a white powder at room temperature. The synthesized salts are stored in a desiccator over P_2O_5 before use. The structures were confirmed by IR spectroscopy (Fig. S-1 of the Supplementary material to this paper). Chloride content was also checked by potentiometric titration with silver nitrate solution and the purity of both salts were higher than 99 %. Thermogravimetric (TG) and differential scanning calorimetric (DSC) curves of creatine hydrochloride and GAA hydrochloride are given in the Supplementary material as Fig. S-2.

Infrared spectra

The infrared spectra were recorded as neat samples from 4000 to 650 cm^{-1} on a Thermo Nicolet Nexus 670 spectrometer fitted with a Universal ATR Sampling Accessory. The measurements were performed with a total of 60 scans, at $T = 298.15\text{ K}$, and a spectral resolution of 2 cm^{-1} in a range of wave number from 4000 to 650 cm^{-1} . The software package Omnic version 6.2 was used in the data acquisition and spectral analysis.

Solubility measurements

The solubility determination was performed at five temperatures $T = 293.15, 298.15, 303.15, 308.15$ and 313.15 K , using the gravimetric method already described in work by Romero and Oviedo.⁷ An excess amount of the investigated compound was added to the double-layer glass flask containing 40 cm^3 of ultrapure water, and a small magnetic stirrer bar was capped tightly. Then, the suspensions were stirred for 12 h to saturation with the temperature control of $\pm 0.01\text{ K}$ (Lauda E-100 circulator) at selected temperatures. After, the samples stirrer was turned off to allow the undissolved solute to precipitate for the next 12 h at each temperature. Then, the solution was tested on creatinine content using Jaffe's method,⁸ and it was determined that the amount of formed creatinine after 12 h of mixing was negligible.

Finally, after separating the liquid layer and excess solute, the upper phase (solute-saturated aqueous solution) was carefully taken using a 3 cm^3 syringe and a needle. To prevent the undissolved solute from causing inaccurate results, the taken solution was filtered off in 10 cm^3 pre-weighed glass flasks through a 0.45 μm pore size mixed cellulose esters membrane. The mass was measured with an accuracy of $\pm 1 \times 10^{-5}\text{ g}$ in the lower range. The samples were placed in the dryer at 423.15 K, evaporated to dryness, and then placed in a vacuum desiccator to recover the solid compound. The mass of the solute was determined gravimetrically. Each obtained value represents the average of at least five independent measurements. The uncertainty in the mass fraction solubility is ± 0.001 . The reproducibility was found to be better than ± 0.002 .

Thermal analysis

A TA Instruments SDT Q600 TG/DSC thermal analyser was used to test the thermal stability of creatine, CR-HCl and GAA-HCl. This device was used to register the change in mass of the sample in the temperature interval from room temperature to 773 K. In addition to the change in mass of the sample as a function of temperature, the change in mass as a function of time can also be monitored on the mentioned device. The sample ($\approx 3.0\text{ mg}$) was placed in an open platinum pan. The measurements were carried out in an argon atmosphere (flow rate $50\text{ cm}^3 \cdot \text{min}^{-1}$) up to 723 K with a heating rate of $20\text{ K} \cdot \text{min}^{-1}$.

RESULTS AND DISCUSSION

Thermal analysis and solubility results

The gravimetric procedure for determining the solubility of compounds involves drying the sample to a constant mass. The creatine from aqueous solutions

crystallizes in the form of creatine monohydrate. The thermogravimetric measurements (Fig. 2a) indicate that creatine monohydrate begins to lose a water molecule at 341 K and that the complete conversion to anhydrous creatine ends at 398 K. The next mass loss starts at 503 K. At that temperature, the creatine molecule converts into creatinine, releasing one water molecule. The thermal decomposition of creatinine molecules occurs in the temperature range of 553–

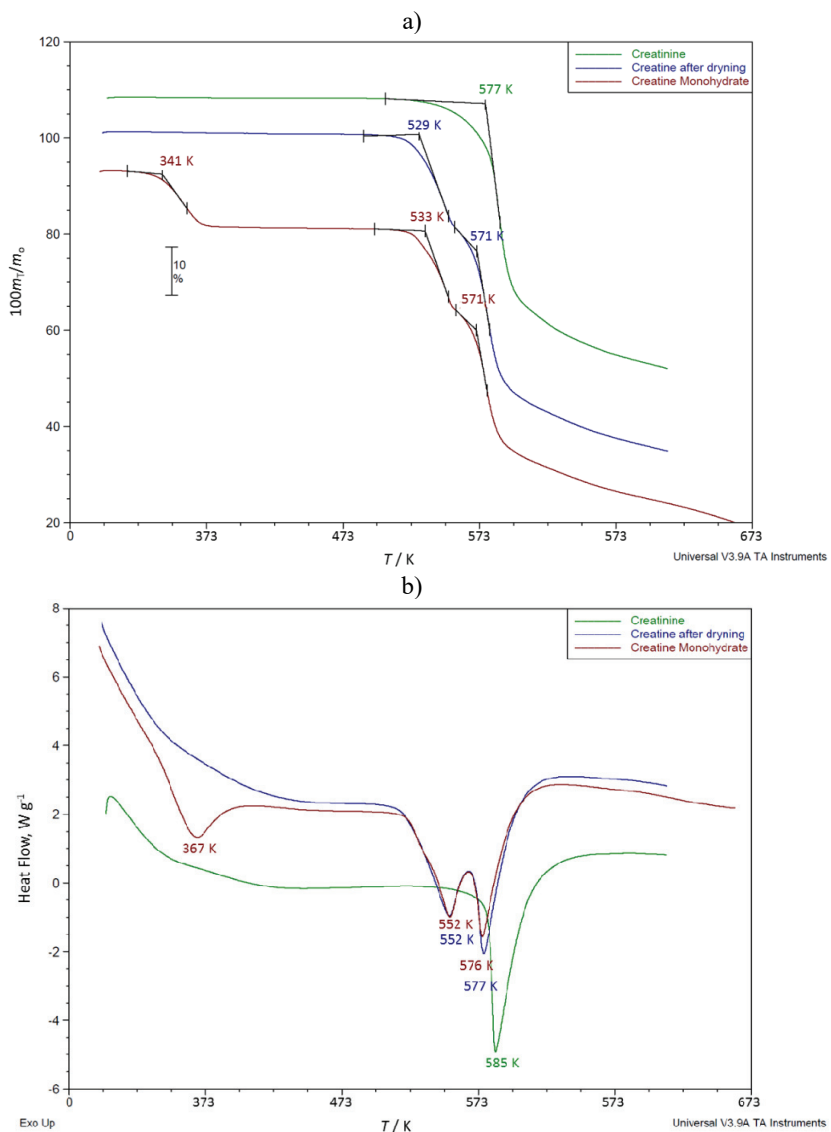


Fig. 2. a) Thermogravimetric and b) DSC curves of creatine monohydrate, creatine after drying and creatinine.

–593 K. The thermal analysis results indicate that after evaporating the water, the obtained creatine monohydrate needs to be dried in the temperature range of 398–503 K, because, in this way, the presence of creatine monohydrate and creatinine is avoided. The drying temperature in this research was between 423–433 K. The obtained onset temperatures of the beginning of decomposition (T_{onset}) and the endothermic peak of samples phase transition are shown on the thermogravimetric and DSC curves in Fig. 2b.

The obtained data for the solubility in water of creatine, creatinine, creatine hydrochloride and GAA hydrochloride, determined by the gravimetric method, are presented in Table I, together with the solubility values of GAA from our previous work.⁶

TABLE I. Water solubility values (R , in g/100 g water) of creatine, creatinine, GAA,⁶ creatine hydrochloride and GAA hydrochloride at atmospheric pressure and in the temperature range T 293.15–313.15 K

T / K	Compound				
	Creatine	Creatinine	GAA ⁶	CR-HCl	GAA-HCl
293.15	1.3172	9.5831	0.357	112.64	36.036
298.15	1.6288	10.419	0.422	118.36	41.646
303.15	1.8787	11.931	0.499	130.09	47.646
308.15	2.2727	13.325	0.583	138.96	53.169
313.15	2.6358	14.712	0.678	146.82	60.138

The literature data on the water solubility of creatine at different temperatures were found. The data showed that at 293.15 K, 1.4 g of creatine dissolves in 100 ml of water,^{2,9} while at 298.15 K, 1.7 g of creatine dissolves in 100 ml of water.⁹ Our experimental findings also agree with these literature water solubility data.

Based on the experimentally obtained water solubility values, it can be observed that the solubility values decrease in order: creatine hydrochloride > GAA hydrochloride > creatinine > creatine > GAA. Additionally, the solubility of each compound increases linearly with temperature. From Table I it can be observed that the solubility of creatinine is about six-fold higher than the solubility of creatine in water, while creatine is about four-fold more soluble than GAA in water. Also, it can be concluded that the solubility of creatine hydrochloride in water is almost three-fold higher than the solubility of GAA hydrochloride.

In Fig. 3, a comparison is made between the solubility values of creatine and GAA and their hydrochloride salts. The diagrams demonstrate that the conversion from zwitterionic to cationic form of both molecules considerably enhances their water solubility. Table II shows the ratio of the increase in solubility of creatine and GAA after the translation into hydrochloride salts. The effect of increasing solubility after the conversion of the molecule from the zwitterionic to the cationic form is more pronounced in the case of the GAA molecule. For both

molecules, the solubility ratio of hydrochloride salts and zwitterionic forms in water decreases with the increase of temperature, with the decrease being less pronounced in the case of the GAA molecule.

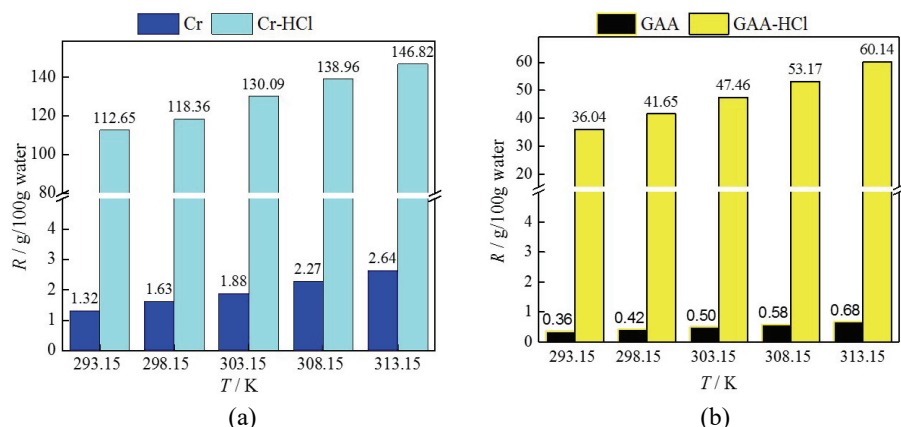


Fig. 3. Comparison of water solubility of a) creatine with creatine hydrochloride and b) GAA with GAA hydrochloride.

TABLE II. The ratio of increase in water solubility values of creatine, GAA and their respective hydrochloride salts in the temperature range T 293.15–313.15 K

T / K	CR-HCl/CR	GAA-HCl/GAA
293.15	84.5	99.9
298.15	71.7	97.7
303.15	68.2	94.5
308.15	60.1	90.2
313.15	54.7	87.7

Thermodynamic model for solubility correlation

When studying the dissolution of compounds in water, the thermodynamic functions related to solution and solvation processes can offer valuable information. These functions, the apparent standard dissolution enthalpy change ($\Delta_{\text{sol}}H^{\circ}$), entropy change ($\Delta_{\text{sol}}S^{\circ}$) and Gibbs energy change ($\Delta_{\text{sol}}G^{\circ}$) of solutes, can be calculated by analysing the temperature-dependent experimental solubility data. The modified van't Hoff equation is a commonly used thermodynamic model to determine these values.^{10,11} This equation relates the temperature and solubility in solution, and $\Delta_{\text{sol}}H^{\circ}$ can be obtained using the following equation:

$$\left(\frac{\partial \ln x_1}{\partial (1/T - 1/T_{\text{hm}})} \right)_p = -\frac{\Delta_{\text{sol}}H^{\circ}}{R} \quad (1)$$

Here, x_1 is the mole fraction of solute in a saturated solution, T is the absolute temperature in Kelvin, and R is the universal gas constant with a value of $8.314 \text{ J}\cdot\text{K}^{-1} \text{ mol}^{-1}$. T_{hm} , the mean harmonic temperature, is calculated using the formula:

$$T_{\text{hm}} = \frac{n}{\sum_{j=1}^n \frac{1}{T_j}} \quad (2)$$

where n equals the number of temperature points, T_j is the experimental temperature, and the resulting value is $T_{\text{hm}} = 302.99 \text{ K}$. $\Delta_{\text{sol}}H^\circ$ represents the apparent standard mole dissolution enthalpy change of solute dissolved in water, obtained from the slope of the fitted line curves $\ln x_1$ versus $(1/T - 1/T_{\text{hm}})$ (Fig. 4).

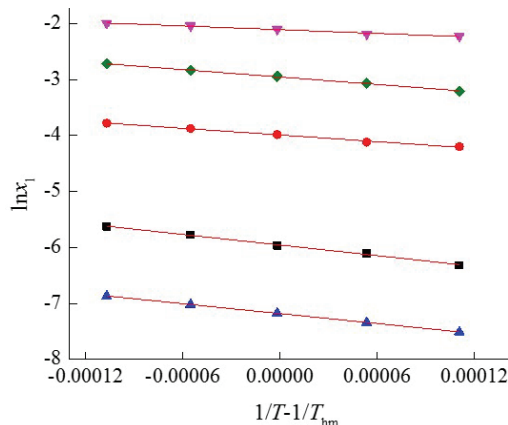


Fig. 4. The plot of natural logarithm of the mole fraction of: creatine (■), creatinine (●), GAA (▲), creatine hydrochloride (▼) and GAA hydrochloride (◆) in a saturated aqueous solution, $\ln x_1$ against $1/T - 1/T_{\text{hm}}$.

The Eq. (3) can be used with the intercept from the modified van't Hoff plot to calculate $\Delta_{\text{sol}}G^\circ$. The Eq. (4) can then be used to obtain $\Delta_{\text{sol}}S^\circ$:

$$\Delta_{\text{sol}}G^\circ = -RT_{\text{hm}} \times \text{Intercept} \quad (3)$$

$$\Delta_{\text{sol}}S^\circ = -\frac{\Delta_{\text{sol}}H^\circ - \Delta_{\text{sol}}G^\circ}{T_{\text{hm}}} \quad (4)$$

To determine the main influence and the contribution to $\Delta_{\text{sol}}G^\circ$ in the dissolving process, the relative contribution of enthalpy (ζ_H), and the relative contribution of entropy (ζ_{TS}) were calculated using the following expressions:^{10,11}

$$\zeta_H = \frac{|\Delta_{\text{sol}}H^\circ|}{|\Delta_{\text{sol}}H^\circ| + |T_{\text{hm}}\Delta_{\text{sol}}S^\circ|} \quad (5)$$

$$\zeta_{TS} = \frac{|T_{hm}\Delta_{sol}S^o|}{|\Delta_{sol}H^o| + |T_{hm}\Delta_{sol}S^o|} \quad (6)$$

Table III provides the obtained values for the apparent thermodynamic properties of $\Delta_{sol}G^o$, $\Delta_{sol}H^o$ and $\Delta_{sol}S^o$, as well as of ζ_H and ζ_{TS} for creatine, creatinine, GAA, creatine hydrochloride and GAA hydrochloride dissolution in water.

TABLE III. The obtained apparent thermodynamics properties values of $\Delta_{sol}G^o$, $\Delta_{sol}H^o$, $\Delta_{sol}S^o$, ζ_H and ζ_{TS} for creatine, creatinine, GAA, creatine hydrochloride and GAA hydrochloride dissolution in water

Parameter	Creatine	Creatinine	GAA	CR-HCl	GAA-HCl
$\Delta_{sol}H^o / \text{kJ mol}^{-1}$	26.21	16.52	24.50	92.60	183.63
$\Delta_{sol}G^o / \text{kJ mol}^{-1}$	15.00	10.05	18.09	53.09	74.41
$\Delta_{sol}S^o / \text{kJ K}^{-1} \text{mol}^{-1}$	0.037	0.021	0.021	0.13	0.36
$\zeta_H / \%$	70	72	79	70	63
$\zeta_{TS} / \%$	30	28	21	30	37

Based on the data in Table III, it is observed that all $\Delta_{sol}G^o$ values for the dissolution in water fall within the positive range of (18–75) kJ mol^{-1} . When considering molecular creatine, creatinine, and GAA separately from creatine hydrochloride and GAA hydrochloride as ionic compounds, it is evident that the values of $\Delta_{sol}G^o$ for compound dissolution are in reverse order of solubility. The findings in Table III indicate that the dissolution process is endothermic in each case due to the positive values of $\Delta_{sol}G^o$ and $\Delta_{sol}H^o$. This can be attributed to the fact that the new solute–water interactions are weaker than the sum of the solute–solute and water–water interactions they replace. The higher value of $\Delta_{sol}H^o$ for creatine and GAA compared to creatinine may be because more energy is required to break the ionic bond between creatine/GAA in the zwitterionic form than to dissolve neutral creatinine. Additionally, the higher value of $\Delta_{sol}H^o$ for GAA hydrochloride than for creatine salt may be due to more energy being required to break the ionic bond of GAA hydrochloride. The positive values for $\Delta_{sol}S^o$ indicate that there is an increase in the disorder of the system during dissolution. Based on the calculated values of the relative contribution of enthalpy and entropy, it can be concluded that during dissolution, the enthalpy affects the values of $\Delta_{sol}G^o$ the most in all five solutions. Also, it can be seen that converting creatine from zwitterionic to cationic form does not affect the relative contribution of enthalpy and entropy values. However, GAA conversion into salt alters the ratio between the enthalpy and the entropy contribution.

The reason for the increased solubility of hydrochloride salts in relation to the zwitterionic structures is a change in the type of interactions that occur bet-

ween the molecules.⁹ Strong electrostatic interactions and intermolecular hydrogen bonds occur between CR and GAA molecules when they are in the zwitterionic form. Therefore, their solubility in water is low. By converting GAA and CR molecules into cationic forms, the attractive electrostatic interactions are replaced by the repulsive ones. On the other hand, the interactions between GAA and CR as cations and Cl ions as anions are significantly weaker. The another reason for increasing the solubility of GAA-HCl and CR-HCl in water is the change in the conformation of the molecules themselves. Our previous research¹² showed that in GAA and CR molecules in zwitterionic form the intramolecular hydrogen bonds occur between the oxygen atom from the carboxylate anion and the hydrogen atom from the guanidino group. These intramolecular H-bonds make molecules rigid and less accessible for the interactions with water molecules. The possibility of intramolecular H-bond formation in CR-HCl and GAA-HCl molecules disappears by protonating the carboxylate anion. Therefore, GAA-HCl and CR-HCl molecules have a greater possibility of free rotations around single bonds after dissolving in water, which increases the entropy of the system and contributes to better solubility.

CONCLUSION

In summary, the hydrochloride salts of creatine and guanidinoacetic acid – creatine hydrochloride and guanidinoacetonium hydrochloride – were successfully synthesized. Further, this study reveals distinct solubility behaviours among creatine, creatinine, creatine hydrochloride and GAA hydrochloride in water. Notably, the solubility follows a descending order from creatine hydrochloride to GAA, with temperature positively impacting the solubility of each compound. Remarkably, the conversion to hydrochloride salts significantly enhances water solubility, especially for GAA, indicating a pronounced effect of shifting from zwitterionic to cationic form. Additionally, the thermodynamic functions of solution and solvation were calculated using a modified van't Hoff equation. These findings provide a fundamental, high-accuracy set of results, filling an essential gap in the literature, but also highlighting differential solubility characteristics and the impact of structural changes, which hold substantial implications for pharmaceutical and biomedical applications, where precise solubility control is crucial.

SUPPLEMENTARY MATERIAL

Additional data and information are available electronically at the pages of journal website: <https://www.shd-pub.org.rs/index.php/JSCS/article/view/12431>, or from the corresponding author on request.

Acknowledgement. The authors are grateful for the financial support of Provincial Secretariat for Higher Education and Scientific Research, grant number: 142-451-2545/2021-01.

И З В О Д
УТИЦАЈ КОНВЕРЗИЈЕ КРЕАТИНА И ГВАНИДИНОСИРЂЕТНЕ КИСЕЛИНЕ ИЗ
ЦВИТЕРЈОНСКОГ У КАТЈОНСКИ ОБЛИК НА ЊИХОВУ РАСТВОРЉИВОСТ
У ВОДИ – ТЕРМОДИНАМИЧКА СТУДИЈА

МИЛАН Б. ВРАНЕШ И ЈОВАНА Ј. ПАНИЋ

*Природно-математички факултет, Департман за хемију, биохемију и заштитну живојне средине,
Универзитет у Новом Саду, Трг Доситеја Обрадовића 3, 21000 Нови Сад*

У овом раду је одређена и упоређена растворљивост креатина, креатинина, гванидиносирујеће киселине и њихових хидрохлорида у води на атмосферском притиску и у температурном опсегу $T = 293,15\text{--}313,15$ K гравиметријском методом. Израчунати су термодинамички параметри растварања у води за наведена једињења. Добијени резултати указују да се растворљивост значајно повећава претварањем цвiterјонских структура креатина и гванидиносирујеће киселине у катјонски облик, тј. хидрохлоридну со. Ефекат повећања растворљивости је израженији за гванидиносирујећу киселину и опада са температуром за оба једињења. Једноставан процес конверзије електро-неутралних цвiterјонских структура у катјоне представља добар начин да се повећа растворљивост у води и биодоступност биолошки активних једињења.

(Примљено 10. јуна, ревидирано 19. јула 2023, прихваћено 4. априла 2024)

REFERENCES

- R. Cooper, F. Naclerio, J. Allgrove, A. Jimenez, *J. Int. Soc. Sports Nutr.* **9** (2012) 33 (<https://doi.org/10.1186/1550-2783-9-33>)
- R. Jäger, M. Purpura, A. Shao, T. Inoue, R. B. Kreider, *Amino Acids* **40** (2011) 1369 (<https://doi.org/10.1007/s00726-011-0874-6>)
- S. Ostojić, B. Niess, M. Stojanović, M. Obrenović, *Int. J. Medical Sci.* **10** (2013) 141 (<https://doi.org/10.7150/ijms.5125>)
- S. Ostojić, M. Stojanović, P. Drid, J. R. Hoffman, D. Sekulić, N. Zenić, *Nutrients* **8** (2016) 72 (<https://doi.org/10.3390/nu8020072>)
- S. C. Forbes, D. M. Cordingley, S. M. Cornish, B. Gualano, H. Roschel, S. M. Ostojić, E. S. Rawson, B.D. Roy, K. Prokopidis, P. Giannos, D.G. Candow, *Nutrients* **14** (2022) 921 (<https://doi.org/10.3390/nu14050921>)
- M. Vraneš, S. Ostojić, A. Tot, S. Papović, S. Gadžurić, *Food Chem.* **237** (2017) 53 (<https://doi.org/10.1016/j.foodchem.2017.05.088>)
- C. M. Romero, C. D. Oviedo, *J. Solution Chem.* **6** (2013) 1355 (<https://doi.org/10.1007/s10953-013-0031-9>)
- M. Jaffé, *Biol. Chem.* **10** (1886) 391 (<https://doi.org/10.1515/bchm1.1886.10.5.391>)
- M. Vraneš, S. Papović, in *Human health and nutrition: New forms of creatine in human nutrition*, S. Ostojić, Ed., Nova Science Publishers, Nova Biomedical, New York, 2015, p. 105 (<https://open.uns.ac.rs/handle/123456789/5425>)
- J. Sha, T. Ma, R. Zhao, P. Zhang, R. Sun, G. Jiang, Y. Wan, H. He, X. Yao, Y. Li, T. Li, B. Ren, *J. Chem. Thermodyn.* **144** (2020) 106073 (<https://doi.org/10.1016/j.jct.2020.106073>)
- F. Shakeel, M. Imran, N. Haq, S. Alshehri, M. K. Anwer, *Molecules* **24** (2019) 3404 (<https://doi.org/10.3390/molecules24183404>)
- M. Vraneš, S. Ostojić, Č. Podlipnik, A. Tot, *J. Chem. Res.* **45** (2021) 467 (<https://doi.org/10.1177/1747519820978583>).

SUPPLEMENTARY MATERIAL TO
**The influence of conversion creatine and guanidinoacetic acid
from zwitterionic to cationic form on their solubility in water –
A thermodynamic study**

MILAN B. VRANEŠ AND JOVANA J. PANIĆ *

Faculty of Sciences, Department of Chemistry, Biochemistry and Environmental Protection,
University of Novi Sad, Trg Dositeja Obradovića 3, 21000 Novi Sad, Serbia

J. Serb. Chem. Soc. 89 (7–8) (2024) 1067–1076

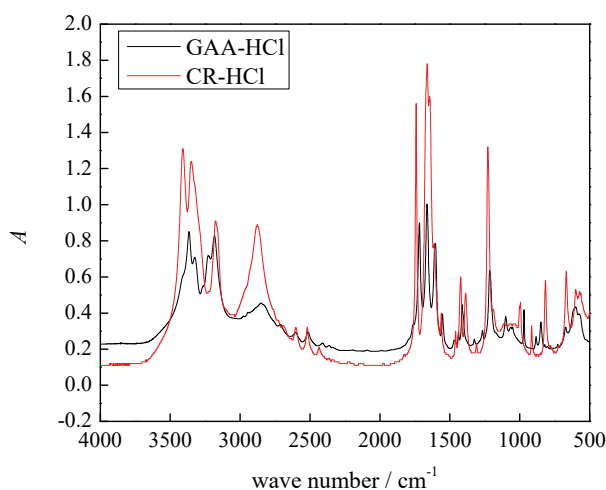


Fig. S-1. IR spectra of creatine hydrochloride and GAA hydrochloride where prominent vibrational bands at ~3000–3500 cm⁻¹ are related to NH stretching vibrations, and at ~900–1800 cm⁻¹ to CH and CHO stretching vibrations.

*Corresponding author. E-mail: jovanap@dh.uns.ac.rs

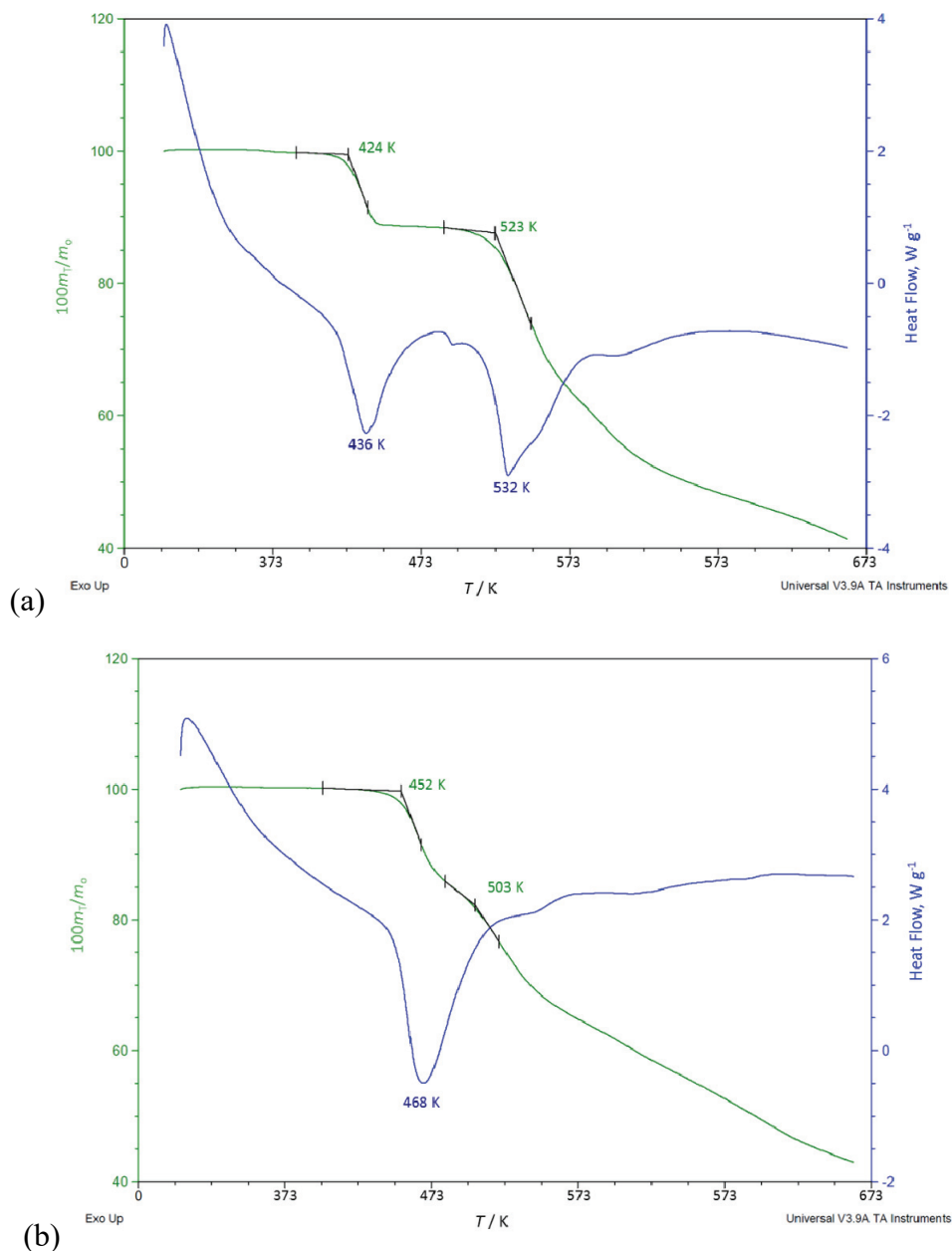


Fig. S-2. a) Thermogravimetric and b) DSC curves of creatine hydrochloride and GAA hydrochloride.



Neem (*Azadirachta indica*) oil coated urea as a novel controlled release fertilizer: Physical and chemical analysis of structure and its nutrient release behaviour

SHIV OM MEENA, MANISH VASHISHTHA* and MEEENU

Department of Chemical Engineering, Malaviya National Institute of Technology, Jaipur,
Rajasthan, India

(Received 28 February, revised 25 June 2023, accepted 10 February 2024)

Abstract: The development of controlled release fertilizers (CRF) is a green technology that not only reduces nitrogen loss, caused by volatilization and leaching, but also alters the kinetics of nitrogen release, which, in turn, provides nutrients to plants at a pace that is more compatible with their metabolic needs. With an increasing awareness towards human health and environmental protection, there is a rapid shift towards the development of eco-friendly fertilizers based on natural resources. Majority of the literature on CRF pertains to organic and inorganic material based coatings on fertilizers and among them in the case of neem oil coated urea (NCU) most of the literature is confined to the elucidation of coating effect on increasing the crop yield and plant growth. However, literature lacks any comprehensive study on NCU as a CRF, covering major aspects such as its characterization, determination of nutrient release rate, and comparison with other CRF. The present work is an attempt to fill this gap in scientific knowledge about NCU. In the present study, neem oil coated urea (NCU) was prepared to achieve the controlled release mechanism necessary to meet crop requirements. The characterizations of the uncoated urea (UCU) and NCU were done using scanning electron microscopy (SEM) with energy dispersive X-ray analysis (EDX), Fourier transform infra-red (FTIR), refractive index (RI) and crushing strength test. To establish the superior behaviour of NCU as a CRF, the results were also compared to the literature data of other CRF, namely phosphate slimes (PCU) and bentonite coated (BCU) with chitosan as a binder. The nutrient release experiments showed that NCU gave a release of 1.03 and 45.03 % at the first day and day 30, respectively. The crushing strength test was carried out for the same size particles, and the results showed that NCU has better mechanical strength as compared to UCU, PCU and BCU.

Keywords: urea; nutrient release; refractive index; fertilizer.

* Corresponding author. E-mail: mvashishtha.chem@mnit.ac.in
<https://doi.org/10.2298/JSC230228033M>

INTRODUCTION

Earth's population has witnessed an exponential growth in the past few decades and has now reached approximately 7.0 billion, and this is further expected to reach 9.5 billion by 2050.^{1–3} This population growth, on one hand, has fuelled the global food requirements and the per capita food requirement is expected to double by 2050 from the present levels.⁴ On the other hand, the cultivable land area is diminishing due to rapid industrialization, increasing urbanization, desertification and land degradation.^{5,6} These intimidating factors pose a serious threat to the global food security and need an immediate response and solution. Different interventions to meet the challenges of food security have already been undertaken worldwide; prominent among these is to improve the efficiency of agricultural systems to produce more food from a given area of land. One such intervention aimed to meet the increasing food demands is to employ enormous quantities of fertilizers in the agricultural sector, although this has led to adverse environmental impacts. The use of fertilizers bears a direct or indirect impact on the soil biota and its functioning.⁷ Hence, it is the need of the hour to develop such systems, which, along with ramping up production, also alleviate environmental problems.⁸

Fertilizers are chemical compounds used to improve agricultural productivity as they are able to supply the necessary nutrients required for the plant growth⁹. Urea is among the most widely used N fertilizers, which contains 46 % nitrogen.^{3,10} However, a large proportion of urea gets hydrolysed before its uptake by the plant.¹¹ When uncoated urea (UCU) is applied to the soil, the urea (Amide) nitrogen is rapidly converted to ammonical nitrogen and subsequently to nitrite and nitrate forms. Nitrogen in these forms, besides being absorbed by plants, is also rapidly lost from the soil due to leaching, run off, volatilization, and de-nitrification, leading to environmental pollution and disturbing the soil ecology.¹² Controlled release compounds are widely used in biotechnology, medical purposes and predominantly as fertilizers in agricultural production.^{13,14} The controlled release fertilizers (CRF), in contrast to conventional fertilizers, can overcome the loss of nutrients caused due to off stream losses, leaching, and volatilization since they have more sustainable release characteristics and better uptake and stability.¹⁵ A large varieties of commercial CRF are produced in which fertilizer products are coated with alkyd resin, polyurethane and polyolefin; however, these materials do not degrade appropriately in soil solution phases and thereby, their accumulation over a period of time results in the loss of soil fertility and defeats the very purpose of carrying out the sustainable agriculture of arable lands. However, it is crucial to take into account the materials that were applied for the urea coating, especially in terms of how quickly they degrade.¹⁶

Recent studies have explored the possibilities of choosing coating materials that have twin advantages of being not only eco-friendly, but also cost effective

one such study was reported using bentonite and organic polymer.¹⁷ Also, neem oil coated urea (NCU) is a fast emerging as an important CRF because of its multiple benefits. Neem, *Azadirachta indica*, is a native to the arid regions of the Indian sub-continent, where it grows to 12–24 m high. It can be propagated easily by seed, or by 9–12-month-old saplings can also be transplanted. Fresh fruit yield per neem tree ranges between 37 and 50 kg per year. Forty kg fruit yields nearly 24 kg of dry fruit (60 %), which in turn gives 11.52 kg of pulp (48 %), 1.1 kg of seed coat (4.5 %), 1 kg of husk (25 %), and 5.5 kg of kernel (23 %). The kernel gives about 2.5 kg of neem oil (45 %) and 3.0 kg of neem cake (55 %). Neem oil extracted from the seeds of the neem tree has insecticidal and medicinal properties due to which it has been widely used in pest control. The cake (containing 5 % N) left after oil extraction is generally used as manure and also for making neem cake-coated urea.

Neem oil contains melicians (generally known as neem bitters), of which epinimbin, deacetyl, salanin and azadirachtin are the active fractions, which showed dose dependent nitrification inhibition action. When NCU is applied to soil, the neem triterpenes inhibit the activity of nitrifying bacteria, which results in delayed transformation of ammonical nitrogen into nitrite nitrogen. This leads to a substantial reduction in the loss of fertilizer and pollution of groundwater. NCU ensures slow and continuous availability of nitrogen throughout the crop growth, nourishing the saplings for a longer period and thus avoiding the repeated use of fertilizer.¹⁸ Other potential benefits of using NCU includes an increase in crop yield, efficient pest control management leading to savings, increases in the shelf life of the product, and preventing its misuse as feedstock for use in other chemical industries.

MATERIAL AND METHODS

Materials for preparation of NCU

The commercial UCU granules with a nitrogen content of 46.44 % (label specification) and distribution of particle diameter from 0.5–2.8 mm (determined using sieve analysis) were supplied from Chambal Fertilizers & Chemicals Limited (CFCL) Gadepan, Kota (India). The urea particles were coated with Neem oil supplied by Shubhra Industries, Jaipur (India).

Various methods are available for making coated urea, which acts as CRF. Among the available techniques, the fluidized bed coating process, being one of the oldest and experimentally simple to design and operate, for forming small coated particles, also holds promise for making NCU of reasonable quality. The line diagram of the experimental set up used is shown in Fig. 1a. The NCU obtained after coating is shown in Fig. 1b.

The fluidized bed was made from a flexi glass. A spraying nozzle of an air-atomized nozzle was centrally set above the fluidized bed. A batch of UCU 210 g in weight was put in the fluidized bed, which was fluidized at higher than their minimum fluidization. For coating, 20 ml of neem oil at room temperature and flow rate of 0.35 ml min⁻¹, under a pressure was atomized with compressed air and sprayed onto the urea particles in the fluidized bed for coating. Steady state was indicated by a constant bed temperature and constant head. Final

product samples were collected after 20–30 min of fluidization. By this time, urea particles were uniformly coated with the neem oil.



Fig. 1. a) Experimental set up of fluidized bed coater; b) NCU obtained from UCU after coating in fluidized bed coater.

Physical and chemical analysis

The properties of neem oil and urea are given in Table I.

TABLE I. Properties of neem oil and urea

Neem oil	Urea
Iodine index	81.28
Kinematic viscosity (30°C), m ² /s	43.75
Saponification value	199.86
Physical state at room temperature	Liquid (golden yellow)
Acid value	32.538
Cloud point, °C	13
Pour point, °C	7.0
Density at room temperature, kg/m ³	918.2
Chemical formula	(NH ₂) ₂ CO
Molecular weight	60.06
Odor	Odorless
Absolute viscosity (20 °C), kg/(m s)	0.185
Density, kg/m ³	1320
Melting point, °C	133–135
Flowing time (20°C), s	25–40
Solubility in water, kg/m ³	1079 at 20 °C 1670 at 40 °C

Particle size analysis

The particle size of fertilizer products and/or fertilizer raw materials is defined as the particle diameter ranges of the test material. Particle size affects agronomic response, granulation techniques, storage, handling and blending properties. The particle size distribution was determined for both UCU and NCU using the sieve analysis (dry sieving as per IFDC S-107).¹⁹ For this analysis, a sample weight of 210 g was used for both UCU and NCU, and the resultant distribution is shown in Fig. 2.

It can be seen from the figure that maximum particles are available in the diameter range of 1.7 mm and 2.0 mm. Also, it can be inferred from these results that the particle strength increases due to coating (reduction in particle breakage after neem oil coating), since smaller number of particles of NCU are present in lower size distribution ranges.

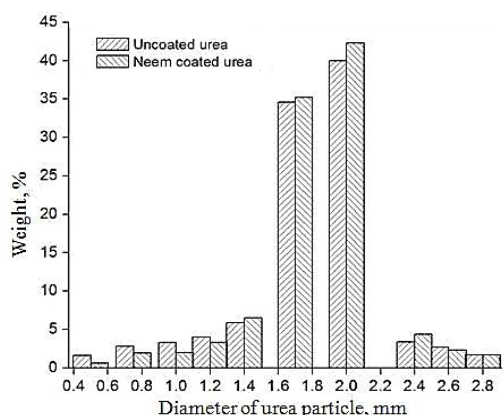


Fig. 2. UCU and NCU particle size distribution.

Percent coating

The actual coating % is determined by taking a 10 g NCU sample, immersed in 100 ml of distilled water. After thorough shaking, the urea gets dissolved in the water, and as a result, the coating was liberated from NCU. The subsequent filtration and water evaporation gives the coating % which is calculated as:

$$\text{Coating \%} = 100 \frac{M_i - M_0}{M} \quad (1)$$

where M_i = weight of filter paper with urea sample, after evaporation (g), M_0 = weight of filter paper (g), M = weight of urea sample (g), % coating = $100 \times 0.57/10 = 5.7\%$.

Nitrogen content

The nitrogen content of NCU is estimated using the standard Kjeldahl method. The sample was treated with sulphuric acid to yield ammonium sulphate. The hydrolysis of ammonium sulphate yields the nitrogen content. Also, the nitrogen content can be calculated mathematically using the total coating percentage as given in the Eq. (2). The nitrogen content values of UCU and NCU obtained experimentally and using Eq. 2 are almost the same, which are shown in Table II. The value obtained by Eq. (2) is used in the present work:

$$N\% = 46.44 \frac{100 - \% \text{ Coating}}{100} \quad (2)$$

TABLE II. Nitrogen content in UCU and NCU

Sample	Coating, %	Urea, %	Nitrogen, %
UCU	0.00	100	46.44
NCU	5.7	94.3	43.79

Dustiness factor

Dustiness is a physical property of fertilizer. Due to the large quantities of fertilizer produced and raw materials handled in bulk, their dustiness is of particular concern and can cause problems like significant material losses during processing, handling, and application thereby resulting in loss of revenues. Also, environmental pollution and exposure of employees to hazardous levels of dust is not indicative of a responsible organization. So, dustiness of fer-

tizer is an undesirable property. The dustiness was measured by taking 10 g of NCU in a bunker funnel, in which compressed air (10 psi* of pressure) is passed from the bottom. After 5 min, the sample is removed from the bunker funnel and weighed. The weight loss is then calculated. The amount of weight loss is called dust. In the present case, the loss in mass of the sample is 0.037 g, so % Dustiness = $100 \times 0.037/10 = 0.37\%$, which is in agreement with the values reported in the literature for other CRF.

Dissolution rate

The UCU obtained from the market and NCU samples prepared as discussed above were analysed for the dissolution rate for which a 5 g of sample particles (of same diameter of 1.7 mm) were put in a beaker containing 50 ml of double distilled water. For mixing, a magnetic stirrer was used at constant speed. The time required for the complete dissolution of urea was noted. The temperature was also varied to see its effect on dissolution, and as expected, the dissolution rate was slower for NCU as compared to UCU. The dissolution rate (indicated by lower dissolution time) increases with temperature, as can be seen from the results in Table III.

TABLE III. Dissolution time, s, of UCU and NCU

Sample (diameter = 1.7 mm)	Dissolution temprature, °C				
	30	35	40	45	50
UCU	324	300	287	239	210
NCU	482	445	426	372	357

Crushing strength

The crushing strength is an important parameter that indicates the ability of particles to withstand physical handling throughout the supply chain. Experimentally, it is measured by applying pressure to individual granules, usually of a specified size, and noting the required pressure to fracture each granule. In the present work, the test was performed on different sizes (1.7 and 2.0 mm) of NCU and UCU. A tensile strength tester (make Shimadzu available at material research centre of Malaviya National Institute of Technology, Jaipur) was used for measuring the crushing strength in which granules were subjected to a force applied by a metal plunger that was a part of the apparatus, and the values were noted.

Morphology and microscopic analysis (SEM) of the surface

Scanning electron microscopy (SEM) with an energy dispersive analysis system of X-ray spectrometer (EDX) is one of the powerful analytical tools to study the morphology and relative elemental composition of the granules. Thus, morphology and relative elemental concentration of UCU and NCU were determined using scanning electron microscopy (SEM, make: Nova Nanosem-450 FEI, available at material research centre of Malaviya National Institute of Technology, Jaipur), which was equipped with an energy dispersive analysis system of X-ray spectrometer, EDX. For analysis, UCU and NCU samples were dispersed over a carbon tape pasted on the surface of a metallic disk (stub). Then, the disk was coated with gold in an ionization chamber, and the samples were ready to be analysed.

FTIR Analysis

Fourier transform infrared (FTIR) spectroscopy is a powerful tool to study the chemical species and the functional groups present in a sample. FTIR spectrophotometer (Make: Perkin Elmer company available at material research centre of Malaviya National Institute of Tech-

* 1 psi = 6894.757 Pa

nology, Jaipur) was used to analyse the fertilizer samples. The UCU and NCU granules were dispersed in dry KBr powder and ground to obtain fine particles. These particles were analysed at wavelengths from 4500–400 cm⁻¹. All spectra were recorded at ambient temperature.

X-ray diffraction (XRD) analysis

It is a rapid analytical technique primarily used for the phase identification of crystalline materials and can provide information on unit cell dimensions. The analysed materials are finely ground homogenized, and the average bulk composition is determined by XRD (make: "X" Pert powder, available in Material Research Centre in Malaviya National Institute of Technology, Jaipur). It works on Bragg's law ($2ds\sin\theta = n\lambda$). The XRD patterns were recorded in the range of 2θ equal to 20–80°. It was used to explain the interference pattern of X-rays scattered by the crystals.

Experimental determination of nutrient release from NCU in water domain by refractive index

An accurate estimate of the nutrient release pattern from CRF is required both for manufacturers as well for farmers, since it helps them in understanding fertilizer potency and nutrient planning for the crops. Although the field tests provide a better estimation of the nutrient release behaviour, however, it suffers from inherent constraints of being influenced by the variation in environmental conditions like temperature, soil moisture, soil pH, soil microbes population and porosity, etc. Thus, the determination of nutrient release under laboratory conditions provides a convenient, useful, and nearly accurate approach to understand the nutrient release mechanism. Other researchers had also pointed that laboratory experiments were successful in predicting the nutrient release rate of CRF.²⁰ In actual practice, the estimation of nutrient release in the soil is more pertinent since it depicts the actual behaviour under field conditions; however, as explained, the mechanism of nutrient behaviour in CRF is mainly governed by water penetration into the core through the coating. Thus, the study of nutrient behaviour in the water domain gives a fairly accurate picture of nutrient release, and this is experimentally done first, followed by studies in the soil domain to improve the predictions. In the present work, the nutrient release in water from NCU is experimentally determined using a refractometer.

To determine the urea release, 50 g sample (UCU and NCU) were placed in 250 ml distilled water in a separate Erlenmeyer flask and sealed. The refractive index (*RI*) of both the samples were measured using a refractometer (make: Atago available at Thermodynamics Research Lab in Malaviya National Institute of Technology, Jaipur) to get the urea release in the solution. The instrument was calibrated daily before measurements against a known refractive index of water, and *RI* of urea samples were measured at 25 and 40 °C as a function of time for 3, 7, 11, 15, 19, 23, 26 and 30 days. The value of (*RI*) is related to the concentration of urea dissolved in water.

RESULTS AND DISCUSSION

Morphology and microscopic analysis of the surface

SEM pictures of the UCU and NCU's surfaces and sections were used to investigate the morphological alterations brought on by the neem oil coating. Some portions of UCU (Fig. 3a) were rough, but the majority of it was smooth. While Fig. 3b confirms agglomeration. Fig. 3c and d shows the layer that results from the application of neem oil; it was smooth compared to UCU. Layering is a desirable trait for the particle coating. An irregularity in the coating thickness and the shape

of granules was observed. UCU and NCU particles of 1.7 mm diameter were selected randomly and observed under SEM at magnifications of 500 \times and 1000 \times . SEM images are shown in Fig. 3a and b for UCU and Fig. 3c and d for NCU.

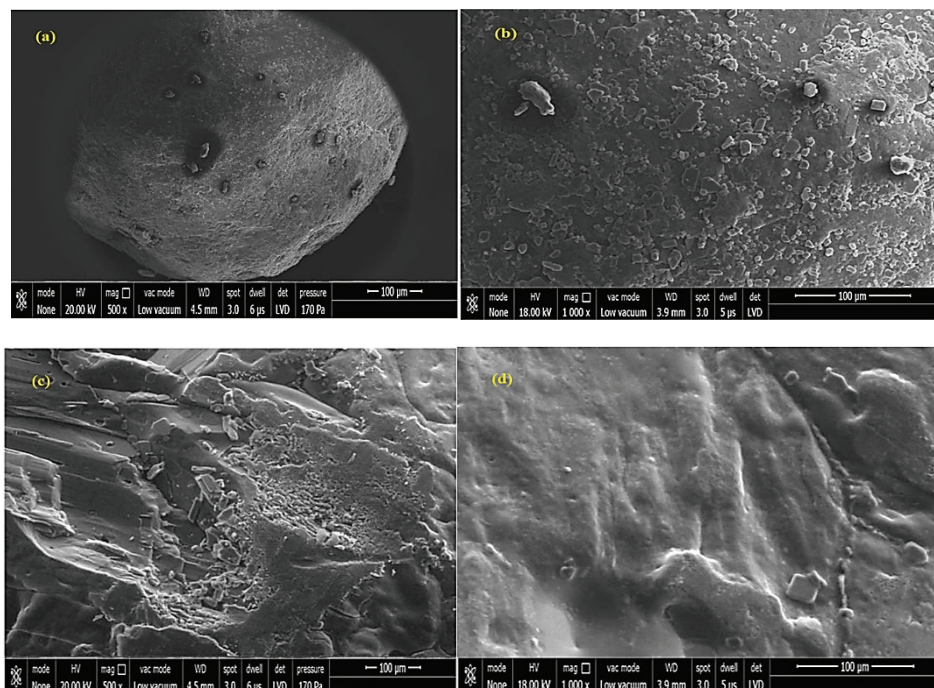


Fig. 3. SEM image of UCU granules at a) 500 \times and b) 1000 \times magnification and NCU granules at c) 500 \times and d) 1000 \times magnification.

In the case of UCU, long crystals were tightly cemented with the finer ones on the urea surface (Fig. 3a and b). This morphology can be attributed to the fact that uncoated granular urea production involves agglomeration. Some pores and gaps were also visible. However, in the case of NCU (Fig. 3c and d), the coating imparts more homogeneity to the surface, and since neem oil coating is dense, no visible signs of gaps or cavities in the coating layer were observed. The enclosing of urea granule gaps or cavities due to neem oil layering altered its release behaviour, making them CRF as demonstrated by NCU SEM results. To get an estimate of coating thickness, NCU particles were cut with a sharp knife, and these broken particles were scanned using SEM, as shown in Fig. 4a and b. A variable coating thickness lying between 51.9–65.56 μ m was observed.

As can be seen in the images, the coating layer is very dense, and the contact between the coating layer and the urea granule was thorough. This dense coating is responsible for imparting controlled release behaviour to urea. It is reported that the coating thickness affects the release pattern of nitrogen from fertilizers.²¹

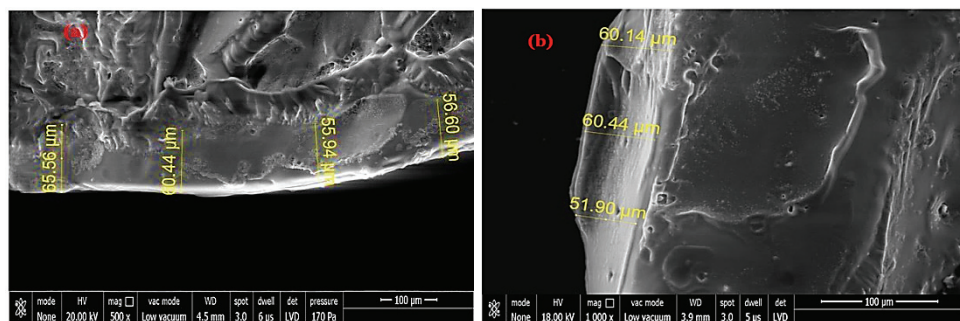


Fig. 4. SEM image of a section of NCU granules: a) 500 \times and b) 1000 \times magnification.

EDX of UCU and NCU

The EDX of UCU (Fig. 5a) and NCU (Fig. 5b) showed no remarkable difference in the presence of any extra elements in NCU compared to UCU. However, a lower peak of nitrogen in the case of NCU suggests that about 2 % reduction in total N was observed for NCU compared to UCU. It is due to the inherent nature of the coating process, in which the urea granule undergoes spraying, wetting and drying processes, which may cause some loss of nitrogen. However, variations in the contents of O, C, Fe, and Al were also noted.

XRD analysis for UCU and NCU

The XRD spectra of the UCU and NCU of particle diameter 1.7 mm were compared in Fig. 6. The figure makes it clear that both particles had crystalline structure and the peaks of urea, urea ammonium nitrate, and ammonium nitrate were visible only, and no characteristic peaks of other impurities were found to be seen. The main cause of this variation in peak intensity was that neem oil blocks the sites when it penetrates the micro cracks of UCU. This was attributed to the strong physical adherence of neem oil with the outer coating of the urea base. All the recorded peaks correspond to the components of the fertilizer. Since no new peaks in the spectra of NCU are observed, it may be inferred that no new phases are formed during the coating process. This shows that the interactions between the neem oil and urea are basically physical and not chemical in nature.

FTIR spectra analysis for UCU and NCU

The FTIR spectra of UCU and NCU (Fig. 7) demonstrate that all the peaks were in the same positions. Peak shifting was not observed. Both the samples show similar strong peaks of the amide group, N–H, at 3500 cm⁻¹, indicating the presence of urea molecules. This is followed by the double peaks of C=O bonds at around 1682 cm⁻¹ and the C–N bond at around 1465 cm⁻¹. No additional functional groups were observed in NCU; only the changes in the intensity of the

functional groups are seen, implying that the interaction between the UCU and the neem oil is physical.

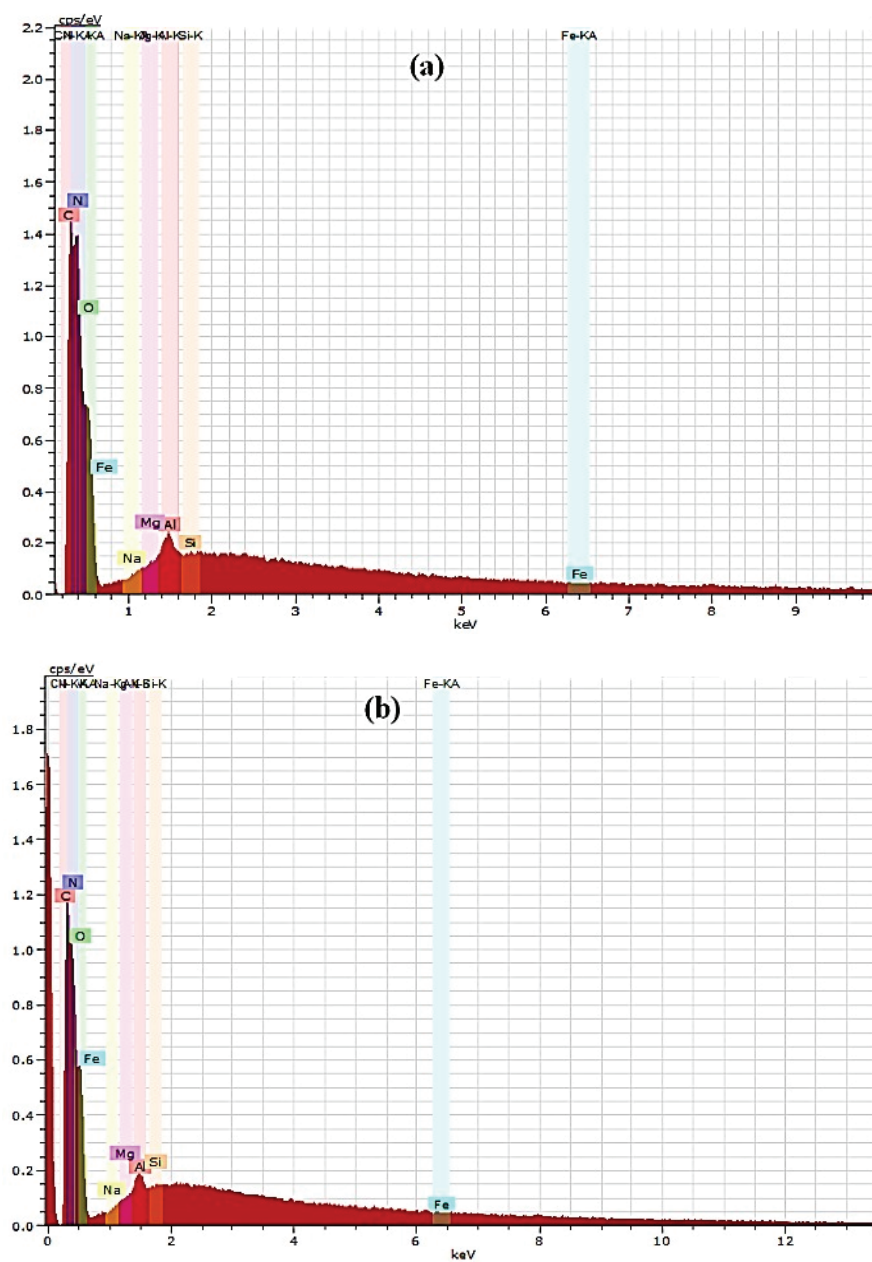


Fig. 5. EDS diagram of (a) UCU and (b) NCU.

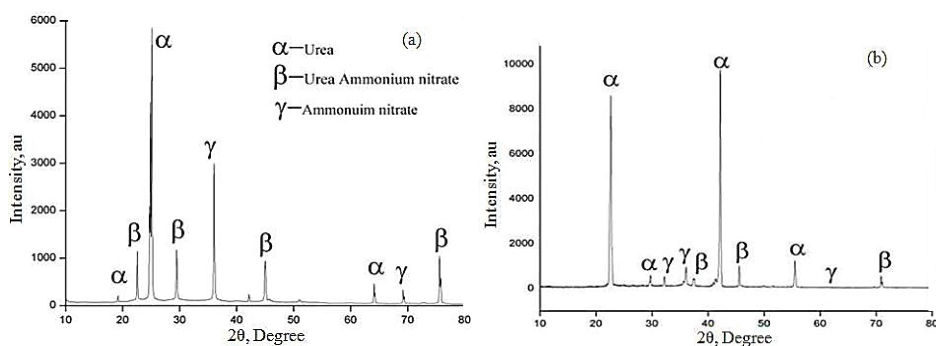


Fig. 6. XRD Diagram of: a) UCU and b) NCU.

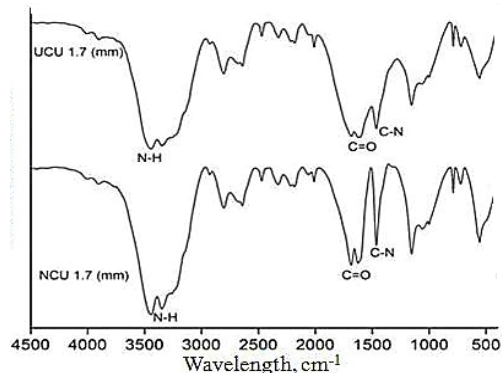


Fig. 7. FTIR diagram of NCU and UCU (both at 1.7 mm diameter).

Determination of nutrient release using refractive index

The refractive index can be used to measure the concentration of urea in solution directly and thus provides a fair estimate of nutrient release from the sample. This method offers distinct advantages like fast analysis, high efficiency, and free from chemical or reagent consumption. In the present work, the percentage of urea release in terms of nitrogen content and refractive index values for NCU was measured and compared to UCU and other materials such as PCU and BCU using chitosan as a binder. The PCU and BCU data taken from literature²² are compared to show the superior slow release behaviour of NCU.

Fig. 8 shows the NCU calibration curve in distilled water constructed with the standards from 0 to 250000 ppm at 25 and 40 °C. The two temperatures are selected to see the effect of temperature on the release mechanism. The curve depicts the linearity over a wide range, which helps in the measurement of nitrogen release from NCU without dilution of samples.

The refractive index values for NCU at 25 and 40 °C and the corresponding urea release percentages (using the calibration curves) are plotted in Fig. 9a and b, respectively. The nutrient release rate increases with temperature. This tempe-

temperature dependency helps in ascertaining the urea availability to the crop as per ambient and corresponding soil temperature.

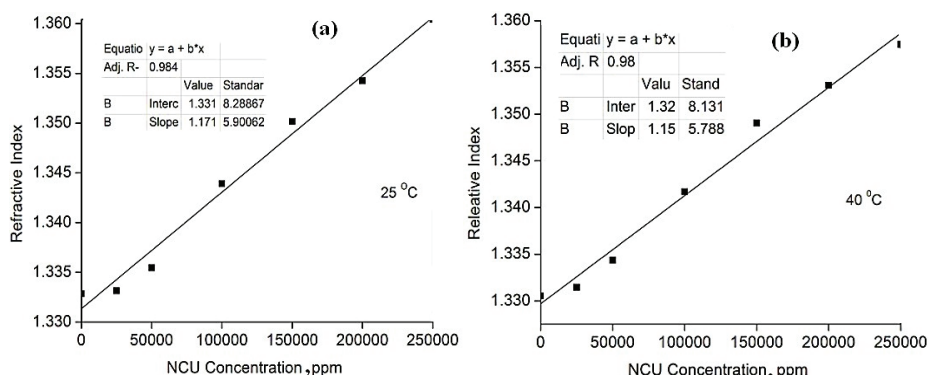


Fig. 8. Calibration curves for NCU at different temperatures.

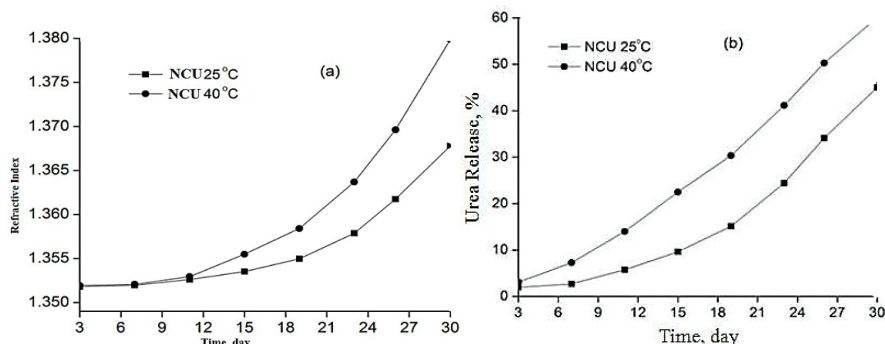


Fig. 9. NCU: a) refractive index values and b) urea release percentage.

In order to compare the controlled release efficiency of NCU with UCU and other coated fertilizers, namely PCU and BCU, the refractive index values and urea release percentages at 25 °C were measured. The results are shown in Fig. 10a and b, respectively.

The results show that 1.03, 4 and 4.8 % of nitrogen of NCU, PCU and BCU, respectively, were released into the water during the first day, and the release rate values at day 30 were 45.03, 63.4 and 81.9 %, for NCU, PCU and BCU respectively. On the other hand, the uncoated urea released all its nitrogen content within one hour.

These release data show the slow release properties of NCU, PCU and BCU samples, which also follow the standards of slow release fertilizers of Comité Européende Normalization (CEN). According to CEN, a fertilizer can be described as having controlled release properties if nutrient release is not more than 15 % after 1 day or not more than 75 % after 28 days. Also, the release from

NCU is slower for any particular time as compared to PCU and BCU; this indicates better control over nutrient release when urea is coated with neem oil. So NCU is a novel CRF, which exhibits excellent slow-release behaviour, apart from being biodegradable, and neem oil acting as biopesticide and insecticide.

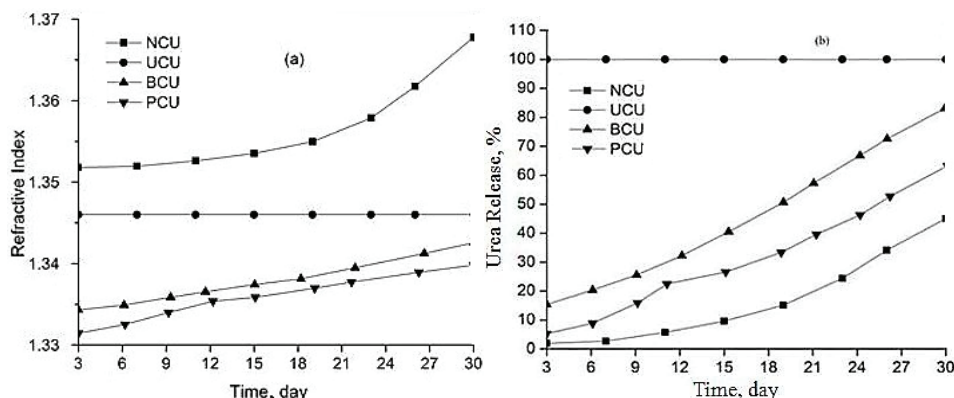


Fig.10. UCU, BCU, PCU, and NCU: a) refractive index values and b) urea release percentage.

The results show that 1.03, 4 and 4.8 % of nitrogen of NCU, PCU and BCU, respectively, were released into the water during the first day, and the release rate values at day 30 were 45.03, 63.4 and 81.9 %, for NCU, PCU and BCU, respectively. On the other hand, the uncoated urea released all its nitrogen content within one hour.

These release data show the slow release properties of NCU, PCU and BCU samples, which also follow the standards of slow release fertilizers of Comité Européende Normalization (CEN). According to CEN, a fertilizer can be described as having controlled release properties if nutrient release is not more than 15 % after 1 day or not more than 75 % after 28 days. Also, the release from NCU is slower for any particular time as compared to PCU and BCU; this indicates better control over nutrient release when urea is coated with neem oil. So NCU is a novel CRF, which exhibits excellent slow-release behaviour, apart from being biodegradable, and neem oil acting as biopesticide and insecticide.

Crushing strength

The crushing strength of NCU and UCU for two diameters, namely 1.7 and 2.0 mm, were measured using a tensile tester, and results are shown in Table IV.

TABLE IV. Crushing strength, N mm^{-2} , of NCU and UCU

Sample	dia / mm	
	1.7	2.0
UCU	1.49	1.62
NCU	2.50	2.96

From the table values, it can be inferred that NCU particles have higher crushing strength as compared to UCU of the same size, indicating its higher mechanical strength. Higher crushing strength also leads to a reduction in attrition during storage and transportation and also reduces the dustiness factor. The crushing strength increases with the increase in the size of particles for the same sample.

In order to compare the crushing strength of NCU with PCU and BCU, the literature values were taken, and the results are shown in Table V. These particular CRF particles were selected because the literature values of the crushing strength of these CRFs were available for particles with the same urea core radius and coating thickness as the NCU prepared. From the table, it is clear that NCU has higher crushing strength as compared to PCU and BCU, indicating its better performance as CRF due to improved strength.

TABLE V. Comparison of crushing strength, $N\ mm^{-2}$, of NCU, UCU, PCU and BCU ($dia = 2.0\ mm$)

Sample	Value
UCU	1.62
NCU	2.96
PCU	1.80
BCU	1.67

CONCLUSION

In order to raise the crop productivity, contemporary technologies must be used, to improve food output. Using CRF is one such strategy which is used worldwide, in the present work various aspects of an environmentally friendly CRF namely NCU is scientifically explored using various analytical and experimental techniques to determine its suitability as an effective CRF. NCU was prepared using neem oil as a coating material in a fluidized bed. Crushing strength test results showed that NCU ($2.96\ N\ mm^{-2}$) has better mechanical strength as compared to the UCU ($1.62\ N\ mm^{-2}$), PCU ($1.80\ N\ mm^{-2}$), and BCU ($1.67\ N\ mm^{-2}$). Higher crushing strength aids in safe storage and transportation of a CRF. The analysis carried using FTIR and XRD showed that the neem oil coating did not react, and no new chemical interactions take place, as well as the adherence of oil is mainly due to surface forces. SEM images show a variable coating thickness lying between 51.9 to 65.56 μm . Its release characteristics show the controlled release behaviour because strong adherence of oil fills the void in the urea particle, which manifest itself in an increased nutrient release time. NCU release characteristics were also in accordance with the prescribed standards of CEN. To establish the superior behaviour of NCU as a CRF its release rate results were also compared with literature data of other CRF, namely phosphate slimes (PCU) and bentonite coated (BCU) with chitosan as a binder. The results

show that 1.03, 4 and 4.8 % of Nitrogen of NCU, PCU and BCU, respectively, were released into the water during the first day, and the release rate values at the day30 were 45.03, 63.4 and 81.9 %, for NCU, PCU and BCU respectively. On the other hand, the uncoated urea released all its nitrogen content within one hour. Therefore, NCU shows a promise of becoming a preferred CRF using abundant, low-cost natural resources that is neem oil. In summary, NCU proves to be a novel CRF.

Acknowledgment. The authors would like to thank the staff of Material Research Centre, Malaviya National Institute of Technology, Jaipur (India), for their support to make available analytical instruments.

ИЗВОД

УРЕА ОБЛОЖЕНА НЕЕМ (*Azadirachtaindica*) УЉЕМ, НОВО ЂУБРИВО СА КОНТРОЛИСАНИМ ОСЛОБАЂАЊЕМ: ФИЗИЧКА И ХЕМИЈСКА АНАЛИЗА СТРУКТУРЕ И ПОНАШАЊЕ ПРИ ОСЛОБАЂАЊУ ХРАНЉИВИХ МАТЕРИЈА

SHIV OM MEENA, MANISH VASHISHTHA и MEENU

Department of Chemical Engineering, Malaviya National Institute of Technology, Jaipur, Rajasthan, India

Развој ђубрива са контролисаним ослобађањем (CRF) је зелена технологија која не само да смањује губитак азота узрокован испарањем и испирањем, већ мења и кинетику ослобађања азота, што заузврат обезбеђује хранљиве материје биљкама, темпом који је компатибилан са њиховим метаболичким потребама. Уз све већу свест о људском здрављу и заштити животне средине, долази до брзог померања ка развоју еколошки прихватљивог ђубрива заснованог на природним ресурсима. Већина литературе о CRF се односи на превлаке на бази органских и неорганских материјала на ђубривима. У случају урее обложене уљем Neem (NCU) литература је ограничена на разјашњавање ефеката премаза на повећање приноса усева и раст биљака. Међутим, у литератури недостаје било каква свеобухватна студија о NCU као CRF, која покрива главне аспекте као што су његова карактеризација, одређивање брзине ослобађања хранљивих материја и поређење са другим CRF. Овај рад је покушај да се попуни овај јаз у научним сазнањима о NCU. У овој студији, уреа обложена уљем Neem (NCU) је припремљена да би се постигао механизам контролисаног ослобађања неопходан за испуњавање захтева усева. Карактеризације необложене урее (UCU) и NCU су урађене коришћењем скенирајуће електронске микроскопије (SEM) са енергетско дисперзивном рендгенском анализом (EDX), инфрацрвеном спектроскопијом (FTIR), мерењем индекса преламања (RI) и тестом чврстоће на дробљење. Да би се утврдило супериорно понашање NCU као CRF, резултати су упоређени са литературним подацима других CRF, односно фосфатне слузи (PCU) и бентонита (BCU) обложених хитозаном као везивом. Експерименти ослобађања хранљивих материја су показали вредности од 1,03 (први дан) и 45,03 % (тридесети дан). Испитивање чврстоће на дробљење је спроведено за честице исте величине, а резултати су показали да NCU има бољу механичку чврстоћу у поређењу са UCU, PCU и BCU.

(Примљено 28. Фебруара, ревидирано 25. јуна 2023, прихваћено 10. фебруара 2024)

REFERENCES

1. P. W. Gerbens-Leenes, S. Nonhebel, W. P. M. F. Ivens, *Agric. Ecosyst. Environ.* **90** (2002) 47 ([https://doi.org/10.1016/S0167-8809\(01\)00169-4](https://doi.org/10.1016/S0167-8809(01)00169-4))
2. A. S. M. Ghumman, R. Shamsuddin, M. M. Nasef, E. G. Krivoborodov, S. Ahmad, A. A. Zanin, Y. O. Mezhuev, A. Abbasi, *Polymers (Basel)* **13** (2021) 4040 (<https://doi.org/10.3390/polym13224040>)
3. B. Beig, M. B. K. Niazi, B. Ullah, A. N. Gondal, Z. Jahan, M. Zia, N. Ahmad, *J. Coatings Technol. Res.* **21** (2023) 199 (<https://doi.org/10.1007/s11998-023-00810-6>)
4. M. E. Brown, N. Higgins, *Environ. Sci. Technol.* **43** (2009) 8016 (<https://doi.org/10.1021/es901162d>)
5. C. Jie, C. Jing-zhang, T. Man-zhi, G. Zi-tong, *J. Geogr. Sci.* **12** (2002) 243 (<https://doi.org/10.1007/BF02837480>)
6. A. S. M. Ghumman, R. Shamsuddin, R. Sabir, A. Waheed, A. Sami, H. Almohamadi, *RSC Adv.* **13** (2023) 7867 (<https://doi.org/10.1039/d3ra00256j>)
7. P. K. Dash, P. Bhattacharyya, M. Shahid, U. Kumar, S. R. Padhy, C. K. Swain, A. Senapati, P. Bihari, A. K. Nayak, *Environ. Geochem. Health* **45** (2023) 7979 (<https://doi.org/10.1007/s10653-023-01713-6>)
8. X. Fan, S. Zhang, X. Mo, Y. Li, Y. Fu, Z. Liu, *Pedosphere* **27** (2017) 1027 ([https://doi.org/10.1016/S1002-0160\(17\)60379-5](https://doi.org/10.1016/S1002-0160(17)60379-5))
9. S. K. Behera, R. K. Panda, *Agric. Water Manage.* **96** (2009) 1532 (<https://doi.org/10.1016/j.agwat.2009.06.016>)
10. S. O. Meena, M. Vashishtha, A. Meena, *Chem. Methodol.* **2** (2018) 299 (<https://doi.org/10.22034/chemm.2018.66186>)
11. B. Ni, M. Liu, S. Lü, *Chem. Eng. J.* **155** (2009) 892 (<https://doi.org/10.1016/j.cej.2009.08.025>)
12. A. S. M. Ghumman, R. Shamsuddin, M. M. Nasef, W. Z. N. Yahya, A. Abbasi, H. Almohamadi, *Sci. Total Environ.* **846** (2022) 157417 (<http://dx.doi.org/10.1016/j.scitotenv.2022.157417>)
13. R. Hussain, R. R. Devi, T. K. Maji, *Iran. Polym. J.* **21** (2012) 473 (<https://doi.org/10.1007/s13726-012-0051-0>)
14. A. Jarosiewicz, M. Tomaszevska, *J. Agric. Food Chem.* **51** (2003) 413 (<https://doi.org/10.1021/jf020800o>)
15. V. Ghormade, M. V Deshpande, K. M. Paknikar, *Biotechnol. Adv.* **29** (2011) 792 (<https://doi.org/10.1016/j.biotechadv.2011.06.007>)
16. R. Kavitha, O. Latifah, O. H. Ahmed, P. W. Charles, K. Susilawati, *Polymers (Basel)* **15** (2023) 1863 (<https://doi.org/10.3390/polym15081863>)
17. N. Xiaoyu, W. Yuejin, W. Zhengyan, W. Lin, Q. Guannan, Y. Lixiang, *Biosyst. Eng.* **115** (2013) 274 (<https://doi.org/10.1016/j.biosystemseng.2013.04.001>)
18. S. O. Meena, M. Vashishtha, A. Meena, *J. Adv. Agric. Technol.* **6** (2019) 32 (<https://doi.org/10.18178/joaat.6.1.32-37>)
19. G. M. Blouin, D. W. Rindt, O. E. Moore, *J. Agric. Food Chem.* **19** (1971) 801 (<https://doi.org/10.1021/jf60177a039>)
20. D. Liang, Y. Wang, H. Shi, Z. Luo, R. L. Quirino, Q. Lu, C. Zhang, *Ind. Crops Prod.* **189** (2022) 115803 (<https://doi.org/10.1016/j.indcrop.2022.115803>)
21. M. Marcińczyk, P. Oleszczuk, *J. Clean. Prod.* **339** (2022) 130685 (<https://doi.org/10.1016/j.jclepro.2022.130685>)
22. M. M. Hanafi, S. M. Eltaib, M. B. Ahmad, *Eur. Polym. J.* **36** (2000) 2081 ([https://doi.org/10.1016/S0014-3057\(00\)00004-5](https://doi.org/10.1016/S0014-3057(00)00004-5)).



Enhancing longevity and performance: The effects of ZrO₂ and TaC coatings on pistons in internal combustion engines

SATHISH RENGARAJAN¹, RAMEEZA MUHAMMED^{1*}, D. VIJAYAN²
and MUHAMMED ABRAR³

¹Department of Mechanical Engineering, St. Joseph's College of Engineering OMR, Chennai, Tamil Nadu, India, ²Department of Mechanical Engineering, SCSVMV University, Enathur, Kanchipuram, Tamil Nadu, India and ³Department of Mechanical Engineering, St. Joseph's Institute of Technology, OMR, Chennai, Tamil Nadu, India

((Received 24 February, revised 8 April, accepted 21 May 2024)

Abstract: Coating of pistons with ZrO₂ and TaC improves their longevity and performance in internal combustion engines by enhancing the resistance to wear, heat and corrosion. In this study the plasma spray coating is performed on crown of the piston with the combination of the percentage composition namely, 95 % ZrO₂ + 5 % TaC, 98 % ZrO₂ + 2 % TaC and 100 % ZrO₂. Among the three 95 % ZrO₂ + 5 % TaC composition shows better results. The increase in ZrO₂ content leads to the formation of a more integrated scale with fewer pores. Higher concentrations of ZrO₂ in the coatings lead to the increased interaction with discharge sparks and instability of the process. At elevated temperatures, a two-phase material of cubic zirconium dioxide and hexagonal corundum was formed. The bonding strength of the coating is influenced by the addition of TaC and the power input during the spraying operation. The microstructure of ZrO₂ and TaC coatings on aluminium alloy is characterized by granular structure, tightly packed pores and partially melted ZrO₂ particles. The coating had a uniform structure with columnar and cluster-like elements, influenced by ZrO₂ concentration.

Keywords: plasma spray; bond strength; scanning electron microscope; nanoparticles.

INTRODUCTION

The surface characteristics of engineering materials are regarded as crucial in the design process to improve the durability and functionality of components.^{1,2} Wear, corrosion or fatigue mechanisms are the most common causes of damage to engineering parts, which often begins at the surface and occurs during use. The thermal spray coating process is very adaptable and widely recognized

*Corresponding author. E-mail: rama.5.rsj@gmail.com
<https://doi.org/10.2298/JSC240224053R>

as an efficient and cost-effective technique for surface engineering. The most prevalent technique for producing heat barrier coatings in production is plasma spray coatings. Its external high flame temperature makes it an ideal approach for spraying ceramic materials. This technique involves the creation of a coating by propelling small particles that are either melted, semi-molten, or softened towards the surface of the component. When particles strike repeatedly, they mechanically interlock with the surface they are deposited on, forming platelets called splats. These splats build up many layers, resulting in a coating with a certain thickness. The application of tantalum carbide and zirconium cobalt alloy coatings on pistons is revolutionizing the automotive sector due to their remarkable durability and performance. These cutting-edge coatings, which are composed of ZrO_2 and TaC, have great advantages that extend the life and efficiency of pistons in internal combustion engines.^{3,4} Improving the resistance of pistons to wear, heat and corrosion is the main goal of coating them with ZrO_2 and TaC. These coatings have exceptional mechanical qualities, such as good temperature stability, low friction coefficient and high hardness.^{3,5} They can therefore tolerate the severe operating conditions found inside the engine, which include high temperatures, high pressures and continuous friction.^{4–7} Manufacturers can greatly increase the lifespan of pistons and lower the frequency of replacements and related maintenance expenses by using ZrO_2 and TaC coatings. Furthermore, by lowering the frictional losses and enhancing the heat dissipation, these coatings help to improve fuel efficiency.^{6,8} This results in decreased emissions, improved engine performance, and ultimately, a more ecologically friendly and sustainable driving experience. In recent times, there has been a substantial increase in the need for advanced materials exhibiting enhanced high-temperature characteristics. This surge in demand can be attributed to their pivotal role in diverse sectors including aerospace, energy and automotive.^{7–10} Materials used in high-temperature applications need the preservation of their inherent properties and structural integrity across a range of temperatures. The criticality of high-temperature stability cannot be overstated when considering materials that are exposed to exceedingly elevated thermal conditions.^{9,11} Thermal conductivity, an essential property, assumes a pivotal role in the processes of heat transfer and dissipation. The mechanical strength of materials holds significant importance, especially in high-temperature environments where maintaining structural integrity is crucial, alongside their thermal properties.^{10,12} Hence, the investigation of superior mechanical, thermal and thermomechanical properties is of great scientific significance. As the temperature rises, the physical and mechanical characteristics of materials experience alterations, resulting in a decline in material properties and diminished structural dependability.^{11,13} Sivakumar and Kumar conducted a study to investigate the effects of yttria stabilized zirconia coating on the performance of diesel engines and the pollutants they produce.^{12,14} A comparison

was made between the impact of the thermal barrier coating (TBC) on the performance and emission metrics and the characteristic curves of the baseline engine. The material's notable characteristics, such as its high thermal expansion coefficient, low thermal conductivity, high Poisson's ratio and stable phase structure at elevated temperatures, are easily noticeable.^{13–16} The experiment improved thermal efficiency by 5 %, decreased heat loss to the cooling medium by 5 %, decreased HC emission by 35 %, decreased brake specific fuel consumption by 28.3 % and raised thermal efficiency by 5 %. The aim of this research is to explore the impact of ZrO₂ and TaC coatings on a piston by altering their proportions. To the authors knowledge and from the literature above plenty of work has been carried on material performance coating on the piston to improve the efficiency like indicated power, fuel consumption, emission, *etc.*, but only few researchers are focused on the evaluating of the zirconium oxide and tantalum coating. This study seeks to demonstrate the influence of varying coating percentages on the surface morphology and quality of the component. This study will present the surface features, the microstructure as depicted in SEM images, and the mechanical attributes of the examined piston. The findings demonstrate that the active polar oxygen-containing functional groups are introduced onto the PET surface as a result of plasma modification.³⁴ The coating provides exceptional resistance to exposure to abrasive chemicals, mechanical strength against extensive abrasion, and high hardness for the substrate.³⁵

EXPERIMENTAL

Materials, methods and experimentation

The tantalum carbide nano-powder was purchased by US Research Nano materials Inc. The ZrO₂ was purchased Sigma Aldrich. The chemical composition is shown in Fig. 1a. The coating is performed on the aluminium alloy which is used as a substrate shown in Fig. 1b–d. The coating is done by plasma spray coating process, using varying process parameters on Spraymet Surface Technologies Pvt. Ltd., Bangalore. Fig. 1e shows the machine which consists of 3MB of plasma spray gun, nozzle with Group hole (GH) nozzle type, stand-off distance of maximum of 101 mm with the pressure of hydrogen of 3.5 bar and the flow rate up to 450 m/s. The samples were received and placed into a graphite crucible with a mixed powder composition of 95 % ZrO₂ + 5 % TaC, 98 % ZrO₂ + 2 % TaC and 100 % ZrO₂, then the coating was carried out on the samples using supersonic plasma spraying. The crucible was subsequently placed in a furnace and maintained at a temperature of 2000–2200 °C for a duration of 2 h. The TaC grains had a size ranging from 1–1.5 mm. The primary and carrier gas used was argon, while hydrogen served as the secondary gas. The samples were examined by the field emission scanning electron microscope (FESEM) FEI make, Quanta 200F model. The chemical composition of the coated piston, which had different compositions, were analysed using a FEGSEM and an attached energy-dispersive X-ray (EDX) spectrometer, the magnification varied from 10×–300,000×, with a resolution of 5 nm. The X-ray diffraction (XRD) pattern of the ZrO₂ and TaC powder was obtained using a powder X-ray diffractometer done in SRM institute of Science and Technology, Chennai, having PAN analytical make with Benchtop Shimadzu model with CuKα radiation. The size of the crystallite was calculated by X-ray

spectrum peaks using Scherrer's formula. To validate the coating, the samples were subjected to surface morphology and porosity measurement using image analysis software with ASTMB487 standards (De-winter material plus version-2 wth a magnification 50 \times –800 \times with 5 megapixel camera at Metmech Analytical Engineers, Chennai).

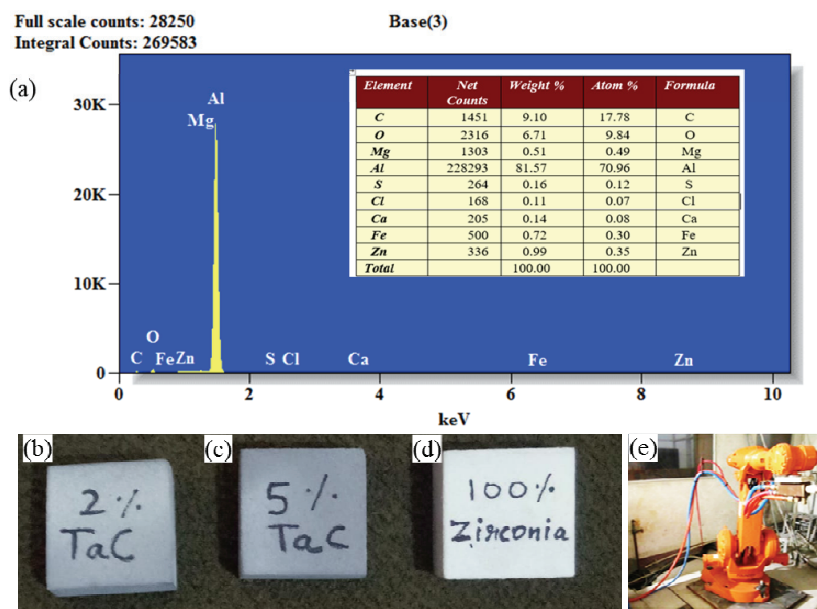


Fig. 1. a) Chemical composition of aluminum alloy, b) 98 % + 2 % TaC, c) 95 % ZrO₂ + 5 % TaC, d) 100 % ZrO₂ and e) plasma spray machine (Spraymet Surface Technologies Pvt. Ltd.).

RESULTS AND DISCUSSION

Fig. 2 shows the TaC and ZrO₂ powder XRD pattern reveals that the presence of diffraction peaks in the pattern indicates a high degree of crystalline nature the diffraction angles. TaC powder shows standard cubic structure with 2θ values of 34.9260, 40.5480, 58.6870, 70.1470, 73.7650 and 87.7400°; TaC powder have pattern reflection of (*h k l*) of (0 2 0), (0 2 2), (1 3 1), (2 2 2) and (0 4 0) which satisfy the JCPDS 96-101-0655. Regarding the diffraction peaks of ZrO₂ shows monoclinic crystal system, they become more distinct and smaller, and their intensity noticeably increases. This indicates a significant improvement in the crystallinity of the ZrO₂ nanocrystals. The enhancement is due to the enlargement of particle size, which leads to an increase in the number of crystalline planes.

The EDS pattern signified the existence of Zr, O and C, without any contamination from impurities shown in Fig. 3a. In contrast, the interior layer, which has been partially oxidized, appears to be more compact and largely composed of ZrO₂ components. The micro-particle-like diameters of some ZrO₂ match XRD

results, indicating amorphous compounds, which agrees with the results.^{18–20} The SEM image shows in Fig. 3b the aggregation 100 nm of the average size having the appearance of the particles in the shape of micro crystal with non-homogeneous particles sphere with the interstitial spaces between the spheres.

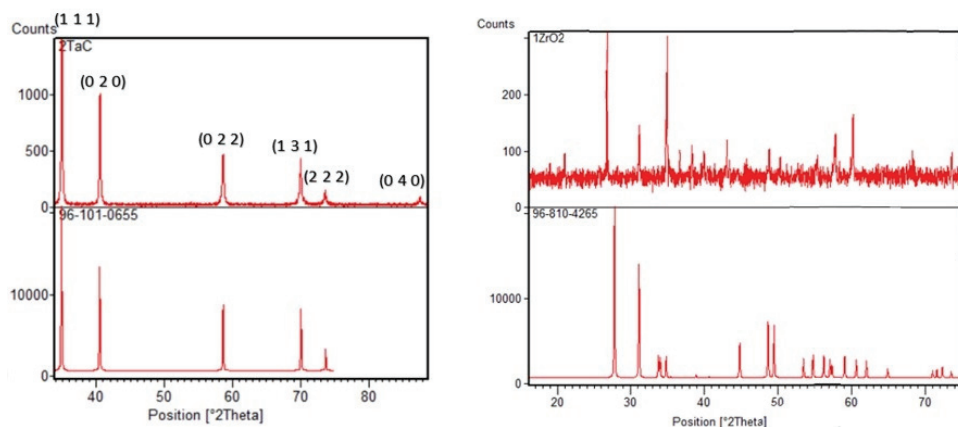


Fig. 2. XRD patterns for TaC and ZrO₂.

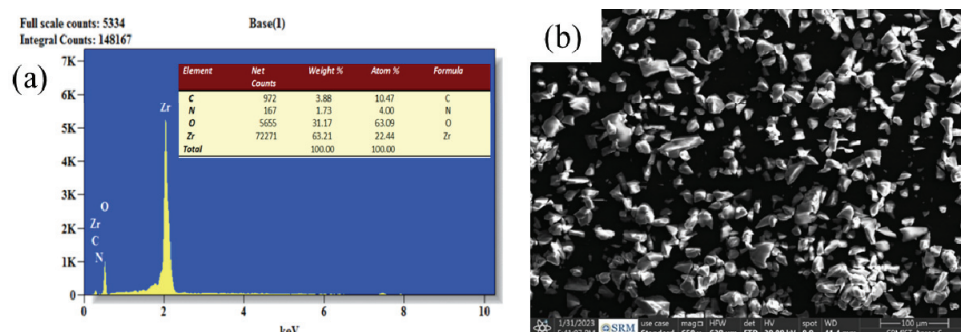


Fig. 3. a) EDS and b) powder SEM analysis for zirconium oxide.

Fig. 4a and b show the images acquired by SEM and EDX of tantalum powder which reveals the irregular or rise and fall surface.

Fig. 5a and b reveal that the ZrO₂ coating on aluminium alloy exhibits a granular structure which is densely packed with pores. The inadequate heat conduction between the ZrO₂ particles during the deposition phase results in partial melting.^{15,21} The amalgamation of partially and entirely liquefied ZrO₂ particles results in the formation of pores on the surface. When ZrO₂ is sprayed, it has a reaction with the gas molecules nearby, leading to a proper distribution of the coating on the substrate. The presence of oxide molecules in the air acts as a barrier, preventing the molten ZrO₂ particles from adhering to the substrate during

the deposition process.^{16,22} Moreover, the intense stress encountered during the solidification of ZrO₂ leads to the development of micro-cracks inside its structure. A layer of ZrO₂ has been applied to the surface of the aluminium alloy, resulting in a visible white zone. The spherical shape of the spray-dried composite powder is evident. The utilization of nanoscale particles as starting materials enables the fabrication of nanostructured powders that possess a homogeneous distribution of ZrO₂. The stability of the ceramic coatings is ensured by the plasma spraying process, which allows for optimal fluidity and homogeneous heating.^{17,23} The coatings exhibit predominantly tetragonal ZrO₂ phases, indicating the successful suppression of the change to the monoclinic phase.

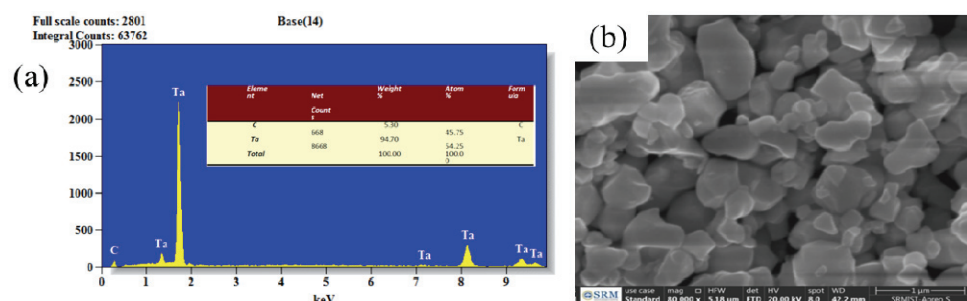


Fig. 4. a) EDS and b) powder SEM analysis for tantalum carbide.

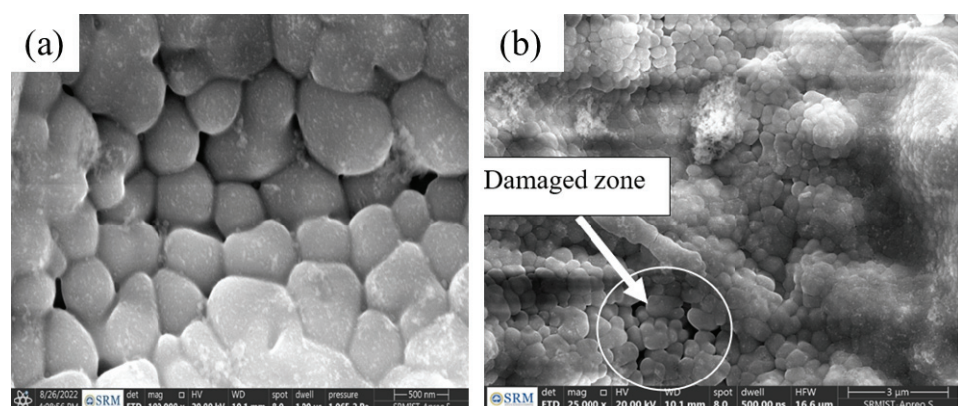


Fig. 5. a) 100 % ZrO₂ coated aluminium alloy; b) apparent gaps near the intersection (100 % ZrO₂ coated aluminium alloy).

The coating composed of 95 % ZrO₂ and 5 % TaC has a columnar structure and lacks sensitive regions such as grain boundaries, dislocations and second-phase precipitates. The columns have a width ranging from 30 to 60 μm . The structure of the coating exhibits quasi-regular vertical fissures that span the whole surface. The high-magnification photos reveal that the structural parts of

the coating primarily have a size ranging from 0.2 to 1 μm , which aligns with the size of the particles that collide with the surface of the substrate. The higher density of the SPS coating is linked to a larger average particle size of material clusters in the suspension, ranging from 1 to 5 μm . The absence of unmelted particles in the coating suggests that the plasma jet has generated enough thermal power. The coating often exhibits a size structure with splats ranging in thickness from 1 to 3 μm . The surface morphology changed from a common pancake-shaped structure to a cluster-shaped structure, depending on the concentrations of ZrO_2 and TaC . Similar observations were also reported.^{20,24}

Furthermore, the interface layer of the 95 % ZrO_2 and 5 % TaC coatings does not show significant defects or pores due to the stability of the process shown in Fig. 6a and b. Fig. 6c and d show the microstructure of the intersection area which shows minimum pores. The porosity measurement shows minimum pores area of 1.801 % and the non-porous area of 98.19 %, Fig. 6e. The TaC particles were unable to react with aluminium, compromising the interfacial bonding strength.

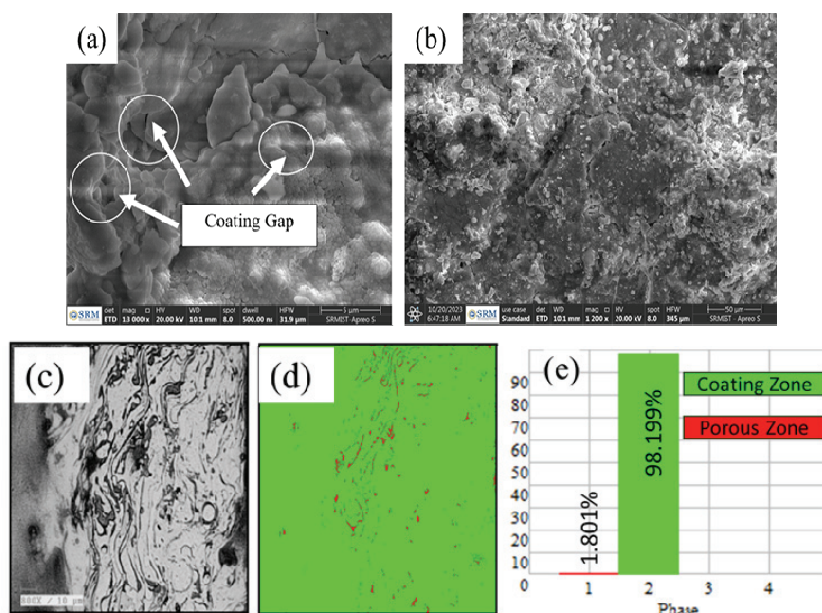


Fig. 6. a) Morphology of the coated surface; b) few pores on 95 % ZrO_2 + 5 % TaC coating surface; c) and d) microstructure and phase analysis; e) porosity measurement.

The plasma spraying method causes the described flaws when the surrounding gas interacts with the molten ZrO_2 droplets. Subsequently, when the droplets are deposited on the surface of the substrate, holes are formed due to inadequate overlap and quick solidification trapping internal gas.²⁷ The thickness of the

coatings, as determined by the cross-sectional analysis, increases simultaneously with ZrO_2 concentration. Beyond a concentration of 3 g/L of ZrO_2 , the inner layer suffered severe damage, leading to a halt in the increase of thickness. Nevertheless, up to this point, the trend of thickness increase becomes more prominent. This finding proves the ZrO_2 coating was adequately applied to the aluminium alloy. The presence of polyhedral or spherical grains, as well as unevenly formed grains, characterizes the densified microstructure. These granules are tightly bound together, providing a strong barrier that efficiently prevents oxygen from penetrating the piston material's surface.²⁹ Furthermore, the coating's structure contains a trace of mullite, which may be detected by its finest needle-shaped crystals. It should be noted that the powder rapidly melts and conducts a partial reaction with the oxygen present in the surrounding air during the spraying operation.

Microcracks, in other words the pores with dense structure, are seen in the plasma-sprayed ZrO_2 coating shown in Fig. 7a and b. In the examination carried out by EDX shown in Fig. 7c, Zr was identified in the luminous sections of the TaC layer within the ZrO_2 -TaC coating applied on the aluminium alloy. In reg-

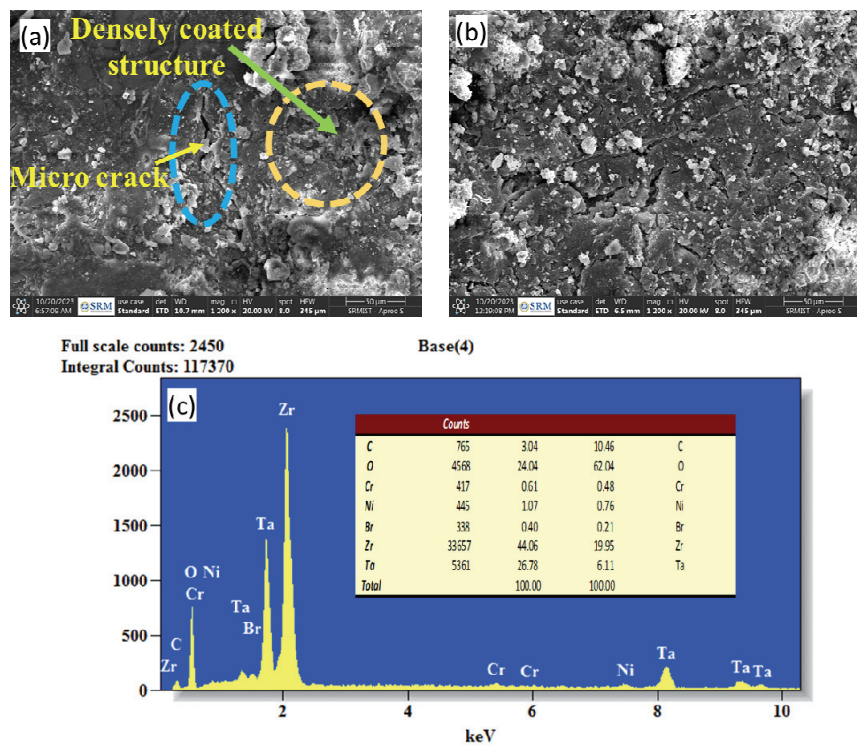


Fig. 7. a) 95 % ZrO_2 and 5 % TaC zone of dense particle, b) tiny pores on a coated surface (95 % ZrO_2 and 5 % TaC), c) EDX of the coated sample.

ard to the dynamic segregation theory for ZrO_2 , the reaction mechanism of ZrO_2 particles offers additional insight. It is theoretically possible for the reactive elements, even in their oxide form, to enhance the oxidation resistance.^{18,25} The participation of Zr in oxidation was observed in the study of ZrO_2 nanoparticles, ultimately being released from the ZrO_2 particles through reactions with Al.^{19,26} Furthermore, the interfaces between the coatings and substrates are transparent and strongly adhered, and the resulting coatings are homogeneous, dense, and of sufficient quality.

This provides more evidence that the process is unstable at higher concentrations, more especially the nano particles concentration of ZrO_2 which is around 8 g/L. Damage is caused to the inner layer or interface when larger concentrations are present, such as when there is 98 % ZrO_2 and 2 % TaC or when there is 100 % ZrO_2 .

The surface consisting of 98 % ZrO_2 and 2 % TaC was entirely coated with a cluster-like formation. The presence of ZrO_2 nanoparticles and localised plasma discharges contribute to the production of cluster-like formations. This phenomenon decreases the intensity of the discharges and causes instability.²⁸ With an increase in processing time, there is a corresponding increase in the size of the pancakes, which is a typical characteristic observed in plasma coating. Nevertheless, the impact of different ZrO_2 concentrations on this rise was not as prominent. Furthermore, the morphology of the pancakes was altered as the concentration of ZrO_2 increased, shifting from the uniform spherical shapes to the irregular and fragmented shapes shown in Fig. 8a. The reason for this could be attributed to the elevated content of ZrO_2 , which hampers the even dispersion of discharge channels. Regions that appear bright correspond to locations with a greater abundance of Zr, whereas the regions that appear dark correspond to areas with a lesser abundance of Zr. The presence of brilliant patches around the discharge channel is observed for low concentrations of ZrO_2 .²⁹ In addition, a multitude of minuscule pores appeared on the surface of the ZrO_2 coating. These pores can be linked to the chemical reaction between TaC and the gaseous by-products of SiO(g) , CO(g) and $\text{H}_2\text{(g)}$, Ni and N shown in Fig. 8b. Evidently, the interlayer cracks, resulting from thermal mismatch, originated in the ZrO_2 covering and separated the scale into two distinct sections. The damage occurs when a greater amount of ZrO_2 species is transported through the low-intensity discharge sparks, which do not induce interactions with the supplied species and thus harm the pre-existing inner layers. The porosity of this sample shows the maximum pore of 15.515 % with the coated area of 84.485 % shown in Fig. 8c and d, respectively. The aforementioned trend is less conspicuous in coatings including 95 % ZrO_2 with 5 % TaC, as well as those composed entirely of 100 % ZrO_2 , when compared to the coating consisting of 98 % ZrO_2 with 2 % TaC and its elements shown in Fig. 8e.

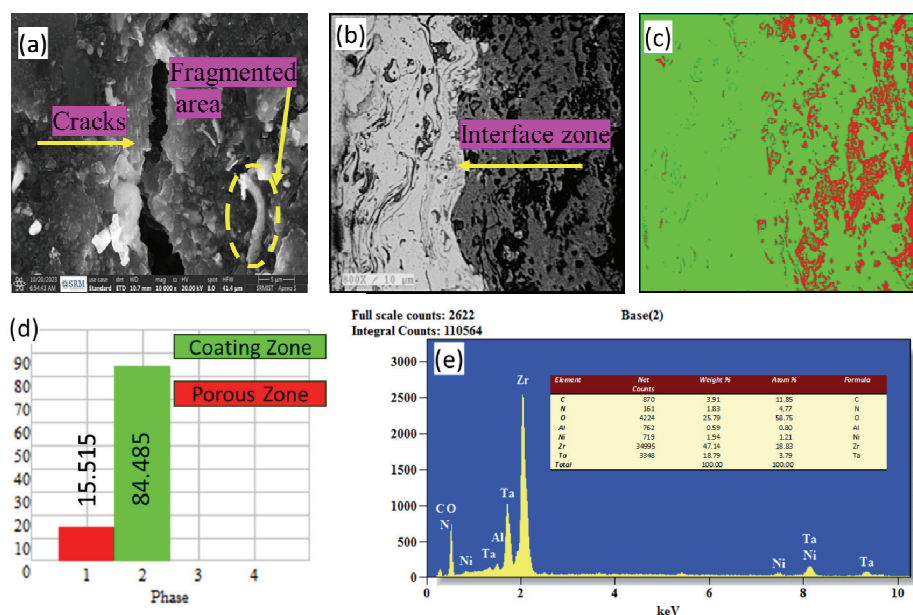


Fig. 8. a) 98 % ZrO_2 + 2 % TaC coating; b) and c) microstructure and phase analysis; d) porosity measurement; e) EDX analysis.

Following a thorough analysis, it was identified that the spray-applied coating possesses a compact microstructure.³⁰ This microstructure is made up of totally melted regions interspersed with a few particles that have remained unmelted. Surprisingly, a two-phase material is created within the coating when the temperature is elevated to 1400 °C.³¹ This substance is made up of cubic zirconia dioxide, which has a white appearance, and hexagonal corundum, which has a dark grey colour. Also, the coating possesses the occupied area of 84.485 % and the porosity of it includes 15.515 %. Thus, it may be inferred that an increased concentration of ZrO_2 and an extended processing duration can lead to severe damage to the inner layers which is consistent with earlier reports.^{32,33}

CONCLUSIONS

1. The microstructure of the zirconium dioxide and titanium aluminium carbide plays a crucial role in influencing the metallurgical and mechanical attributes of the surface coating. The oxide molecules in the air serve as a barrier, impeding the melted ZrO_2 particles from adhering to the substrate during deposition.
2. The appearance of the surface changed from a usual flat structure to a structure resembling clusters, with different amounts of ZrO_2 and TaC. Specifically, the surface with 98 % ZrO_2 and 2 % TaC was completely covered by the cluster-like structure.

3. Higher concentrations of ZrO_2 in the coatings lead to the increased interaction with discharge sparks and the instability of the process. The concentrations of 98 % ZrO_2 and 2 % TaC or 100 % ZrO_2 result in damage to the inner layer/interface. Higher concentrations and longer processing time can cause severe damage to the inner layers.

4. The plasma-sprayed ZrO_2 coatings exhibit microcracks and pores due to the interaction of gas with molten ZrO_2 droplets. The amount of thickness of the coatings is directly proportional to the concentration of ZrO_2 and the duration of the processing. The uneven layers and the particle fusion are observed in the ZrO_2 coating, while the ZrO_2 coating also has a relatively dense structure with cracks and tiny pores.

5. At elevated temperatures, a two-phase solid was made up of hexagonal corundum and cubic zirconia dioxide. It was made up of polyhedral or circular grains and a small amount of mullite.

Acknowledgement. The authors are very much thankful to St. Joseph's College of Engineering, OMR-Chennai.

ИЗВОД

ПОВЕЋАЊЕ ДУГОВЕЧНОСТИ И ПЕРФОРМАНСИ: ЕФЕКТИ ZrO_2 И ТАС ПРЕМАЗА НА КЛИПОВЕ У МОТОРИМА СА УНУТРАШЊИМ САГОРЕВАЊЕМ

SATHISH RENGARAJAN¹, RAMEEZA MUHAMMED¹, D. VIJAYAN² и MUHAMMED ABRAR³

¹Department of Mechanical Engineering, St. Joseph's College of Engineering OMR, Chennai, Tamil Nadu, India, ²Department of Mechanical Engineering, SCSVMV University, Enathur, Kanchipuram, Tamil Nadu, India и ³Department of Mechanical Engineering, St. Joseph's Institute of Technology, OMR, Chennai, Tamil Nadu, India

Облагање клипова са ZrO_2 и TaC побољшава њихову дуговечност и перформансе у моторима са унутрашњим сагоревањем повећавајући отпорност на хабање, топлоту и корозију. У овом истраживању вршило се наношење плазма спреја на круну клипа комбинацијом процентуалног састава и то 95 % ZrO_2 + 5 % TaC, 98 % ZrO_2 + 2 % TaC и 100 % ZrO_2 . Најбоље резултате показао је састав 95 % ZrO_2 + 5 % TaC. Повећање садржаја ZrO_2 доводи до формирања интегрисаније скале са мање пора. Веће концентрације ZrO_2 у премазима доводе до повећане интеракције са варницима приликом процеса пражњења и доводе до нестабилности процеса. На повишеним температурама настаје двофазни материјал од кубног цирконијум-диоксида и хексагоналног корунда. На снагу везивања премаза утиче додавање TaC, као и улазна снага током операције распршавања. Микроструктуру ZrO_2 и TaC превлака на легури алуминијума карактерише грануларна структура, чврсто збијене поре и делимично растопљене честице ZrO_2 . Превлака је имала уједначену структуру са стубастим и кластероликим елементима, под утицајем концентрације ZrO_2 .

(Примљено 24. јануара, ревидирано 8. априла, прихваћено 21. маја 2024)

REFERENCES

1. P.L. Fauchais, J.V.R. Heberlein, M.I. Boulos, *Overview of Thermal Spray*. In: *Thermal Spray Fundamentals*, Springer, Boston, MA, 2014, p. 17 (https://doi.org/10.1007/978-0-387-68991-3_2)
2. L. Pawlowski, *The Science and Engineering of Thermal Spray Coatings*, 2. ed., Wiley, New York, 2008 (ISBN 978-0-471-49049-4)
3. Y. Hu, Q. Dou, Q. Fu, X. Li, L. Zhou, J. Zhang, *Surf. Coat. Technol.* **435** (2022) 128243 (<https://doi.org/10.1016/j.surfcoat.2022.128243>)
4. Y. Zhang, J. Sun, L. Guo, X. Zhang, D. Cui, Q. Fu, *Corros. Sci.* **205** (2022) 110423 (<https://doi.org/10.1016/j.corsci.2022.110423>)
5. Z. Fu, X. Li, Y. Ren, M. Zhang, X. Geng, Q. Zhu, J.G. Li, X. Sun, *J. Eur. Ceram. Soc.* **39** (2019) 4996 (<https://doi.org/10.1016/j.jeurceramsoc.2019.07.011>)
6. Z. L. Mao, X. J. Yang, S. L. Zhu, Z. D. Cui, Z. Y. Li, Y. Q. Liang, *Mater. Express.* **5** (2015) 518 (<https://doi.org/10.1166/mex.2015.1267>)
7. G. Feng, H. Li, X. Yao, L. Chen, Y. Yu, H. Wang, M. Chen, *Ceram. Int.* **47** (2021) 21721 (<https://doi.org/10.1016/j.ceramint.2021.04.187>)
8. N. B. Dahotre, S. J. S. Nayak, *Surf. Coat. Technol.* **194** (2005) 58 (<https://doi.org/10.1016/j.surfcoat.2004.05.006>)
9. Z. Yao, Z. Song, H. Hao, Z. Yu, M. Cao, S. Zhang, M.T. Lanagan, H. Liu, *Adv. Mater.* **29** (2017) 1601727 (<https://doi.org/10.1002/adma.201601727>)
10. C. Suryanarayana, *Research* **10** (2019) 4219812 (<https://doi.org/10.34133/2019/4219812>)
11. V. Gvozdetskyi, B. Owens-Baird, S. Hong, and J.V. Zaikina, *Mater.* **12** (2018) 48 (<https://doi.org/10.3390/ma12010048>)
12. L. Wang, D. C. Li, J. S. Yang, F. Shao, X. H. Zhong, H. Y. Zhao, K. Yang, S. Y. Tao, Y. Wang, *J. Eur. Ceram. Soc.* **36** (2016) 1313 (<https://doi.org/10.1016/j.jeurceramsoc.2015.12.038>)
13. R. Darolia, *Int. Mater. Rev.* **58** (2013) 315 (<https://doi.org/10.1179/1743280413Y.0000000019>)
14. G. Sivakumar, S. S. Kumar, *Alex. Eng. J.* **53** (2014) 787 (<https://doi.org/10.1016/j.aej.2014.08.003>)
15. E. Vural, S. Ozel, B. Ozdalyan, *Optoelectr. Adv. Mat.* **8** (2014) 515 (<https://oamrc.inoe.ro/articles/the-investigation-of-microstructure-and-mechanical-properties-of-oxide-powders-coated-on-engine-pistons-surface/fulltext>)
16. J. Liang, Z. Peng, R. Li, B. Wang, *Ceram. Int.* **49** (2023) 29133 (<https://doi.org/10.1016/j.ceramint.2023.06.192>)
17. L. K. Brar, G. Singla, O. P. Pandey, *RSC. Adv.* **5** (2015) 1406 (<https://doi.org/10.1039/C4RA12105H>)
18. R. Sukanya, S. Ramki, S. M. Chen, *Microchim. Acta* **187** (2020) 342 (<https://doi.org/10.1007/s00604-020-04314-7>)
19. D. Manoharan, A. Loganathan, V. Kurapati, V. J. Nesamony, *Ultrason. Sonochem.* **23** (2015) 174 (<https://doi.org/10.1016/j.ultsonch.2014.10.004>)
20. E. A. Abdel Wahab, K.S. Shaaban, R. Elsaman, E. S. Yousef, *Appl. Phys., A* **125** (2019) 869 (<https://doi.org/10.1007/s00339-019-3166-8>)
21. M. Kovaleva, I. Goncharov, V. Novikov, M. Yapryntsev, O. Vagina, V. Sirota, Y. Tyurin, O. Kolisnichenko, *Mater. Today: Proc.* **49** (2022) 1423 (<https://doi.org/10.1016/j.matpr.2021.07.132>)

22. I. Gulyaev, V. Kuzmin, E. Kornienko, S. Vashchenko, D. Sergachev, *Mater. Today: Proc.* **11** (2019) 430 (<https://doi.org/10.1016/j.matpr.2019.01.008>)
23. Z. U. Rehman, D. Choi, *J. Magnes. Alloys* **7** (2019) 555 (<https://doi.org/10.1016/j.jma.2019.10.001>)
24. J. Jakubowicz, M. Sopata, G. Adamek, P. Siwak, T. Kachlicki, *Adv. Mater. Sci. Eng.* **2018** (2018) 2085368 (<https://doi.org/10.1155/2018/2085368>)
25. B. A. Pint, *Oxid. Met.* **45** (1996) 1 (<https://doi.org/10.1007/BF01046818>)
26. X. Luo, X. Yang, Q. Huang, A. Shi, C. Fang, Y. Weng, *J. Therm. Spray Technol.* **30** (2021) 1582 (<https://doi.org/10.1007/s11666-021-01215-w>)
27. G. Shao, Q. Wang, X. Wu, C. Jiao, S. Cui, Y. Kong, J. Jiao, X. Shen, *Corros. Sci.* **126** (2017) 78 (<https://doi.org/10.1016/j.corsci.2017.06.017>)
28. Y. H. Cui, Z. C. Hu, Y. D. Ma, Y. Yang, C. C. Zhao, Y. T. Ran, P. Y. Gao, L. Wang, Y. C. Dong, D. R. Yan, *Surf. Coat. Technol.* **363** (2019) 112 (<https://doi.org/10.1016/j.surfcoat.2019.02.059>)
29. G. Shao, X. Wu, S. Cui, X. Shen, Y. Lu, Q. Zhang, Y. Kong, *J. Alloys Compd.* **690** (2017) 63 (<https://doi.org/10.1016/j.jallcom.2016.08.073>)
30. A. A. Ali, S. A. Shama, A. S. Amin, S. R. EL-Sayed, *Mater. Sci. Eng., B* **269** (2021) 115167 (<https://doi.org/10.1016/j.mseb.2021.115167>)
31. R. Vaßen, D.E. Mack, M. Tandler, Y. J. Sohn, D. Sebold, O. Guillon, *J. Am. Cer. Soc.* **104** (2021) 463 (<https://doi.org/10.1111/jace.17452>)
32. D. Wang, B. Yang, Z. Tian, L. Shen, Y. Huang, *Trans. China Weld.* **34** (2013) 10 (<http://hjxb.hwi.com.cn/hjxb/en/article/id/20130303>)
33. K. H. Kim, S. Hoon, J. H. Kim, K. W. Hong, J. Y. Park, *J. Nanosci. Nanotechnol.* **17** (2017) 8598 (<https://doi.org/10.1166/jnn.2017.15171>)
34. S. Samipour, H. Taghvaei, D. Mohebbi-Kalhor, M. R. Rahimpour, *Surf. Innov.* **8** (2019) 76 (<https://doi.org/10.1680/jsuin.19.00030>)
35. K. Zhang, Y. Zhu, Z. Chen, Z. Zhang, Y. Gao, *Surf. Innov.* **40** (2022) 1 (<https://doi.org/10.1680/jsuin.22.01049>).



The performance of an eco-friendly adsorbent for methylene blue removal from aqueous solution: Kinetic, isotherm and thermodynamic approaches

RAJAE GHIBATE^{1*}, MERYEM BEN BAAZIZ², ALI AMECHROUQ³,
RACHID TAOUIL⁴ and OMAR SENHAJ³

¹Laboratory of Physical Chemistry, Materials and Environment, Faculty of Sciences and Technologies, Moulay Ismail University of Meknes, Errachidia, Morocco, ²Laboratory of Materials Engineering for the Environment and Natural Resources, Faculty of Sciences and Technologies, Moulay Ismail University of Meknes, Errachidia, Morocco, ³Laboratory of Biomolecular and Macromolecular Chemistry, Moulay Ismail University of Meknes, Meknes, Morocco and ⁴Laboratory of Mechanics, Energetics, Automation, and Sustainable Development, Faculty of Science and Technology, Moulay Ismail University of Meknes, Errachidia, Morocco

(Received 17 March, revised 1 May 2023, accepted 26 March 2024)

Abstract: The current study aims to determine how well pomegranate peel can remove methylene blue (MB) from an aqueous solution. For this purpose, kinetic, isotherm and thermodynamic adsorption studies were performed in a batch system. The rate of MB adsorption was rapid and reached the equilibrium at about 60 min. The adsorption capacity reached approximately 42.71 mg g^{-1} at the initial dye concentration of 100 mg L^{-1} . The kinetic modelling of MB adsorption was performed using pseudo-first-order, pseudo-second-order, Elovich and intraparticle diffusion models. The pseudo-second-order model was found to be the most adequate for fitting the kinetic data based on R^2 , RMSE, ARE and χ^2 values. It was also discovered that MB adsorption onto pomegranate peel is not simply rate-limited by intraparticle diffusion. The isotherm approach showed a maximum adsorption capacity of 67.78 mg g^{-1} at 298 K using 2 g L^{-1} of pomegranate peel. The equilibrium modelling was also conducted. The four statistical values highlighted the better fit of the Langmuir model than the Freundlich model. Additionally, the exothermic and spontaneous nature of the adsorption process was revealed by thermodynamic research. These findings demonstrate the effectiveness of pomegranate peel as an eco-friendly adsorbent for MB removal.

Keywords: adsorption; kinetic; pomegranate peel; methylene blue; isotherm, thermodynamic.

*Corresponding author. E-mail: rajae.ghibate@gmail.com
<https://doi.org/10.2298/JSC230317037G>

INTRODUCTION

Methylene blue (MB) is one of the most widely utilized synthetic dyes in various industrial sectors.¹ It is known for the promising potential in dyeing cotton, wool, and silk,² making it a common choice in the textile industry. However, the release of MB into the environment poses aesthetic issues and dramatic effects on aquatic life,³ attributed to its visibility, low biodegradability and bio-accumulation through the food chain, posing a danger to human health. The acute exposure to MB can cause tachycardia, cyanosis, jaundice, quadriplegia and tissue necrosis in humans.⁴ It also causes eye burns, leading to permanent injury to the eyes of humans and animals.⁵ Other adverse effects of MB, such as hypertension, acute kidney failure and hemolytic anemia, have been reported in the literature.^{6,7} In this context, various conventional methods have been investigated to remediate water pollution caused by MB. These methods include adsorption,^{8–12} classical and advanced chemical oxidation,^{13–17} membrane separation^{18,19} and coagulation/flocculation.^{20–22} Among these approaches, adsorption is an effective and low-cost technique to remove different pollutants from aqueous solutions,^{23–26} including MB. The significant advantages of the adsorption process include its effectiveness and economical dye removal, low sludge production and simplicity in execution.²⁷ Additionally, using agricultural waste as a biosorbent offers a low-cost and eco-friendly approach to a circular economy.²⁸ Several researchers have demonstrated the potential of various agricultural wastes for MB removal, such as sugarcane bagasse,²⁹ rice husk,⁴ date pits,³⁰ peanut hull,³¹ soursop residues,²⁹ wheat straw³² and orange and banana peels.³³

The pomegranate is a prized fruit, valued for its unquestionable qualities that promote consumption. Global pomegranate production continues to rise owing to the high demand for the fruit and its derivatives, such as juice, syrup and jam. However, the peel, constituting approximately 50 % of the fruit's mass,³⁴ is often discarded as waste despite its potential uses. The worldwide generation of pomegranate peel was estimated at around 1.9 million tons five years ago.³⁵ Furthermore, Morocco produces a substantial amount of pomegranate fruit, with an estimated annual production of pomegranate peel reaching 29,000 tons based on the approximately 58,000 tons of fruit harvested annually.³⁶ In this context, this research aims to enhance the performance of pomegranate peel as an eco-friendly adsorbent for removing MB from an aqueous solution. A preliminary study revealed its potential use for the adsorption of MB.³⁵ Therefore, the present work focuses on studying the kinetic, isotherm and thermodynamic approaches to gather more information on the mechanism of MB adsorption by pomegranate peel.

EXPERIMENTAL

Adsorbate

Methylene blue, with the molecular formula C₁₆H₁₈ClN₃S (Fig. 1), was supplied by Loba Chemie. It was used without further purification to prepare the stock solution (1000 mg

L^{-1}). The working solutions of MB were subsequently prepared by diluting the stock solution with distilled water.

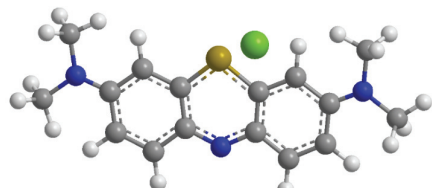


Fig. 1. Chemical structure of methylene blue dye.

Biosorbent preparation

After the separation from pomegranate, the peel is cleaned with distilled water and dried in the sun for about three weeks. The fragments are ground into a powder and washed repeatedly with distilled water until a colourless solution is obtained. The powdered pomegranate peel is then dried at 60 °C for 48 h before being placed in a desiccator, awaiting usage.

ATR-FTIR characterization

The surface functionalities of the produced pomegranate peel powder were identified using attenuated total reflectance-Fourier transform infrared (ATR-FTIR) on a ThermoScientific Nicolet iS10 FTIR spectrometer. The samples were recorded in transmittance mode.

Adsorption experiments

The adsorption experiments in the present study were conducted in a batch system using the initial pH of the MB solution. For each experiment, 0.1 g of powdered pomegranate peel was added to 50 mL of the MB solution (100 mg L^{-1}) in a 100 mL Erlenmeyer flask. The suspensions were shaken at 300 rpm by an electromagnetic stirrer. The studied concentration was chosen based on the preliminary investigation assessing the effective MB concentration in textile wastewater. The adsorption kinetic approach was carried out from 0 to 300 min at room temperature. The adsorption isotherm approach was performed at 298 K for 120 min by varying the initial dye concentration from 0 to 500 mg L^{-1} . The thermodynamic approach was conducted at varying temperatures from 298 to 328 K for 120 min. At the end of each adsorption experiment, the suspensions were centrifuged at 3800 rpm for 5 min. Then, the residual concentration of MB in the supernatant was determined using a double-beam UV–Vis spectrophotometer at 665 nm. The amount of MB adsorbed per unit mass of adsorbent (q_t) was calculated using the following equation:

$$q_t = \frac{C_0 - C_t}{m} V \quad (1)$$

where C_0 and C_t are, respectively, the initial and time t concentrations of MB in solution, mg L^{-1} , V is the MB solution volume, L, and m is the mass of the powdered pomegranate peel, g.

Kinetic study

The kinetic approach was investigated to determine the order of the adsorption reaction and the mechanism controlling the process. In this regard, four well-known models were used to study the kinetic of MB adsorption onto pomegranate peel: pseudo-first-order (PFO), pseudo-second-order (PSO), Elovich and intraparticle diffusion (IPD), as given in Table I, where q_e / mg g⁻¹ and K_1 / min⁻¹ represent, respectively, the amount of MB adsorbed at equilibrium and the rate constant of PFO; K_2 / g mg⁻¹ min⁻¹ represents the rate constant of PSO; α_E / mg g⁻¹

min^{-1} and $\beta_E / \text{g mg}^{-1}$ represent the rates constants of adsorption and desorption of Elovich, respectively; $K_{ID} / \text{mg g}^{-1} \text{ min}^{-1/2}$ represents the IPD rate constant and c the constant related to the thickness of the boundary layer.

TABLE I. Adsorption kinetic models

Kinetic model	Non-linear	Linear	Plot	Ref.
PFO	$\frac{dq_t}{dt} = K_1(q_e - q_t)$	$\ln(q_e - q_t) = \ln q_e - K_1 t$	$\ln(q_e - q_t) \text{ vs. } t$	³⁷
PSO	$\frac{dq_t}{dt} = K_2(q_e - q_t)^2$	$\frac{1}{q_t} = \frac{1}{K_2 q_e^2} + \frac{1}{q_e} t$	$t / q_t \text{ vs. } t$	³⁸
Elovich	$\frac{dq_t}{dt} = \alpha_E \exp(-\beta_E q_t)$	$q_t = \frac{1}{\beta_E} \ln(\alpha_E \beta_E) + \frac{1}{\beta_E} \ln t$	$q_t \text{ vs. } \ln t$	³⁹
IPD	—	$q_t = K_{ID} t^{1/2} + C$	$q_t \text{ vs. } t^{1/2}$	⁴⁰

Isotherm study

The study of the adsorption isotherm is essential for quantifying and comparing the performance of pomegranate peel in MB removal. In this regard, Langmuir and Freundlich models were employed. The Langmuir isotherm model presupposes that all adsorption sites on the adsorbent are structurally homogeneous, that the adsorption is confined to a monolayer, and also that molecules adsorbed on neighbouring sites do not interact.⁴¹ Accordingly, when an adsorbent reaches an equilibrium saturation point, no further adsorption occurs, indicating a finite capacity for adsorption:

$$q_e = \frac{q_{\max} K_L C_e}{1 + K_L C_e} \quad (2)$$

The Langmuir equation may be expressed in its linearized form as follows:

$$\frac{C_e}{q_e} = \frac{1}{K_L q_{\max}} + \frac{C_e}{q_{\max}} \quad (3)$$

where $q_{\max} / \text{mg g}^{-1}$ denotes the maximum adsorption capacity and $K_L / \text{L mg}^{-1}$ represents the Langmuir constant.

The Freundlich adsorption isotherm is an empirical model used to elucidate the multi-layer adsorption with the interactions between molecules adsorbed on heterogeneous surfaces featuring non-identical sites and varied adsorption energies. This model is not restricted to the formation of monolayers of adsorbate molecules on the adsorbent.⁴² The Eq. (4) illustrates the Freundlich isotherm model:

$$q_e = K_F C_e^{1/n} \quad (4)$$

The linearized form of the Freundlich model can be expressed as follows:

$$\ln q_e = \ln K_F + \frac{1}{n} \ln C_e \quad (5)$$

where $K_F / (\text{mg g}^{-1})(\text{L g}^{-1})^n$ is the Freundlich constant and n is the Freundlich exponent.

Analysis of models

The use of error functions is an effective way to assess the fit of a model and its underlying assumptions. This study employed four statistics: coefficient of determination (R^2), root mean square error ($RMSE$), average relative error (ARE), and chi-square (χ^2). The optimal model should have a coefficient of determination close to one and the lowest values of $RMSE$, ARE and χ^2 .

The $RMSE$, ARE and χ^2 are calculated using the following expressions:

$$RMSE = \sqrt{\frac{\sum_{i=1}^N (q_{t,\text{cal}} - q_{t,\text{exp}})^2}{N}} \quad (6)$$

$$ARE = \frac{100}{N} \sum_{i=1}^N \left| \frac{q_{t,\text{exp}} - q_{t,\text{cal}}}{q_{t,\text{exp}}} \right| \quad (7)$$

$$\chi^2 = \sum_{i=1}^N \frac{(q_{t,\text{exp}} - q_{t,\text{cal}})^2}{q_{t,\text{cal}}} \quad (8)$$

where N is the number of the experimental data points, $q_{t,\text{exp}} / \text{mg g}^{-1}$ is the experimental value, and $q_{t,\text{cal}} / \text{mg g}^{-1}$ is the predicted value of q_t with the investigated model.

RESULTS AND DISCUSSION

ATR-FTIR characterization

The ATR-FTIR spectrum of the studied biosorbent is illustrated in Fig. 2. The infrared spectrum of pomegranate peel exhibits bands at 3,368 (hydroxyl group of carboxylic acid or phenol), 2925 and 2853 (C–H stretching vibrations of lignocellulosic components), 1730 (C=O stretching vibration of carboxyl groups), 1615 (aromatic C=C or COO⁻ stretching vibration of carboxylic acids), 1444 (asymmetric deformation of C–H bond of methyl and methylene groups) and 1327 cm⁻¹ (symmetrical deformation of C–H bond of methyl group). The other

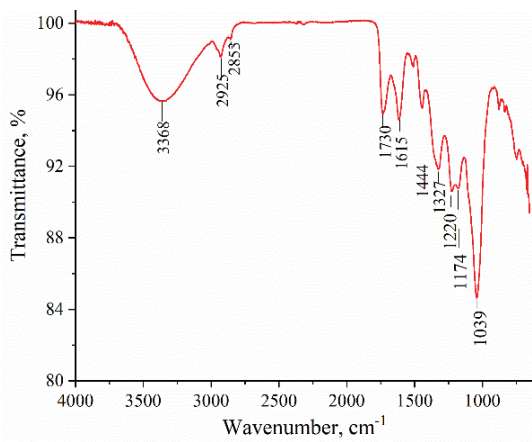


Fig. 2. ATR-FTIR spectrum of pomegranate peel powder.

bands are attributed to the C–O vibration of primary alcohols (C–OH) of cellulose and hemicellulose.

Adsorption kinetics

The kinetic study of MB adsorption onto pomegranate peel was conducted over a range of contact times from 5 to 300 min. The results depicted in Fig. 3 clearly illustrate a two-stage adsorption process. Initially, there was a rapid increase in MB adsorption, reaching 33.94 mg g^{-1} within just 10 min. Subsequently, the rate of MB adsorption slowed down, gradually reaching its maximum around 60 min, with no significant changes observed thereafter. This behaviour can be attributed to numerous vacant sites on the pomegranate peel surface during the initial stage, which were rapidly occupied by MB molecules until saturation was achieved.

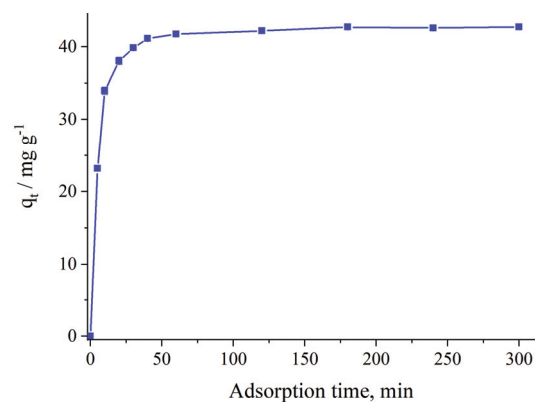


Fig. 3. MB adsorption kinetic onto pomegranate peel.

Additionally, to understand better the adsorption ability of the produced biosorbent, the adsorption kinetic of rhodamine B (RhB) dye onto pomegranate peel was previously investigated. The rate of RhB adsorption was rapid, reaching the equilibrium at approximately 120 min, with an adsorption capacity of around 30.47 mg g^{-1} .²⁷ However, it's noteworthy that this value is lower than that observed for MB adsorption, which reached 42.71 mg g^{-1} , indicating a higher affinity of pomegranate peel for MB dye.

Kinetic modeling

Four kinetic models were fitted to the obtained kinetic data: PFO, PSO, Elovich and IPD (Fig. 4). The kinetic parameters and the associated statistical analysis of each model are presented in Table II. The suitability of the PSO model to fit the MB adsorption onto pomegranate peel can be inferred from a simple review of the Table II. Indeed, this model presents the highest coefficient of determination ($R^2 = 1$) and the lowest values of *RMSE*, *ARE* and χ^2 . Additionally, the fit ade-

quacy of the PSO model for MB adsorption has been revealed by other researchers as well.⁴³

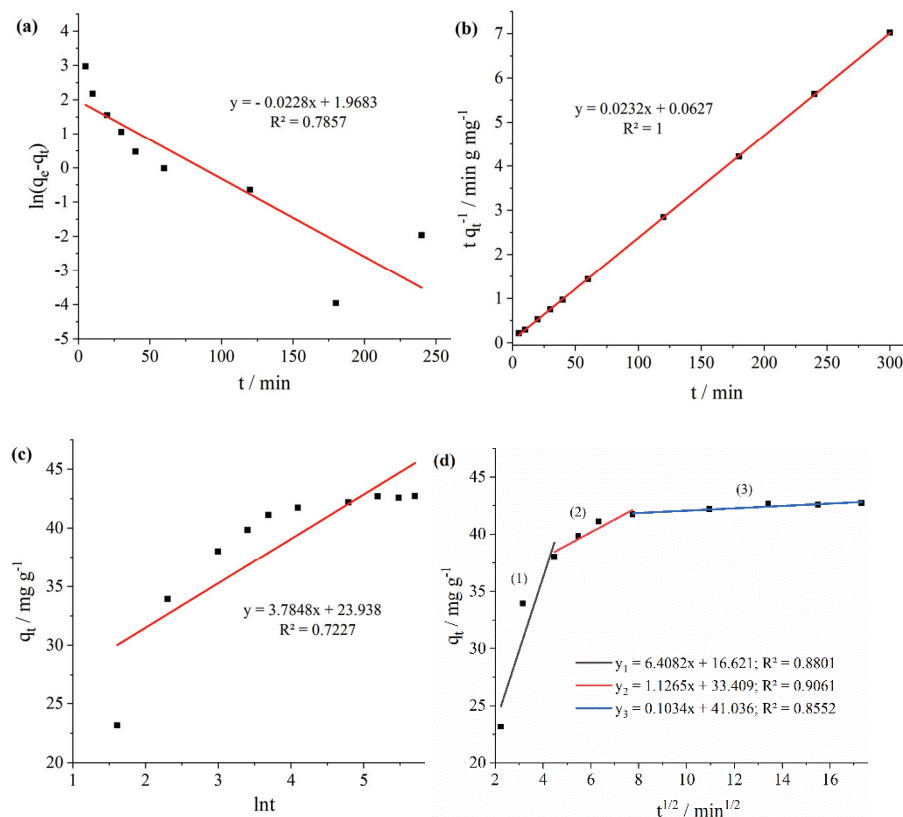


Fig. 4. a) PFO, b) PSO, c) Elovich and d) IPD linear plots for MB adsorption onto pomegranate peel at 298 K.

TABLE II. Kinetic parameters for the adsorption of MB onto pomegranate peel

Kinetic model	Kinetic parameters at 298 K		Statistical analysis			
	$q_{e,cal}$ / mg g ⁻¹	K_1 / min ⁻¹	R^2	RMSE	ARE / %	χ^2
PFO	7.16	0.02	0.7857	34.43	88.75	3.51×10^3
PSO	43.14	0.009	1	1.56	2.52	0.86
Elovich	α_E / mg g ⁻¹ min ⁻¹ 2.11×10^3	β_E / g mg ⁻¹ 0.26	0.7227	3.07	7.55	2.78
IPD (2)	K_{ID} / mg g ⁻¹ min ^{-1/2} 1.13	c 33.41	0.9061	6.26	13.37	9.10

Furthermore, Fig. 4d illustrates the tri-linearity observed in the IPD plot, which doesn't pass through the origin. This suggests that the intraparticle diffusion is not the only rate-limiting step, and the MB adsorption process is controlled by three mechanisms. Indeed, the first linear section with a sharp slope represents the bulk diffusion at the adsorbent's external surface (instantaneous adsorption). The second section depicts the intraparticle diffusion (gradual adsorption), and the last one, the plateau portion, represents the equilibrium.⁴⁴ The intercept of the second section provides information on the thickness of the boundary layer (Table II). A higher intercept indicates a thicker boundary layer, amplifying its effect.^{45,46} Other researchers have reported similar findings regarding the adsorption of MB onto tea residues and diatomite.^{47,48}

Models validation

Fig. 5a depicts the accuracy of the PSO model in describing the MB adsorption kinetic data. This observation is further supported by Fig. 5b, which provides a graphical comparison of the experimental and the predicted equilibrium adsorption capacities for each model. The figure highlights the predictive quality of the PSO model in representing MB adsorption onto pomegranate peel, as evidenced by its closest predicted value ($q_{e,cal} = 42.76 \text{ mg g}^{-1}$) to the experimental value ($q_{e,exp} = 42.71 \text{ mg g}^{-1}$).

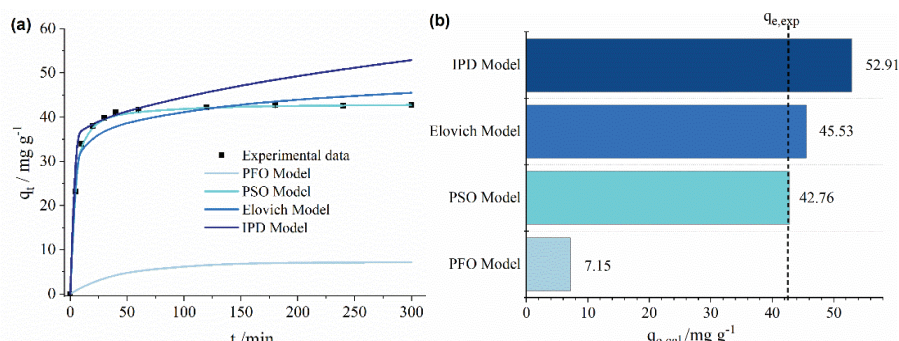


Fig. 5. Kinetic models validation with experimental data.

Adsorption isotherm and modeling

The equilibrium mechanisms between MB and the pomegranate peel surface were studied through Langmuir and Freundlich models. The adsorption isotherm was simulated at 298 K (Fig. 6), and the associated parameters were determined and grouped with statistical analysis in Table III. The linear fitting plots of the Langmuir and Freundlich models are represented in Fig. 6. The Langmuir model provided a better fit to the experimental data, with a coefficient of determination closer to one ($R^2 = 0.9998$) and lower RMSE, ARE and χ^2 values compared to the

Freundlich model (Table III). This adequacy indicates the monolayer adsorption of MB onto pomegranate peel.

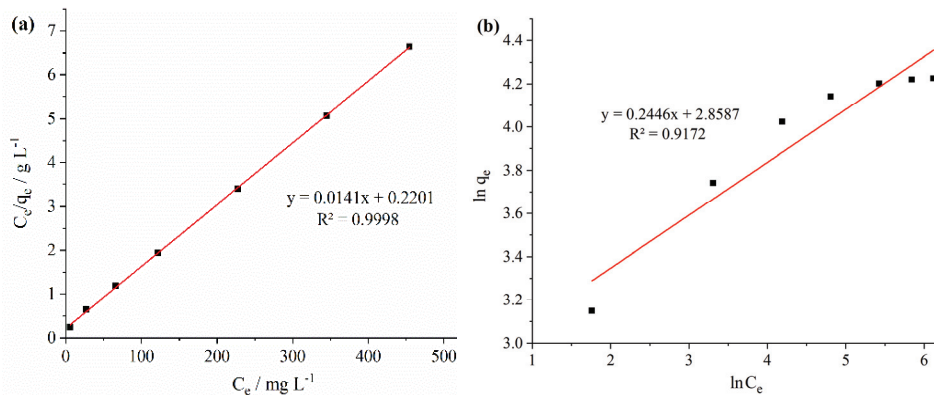


Fig. 6. a) Langmuir and b) Freundlich linear isotherm plots for MB adsorption onto pomegranate peel at 298 K.

TABLE III. Equilibrium parameters for MB adsorption onto pomegranate peel at 298 K

Isotherm model	Isotherm parameters at 298 K		Statistical analysis			
	q_{\max} / mg g ⁻¹	K_L / L g ⁻¹	R^2	RMSE	ARE / %	χ^2
Langmuir	70.96	0.06	0.9998	2.00	4.05	1.10
Freundlich	4.09	K_F / (mg g ⁻¹)(L g ⁻¹) ⁿ	0.9172	5.72	9.69	4.01

The Langmuir model's adequacy is further supported by Fig. 7, which displays the experimental and predicted isotherms of MB adsorption onto pomegranate peel. A simple examination of the figure confirms the Langmuir model's predictive quality. Indeed, the Langmuir maximum adsorption capacity (70.96 mg g⁻¹) is close to the maximum experimental adsorption capacity (67.78 mg g⁻¹).

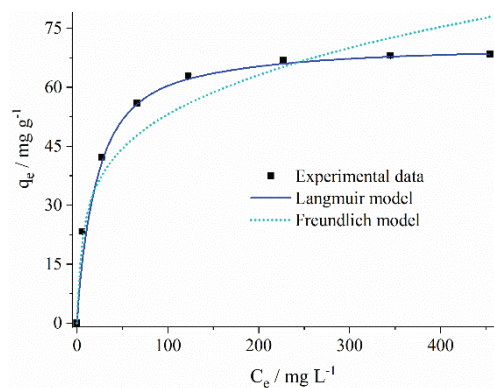


Fig. 7. MB adsorption isotherm onto pomegranate peel.

Moreover, it is advisable to compare the adsorption capacity of pomegranate peel with that of other biomass reported in previous research. Table IV demonstrates that pomegranate peel has a higher adsorption capacity than other biomass, suggesting it could be used as an inexpensive and environmentally friendly adsorbent for the removal of MB.

TABLE IV. Comparison of maximum adsorption capacities of various biomass for MB dye

Biomass	q_{\max} / mg g ⁻¹	Reference
Rice husk	40.59	4
Soursop residues	55.40	29
Sugarcane bagasse	17.43	29
Date pits	80.29	30
Wheat straw	60.66	32
Orange peel	18.60	33
Banana peel	20.80	33
Orange albedo	77.79	49
Potato peel	97.08	50
Avocado peel	62.11	51
Hamimelon peel	58.60	51
Dragon fruit peel	62.58	51
Tucuma cake	17.24	52
Pomelo peel	81.71	53
Pomegranate peel	67.78	This work

Thermodynamic study

The thermodynamic study plays an essential role in understanding the adsorption process of MB onto pomegranate peel. In this respect, the thermodynamic parameters of MB adsorption, namely the free energy change, ΔG° / kJ mol⁻¹, the enthalpy change, ΔH° / kJ mol⁻¹, and the entropy change, ΔS° / J mol⁻¹·K⁻¹ were determined using the following equations:

$$\Delta G^\circ = -RT \ln K_d; K_d = \frac{q_e}{C_e} \quad (9)$$

$$\Delta G^\circ = \Delta H^\circ - T\Delta S^\circ \quad (10)$$

$$\ln K_d = \left(\frac{\Delta S^\circ}{R} \right) - \left(\frac{\Delta H^\circ}{R} \right) \frac{1}{T} \quad (11)$$

where K_d is the distribution coefficient for adsorption, C_e / mg L⁻¹ is the equilibrium concentration of MB, q_e / mg g⁻¹ is the amount of MB adsorbed at equilibrium, T / K is the absolute temperature and R is the gas constant (8.314 J mol⁻¹ K⁻¹).

The slope and intercept of the $\ln K_d$ vs. T^{-1} plot, shown in Fig. 8, were used to calculate the values for ΔH° and ΔS° . The obtained results are presented in Table V.

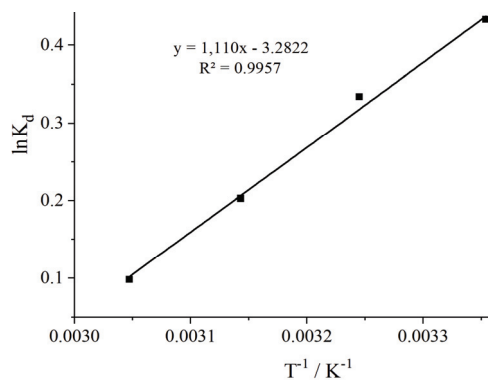


Fig. 8. The plot of $\ln K_d$ vs. T^{-1} for the MB adsorption onto pomegranate peel.

TABLE V. Thermodynamic parameters

T / K	$\Delta G^\circ / \text{kJ mol}^{-1}$	$\Delta H^\circ / \text{kJ mol}^{-1}$	$\Delta S^\circ / \text{J mol}^{-1} \cdot \text{K}^{-1}$
298	-1.07	-9.23	-27.29
308	-0.86		
318	-0.54		
328	-0.27		

The negative values of ΔG° for the various temperatures examined, as shown in Table V, demonstrate the spontaneity of MB adsorption. The negative value of ΔH° supports the exothermic nature of the adsorption process and suggests that no energy needs to be added in order to transfer MB from the aqueous phase to the solid. Moreover, the negative value of ΔS° suggests a reduction in randomness at the adsorbent/adsorbate interface during the adsorption process, without any significant change in the adsorbent structure.⁵⁴ Similar findings were also reported by Miraboutalebi *et al.*⁵⁵ for the adsorption of MB onto corn silks.

CONCLUSION

The findings indicate that pomegranate peel possesses a strong MB adsorption capacity. The MB adsorption occurred rapidly, reaching the equilibrium around 60 min, with an adsorption capacity close to 42.71 mg g^{-1} at an initial dye concentration of 100 mg L^{-1} . The results from the kinetic approach suggest that MB adsorption onto pomegranate peel perfectly follows pseudo-second-order kinetic and that the intraparticle diffusion is not the only rate-limiting step in the adsorption process. Additionally, a maximum adsorption capacity of 67.78 mg g^{-1} was observed with the isotherm approach, and the equilibrium data showed good compliance with the Langmuir model. The exothermicity and spontaneity of the adsorption process were indicated by the negative values of ΔG° and ΔH° , res-

pectively. In terms of ΔS° , the negative value suggested an increase in disorder at the adsorbent/adsorbate interface during the adsorption process. Moreover, the pomegranate peel exhibited a comparatively higher adsorption capacity for MB compared to other biomass. These findings highlight the potential of pomegranate peel as an environmentally friendly absorbent for effluent containing MB.

Acknowledgement. The authors acknowledge the CNRST (National Centre for Scientific and Technical Research, Morocco) for the partial support of this study.

ИЗВОД

ПЕРФОРМАНСЕ ЕКОЛОШКИ ПРИХВАТЉИВОГ АДСОРБЕНТА ЗА УКЛАЊАЊЕ МЕТИЛЕНСКОГ ПЛАВОГ ИЗ ВОДЕНОГ РАСТВОРА: КИНЕТИЧКИ, ИЗОТЕРМНИ И ТЕРМОДИНАМИЧКИ ПРИСТУПИ

RAJAE GHIBATE¹, MERYEM BEN BAAZIZ², ALI AMECHROUQ³, RACHID TAOUIL⁴ и OMAR SENHAJI³

¹Laboratory of Physical Chemistry, Materials and Environment, Faculty of Sciences and Technologies, Moulay Ismail University of Meknes, Errachidia, Morocco, ²Laboratory of Materials Engineering for the Environment and Natural Resources, Faculty of Sciences and Technologies, Moulay Ismail University of Meknes, Errachidia, Morocco, ³Laboratory of Biomolecular and Macromolecular Chemistry, Moulay Ismail University of Meknes, Meknes, Morocco и ⁴Laboratory of Mechanics, Energetics, Automation and Sustainable Development, Faculty of Science and Technology, Moulay Ismail University of Meknes, Errachidia, Morocco

Престављена студија има за циљ да утврди колико добро кора нара може уклонити метиленско плаво (MB) из воденог раствора. У ту сврху су спроведене кинетичке, изотермне и термодинамичке студије адсорпције у шаржном систему. Брзина адсорпције MB је била брза и достигла је равнотежу за око 60 min. Достигнуту капацитет адсорпције је близу 42,71 mg g⁻¹ при почетној концентрацији боје од 100 mg l⁻¹. Кинетичко моделовање адсорпције MB је спроведено коришћењем модела псевдо-првог, псевдо-другог реда, Еловичевог модела и модела дифузије унутар честица. Утврђено је да је модел псевдо-другог реда најадекватнији за уклањање кинетичких података на основу вредности R^2 (кофицијент детерминације), RMSE (квадратна средња грешка), ARE (просечна релативна грешка) и χ^2 (хи-квадрат). Такође је откријено да адсорпција MB на кори нара није једноставно ограничена брзином дифузије унутар честица. Изотермни приступ је показао максимални капацитет адсорпције од 67,78 mg l⁻¹ на 298 K коришћењем 2 g l⁻¹ коре нара. Такође је спроведено моделовање равнотеже. Четири статистичке вредности су истакле да се Лангмуров модел најбоље уклапа у односу на Фројндлихов модел. Додатно, егзотермна и спонтана природа процеса адсорпције је откријена термодинамичким истраживањем. Приказани резултати показују ефикасност коре нара као еколошки прихватљивог апсорбента за уклањање MB.

(Примљено 17. марта, ревидирано 1. маја 2023, прихваћено 26. марта 2024)

REFERENCES

1. Z. Y. Velkova, G. K. Kirova, M. S. Stoytcheva, V. Gochev, *J. Serb. Chem. Soc.* **83** (2018) 107 (<https://doi.org/10.2298/JSC170519093V>)
2. I. Khan, K. Saeed, I. Zekker, B. Zhang, A. H. Hendi, A. Ahmad, S. Ahmad, N. Zada, H. Ahmad, L. A. Shah, T. Shah, I. Khan, *Water* **14** (2022) 242 (<https://doi.org/10.3390/w14020242>)

3. H. Elmontassir, K. Elfalaki, Y. Karhat, M. Afdali, *Mor. J. Chem.* **7** (2019) 493 (<https://doi.org/10.48317/IMIST.PRSN/morjchem-v7i3.15882>)
4. V. Vadivelan, K. V. Kumar, *J. Colloid Interface Sci.* **286** (2005) 90 (<https://doi.org/10.1016/j.jcis.2005.01.007>)
5. T. K. Sen, S. Afroze, H. M. Ang, *Water. Air. Soil Pollut.* **218** (2011) 499 (<https://doi.org/10.1007/s11270-010-0663-y>)
6. M. W. Shannon, S. W. Borron, M. J. Burns, L. M. Haddad, J. F. Winchester, Eds., *Haddad and Winchester's clinical management of poisoning and drug overdose*, 4. ed, Saunders/Elsevier, Philadelphia, PA, 2007 (ISBN 10: 0721606938 ISBN 13: 978-0721606934)
7. Z. Cheng, R. Yang, X. Zhu, *Desalination Water Treat.* **57** (2016) 25207 (<https://doi.org/10.1080/19443994.2016.1144535>)
8. H. Xue, X. Wang, Q. Xu, F. Dhaouadi, L. Sellaoui, M. K. Seliem, A. Ben Lamine, H. Belmabrouk, A. Bajahzar, A. Bonilla-Petriciolet, Z. Li, Q. Li, *Chem. Eng. J.* **430** (2022) 132801 (<https://doi.org/10.1016/j.cej.2021.132801>)
9. A. E. Badraoui, Y. Miyah, L. Nahali, F. Zerrouq, B. E. Khazzan, *Mor. J. Chem.* **7** (2019) 416 (<https://doi.org/10.48317/IMIST.PRSN/morjchem-v7i3.16742>)
10. N. Badri, Y. Chhiti, F. Bentiss, M. Bensitel, *Mor. J. Chem.* **6** (2018) 767 (<https://doi.org/10.48317/IMIST.PRSN/morjchem-v6i4.14350>)
11. A. Kesraoui, M. Seffen, F. Brouers, *Mor. J. Chem.* **5** (2017) 659 (<https://doi.org/10.48317/IMIST.PRSN/morjchem-v5i4.7250>)
12. S. Akazdam, W. Yassine, M. Chafi, B. Gourich, *Mor. J. Chem.* **7** (2019) 300 (<https://doi.org/10.48317/IMIST.PRSN/morjchem-v7i2.14014>)
13. P. Colindres, H. Yee-Madeira, E. Reguera, *Desalination* **258** (2010) 154 (<https://doi.org/10.1016/j.desal.2010.03.021>)
14. A. H. Konsowa, *Desalination* **158** (2003) 233 ([https://doi.org/10.1016/S0011-9164\(03\)00458-2](https://doi.org/10.1016/S0011-9164(03)00458-2))
15. D. Wu, Z. Yang, W. Wang, G. Tian, S. Xu, A. Sims, *Chemosphere* **88** (2012) 1108 (<https://doi.org/10.1016/j.chemosphere.2012.05.011>)
16. M. Ouhammou, M. Bouchdoug, A. Jaouad, R. Ouaabou, B. Nabil, *Mor. J. Chem.* **7** (2019) 516 (<https://doi.org/10.48317/IMIST.PRSN/morjchem-v7i3.16009>).
17. G. A. Ismail, H. Sakai, *Chemosphere* **291** (2022) 132906 (<https://doi.org/10.1016/j.chemosphere.2021.132906>)
18. Q. Li, Y. Li, X. Ma, Q. Du, K. Sui, D. Wang, C. Wang, H. Li, Y. Xia, *Chem. Eng. J.* **316** (2017) 623 (<https://doi.org/10.1016/j.cej.2017.01.098>)
19. J. Cheng, C. Zhan, J. Wu, Z. Cui, J. Si, Q. Wang, X. Peng, L.-S. Turng, *ACS Omega* **5** (2020) 5389 (<https://doi.org/10.1021/acsomega.9b04425>)
20. Y.-Y. Lau, Y.-S. Wong, T.-T. Teng, N. Morad, M. Rafatullah, S.-A. Ong, *RSC Adv.* **5** (2015) 34206 (<https://doi.org/10.1039/C5RA01346A>)
21. A. Othmani, A. Kesraoui, M. Seffen, *Euro-Mediterr. J. Environ. Integr.* **2** (2017) 1 (<https://doi.org/10.1007/s41207-017-0016-y>)
22. Q. Wei, F. O. Meyotto, C. W. K. Chow, Z. Nadeem1, Z. Li, J. Liu, S. Desk, *J. Earth Sci. Environ. Stud.* **5** (2020) 51 (<http://dx.doi.org/10.25177/JESES.5.2.RA.10648>)
23. R. Ghilate, F. Sabry, O. Senhaji, R. Taouil, M. Touzani, *Int. J. Innov. Res. Sci. Technol.* **2** (2015) 39 (<http://www.ijirst.org/articles/IJIRSTV2I7003.pdf>)

24. L. Rozumová, O. Životský, J. Seidlerová, O. Motyka, I. Šafařík, M. Šafaříková, *J. Environ. Chem. Eng.* **4** (2016) 549 (<https://doi.org/10.1016/j.jece.2015.10.039>)
25. N. Karić, A. S. Maia, A. Teodorović, N. Atanasova, G. Langergraber, G. Crini, A. R. L. Ribeiro, M. Đolić, *Chem. Eng. J. Adv.* **9** (2022) 100239 (<https://doi.org/10.1016/j.ceja.2021.100239>)
26. S. D. Abkenar, M. Hassannezhad, M. Hosseini, M. R. Ganjali, *J. Serb. Chem. Soc.* **84** (2019) 701 (<https://doi.org/10.2298/JSC181228038D>)
27. R. Ghilate, O. Senhaji, R. Taouil, *Case Stud. Chem. Environ. Eng.* **3** (2021) 100078 (<https://doi.org/10.1016/j.cscee.2020.100078>)
28. Q. Wang, Y. Wang, Z. Yang, W. Han, L. Yuan, L. Zhang, X. Huang, *Chem. Eng. J. Adv.* **11** (2022) 100295 (<https://doi.org/10.1016/j.ceja.2022.100295>)
29. L. Meili, P. V. S. Lins, M. T. Costa, R. L. Almeida, A. K. S. Abud, J. I. Soletti, G. L. Dotto, E. H. Tanabe, L. Sellaoui, S. H. V. Carvalho, A. Erto, *Prog. Biophys. Mol. Biol.* **141** (2019) 60 (<https://doi.org/10.1016/j.pbiomolbio.2018.07.011>)
30. F. Banat, S. Al-Asheh, L. Al-Makhadmeh, *Process Biochem.* **39** (2003) 193 ([https://doi.org/10.1016/S0032-9592\(03\)00065-7](https://doi.org/10.1016/S0032-9592(03)00065-7))
31. R. Gong, M. Li, C. Yang, Y. Sun, J. Chen, *J. Hazard. Mater.* **121** (2005) 247 (<https://doi.org/10.1016/j.jhazmat.2005.01.029>)
32. Y. Wu, L. Zhang, C. Gao, J. Ma, X. Ma, R. Han, *J. Chem. Eng. Data* **54** (2009) 3229 (<https://doi.org/10.1021/je900220q>)
33. G. Annadurai, R. Juang, D. Lee, *J. Hazard. Mater.* **92** (2002) 263 ([https://doi.org/10.1016/S0304-3894\(02\)00017-1](https://doi.org/10.1016/S0304-3894(02)00017-1))
34. R. R. Mphahlele, P. B. Pathare, U. L. Opara, *Sci. Afr.* **5** (2019) 1 (<https://doi.org/10.1016/j.sciaf.2019.e00145>)
35. R. R. Ghilate, O. Senhaji, R. Taouil, *Int. J. Eng. Res. Appl.* **10** (2020) 19 (<http://www.ijera.com/papers/vol10no11/Series-1/C1011011922.pdf>)
36. I. Hmid, H. Hanine, D. Elothmani, A. Oukabli, *J. Saudi Soc. Agric. Sci.* **17** (2018) 302 (<https://doi.org/10.1016/j.jssas.2016.06.002>)
37. S. Azizian, *J. Colloid Interface Sci.* **276** (2004) 47 (<https://doi.org/10.1016/j.jcis.2004.03.048>)
38. Y. S. Ho, G. McKay, *Process Biochem.* **34** (1999) 451 ([https://doi.org/10.1016/S0032-9592\(98\)00112-5](https://doi.org/10.1016/S0032-9592(98)00112-5))
39. Y. S. Ho, G. McKay, *Process Saf. Environ. Prot.* **76** (1998) 332 (<https://doi.org/10.1205/095758298529696>)
40. M. Toor, B. Jin, *Chem. Eng. J.* **187** (2012) 79 (<https://doi.org/10.1016/j.cej.2012.01.089>)
41. I. Langmuir, *J. Am. Chem. Soc.* **38** (1916) 2221 (<https://doi.org/10.1021/ja02268a002>)
42. A. H. Jawad, Y. S. Ngoh, K. A. Radzun, *J. Taibah Univ. Sci.* **12** (2018) 371 (<https://doi.org/10.1080/16583655.2018.1476206>)
43. H. Li, V. L. Budarin, J. H. Clark, M. North, X. Wu, *J. Hazard. Mater.* **436** (2022) 129174 (<https://doi.org/10.1016/j.jhazmat.2022.129174>)
44. N. S. Randhawa, N. N. Das, R. K. Jana, *Desalination Water Treat.* **52** (2014) 4197 (<https://doi.org/10.1080/19443994.2013.801324>)
45. F.-C. Wu, R.-L. Tseng, R.-S. Juang, *Chem. Eng. J.* **153** (2009) 1 (<https://doi.org/10.1016/j.cej.2009.04.042>)
46. G. Crini, E. Lichtfouse, *Green adsorbents for pollutant removal : fundamentals and design*, Springer, Berlin, 2018 (<https://doi.org/10.1007/978-3-319-92111-2>)

47. N. Nasuha, B. H. Hameed, A. T. M. Din, *J. Hazard. Mater.* **175** (2010) 126 (<https://doi.org/10.1016/j.jhazmat.2009.09.138>)
48. M. A. Al-Ghouti, M. A. M. Khraisheh, M. N. M. Ahmad, S. Allen, *J. Hazard. Mater.* **165** (2009) 589 (<https://doi.org/10.1016/j.jhazmat.2008.10.018>)
49. C. E. de F. Silva, B. M. V. da Gama, A. H. da S. Gonçalves, J. A. Medeiros, A. K. de S. Abud, *J. King Saud Univ. Eng. Sci.* **32** (2020) 351 (<https://doi.org/10.1016/j.jksues.2019.04.006>)
50. K. Ben Jeddou, F. Bouaziz, F. Ben Taheur, O. Nouri-Ellouz, R. Ellouz-Ghorbel, S. Ellouz-Chaabouni, *Water Sci. Technol.* **83** (2021) 1384 (<https://doi.org/10.2166/wst.2021.075>)
51. R. Mallampati, L. Xuanjun, A. Adin, S. Valiyaveettil, *ACS Sustain. Chem. Eng.* **3** (2015) 1117 (<https://doi.org/10.1021/acssuschemeng.5b00207>)
52. Z. M. Magriotis, S. S. Vieira, A. A. Saczk, N. A. V. Santos, N. R. Stradiotto, *J. Environ. Chem. Eng.* **2** (2014) 2199 (<https://doi.org/10.1016/j.jece.2014.09.012>)
53. Y. Ren, C. Cui, P. Wang, *Molecules* **23** (2018) 1342 (<https://doi.org/10.3390/molecules23061342>)
54. L. A. da Silva, S. M. S. Borges, P. N. Paulino, M. A. Fraga, S. T. de Oliva, S. G. Marchetti, M. do C. Rangel, *Catal. Today* **289** (2017) 237 (<https://doi.org/10.1016/j.cattod.2016.11.036>)
55. S. M. Miraboutalebi, S. K. Nikouzad, M. Peydayesh, N. Allahgholi, L. Vafajoo, G. McKay, *Process Saf. Environ. Prot.* **106** (2017) 191 (<https://doi.org/10.1016/j.psep.2017.01.010>).